Pre-clinical Imaging Evaluation of the PARP inhibitor Rucaparib

Gilberto Serrano de Almeida

Thesis submitted for the degree of Doctor of Philosophy

Northern Institute for Cancer Research

Faculty of Medical Sciences

The Medical School

Newcastle University

December 2012

Abstract

Poly(ADP-ribose) polymerase 1 (PARP1) is a DNA-binding enzyme involved in DNA repair by the base-excision pathway. The inhibition of PARP1 is being investigated as a cancer treatment. Rucaparib (CO338) is a potent PARP inhibitor currently in Phase II clinical development. In this thesis ^{31}P *in vivo* MR Spectroscopy (MRS) and Dynamic Contrast Enhanced (DCE) MRI were used to study acute effects of rucaparib on energy metabolism and tumour vasculature. *Ex vivo* ^{1}H and ^{31}P-MRS, and *in vivo* [^{18}F]FLT and [^{18}F]FDG-PET, were used to study effects of treatment with rucaparib on tumour metabolism and proliferation.

A2780 and SW620 tumours implanted in mice were scanned in a horizontal Varian 7T MR system. Two *i.v.* injections of the MRI contrast agent gadoteridol were given 90 minutes apart with dynamic phosphorus MRS acquired following the injection of rucaparib, temozolomide or both drugs in combination. The same tumours were evaluated by [^{18}F]FLT- and [^{18}F]FDG-PET after 5 daily treatments with rucaparib, temozolomide or the combination, and the livers of PARP1 knock out (KO) and wild type (WT) mice treated in a similar manner were analysed by *ex vivo* ^{1}H and ^{31}P-MRS.

Tumour uptake of gadoteridol changed significantly after treatment with hydralazine and higher doses of rucaparib in SW620 tumours, and following hydralazine and 1mg/Kg of rucaparib in A2780 tumours. ^{31}P-MRS studies revealed an increase in the inorganic phosphate (Pi) to β-NTP ratio, consistent with impairment of tumour energy metabolism following hydralazine treatment. [^{18}F]FLT-PET demonstrated a significant reduction in the SUV values in the rucaparib/temozolomide combination group in SW620 tumours, and [^{18}F]FDG-PET revealed a non-significant reduction in tumour metabolism in A2780 tumours. ^{1}H *ex vivo* MRS demonstrated an increase in the liver NAD concentrations after treatment with rucaparib, but a decrease following the treatment with temozolomide, regardless of the PARP1 status.

Together, these pre-clinical imaging studies have shown that MR can be used to investigate the acute anti-vascular effects of rucaparib, that [^{18}F]FLT-PET predicted subsequent changes in tumour volume following combined rucaparib and temozolomide treatment, and that *ex vivo* ^{1}H-MRS can be used in mechanistic studies of PARP inhibition. Both MRI/MRS and PET are potential pharmacodynamic and surrogate response imaging biomarkers for PARP inhibitors.

Acknowledgments

Firstly, I would like to thank Herbie Newell and Ross Maxwell for the opportunity they gave me. I am extremely grateful for their support and guidance and will always be in debt to them for their faith and trust in me.

A big thank you to Ian Wilson who taught me all the techniques in the lab and for his personal teachings. He made this PhD possible to accomplish.

Thanks also to Huw Thomas and Yan Zao who helped me in different techniques, providing cells, and filling the nitrogen dewar when the extraction protocol was on its way.

Thank you to Carlo Bawn for his patience and invaluable help in the extraction protocol. It was a long road but his help made us reach the destination.

I would like to thank Adele Kitching and all the technicians and staff in the Keith Unit and CBC for their help.

A great thank you to the staff, colleagues and friends from the Newcastle Magnetic Resonance Centre and Institute of Aging and Health who welcomed me and treated me very kindly (specially my friends from the Millennium Room and the secretaries).

Thank you to the staff and colleagues in the Northern Institute of Cancer Research for their help in so many different aspects of this PhD.

A final and very strong thank you to all my family and friends, from Portugal and from Newcastle, who supported and encouraged me to carry on on this trip and were always there for me.

All the work described in this thesis was performed by me apart from the *ex vivo* spectroscopy acquisition/analysis performed by Carlo Bawn and PET data analysis performed by Ian Wilson.

Contents

List of Figures

List of tables

Abbreviations

ADP:	Adenosine 5'-diphosphate
ADP ribose:	Adenosine 5'-diphosphoribose
AIF:	Apoptosis Inducing Factor
AMP:	Adenosine 5'-monophosphate
ATP:	Adenosine 5'-triphosphate
AUC:	Area Under the Curve
AVI:	Anti-Vascular Index
BER:	Base-Excision Repair
CT:	Computerized Tomography
D_2O:	Deuterium Oxide
Da:	Dalton
dB:	Decibel
DCE-MRI:	Dynamic Contrast Enhanced Magnetic Resonance Imaging
DNA:	Deoxyribonucleic Acid
DSB:	Double Strand Break
eV:	Electron volt
FBS:	Foetal Bovine Serum
FDG:	Fluoro-2-deoxy-2-D-glucose
FID:	Free Induction Decay
FLT:	3'-Deoxy-3'-fluorothymidine
FOV:	Field of View
FSEMS:	Fast Spin Echo Multi Slice imaging sequence
Gd:	Gadolinium
GEMS:	Gradient echo Multi Slice imaging sequence
HR:	Homologous recombination
Hz:	Hertz
ID:	Inner Diameter
ISIS:	Image Selected *in vivo* Spectroscopy
kDa:	kilodalton
KO:	Knock Out
KOH:	Potassium hydroxide
L-Glu:	L-Glutamine
LOR:	Line of response
MBq:	Mega Becquerel

MDP:	Methylenediphosphonic acid
MMR:	Mismatch Repair
MRS:	Magnetic Resonance Spectroscopy
NAD:	Nicotinamide Adenosine Diphosphate
NER:	Nucleotide Excision Repair
NHEJ:	Non-Homologous End-Joining
NTP:	Nucleoside Triphosphate
OD:	Outer Diameter
OSEM:	Ordered Subset Expectation Maximization
PARP:	Poly(ADP-ribose) Polymerase
PBS:	Phosphate Buffered Saline
PCA:	Perchloric Acid
PCr:	Phosphocreatine
Pen Strep:	Penicillin Streptomycin
PET:	Positron Emission Tomography
Pi:	Inorganic Phosphate
PMT:	Photomultiplier tube
ppm:	parts per million
PRESS:	Point resolved spectroscopy
pw:	pulse width
RCF:	Relative Centrifugal Force
RF:	Radio Frequency
ROI:	Region of Interest
Rpm:	Rotation per minute
RTV4:	Relative Tumour Volume 4 times
SNR:	Signal to Noise Ratio
SPECT:	Single Positron Emission Tomography
SSB:	Single Strand Break
STEAM:	Stimulated Echo Acquisition Mode
SUV:	Standardised Uptake Value
T:	Tesla
TE:	Echo Delay Time
TK1:	Thymidine Kinase 1
tof:	transmitter offset
tpwr:	transmitter pulse power

TR:	Repetition Time
TSP:	3-(Trimethylsilyl)propionic-2,2,3,3-d4 acid
TMZ:	Temozolomide
VEGF:	Vascular Endothelial Growth Factor
VOI:	Volume of interest
WT:	Wild Type

Chapter 1. Introduction

1.1 Cancer

Hippocrates observed tumour angiogenesis for the first time, using the word "cancer" to describe the large blood vessels which supply tumours and which have a visual similarity with the claws of a crab (reviewed by Feinberg *et al.*, 2006). However, there are earlier Egyptian papyrus documents dating from 1600BC which describe eight breast cancer cases treated by cauterization (in a review by Visvader, 2011). In the middle of the nineteenth century, Theodore Schwann described the properties of cells from animals and plants (Schwann, 1847), a description which was used by Rudolph Virchow (1859) to develop the concept of cellular pathology (Virchow, 1859), and August Foerster to categorize tumours (Foerster, 1865). Based on Virchow's work, Foerster hypothesised that tumours develop from connective cells and that vascular tumours grow from already existing small blood vessels as published by Rather, 1978, and reviewed by Wright and Poulsom, 2012). In the early years of the twentieth century, Boveri proposed for the first time that cancer could be caused by chromosomal abnormalities in cells (reviewed by Visvader, 2011).

Tumours are very heterogeneous in several aspects including proliferation rate, cellular morphology, number and type of genetic lesions and the way they respond to treatment. Each aspect of this heterogeneity is very important in the study and comprehension of cancer and in the search for possible treatments (reviewed by Visvader, 2011). Despite advances in basic cancer research, adult solid tumours are still being treated primarily with non-specific cytotoxic drugs and radiation. However, recent studies have identified genetic changes and epigenetic alterations that underlie cancer and these insights are leading to the development of specific and personalised targeted therapies.

There are two main models for the development of cancer: the clonal genetic model of cancer and the epigenetic progenitor model of cancer.

<u>Clonal genetic model</u>

In the clonal genetic model (Figure 1.1), a single cell (cancer stem cell) undergoes several genetic alterations which cause continued clonal selection and tumour cell heterogeneity. Cancer cells in individual patients are

heterogeneous in their phenotype and cells with the capacity to propagate and/or sustain the disease represent a subset (reviewed by Greaves, 2010). Tumour proliferation, metastatic capacity and resistance to drug treatments are some of the consequences of the clonal genetic alterations, and dominantly acting oncogenes and silenced tumour suppressor genes give some support to the clonal genetic model. Colorectal cancer is an example where a series of modifications in oncogenes and tumour-suppressor genes allow evolution from small benign masses (adenomas) to advanced stage tumours with metastatic capability (reviewed by Feinberg *et al.*, 2006). Gatekeeper genes with a role in promoting apoptosis in ageing cells to avoid oncogenesis are often mutated in cancer, and mutations in such genes are incorporated into the clonal genetic model.

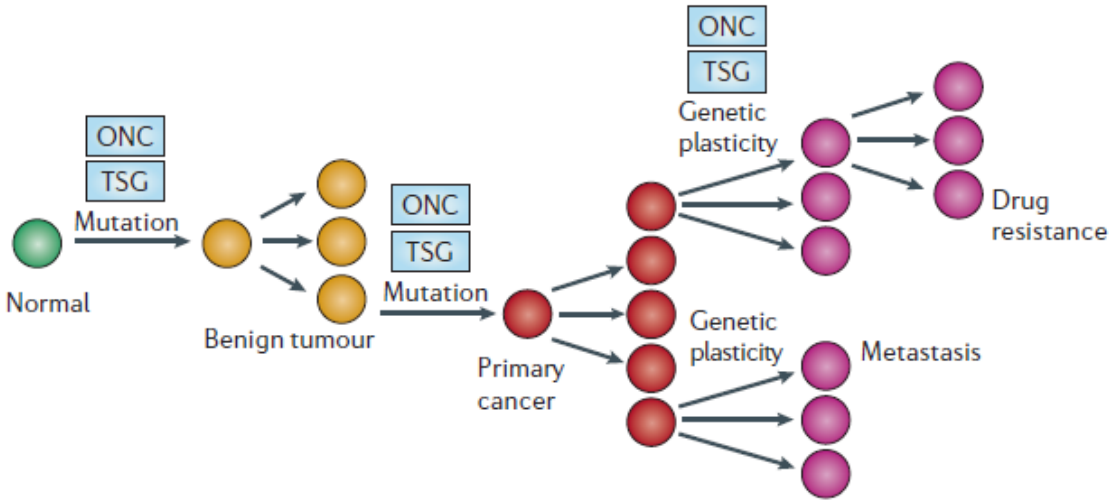

Figure 1.1: Depiction of the clonal genetic model of cancer. A single cell suffers mutations resulting in dominantly acting oncogenes (ONC) paired with inactivated tumour suppressors (TSG). Each mutation causes selective overgrowth of a monoclonal tumour cell population. The mutation accounts for tumour properties like drug resistance and/or metastasis while epigenetic changes are regarded as surrogate alterations for mutations. Copied from Feinberg *et al.* (2006).

Different oncogenes and different sets of mutations can cause normal stem or progenitor cell changes resulting in long term self-renewing capacity. Intra-clonal genetic diversity is also a fundamental element of cancer and leads to the Darwinian selection of sub-clones through major bottlenecks and progressive evolution of the disease (Figure 1.2, reviewed by Greaves, 2010).

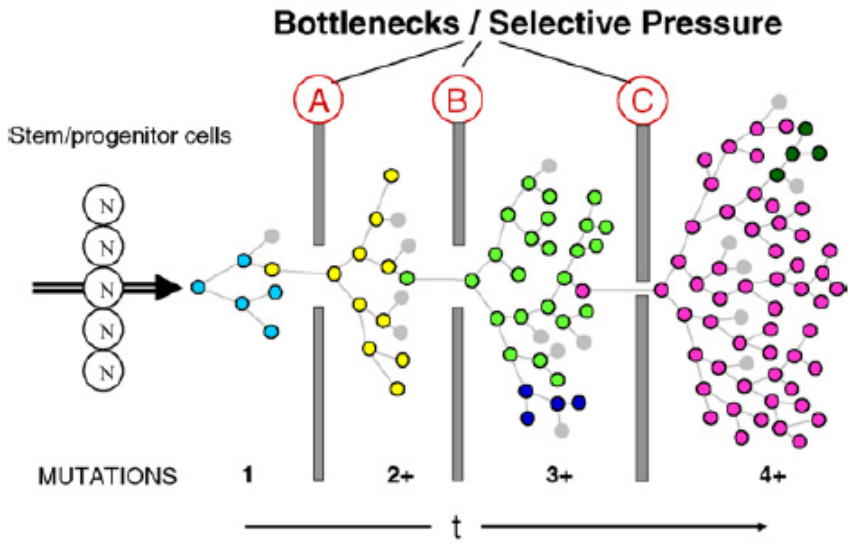

Figure 1.2: Depiction of the clonal evolution of cancer. N stands for normal cells, where A and B are intracellular and intercellular/microenvironmental constraints and C decimation by therapy. This last event is equivalent to a catastrophic environmental change in speciation. t is time and the different colours in the cells represent distinctive mutant genotypes. Copied from Greaves (2010), which in turn was adapted from Nowell (1976).

Notwithstanding its strengths, the clonal model has limitations. In colorectal cancer, for example, specific stages of tumour progression can be reached without known mutations. Furthermore, gene expression alterations can be related to properties without underlying gene mutations. Tumour kinetics are also hard to correlate with multiple clonally-selected mutations (reviewed by Feinberg *et al.*, 2006).

Epigenetic progenitor model

Pathological epigenetic changes are non-sequence based alterations inherited through cell division. These changes represent an alternative to mutations and chromosomal alterations for disrupting gene function, and can lead to abnormal activation of growth promoting genes and silencing of tumour suppressor genes. Examples of pathological epigenetic changes are altered DNA methylation (hypo- and hyper-methylation) and/or changes in chromatin structure (reviewed by Feinberg *et al.*, 2006). These changes have also been reviewed by Thomas Lindhal (1993) and Shikhar Sharma *et al.* (2010). Although clonal genetic changes are common in tumours, epigenetic alterations are present too and represent an alternative to genetic changes. In the early stages of tumour genesis, epigenetic changes are present and they are also important in normal

tissue. Furthermore epigenetic changes may explain heterogeneity in tumour cell growth, invasion, metastasis and resistance to therapy.

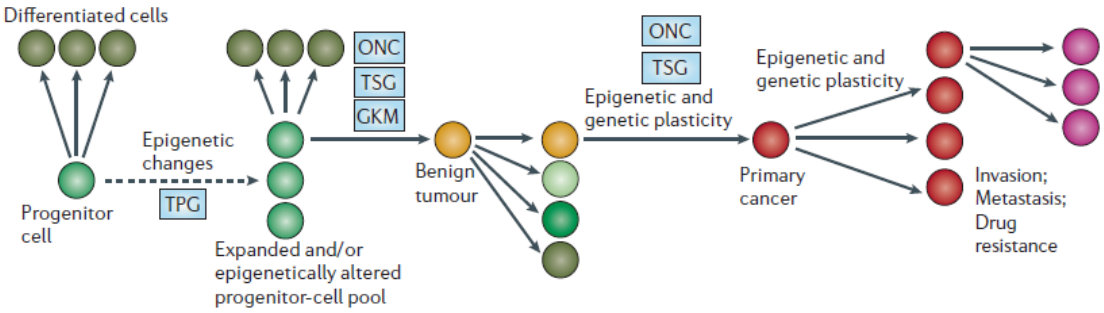

Figure 1.3: Depiction of the epigenetic progenitor model. In a first step, stem/progenitor cells suffer epigenetic alterations mediated by abnormal regulation of tumour progenitor genes (TPG). These alterations can be caused by internal events in the stem cells or by externally inflicted damage. Secondly, tumour suppressor genes (TSG) in solid tumours or oncogenes (ONC) in leukaemia and lymphoma, cause mutation of the gatekeeper (GKM). Finally the tumour evolves due to genetic and epigenetic instability. Copied from Feinberg *et al.* (2006).

In the epigenetic progenitor model (Figure 1.3) progenitor cells in a given organ or system originate from a polyclonal precursor population of “neoplasia ready” cells when they are disrupted by epigenetic changes. In the earliest stages of the process mutations are initiated and are specific to the tumour type. These mutations can be substituted for by epigenetic changes resulting in oncogene activation or tumour suppressor gene silencing. Cancer develops in a manner that enhances the ability of tumour cells to evolve and this evolution in promoted by epigenetic and genetic plasticity. As opposed to genetic changes arising from mutations and chromosomal rearrangements, epigenetics changes can be reversed. However, in the process of reversing the epigenetic changes, other irreversible genetic changes can be initiated (reviewed by Feinberg *et al.*, 2006).

Cellular hierarchy within tissues is an important step in identifying cells of origin in cancer. In normal tissues stem cells evolve to progenitor cells and then to differentiated cells which constitute tissues or organs. Stem cells are candidates to become cancer precursors due to their self-renewal and longevity, which encases the possibility of sequential accumulation of genetic or epigenetic alterations. Nonetheless, any cell with proliferative capacity can originate cancer. If the proliferative cell acquires mutations which provide it with an indefinite self-renewal capacity and avoids cell differentiation, cancer may arise (reviewed by Visvader, 2011).

A valuable tool in research into cellular cancer origins are genetically engineered mouse models. Transgenic or conditionally targeted gene technologies are used to study the effect of oncogenes and tumour suppressors genes in a whole animal context. This is achieved by the use of cell specific engineered expression of oncogenes and/or deletion of tumour suppressor genes *in vivo.* A second approach involves the use of cell sub-populations genetically manipulated *ex vivo* and their subsequent orthotopic transplantation into mice to study tumour induction. One example of the development of transgenic mice is provided by Josiane Ménissier-de Murcia *et al.* (1997), where the PARP1 gene exon 1 was disrupted generating $PARP1^{-/-}$ (PARP1 deficient) mice (de Murcia *et al.*, 1997). Piskunova *et al.* have studied the effects of the $PARP1^{-/-}$ status in aging and carcinogenesis in mice and have shown that $PARP1^{-/-}$ mice have a mean life span 13.3% lower than $PARP1^{+/+}$ mice indicating an ageing effect due to the PARP1 deletion. Although the both $PARP1^{-/-}$ and $PARP1^{+/+}$ had a similar incidence of spontaneous carcinogenesis (72% approximately), the $PARP1^{-/-}$ had a 20.5% higher incidence of malignant tumours as well as an earlier tumour development when compared to $PARP1^{+/+}$ mice (Piskunova *et al.*, 2008).

Cancer hallmarks

As reviewed by Hanahan and Weinberg (2011) cancer possesses distinctive and complementary capabilities which underly tumour growth and metastatic dissemination. While normal tissue cells control the production and release of growth promoting signals through the cell cycle, cancer cells proliferate chronically. The proliferation signalling can be sustained by the production of growth factors by the cancer cells or by mutations in signal transduction pathways thereby promoting self-proliferation.

Cancer cells also need to evade growth suppressors. Many of these suppressors are the products of tumour suppressor genes that downregulate cell proliferation. Contact inhibition is a property of normal tissues where cell contact with each other leads to the release of growth inhibition factors which cause delay or stop cell growth.

Failure to engage cell death pathways is also an important hallmark of cancer and apoptosis is the name given to the process of programmed cell death. Normal cells possess mechanisms to identify the number of divisions they can go through and at the end of the lifetime, or if an accumulation of genetic errors reaches high levels, the apoptotic machinery is activated to promote cell death. In cancer cells, apoptotic machinery is restricted or circumvented by the deactivation of apoptosis promoter genes, for example *TP53*.

Cancer cells, unlike normal cells, have unlimited replicative capability, also known as replicative immortality. As mentioned above, normal cells have a pre-determined number division cycles at the end of which they enter a senescent state (nonproliferative but viable) or undergo crisis ending in cell death. Telomeres protect the end of chromosomes and, as normal cells divide, protection is lost when the telomere becomes eroded to a critical length, at which point cells enter into crisis. Telomerase is the enzyme that adds telomere repeat segments to the ends of telomeric DNA, and in normal cells telomerase is absent. However, telomerase spontaneously immortalizes cells when it is re-expressed at functionally significant levels, and telomerase activation in conjunction with oncogene activation and tumour suppressor gene loss, has been shown to be required for full cellular transformation.

During embryogenesis the development of the vascular system relies on the growth of new endothelial cells and their assembly into tubes (Hanahan and Weinberg, 2011). As summarized by Hanahan and Coussens (2012) adult tissues possess quiescent blood vessels and angiogenesis (growth of new blood vessels from pre-existing ones) is a transient process which occurs in pathophysiological conditions, namely tissue remodelling or during the female reproductive cycle (Hanahan and Coussens, 2012). Tumour cells, like normal cells, require a supply network to obtain nutrients and oxygen, and to remove metabolic waste and carbon dioxide. To acquire the supply network, tumour cells release vascular endothelial growth factors (VEGF) which promotes angiogenesis and hence tumour growth.

Cancer cells not only invade their surrounding space due to their sustained replication, but they also invade nearby blood and lymphatic vessels allowing

tumour cells to travel long distances and form small nodules of cancer cells in a new location in the body, a process called metastasis. This process is potentiated in carcinomas arising from epithelial tissues (Hanahan and Weinberg, 2011).

It is not only genetic instability that is responsible for tumour genesis. Cells from the immune system can be found in neoplastic lesions to different extents, and it was thought that this is a response of the immune system to the arising tumour. However, in the early stages of neoplastic progression, inflammation can foster the development of neoplasia through the release of cytokines and signalling molecules which can accelerate malignancy. This process may explain in part how the immune system allows tumours cells to grow and develop into tumour masses (review by Hanahan and Weinberg, 2011).

Another distinguishing property of tumours is that tumour cells can reprogram their energy metabolism to meet the energy requirements of tumour cells at a time when tumour angiogenesis does not provide a reliable vascular system. In the early twentieth century Otto Warburg *et al.* (1927) made the first measurements of glucose and lactic acid in tumours. They were able to determine that 66% of the glucose used by tumour was used in fermentation (anaerobic respiration) while the remaining 34% were used in (aerobic) respiration (Warburg *et al.*, 1927). Andrei Drabovich *et al.* (2012) developed a targeted proteomic assay for the accurate quantification of protein expression in glycolysis/gluconeogenesis, TCA cycle and pentose phosphate pathways. This assay was performed on human MCF-7 breast cancer cells which had been grown in conditions designed to mimic the exposure of cells in cancer tissue to intermittent hypoxia, glucose deprivation and hormonal stimulation. They were able to identify in MCF-7 cell lysate 4074 proteins annotated to 216 distinct pathways using the KEGG pathway database, with a total of 2738 proteins identified with at least 2 peptides allowing the measurement of protein expression in multiple metabolic pathways and monitor differences in protein expression between healthy and cancer cells (Drabovich *et al.*, 2012).

Advances in the discovery and understanding of cancer hallmarks have made possible the development of targeted therapies which are more effective against

specific tumours types. Figure 1.4 is a representation of the cancer hallmarks and how they are increasingly being targeted by a new generation of therapies (review by Hanahan and Weinberg, 2011).

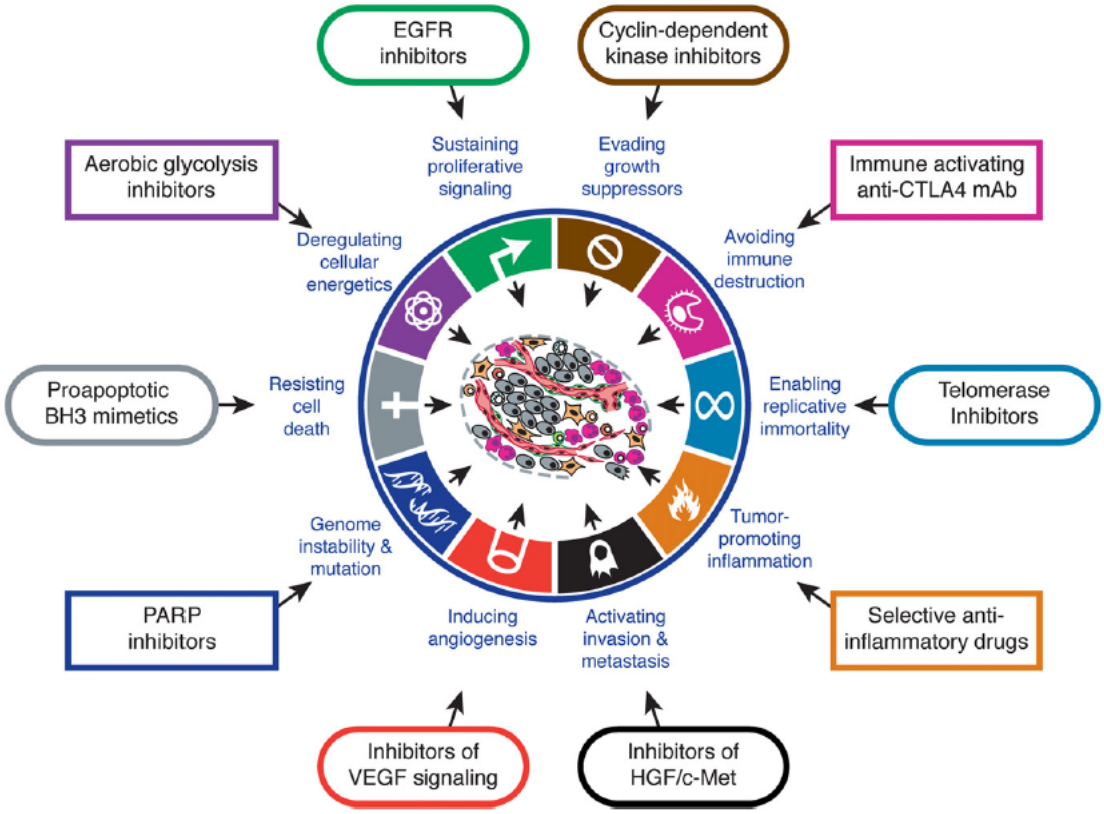

Figure 1.4: Representation of the acquired capabilities necessary for tumour growth and progression (inner circle) with the correspondent drugs being studied to counteract those capabilities. Some of the drugs are already in clinical trials. The number of potential drugs is very high, with different molecular targets and different modes of action. Copied from Hanahan and Weinberg (2011).

Genomic instability

An increased susceptibility to alterations in the genome during the life cycle of cells is referred to as genomic instability. During cell division genomic instability is associated with the failure of parental cells to duplicate the genome in an accurate manner and precisely distribute the genomic material between the progeny cells. Epigenetic alterations such as abnormal DNA methylation including that of tumour suppressor genes and/or chromatin modification are also important factors in genomic instability. There are four major processes in the cell division cycle that minimise genomic instability: high fidelity DNA replication in S-phase of the cell cycle, precise chromosome segregation in mitosis, and coordinated error free cell cycle and sporadic DNA damage repair. With genetic instability, the impact of DNA repair can be diverse. Repair can either remove the damage and cause alteration in the DNA sequence and/or

rearrangement of genome segments during the repair process, in what is known as “error prone” repair, or remove the damage and preserve the original DNA structure in an “error free” repair process (Shen, 2011). The search for factors which cause genomic instability is ongoing, and reducing genomic instability by the inhibition of “error-prone” pathways provides another approach to tumour treatment (for example Rooney *et al.,* 2003, and Yoon *et al.*, 2011). In relation to PARP, Valérie Schreiber *et al.* established a stable HeLa cell line that endogenously produced the 46kDa DNA binding domain of human poly(ADP-ribose) polymerase (PARP-DBD) which resulted in trans-dominant inhibition of PARP activity. When treated with N-methyl-N’-nitro-N-nitrosoguanidine (MNNG), the PARP-DBD expressing cells exhibited chromosomal instability demonstrated by higher frequencies of both spontaneous and MNNG-induced sister chromatid exchanges and characteristic nucleosomal DNA ladder formation (a hallmark of cell death by apoptosis). These results suggest a close connection between genomic stability and PARP function (Schreiber *et al.,* 1995, and reviewed by Kirkland, 2010).

1.2 Poly (ADP-ribose) polymerase (PARP) inhibitors

Poly (ADP-ribose) polymerases (PARPs) are elements of vital importance in the DNA base excision repair pathway that are activated by single DNA strand breaks, one of a number of DNA repair pathways.

DNA Repair pathways

In a review by Orlando *et al.* (2012), DNA repair was defined by the type and extent of the damage inflicted in the DNA chain. Damage that results in double strand breaks initiates one of two main repair pathways: homologous recombination (HR) and nonhomologous end-joining (NHEJ) recombination. The damage can be inflicted by endogenous or exogenous damaging factors such as metabolic, chemical or radiation injury (Orlando *et al.*, 2012). In NHEJ Ku proteins recognise double strand breaks, bind to them and activate DNA-dependent protein kinase (DNA-PK), which in turn leads to the recruitment and activation of end-processing enzymes, polymerases and DNA ligase IV. In NHEJ there is an alternative pathway independent of Ku proteins called microhomology mediated end joining (MMEJ), or alternative end-joining, which also results in sequence deletions.

Homologous recombination (HR) is initiated by DNA single strand generation and promoted by several proteins including the MRE11-RAD50-NBS1 complex. RAD51, BRCA1 or BRCA2 that subsequently catalyse the repair pathway, in which the single stranded DNA invades the complementary undamaged template and DNA ligation and substrate resolution is facilitated by the action of polymerases, nucleases, helicases and other components. The HR repair pathway is also used to restart stalled replication forks and to repair interstrand DNA crosslinks (as reviewed by Jackson and Bartek, 2009). However, the HR pathway is entirely dependent upon access to the complimentary undamaged sister chromatid and hence can only operate when a 4N DNA complement is present in the cell during late S, G2 and early M phases. In contrast, NHEJ can operate throughout the cell cycle.

Ionizing radiation or alkylating agents cause single strand breaks into DNA. These single strand breaks can be repaired by three main repair pathways:

nucleotide excision repair (NER), base excision repair (BER) and mismatch repair (MMR) (reviewed by Orlando *et al.*, 2012).

As reviewed by Jackson and Bartek (2009), helix distorting base lesions are recognized by the nucleotide excision repair system which can follow one of two pathways: transcription coupled NER, which targets lesions that block transcription, or global genome NER. The damage is excised in the form of a 22-30base oligonucleotide (resulting in single strand DNA). In MMR a single strand incision is triggered by the detection of mismatches or insertion/deletion loops. Nuclease, polymerase and ligase enzymes act upon the incision in order to repair the damage. Finally, base excision repair involves the recognition of a damaged base by a DNA glycosylase enzyme, which mediates the base removal prior to completion of repair performed by nuclease, polymerase and ligase proteins (Jackson and Bartek, 2009).

PARP1 is a key component of DNA single strand break repair by the base excision repair pathway (review by Orlando *et al.*, 2012). Poly(ADP-ribose) polymerase-1 (PARP1) is a 116kDa nuclear enzyme present in eukaryotes and the first of a superfamily of 18 proteins. As depicted in Figure 1.5, PARP1 is composed of three main domains: an N-terminal DNA-binding domain which contains two zinc fingers, an automodification domain and a C-terminal catalytic domain.

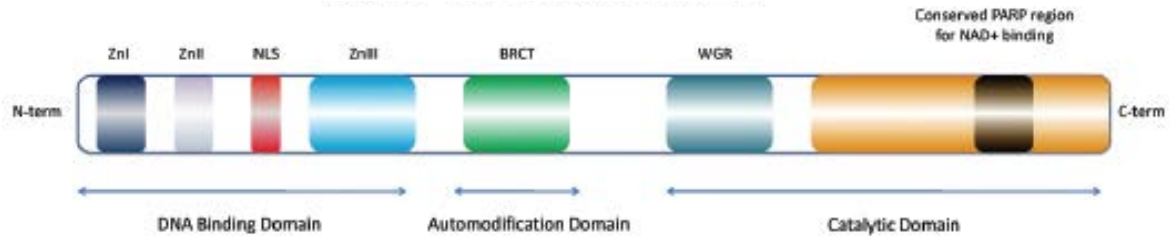

Figure 1.5: Representation of the structure of poly(ADP-ribose) polymerase-1 (PARP1) with its three domains. Copied from Leung *et al.* (2011).

In 1963, Pierre Chambon *et al.* reported several characteristics of what was then a new DNA-dependent polyadenylic acid synthesizing nuclear enzyme. Following the addition of nicotinamide mononucleotide to hen liver cell nuclei effects on the new RNA-polymerase enzyme were studied. The new enzyme was shown to be activated by nicotinamide mononucleotide, DNA-dependent, not stimulated by polyA (i.e. was not an RNA binding protein) and not inhibited

by nucleoside triphosphates or various ribonucleases (published by Chambon *et al.*, 1963, and reviewed by Kummar *et al.*, 2012). In 1976, Payne and Bal used autoradiography to assess the *in vitro* incorporation of [^{3}H]NAD into onion embryo and merismatic tissue, and were able to show a high level of cytological incorporation into merismatic nuclei. At least 30% of the cells showed “heavy” labelling similar to that produced by *in vitro* DNA polymerase activity (Payne and Bal, 1976). Caplan *et al.* (1979) subsequently purified poly (ADP-ribose) polymerase from calf thymus and demonstrated ADP-ribose transfer from NAD as well as kinetic and acceptor characteristics (published by Caplan *et al.*, 1979, and reviewed by Hottiger, 2011).

PARP Functions

Poly(ADP-ribose) polymerases have complex biological roles with numerous functions. PARP1 has an important role in DNA repair and genome integrity maintenance as discussed in the previous section. Delayed DNA base excision repair pathway and high frequency of sister chromatid exchange in PARP1 deficient cells exposed to ionizing radiation or treated with alkylating agents suggest a role for PARP1 function under these conditions. Furthermore, genetically modified mice which do not express PARP1 show increased mortality when exposed to high levels of ionizing radiation or treatment with alkylating agents, when compared to PARP1 wild type mice (de Murcia *et al.*, 1997).

In a review by Virág and Szabó (2002), the role of PARP1 in regulating the function of several transcription factors was discussed with special emphasis on inflammatory mediators such as inducible nitric-oxide synthase, intercellular adhesion molecule 1 and the major histocompatibility complex class II. PARP1 also coactivates NF-kB which is a key transcription factor in the regulation of inflammatory mediators, and PARP1 is also involved in DNA replication and differentiation. In the nuclei of proliferating cells poly(ADP-ribose) undergoes an accelerated metabolism. Additionally, a number of replication factors and centromere proteins have been shown to be substrates for PARP.

The overexpression of tankyrase-1 (PARP5a) induces gradual and progressive elongation of telomeres in telomerase positive human cells, and PARP1 has also been implicated in the maintenance of telomere length. PARP1 activation

is thought to mediate cell death in the form of necrosis; whereas mild genotoxicity activates PARP facilitating DNA repair and cell survival, severe DNA damage causes PARP overactivation which translates into NAD^+ and ATP depletion and, therefore, necrosis. It has also been shown that the base excision machinery can use poly(ADP-ribose) polymer as an emergency source of energy for the synthesis of ATP (Virág and Szabó, 2002).

Besides PARP-catalysed covalent poly(ADP-ribosylation), poly(ADP-ribose) polymers are able to bind non-covalently to specifc $(ADP\text{-}ribose)_n$ binding motifs in proteins, modifying their function, and a final function of poly(ADP-ribosylation) may be the regulation of the cytoskeletal organization (Virág and Szabó, 2002).

Although PARP1 is a molecular sensor for DNA single strand breaks and has a key role in the repair of these lesions, PARP2 is also activated by DNA strand breaks and genetic instability has been shown to increase in PARP2-deficient mice. PARP1 and PARP2 display partially redundant functions (reviewed by Schreiber *et al.*, 2006). This redundancy has been demonstrated by the generation of PARP1 and PARP2 knockout mice. PARP1 mice are viable and fertile indicating that PARP1 activity is not required in the absence of genotoxic stress. However, these mice and cells derived from them are hypersensitive to ionizing radiation and alkylating agents. In response to DNA damage PARP1 deficient cells still generate poly(ADP-ribose) suggesting the presence of a second PARP enzyme (PARP2). PARP2 knockout mice were developed, and again showed viability and fertility but once more delayed DNA repair after exposure to alkylating agents (reviewd by Curtin, 2005). Double null PARP1 and PARP2 knockout mice lack viability dying early in development at the beginning of gastrulation (de Murcia *et al.*, 2003).

PARP3 is thought to have a role in double strand break DNA repair, and studies have shown that PARP3 is recruited to laser-induced DNA damage sites. In human cells depleted of PARP3 delayed double strand break repair is found together with reduced survival in response to irradiation and after PARP1 inhibition. Mouse models with PARP1 and PARP3 disruption reveal increased radiosensitivity suggesting a conjoint role in double strand break repair.

Although the exact molecular mechanism involved remains uncharacterized, it has been hypothesised that PARP3 promotes an alternative non-homologous end joint repair pathway (De Vos *et al.*, 2012).

PARP1 in DNA damage repair

As illustrated in Figure 1.6, when a DNA strand suffers a break, PARP1 and PARP2 use their DNA binding domain to connect to the break. Once attached, hydrolysis of NAD^+ with consequent release of nicotinamide and one proton (H^+) starts the catalytic domain transfer of the ADP-ribose moiety to nuclear protein acceptors. The formation of an ester bond between the amino acid acceptor and the first ADP-ribose initiates the reaction. The formation of a 2'-1'' glycosidic bond is involved in the polymer elongation, and the polymer branches after on average twenty ADP-ribose units with branching points every forty to fifty ribose units. Branching reactions share the chemistry with the elongation reaction due to the equivalent orientation of the 2' OH of the ribose groups relative to the adenine in the elongation mode or to the nicotinamide in the branching mode of NAD^+. To degrade poly(ADP-ribose) glycosidic bonds between ADP-ribose units are cleaved by endo- and exo-glycolytic activities of the nuclear enzyme poly(ADP-ribose) glycohydrolase (PARG). In heavily damaged cells NAD^+ is extensively consumed by the activity of PARP, and regenerated by PARG and NAD^+ recycling enzymes (Schreiber *et al.*, 2006).

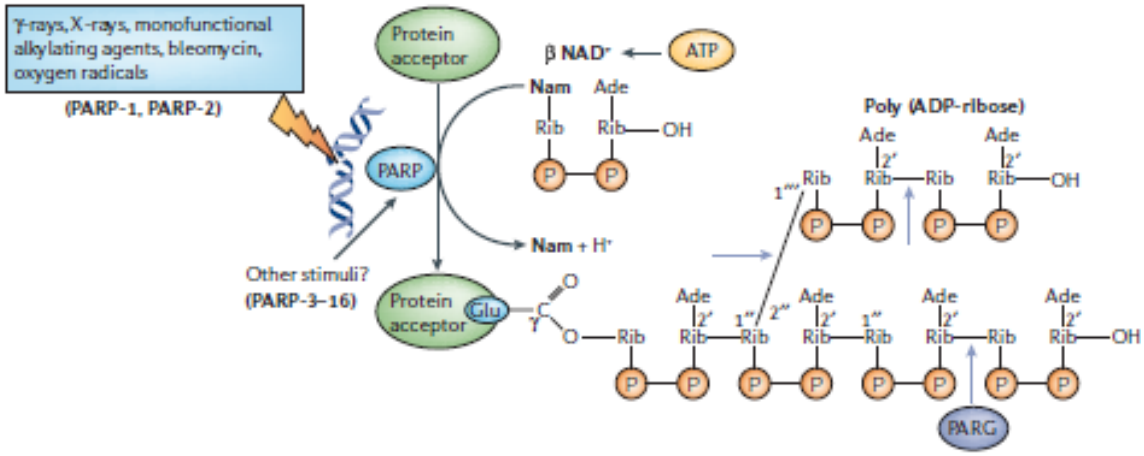

Figure 1.6: Representation of DNA damage and repair and the role of PARP. Copied from Schreiber *et al.* (2006).

PARP is thought to be rapidly activated under several pathophysiological conditions with activation due to the action of DNA damaging anticancer drugs, the most relevant to the studies described in this thesis. Acute and chronic

inflammatory disorders are also important pathologies where PARP is involved at different levels by functioning as a co-activator of the NF-kB and AP-1 transcription factors. When activated, these transcription factors trigger the synthesis of inflammatory mediators such as nitric oxide, and subsequently peroxinitrites and highly reactive hydroxyl radicals. All these toxic species can cause extensive DNA damage which in turn activates the DNA repair function of PARP. Acute neuronal and myocardial cell death following ischaemia reperfusion injury also induces PARP overactivation in association with the flavoprotein apoptosis inducing factor (AIF) release. Activation and consequent toxic effects are decreased in PARP1 or PARP2 knockout mice or by PARP inhibitors. These observations indicate a potential benefit of therapeutically targeting PARP1 and PARP2 in order to treat inflammatory, neurological or cardiac disorders, and several drugs are being studied, some of which have reached human clinical trials (Schreiber *et al.*, 2006). In 2012 Leonardo Cavone and Albano Chiarugi reported preliminary studies of PARP inhibition in mice for multiple sclerosis treatment (reviewed by Cavone and Chiarugi, 2012).

Lastly, poly(ADP-ribose) metabolism is perturbed in tumour cells. PARP1 gene expression is upregulated although there is no increase in mRNA levels. For example, in low-grade malignant non-Hodgkin's lymphoma cells have a high cellular PARP content when compared with normal lymphocytes. PARP activity has also been found to be upregulated in hepatocellular carcinomas when compared with normal liver tissue (reviewed by Virág and Szabó, 2002).

Synthetic Lethality

The development of PARP inhibitors has allowed the concept of synthetic lethality to be studied in patients for the first time. Normal cells possess redundant and interconnecting pathways to prevent lethality caused by single mutations. Tumour cells, as a result of the loss of genetic material can rely for their growth and viability on non-redundant pathways. When that is the case, disruption of the remaining active pathway will eventually cause therapeutic effects. Synthetic lethality is therefore defined as the absence of lethality by the disruption of one normal pathway in normal cells but the presence of lethality in tumour cells lacking redundant pathways following inhibition of the remaining pathway. In accordance with this hypothesis, candidate genes or proteins can

be screened for and identified as targets by the use of gene knockout cell lines or by siRNA in conjunction with small molecule chemicals or drugs (reviewed by Leung *et al.*, 2011).

In particular, synthetic lethality underlies the anti-proliferative activity of PARP inhibitors in DNA repair-defective tumour cells. Hence the formation of single strand breaks in homologous recombination (HR) DNA repair pathway deficient cells induces hypersensitivity to PARP inhibition. The single strand breaks can be the result of endogenous DNA damage or external damaging agents such as ionizing radiation and alkylating agents, and homologous recombination defects derive mainly from BRCA1 or BRCA2 gene mutations. In tumours which meet both requirements, single strand breaks induced by, for example, alkylating agents, if not repaired by PARP activity, become double strand breaks and, due to the homologous recombination deficiency, the tumour cells accumulate damage and cannot survive. PARP inhibition in HR-defective cell is an excellent example of synthetic lethality (published by Bryant *et al.*, 2005, and Farmer *et al.*, 2005, and reviewed by Orlando *et al.*, 2012).

PARP inhibitors

In the early 1980s, 3-substituted benzamides (simple analogues of nicotinamide) were shown to increase alkylating agent cytotoxicity (Durkacz *et al.*, 1980). These first generation PARP inhibitors represent early examples of the development of drugs to enhance antitumour activity in chemo- and radiotherapy. A second generation of PARP inhibitors with increased potency and specificity was developed in the 1990s, Banasik *et al.* (1992) reporting a screening study of 170 compounds and reviewed by Curtin (2005). Third generation PARP inhibitors were shown to possess increased potency and improved pharmacokinetic properties which allowed pre-clinical studies to assess potential efficacy in cancer treatment. Examples of this effort were published by Calabrese (2003) and Thomas (2007), resulting in the identification of the first PARP inhibitor for clinical trials (Calabrese *et al.*, 2003; Thomas *et al.*, 2007). PARP inhibitors exhibit enhanced anti-proliferative activity when used in combination with DNA single strand break-inducing treatments such as the alkylating agent temozolomide, ionizing radiation or topoisomerase-I inhibitors, (for example, Calabrese *et al.*, 2003; Daniel *et al.*, 2009; Spagnolo *et al.*, 2012)

Similarities between the sensitization effect caused by the absence of PARP1 in $PARP1^{-/-}$ cells and PARP1 inhibition in $PARP1^{+/+}$ cells on the cytotoxic effects of anticancer drugs indicates that lack of PARP1 activity is the underlying cause in both cases. Contributions to chemosensitization due to inhibition of other members of the PARP family are not known due to the lack of isoform specific inhibitor (Wahlberg *et al.*, 2012). It is important to note that PARP inhibition is not only toxic to BRCA1 or BRCA2 deficient tumour cells, but that inhibition is also toxic to normal cells with BRCA2 deficiency, suggesting that PARP inhibitors may have a role in the prophylactic treatment of women that are heterozygous for the BRCA2 gene (reviewed by Schreiber *et al.*, 2006). Hay *et al.* reported that PARP inhibition in mouse small intestine BRCA2 deficient cells increases apoptosis to high levels 6 hours after treatment with evidence of tissue repopulation 12 hours after treatment. Also, the repopulation rate was higher in the treated mice when compared against the non-treated ones (Hay *et al.*, 2005). In a review by De Soto and Deng (2006) state that $BRCA^{-/-}$ pre-cancerous cells have higher sensitivity to PARP inhibition when compared to wild type cells whilst cancer cells respond differently to PARP inhibition depending on the conditions. They propose that in early stages of tumourgenesis BRCA1 and BRCA2 mutant cells are sensitive to PARP inhibition, however, in later stages of BRCA deficient tumour cells might become insensitive to PARP inhibition due to further mutations which can lead to cancer development (De Soto and Deng, 2006). However, a prolonged PARP inhibition may leave DNA mutations unrepaired which can lead to malignancy similar to a BRCA carrier. Studies over a long period of time are required to find the effects of a long treatment with PARP inhibitors (Weil and Chen, 2011).

PARP inhibitors which are now in clinical trials include ABT888, AZD2281, INO-1001, BSI-201 and CO338 (rucaparib). These and other PARP inhibitors and their clinical status are summarized in Table 1.1. These agents have different pharmacokinetic and clinical properties, for example, CO338 (rucaparib) is already in Phase II clinical trials where it has been given over 5 days combined with temozolomide by intravenous infusion. Pharmacodynamic measurements of PARP activity in peripheral blood lymphocytes revealed 74-97% PARP inhibition following the administration of 200mg/m^2 of temozolomide combined with 12 mg/m^2 of CO338 (rucaparib) (reviewed by Rodon *et al.*, 2009).

Agent	Company	Route	Clinical status
CO338/rucaparib	Clovis	*i.v.* (oral)	Phase I/II combination
AZD2281/olaparib	AstraZeneca/Kudos	oral	Phase II/III combination
ABT888/veliparib	Abbott	oral	Phase I/II combination
BSI-201 iniparib	BiPar/Sanofi-Aventis	*i.v.*	Phase II/III combination
INO-1001	Inotek	*i.v.*	Phase Ib complete
GPI21016	MGI Pharma/Eisai	oral	Phase I
CEP-9722	Cephalon	oral	Phase I
MK4827	Merck & Co.	oral	Phase I
BMN-673	Biomarin/Lead Pharmaceuticals		Pre-clinical

Table 1.1: PARP inhibitors in clinical development. Adapted from Calvert and Azzarati (2011).

1.3 Biomarkers

A biomarker has been defined by Newton *et al*. (2011) as “an objectively measurable substance that may be used as an indicator of a biological or a pathological state. When applied to a disease process, a biomarker can be used to detect disease, predict prognosis or predict response to a pharmacological agent. A biomarker must facilitate an improvement in life expectancy or quality of life in order to be of use in clinical practice.” (Newton *et al.*, 2011).

Possibly the first description of a cancer biomarker was offered by Henry Jones in 1848 when he described peculiar reactions (precipitation temperature dependent) in urine samples from cancer patients by boiling with strong nitric acid (Jones, 1848). In the 1960’s the prostate specific antigen (PSA) was described as a screening biomarker for prostate cancer and it is still being used today (reviewed by Mishra and Verma, 2010).

Several disciplines and technologies have been applied to the study of cancer biomarkers. In the presence of a tumour, traditional techniques such as biopsy or more invasive surgical procedures can be carried out. However, in the absence of tumour or to avoid an invasive procedure, alternative techniques are available. These techniques include analysis of circulating tumour cells (published by Cristofanilli *et al.*, 2004, reviewed by Tanaka *et al.*, 2012), mutation specific PCR on circulating tumour DNA (published by Anker *et al.*, 1997, and reviewed by Aung *et al.*, 2010), and proteomic approaches to study serum or plasma (published by Li *et al.*, 2002, and reviewed by Mani *et al.*, 2011). Measuring autoantibodies specific for tumour cells is a further non-invasive technique (Harlow *et al.*, 1981; Petras *et al.*, 1998; Neumann *et al.*, 2011). Imaging tumours *in situ* at the molecular level is also possible (Jeswani and Padhani, 2005). The diagram in Figure 1.7 depicts biomarkers grouped by different criteria. These definitions are not rigid and a consensus around cancer biomarker terminology has yet to be reached (Sawyers, 2008).

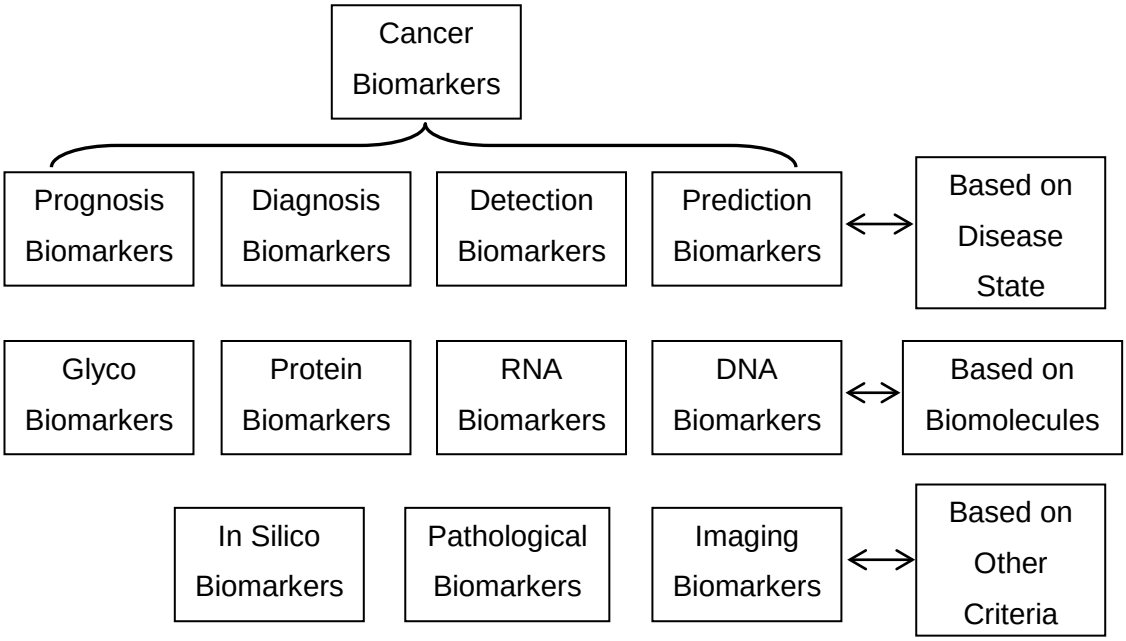

Figure 1.7: Organizational diagram for different cancer biomarkers. On the right are the main criteria by which the biomarkers on the left are organized. Adapted from Mishra and Verma (2010).

Prognostic biomarkers measure features that differentiate between benign and malignant tumours. These biomarkers are also important in staging the tumour and help clinicians to decide what the appropriate treatment is. Predictive biomarkers are used by clinicians to select the most appropriate treatment and response biomarkers assess the effect of a specific treatment on the tumour. Different patients will respond differently to treatments so biomarkers are very important. Even once a treatment is selected, it is necessary to decide the appropriate dose and schedule at which point pharmacokinetic and pharmacodynamic biomarkers are important.

Regarding samples for invasive biomarker studies, DNA, RNA, protein and carbohydrates can be used. DNA can be collected from tissue, saliva, cerebrospinal fluid, bone marrow or tumour cells circulating in the blood. At a molecular level, DNA markers include single nucleotide polymorphisms, loss of heterozygosity, variation in the copy number of genes, chromosomal translocations/fusions, micro-satellite instability, and gene mutations. Also epigenetic modification of nucleic acids and associated proteins (histones and non-histones) can also act as biomarkers. Quantitative Reverse Transcription Polymerase Chain Reaction (RT-qPCR) and Serial Analysis of Gene Expression (SAGE) are examples of methods used in the search for biomarkers

at the level of RNA expression, and micro RNAs (miRNA) are also potential biomarkers.

Proteins have also been widely used to generate biomarker data and methods to study proteins in cancer include two-dimensional fluorescence difference gel electrophoresis (DIGE) (Alban *et al.*, 2003), and mass spectrometry (MS) (Semmes *et al.*, 2005), with studies extending to quantitative proteomics (Chen *et al.*, 2007). Mass spectrometry has also been used in the detection of disease associated carbohydrate biomarkers such as N-linked and O-linked glycans (An *et al.*, 2006; Alley *et al.*, 2010), and glycobiomarkers may be more stable than RNA or proteins so they are suitable for epidemiological studies.

Less invasive biomarker technologies, namely imaging techniques, include X-ray, computed tomography (CT), magnetic resonance imaging (MRI), radionuclide techniques (PET and SPECT) or ultrasound. These techniques can be used to screen, diagnose or stage tumours, and to determine the response to treatment as reviewed by Mishra and Verma (2010).

As shown in Figure 1.8, the development of a biomarker follows a long path before it is available for general use.

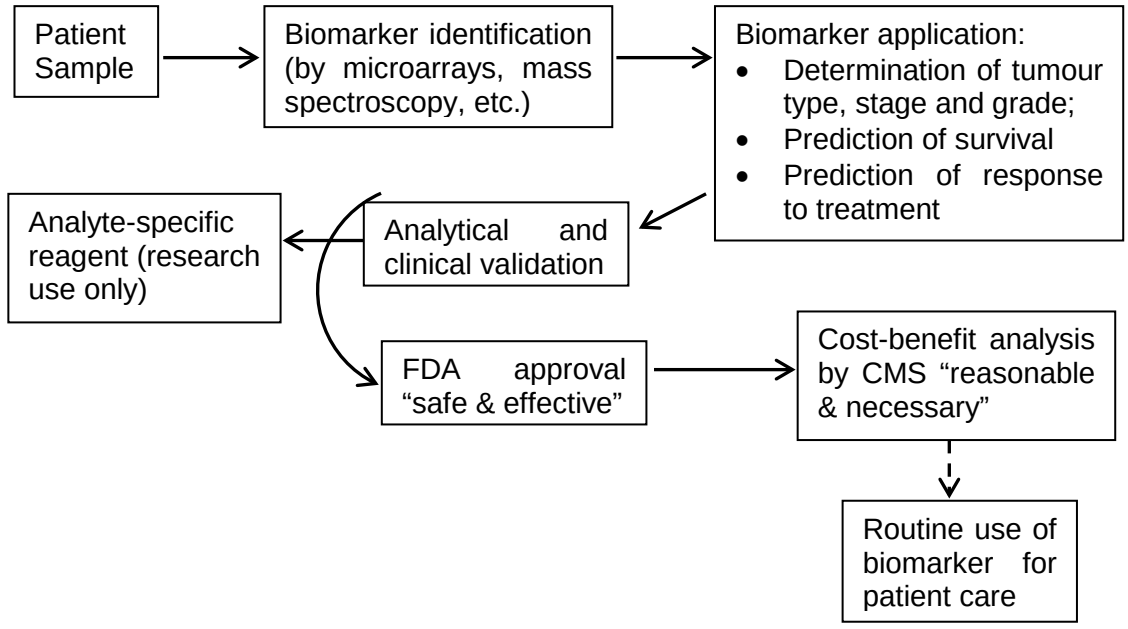

Figure 1.8: Diagram of the development of cancer biomarkers in the USA. After identification, the biomarker needs to be evaluated for a particular clinical application and analytically and clinically validated prior to US Food and Drug Administration (FDA) approval and before the Center for Medicaid and Medicare Services (CMS) determine the "reasonable and necessary" improvement in patient care. Adapted from Ludwig and Weinstein (2005).

There are five conceptual phases in the development of the biomarker: a pre-clinical discovery phase, clinical assay development and validation, retrospective longitudinal studies, prospective evaluation and use in routine cancer management. Although biomarkers should be validated in prospective and well controlled clinical trials, in reality clinical studies are usually retrospective, often generating inconsistent results and involving few patients. In an attempt to speed up the process and lower the costs, multi-institutional teamwork can facilitate analytical and clinical validation (reviewed by Ludwig and Weinstein, 2005, and Sawyers, 2008).

Magnetic Resonance Imaging (MRI) can provide not only anatomical information but also physiological information making it valuable for detecting the size, location and extent of tumour lesions as well as their response to treatment. The principles of MRI will be explained in subsection 1.4.1 with more detail in the case of Dynamic Contrast Enhanced (DCE) MRI, which can provide important information regarding a range of tumour properties. The use of contrast agent allows the measurement of differences in the uptake of the agent in the tumour before and after the treatment, as well as other parameters such as tumour perfusion, permeability and tumour vascular function (Castellani *et al.*, 2009). DCE-MRI is of vital importance in the non-invasive evaluation of new antiangiogenic and antivascular drugs, and the assessment of the delivery of therapeutic agents to the cancer cells, as reviewed by O'Connor *et al.* (2007). A different approach being developed is the attachment of functional contrast agents to specific ligands or targeting moieties enabling them to be substrate specific to cellular processes.

Diffusion-weighted (DW) MRI is used to measure parameters associated with the rate and distance of water molecule diffusion, and does not require the injection of contrast agents. DW-MRI can be useful to assess the likely access of a drug to cells in the tumour (Haider *et al.*, 2007).

An alternative technique in MR which can be used to provide biomarker data is Magnetic Resonance Spectroscopy (MRS). The principles underlying MRS are explained in subsection 1.4.2 in more detail. Through a voxel located in the tumour it is possible by MRS to measure concentrations of biochemicals or

drugs and their metabolites in cells. This information can be used in pharmacokinetic and pharmacodynamic studies. Using proton (^{1}H) MRS concentrations of lactate, choline derivatives, inositides, creatine compounds and glutamine/glutamate, for example, can be measured (Ackerstaff *et al.*, 2001; Benveniste *et al.*, 2012). Using phosphorus (^{31}P) MRS adenosine triphosphate (ATP), phosphomonoesters like phosphocholine, and inorganic phosphate, for example, can be measured(Yan *et al.*, 2011). Intracellular pH can also be measured with ^{31}P-MRS (Nath *et al.*, 2012), and changes in the metabolites present in cells can be used as pharmacodynamics and response markers following treatment. In pharmacokinetic studies, MRS can also provide direct measurements of drug concentrations not only in tumours but also other organs throughout the body (liver, kidneys, brain, for example). Drugs which contain fluorine have relatively high magnetic resonance sensitivity, and background fluorine signals in living tissue are not usually detected (McIntyre *et al.*, 2011). On a direct comparison, ^{31}P-MRS is less sensitive than ^{1}H-MRS (usually described as 6.63% sensitivity of ^{1}H-MRS) and so it needs much larger volume elements to achieve good signal-to-noise (SNR) ratios for the metabolites of interest. However, it covers a wider chemical shift range (around 30ppm for biological phosphates) and does not face the same solvent suppression challenges as ^{1}H-MRS (Gadian, 1995).

The principles underlying Positron Emission Tomography (PET) will be explained in more detail in section 1.5. As an imaging technique based on the injection and detection of radioactive agents in the patient, PET can provide distribution/uptake information for the labelled agent in the tumour and/or across the body of the patient. [^{18}F]-Fluoro-2-deoxy-2-D-glucose (FDG) is the gold standard PET tracer and its uptake is widely used as a metabolism biomarker in tumours. However, [^{18}F]FDG lacks specificity as other metabolically hyperactive tissues or sites of inflammation can have an increased uptake of glucose (Rebollo Aguirre *et al.*, 2009).

[^{18}F]-3'-Deoxy-3'-fluorothymidine (FLT) is used in PET as a marker of DNA synthesis and cell proliferation. FLT-PET can provide information about cellular proliferation within a tumour without relying in volume changes (Grierson *et al.*, 2004). Other labelled compounds that have been used as PET tracers include

[^{11}C]-thymidine, which also marks cellular proliferation (Ullrich *et al.*, 2008), [^{15}O]-H_2O used as a marker of tissue perfusion (Shi *et al.*, 2010), and [^{15}O]-CO which is a marker of blood volume as published by Kurdziel *et al.* (2003) and reviewed by Kluetz *et al.* (2010). Amino acid metabolism can also be studied through PET by the use of, for example, [^{11}C]-methionine (published by Bergström *et al.*, 1983, and reviewed by Langen *et al.*, 2008), and tricarboxylic acid cycle activity can be studied with [^{11}C]-acetate (Ho *et al.*, 2003). Labelled antibodies and peptides are also in development to study receptors on tumour cell membranes. With the current development of gene therapies, PET methods are also being developed to monitor *in vivo* gene expression, and 2'-fluoro-2'deoxy-1β-D-arabinofuranosyl-5-[^{124}I]iodouracil ([^{124}I]-FIAU) is an example of a gene marker (Carlin *et al.*, 2009). There is also an increasing interest in imaging drug resistance pathways, and [^{11}C]-daunorubicin and [^{11}C]-verapamil have been used to monitor P-glycoprotein-mediated multidrug resistance in rodent tumour models (Wanek *et al.*, 2012).

PET can also be used to study pharmacokinetics of drugs. To do so, drugs of interest need to be radiolabelled with positron emitting isotopes such as ^{11}C, ^{13}N, ^{18}F or ^{124}I, and examples of drugs labelled for PET imaging include [^{18}F]-5FU (Zissen *et al.*, 2011), [^{11}C]-temozolomide (Saleem *et al.*, 2003), [^{13}N]-cisplatin (Ginos *et al.*, 1987), and [^{18}F]-tamoxifen (Inoue *et al.*, 2009).

Although it has many advantages, PET also has its limitations. Not all drugs can be labelled. The parent drug needs to contain, for example, a fluorine atom to be labelled with [^{18}F]; however, even then, it might not be possible to achieve radiolabelling. If the radiolabelling requires protracted chemical and purification steps it may not be feasible due to the short half-life of many PET isotopes, and the precursors necessary for radiolabelling may also not be available or the position of the label may not metabolically stable. PET images or physical resolution can be quite poor and there is also a lack of chemical resolution, i.e. PET images do not directly distinguish between the parent radiotracer and its metabolites. Lastly, the costs of the equipment and the radiochemistry necessary might also be a limitating factor as reviewed by Workman *et al.* (2006).

In Table 1.2 are indicated the positron-emitting nuclides of common usage in PET with their individual half-life in minutes.

Nuclide	Half-life (min)
^{11}C	20.4
^{13}N	9.96
^{15}O	2.03
^{18}F	109.8
^{68}Ga	68.3
^{82}Rb	1.25
^{99m}Tc	52
^{124}I	6×10^{3}

Table 1.2: Positron-emitting nuclides of interest in PET. Adapted from Bailey and Towsend (2005).

1.4 Magnetic Resonance Imaging

Purcell, Torrey and Pound, independently with Bloch, Hansen and Packard, formed the two physics groups which in 1946 began the nuclear magnetic resonance field. Purcell and Bloch demonstrated empirically the nuclear magnetic resonance phenomenon by proving that, when placed in a magnetic field, some nuclei (including hydrogen) would rotate with a frequency proportional to the field strength due to their intrinsic magnetic moment (Buxton, 2002). From 1946 until the 1970s the main use for Magnetic Resonance (MR) was in physics and chemistry, with the use of Magnetic Resonance Imaging (MRI) expanding from the 1970s onwards (Reiser *et al.*, 2008).

It was Bloch who first hypothesized that charged particles, when spinning, create a magnetic field and act like a bar magnet (Hashemi *et al.*, 2003). Nuclei have a ground state of non-zero angular momentum or angular spin, *I*, when they possess an odd number of protons and/or neutrons. This property is a result of the intrinsic angular moments and the orbital angular momentums of the protons and neutrons which constitute the nuclei. The angular momentum of an atomic nucleus is proportional to the magnetic moment, μ, and the proportionality factor is the gyromagnetic ratio, γ, which is a characteristic of each nuclide. The hydrogen atom is widely used in MR studies due to 3 characteristics: it has a spin quantum number (s) of ½, it is the most abundant nucleus in biological systems and it has the largest gyromagnetic ratio of all stable nuclei (Reiser *et al.*, 2008).

The angular spin of atomic nuclei is the result of the summation of the spins of all the individual components of the nucleus, i.e. protons and neutrons. In the example of the hydrogen atom, the nuclear spin is caused by the spin of a single proton. From quantum theory, each atomic nucleus has specific energy levels and, in the case of hydrogen example, the proton has two energy states which can be $+\frac{1}{2}$ or $-\frac{1}{2}$, the different energy states depending on the direction that each proton is spinning. The proton can either spin about its axis, creating a magnetic field, pointing north (“parallel”), or south (“anti-parallel”), depending on the direction of spin. The protons in different energy levels can pair in order to cancel out each other’s magnetic field and create a total nuclear magnetic field which is null. In nuclei with an odd number of protons there will be one

unpaired proton in one of the energy states which will create a nuclear net magnetic field or magnetic dipole moment that is non-zero (Hashemi *et al.*, 2003). When subject to a magnetic field, the proton suffers a torque by its net magnetic field which will make the dipole align with the external magnetic field (excluding any other effects). However, due to the angular spin of the proton, it does not align instantly with the magnetic field but rather precesses around it (Buxton, 2002).

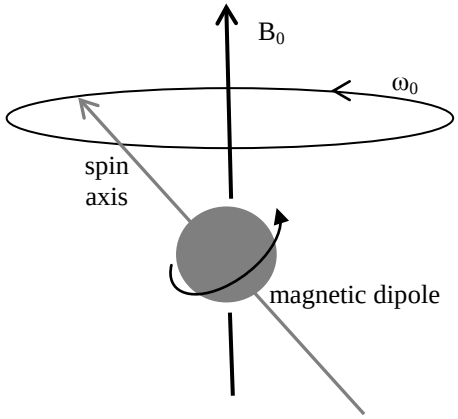

Figure 1.9: Depiction of the precession phenomenon of a magnetic dipole. B_0 stands for the external magnetic field which exerts a torque in the magnetic dipole that due to its spin will precess at an angle with the gravitational field rather than aligning with the external magnetic field. ω_0 is the precession frequency and is proportional to the magnetic field. Adapted from Buxton (2002).

As illustrated in Figure 1.9 the frequency of precession of the proton in the magnetic field, ω_0, is the frequency of nuclear magnetic resonance, also named the Larmor frequency, and it is directly proportional to the strength of the external magnetic field. The equation describing the Larmor frequency (ω_0) is:

$$\omega_0 = \gamma B_0$$

where B_0 stands for the external magnetic field and γ is the previously defined gyromagnetic ratio, unique for each nucleus. The units for ω_0 are MHz/T and the Larmor equation is the fundamental equation in magnetic resonance imaging (Buxton, 2002). As stated previously, all the protons in the nuclei have their own magnetic dipole moment which in the absence of a magnetic field allows them to spin around their own axis in random directions, cancelling each other. When placed in a magnetic field, the protons will align with the external magnetic field. Although approximately half will be parallel and the other antiparallel, and hence cancel each other, more will align with the direction of the magnetic field, B_0, creating a net magnetization, M_0, which is in the same direction as B_0 (Hashemi *et al.*, 2003). As indicated above, once the proton is

placed in a magnetic field, it precesses around the magnetic field axis. The first few rotations only approximate towards the magnetic field axis, but after several rotations the proton will be aligned with the magnetic field as the alignment is the lowest energy state for the system. If the proton is aligned in a direction opposite to the magnetic field it is in the highest energy state and will have to return to the lowest state, precessing towards alignment and releasing the remaining energy as, for example, random thermal motions of molecules. The time a proton takes to undergo this relaxation process is called T_1 or the spin lattice relaxation time.

The net magnetization of a sample, M_0, has the same direction as the external magnetic field, B_0, and so cannot be measured. However, if M_0 changes direction and diverts from B_0 it will subsequently relax and precess towards the lower energy state. To obtain directional deviation the net magnetization vector is altered with a radio frequency (RF) pulse, which is an electromagnetic wave and, hence, an oscillating magnetic field (albeit several orders weaker than B_0). If the RF pulse has a frequency that matches the precession frequency, ω_0, a resonance phenomenon will take place and M_0 will precess in a spiral moving away from the B_0 axis as long as the RF pulse is on. The angle formed by the tipped M_0 and B_0 is called the flip angle, θ (Figure 1.10).

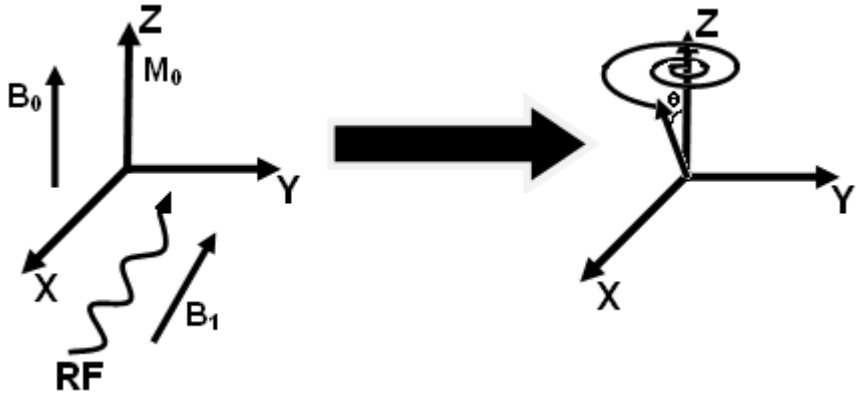

Figure 1.10: Representation of the interaction of a RF pulse and the net magnetization, M_0, of a sample and how that causes M_0 to precess away from the axis of the external magnetic field, B_0. The angle between M_0 and B_0 at the moment the RF pulse is turned off, is represented by the flip angle, θ. Adapted from Hashemi *et al.* (2003).

Tipping of nuclei, a proton in the case of hydrogen, can only occur if the RF pulse and its magnetic field, B_1, oscillate at the precessional frequency of the nuclei. Under such conditions the RF pulse adds energy to the protons in a process called resonance. When the RF pulse is turned off the net magnetization precesses back to alignment with B_0, which translates into a

moving magnetic field that in the presence of a coil will induce a current in it. This current is measurable and proportional to the precessing magnetization and is called the free induction decay (FID), free because as soon as the RF pulse is off the nuclei can precess freely, decay because the signal is transient and induction because it induces a current in the coil (Buxton, 2002).

All magnetic resonance imaging requires a magnet to provide the external magnetic field, B_0, and there are three main types of magnets: permanent magnets, resistive magnets and superconducting magnets. The first are permanently on and have low costs and maintenance. The resistive magnets use the electromagnetic principle by which an electric current running through a magnet generates a magnetic field, and these magnets can be turned on and off. Finally the superconducting magnets are a special version of resistive magnets with the difference that they operate near absolute zero temperatures so the resistance to electrical current is negligible. In superconducting magnets very strong electric currents generate high strength magnetic fields without generating too much energy. To achieve and maintain the low temperatures cryogens have to be used, namely liquid nitrogen and/or liquid helium, making these magnets very expensive to run. Nevertheless superconducting magnets are the most common magnets available in the market.

Another essential component in NMR is the coil. A coil is composed of several loops of wire which can either generate a magnetic gradient (gradient coil) or an oscillating magnetic field (RF coil). RF coils can provide the transmission and/or reception of RF pulses. Gradient coils can cause variations in the magnetic field which can be used for spatial location or to create a more homogeneous magnetic field, B_0 (shim coils). The transmitter/receiver coils have different configurations, from surface to volume coils, and are optimized for different imaging requirements, for example, the time of acquisition, spatial resolution, and signal to noise ratio (SNR).

The flip angle caused by an RF pulse can be controlled by the strength of the pulse (B_1) and its duration, τ. The flip angles are commonly 90° or 180°, but partial flips where the angle is less than 90° can be used depending on the study. The relaxation time, T_1, defined above, refers to the longitudinal

relaxation time that the spins take to realign with the magnetic field, B_0, axis. It is also the time the spins take to dissipate the energy accumulated during the RF pulse to the surrounding lattice, thus T_1 is also known as the spin-lattice relaxation time.

Using a xyz axis, net magnetization, M_0 can be described as the sum of the vectors M_z where the z axis has the same direction as B_0, and M_{xy} where xy is the perpendicular plane to B_0. In the resting state, M_z is equivalent to M_0 as the vector does not possess a component in the xy axis. If a 90° pulse is used to tip M_0, M_z will become null and the M_{xy} will become equal to M_0. As soon as the RF pulse is off, M_z starts to increase as M_{xy} starts to decrease as a result of the precessing of M_0 towards alignment with B_0. At the same moment, all the spins are in phase (lined up in the same direction and spinning at the same frequency). However, due to interactions with other spins (each proton has its own spin and creates its own small magnetic field as a moving particle) and/or due to the inhomogeneities of B_0, the spins start to spin out of phase. If T_1 is the relaxation time that represents the time M_z takes to increase from 0 to M_0, T_2 represents the time M_{xy} takes to go from M_0 to zero. This is called the transverse relaxation time or spin-spin relaxation time and, in the case of ^1H spins within water molecules *in vivo*, is five to ten times shorter than T_1. T_2 depends mainly on the tissues in the sample, and so cannot be controlled. T_2* is equally affected by the spin to spin interaction as well as by the external magnetic field inhomogeneities, making it shorter than T_2. Both T_1 and T_2 are inherent properties of the sample tissue and so not directly controllable (i.e. only by means of contrast agent injection).

Only one signal, from one FID, is not enough to acquire any spatial information from the sample, as it represents signals from all the protons of the sample with no spatial discrimination. One solution is the use of gradient coils to spatially encode the signal. This translates into several RF pulses emitted while the gradient across the sample varies, returning multiple FIDs which will allow the reconstruction into an image. (Hashemi *et al.*, 2003) The series of RF pulses have to have an interval between them to allow the spin to recover before it is tipped again. This interval period is called the Repetition Time (TR). After a net magnetization M_0 is tipped by an RF pulse into the xy plane (M_{xy}) it will start to

precess back to alignment with the z axis with a time constant T_1. After a period of time (TR) another RF pulse is applied to the sample tipping M_z back to the xy plane. If TR is very long (>5xT_1), the spin will have recovered and M_z will be equal to M_0 before the second RF pulse. In most cases TR is smaller (<5xT_1) so that at the moment the spin is tipped again, M_2 is smaller than M_0. The result in terms of signal for this chain of RF pulses will be a series of exponential curves that do not reach full magnetization.

The interval between the turning off of the RF pulse and the acquisition of the FID is controllable and is the echo delay time (TE). Due to this time delay in the acquisition time, the FID is only a fraction of the maximum signal intensity. However, the FID can be corrected by knowledge of the T_1 and T_2 curves. As discussed above, T_1 is specific for each tissue/material and different tissues can be imaged in the same scan. If TR is too short, the differences between tissues will be impossible to determine as the signal acquired will be too weak. If on the other hand TR is too long, the differences in T_1 will not allow differentiation of the tissues. Ideally, TR should be chosen according to the T_1 of the tissue being studied. Another approach to enhancing tissue contrast is to vary the TE. Due to the different compositions of different tissues, T_2 and T_2* are different, and TE can be varied to exploit the differences. If TE is too short, although the signal strength will be high, there will be little difference between tissues. If on the other hand TE is long, the differences in T_2/T_2* in different tissues will accentuate the tissue contrast but with a low SNR. For example, water, due to its sparse molecular structure, has a long T_2 and also a long T_1; solids, in contrast to water, have a compact structure which translates into a short T_2 and an intermediate T_1. Fat has natural motional frequencies identical to the Larmor frequencies where energy transfer to and from the lattice is very efficient when T_1 is very short T_2 intermediate (Hashemi *et al.*, 2003).

MRI is a technique which allows anatomical imaging, very often in three dimensions. Therefore, the localization of a signal acquired from a patient is essential. The knowledge that the resonant frequency generated by an atom is directly proportional to the strength of the magnetic field at the nucleus location is used in the creation of magnetic field gradients in the magnet. Three gradient coils are part of the MRI scanner and each generates linear variation in the

magnetic field along each axis. However, there are alternative means of providing localization in MRI, and slice selection, frequency encoding and phase encoding are three ways of allowing localization in three spatial directions. In slice selection, the RF pulse used is constricted to a narrow range of frequencies centred on the intended frequency v_0. Due to the gradient field, only a narrow spatial band in the body will resonate according to the band of frequencies in the RF pulse. The location of the slice changes when the central frequency v_0 changes and/or with variation in the gradient, and the slice thickness is dependent on the bandwidth of the RF pulse. If the slice selection is able to narrow the location of a signal to a spatial band, the location in the plane perpendicular to the magnetic field B_0 direction is still missing, and hence frequency and phase encoding are used. Considering the direction of B_0 as being the z axis, after an excitation RF pulse a negative field gradient pulse is turned on along the x axis. This negative x-axis pulse is followed by another one, this time a positive x-gradient, causing a gradient echo to occur halfway through the second gradient pulse. The gradient echo can be defined as a gradient which causes dephasing spin vectors to change their precession direction by 180°, forcing them to refocus and phase once more. The frequency encoding process results in a sum of signals over a range of frequencies along the same direction. Each frequency corresponds to a different signal and signal amplitude which, by means of a Fourier Transform, is converted into a spatial location along the x axis. However, the signal is still a line over the y axis. To overcome this issue, a phase encoding technique is used. Similar to the frequency encoding technique, phase encoding applies a gradient along the y axis which makes the transverse magnetization precess at different rates along the axis while the gradient is on. When the gradient is turned off the spins precess at the same rate but at a different phase, depending on their position in the y axis, allowing a precise location of the FID signal (Buxton, 2002).

As discussed above, MRI scans are performed with the use of not one single RF pulse but several RF pulses over a period of time. The RF pulses are optimized (frequency, TR, TE) for each study and are used several times in a sequence. There are three “classical” pulse sequences: saturation recovery sequence, inversion recovery sequence and spin-echo sequence. A system is said to be saturated when the longitudinal magnetization has just been flipped

into the xy plane (perpendicular to B_0 direction) by a 90° pulse. Therefore, a saturation recovery sequence is formed by a series of 90° pulses emitted with a certain time interval between them (TR) (Figure 1.11).

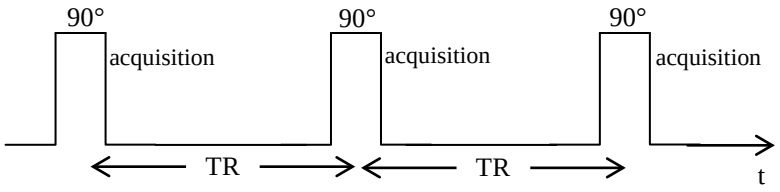

Figure 1.11: Pulse scheme for the saturation recovery sequence. Adapted from Reiser *et al.* (2008).

As shown in Figure 1.12, the inversion recovery method differs from the saturation recovery technique by using a 180° pulse (an inversion pulse which inverts by 180° relative to the longitudinal magnetization) before the emission of a 90° RF pulse (readout pulse). There is a time interval between the 180° and 90° pulse which is called the inversion time T_i. At $t=T_i$ there is a partially relaxed net magnetization along the z axis which the 90° pulse will rotate into the xy plane. As soon as the 90° pulse is off the FID signal is acquired.

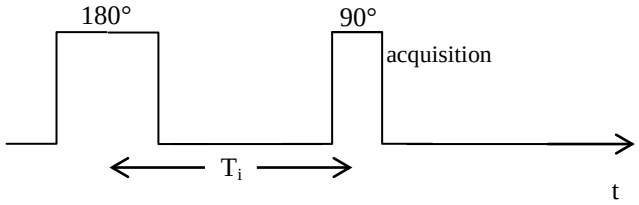

Figure 1.12: Pulse scheme of the inversion recovery sequence. Adapted from Reiser *et al.* (2008).

As described above, T_2 and T_2* are dependent on fluctuating local magnetic fields and inhomogeneities of B_0. While the effect of fluctuating local magnetic fields cannot be reversed, spatial inhomogeneities in the magnetic field B_0 can be compensated for by the use of a spin-echo sequence.

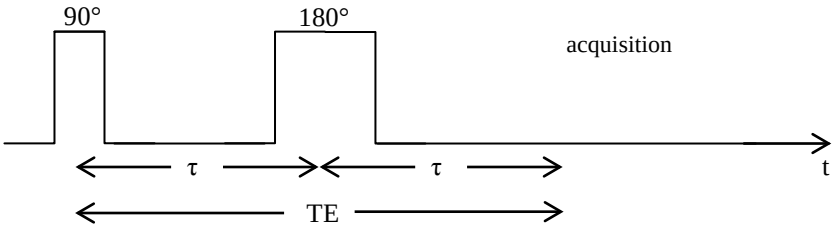

Figure 1.13: Pulse scheme of the spin-echo sequence. Adapted from Reiser *et al.* (2008).

In a spin-echo sequence a first 90° RF pulse is used to tip the magnetization to the xy plane. Once the RF pulse is off, the precession rate towards B_0 is different across the components of the magnetization ending the initial phase coherence. After a brief time interval, τ, a 180° pulse is emitted along the x axis

causing the magnetization components to be mirrored in that axis. This pulse inverts the distribution of the components causing the faster precessing components to follow the slower ones, at which point all the components phase at a time which is the double of τ, maximizing the signal and generating a spin-echo. The FID signal acquisition then starts at t = TE = 2τ (Figure 1.13). The 180° pulse makes the spin-echo signal independent of the inhomogeneities of the magnetic field B_0 but still dependant on the local fluctuating magnetic fields (Reiser *et al.*, 2008).

An MR image can be described as a picture of different precessing magnetizations at a finite time point. At that moment the magnetization will have a transverse magnetization value and a local phase angle. Different spins will have different magnetization values and different phase angles, depending on their precession rate, so the MRI image is a distribution of signal intensities in a xy axis. The imaging process involves measurement of a data matrix in which the signal induced by one phase encoding step constitutes a line in the matrix. The repetition of phase encoding steps allows the construction of a data matrix, named k-space, in which axes are referred to as spatial frequencies (Buxton, 2002). The image can then be reconstructed by means of a two dimensional Fourier method. The slice selection is made by an RF pulse, as previously explained, and the spatial encoding of the spin in the slice is achieved by a combination of frequency and phase encoding by means of two orthogonal gradient fields. The repetition of this process N times with the MR signal being measured M times will create a matrix of NxM data points. The Fourier transformation of this k-space matrix returns an MR image of the selected slice with a resolution of NxM pixels. This method can be extended to a three dimensional method by replacing the slice selection gradient by a second phase encoding gradient. The RF pulse will excite all the spins inside the volume of the RF coil and the spatial information is then encoded by two phase encoding gradients and one frequency encoding gradient. The third element in the k-space matrix is the number of phase encoding steps, K. In this case, the image sequence needs to be repeated NxK times and the Fourier transform of the k-space matrix will return an image with NxMxK pixels (Reiser *et al.*, 2008).

1.4.1 Dynamic Contrast Enhanced Magnetic Resonance Imaging (DCE-MRI)

The development of MRI has benefited the diagnosis, grading and classification of tumours, to such an extent that it is now used for planning of therapy approaches in many tumour types. MRI can provide not only clear anatomical information on structures, but also helps to identify pathological changes in structures. Tumour and tissue morphology can be imaged in several planes or even in three dimensions. With the introduction of contrast agents MRI acquired more tools for diagnostic or staging information, and gadolinium-based contrast agents usually have low molecular weights and are paramagnetic (substances with unpaired orbital electrons which cause an increase in the local magnetic moment) (Jackson *et al.*, 2005).

Dynamic contrast enhanced (DCE) magnetic resonance imaging (MRI) is a technique where several images are acquired before, during and after the administration of a contrast agent. The result of this procedure is influenced by several properties of the tumour, namely tumour perfusion, vessel permeability and extravascular/extracellular space. DCE-MRI is currently used in cancer detection, diagnosis, staging and treatment response assessment. DCE-MRI provides measurements of permeability and its aberration, and tumour microvascular measurements using DCE-MRI are indicators of tumour grade, microvessel density, vascular endothelial growth factor (VEGF) function and recurrence and/or survival outcomes. These properties allow DCE-MRI to be used as both a pharmacodynamic and surrogate response biomarker. DCE-MRI can assess the uptake and clearance of contrast agents in tumour tissue providing information about tumour tissue properties at a microvascular level. Microvascular properties can be altered by treatment with anti-vascular drugs, making DCE-MRI a valuable non-invasive imaging biomarker. In the imaging of brain lesions DCE-MRI provides insight into the extent of the lesion, its microcirculatory properties, angiogenic profile and heterogeneity. Lastly, by characterizing changes in tumours prior to volume changes, DCE-MRI can be used to predict the outcome of a specific treatment (Reiser *et al.*, 2008).

During the initial phase of growth, cancer can develop without vasculature by obtaining nutrients and expelling waste materials through simple diffusion.

However, this limits the size the tumour can achieve and consequently tumours start to develop vasculature through angiogenesis. Tumours are formed by metabolically active cells with a high demand for oxygen and nutrients, and hence new vasculature does not develop with a normal tissue morphology. The vasculature in tumours can be very heterogeneous with distorted and coarse capillaries, and the vessels are often fragile and insufficiently differentiated. Gaps or holes are frequently observed in the capillaries, with enlarged inter-endothelial junctions and an incomplete or non-existent basement membrane. All these defects make the transcapillary permeability very high, in some cases high enough to allow the leakage of red blood cells.

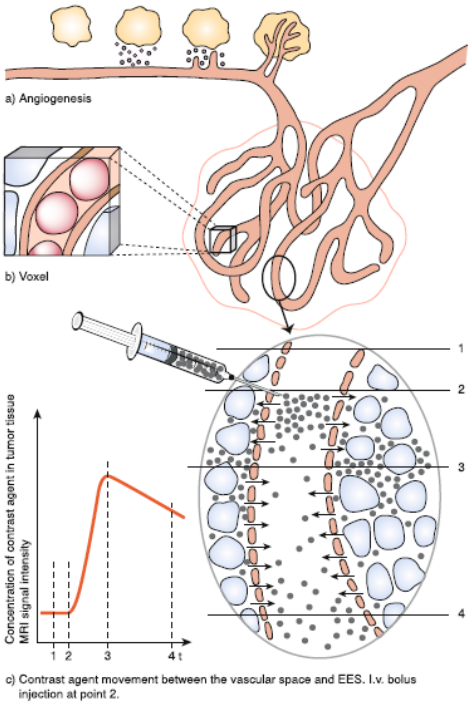

Figure 1.14: a) An avascular tumour releases VEGFs promoting angiogenesis of blood vessels to supply the tumour with nutrients and oxygen. The new blood capillary can be formed from existing small vessels. The capillary develops until it reaches another vessel to allow blood circulation. b) Voxel of a tumour vessel which might be used in the imaging by MRI. Usually, high resolution MRI is required to distinguish the smaller capillaries. c) zoomed region of a tumour vessel. The different numbered lines represent time intervals which correlate with the graph in the lower left. On the right the injection of contrast agent at t=2 is followed by the diffusion of the contrast agent through the gaps in the capillary to the extravascular space. That translates with a peak of contrast agent (and MR signal) at t=3 which precedes an clearance of the contrast agent. Copied from Jackson *et al.* (2005).

As it can be seen in Figure 1.14, straight after the injection of contrast agent given intravenously to a subject it will distribute throughout the vascular system. Healthy tissue is provided with a consistent vascular network, and hence the contrast agent travels through with minimal leakage, causing a momentary increase in the MR signal. However, when it reaches a tumour, due to the leaky nature of the vasculature, the contrast agent extravasates into the extravascular

space by simple diffusion. This extravasation causes a substantial increment in the MR signal from the tumour which persists over time when compared with normal tissues. After a period of time, the contrast agent returns to the vessel and is cleared from the blood system through the kidneys and excreted. Variations in regional blood flow or haematocrit, which can be proportional to blood vessel density and the vascularization of the tumours, or variations in the surface area permeability of the endothelial membranes, are mechanisms which underlie the signal enhancement patterns visible in DCE-MRI. More aggressive tumours can induce faster angiogenesis which can accentuate abnormalities in the new capillaries, and this feature can result in DCE-MRI being a marker of angiogenic activity.

DCE-MRI data can be acquired by two methodologies: relaxivity-based methods and susceptibility-based methods. Relaxivity-based methods use T_1 weighted acquisitions. Susceptibility-based methods use T_2 or T_2* sequences to acquire the data. Both methods have advantages and disadvantages, and are used for different applications. In the studies described in this thesis only relaxivity-based DCE-MRI has been used in which T_1 weighted images assess relaxivity effects while dynamic data are being acquired. Relaxivity contrast mechanisms rely strongly on the contrast agent and so effects can only be visualized in the immediate region surrounding the contrast agent location (Jackson *et al.*, 2005). That is due to the fact that for imaging at fields of 0.1T or higher, the relaxivity of bound water ($1/T_{1m}$) is given by the equation:

$$\frac{1}{T_{1m}} = \frac{C}{r_{GdH}^6}\left[\frac{3\tau_c}{1+\omega_H^2\tau_c^2}\right]$$

where C represents several physical constants, r_{GdH} is the Gd-water distance, τ_c is a correlation time for magnetic fluctuation and ω_H is the Larmor frequency (Dumas *et al.*, 2010).

The pulse sequences used to acquire T_1 weighted DCE-MRI commonly employ gradient echo-based sequences such as GRASS, FISP or FFE.

In DCE-MRI, the essential element is the contrast agent. There are several different contrast agents available for MRI studies and many more being developed. Paramagnetic gadolinium chelates are the most commonly used

contrast agents (Jackson *et al.*, 2005), the gadolinium ion interacting with nearby hydrogen nuclei. This interaction results in a shortening of the T_1 lattice relaxation time in local tissue water, which increases the signal intensity in T_1 weighted images. The enhancement of the signal depends on physiological and physical factors, such as tissue perfusion, arterial input function, volume of the extracellular extravascular leakage space, capillary permeability and capillary surface area (O'Connor *et al.*, 2007). Table 1.3 lists some available gadolinium-based contrast agents.

Generic name	Product/Trade Name
Gadopentetate dimeglumine	Magnevist
Gadoterate meglumine	Dotarem
Gadodiamide	Omniscan
Gadoteridol	ProHance
Gadobutrol	Gadovist
Gadoversetamide	Optimark
Gadobenate disodium	MultiHance
Gadoxetate disodium	Primovist/Eovist
Gadofosveset trisodium	Vasovist/Ablavar

Table 1.3: Gadolinium-based contrast agents. Copied from Singer (2010).

Contrast agents are predominantly excreted by the kidneys and share similar pharmacokinetics, the only exception being gadobenate disodium (MultiHance) which has weak protein binding properties and can be excreted through the liver. Gadomer-17 or albumin-GdDTPA are examples of macromolecular agents with molecular weights (35 and 65 kDa, respectively) which allows them to remain in the intravascular space for several hours. Nevertheless, these complexes still leak out of very permeable capillaries so can be used as a measurement of endothelial permeability (Jackson *et al.*, 2005).

A DCE-MRI study starts with the injection of a contrast agent into the subject. The MRI images are acquired from a single slice or a group of slices covering the tissue of interest. Morphological and/or functional parameters can be extracted from the MRI image, such as fractional plasma volume and transendothelial permeability, which can be used to model the tissue vascularization. A Region Of Interest (ROI) can be then drawn to define the highly vascularized tumour area (Castellani *et al.*, 2009).

From the simple signal intensity *vs* time curve a description of the contrast agent distribution can be inferred. However, for a more robust analysis of contrast agent kinetics, the signal intensity must be converted to contrast agent concentration although the relationship is not linear. Calculation of the initial area under the contrast agent concentration *vs* time curve (IAUC) provides a model-free and reasonably reproducible biomarker for use in clinical trials. However, there are still uncertainties in the relationship between the IAUC and the underlying tumour physiology. Simple pharmacokinetic models, describing the volume transfer coefficient for the contrast agent between the blood plasma and the extracellular/extravascular leakage space (EES) (K^{trans}) and the size of the EES (v_e), complement IAUC in the analysis of the effect of antiangiogenic and vascular disrupting agents in clinical trials (O'Connor *et al.*, 2007). The use of these measurements to assess antiangiogenic and antivascular therapeutics response has been recommended by Leach *et al.* (2003).Lancaster *et al.* (2005) and Walker-Samuel (2006) have demonstrated that IAUC correlates very strongly with K^{trans} and v_e being a quantitative parameter obtained without mathematical modelling. In Table 1.4 is shown a comparison between parameters measured by DCE-MRI based on a paper published by Cheng (2009).

"Quantitative" parameters: K^{trans}, v_e	**"Semi-quantitative" parameter: IAUC**
• Model-based; • Pharmacokinetic parameters measuring blood flow and/or endothelial permeability; • Hard to measure due to parameters coupling, arterial input function (AIF) measurement, water exchange and model fit instability.	• Non-model-based; • Does not require AIF measurement; • Is not affected by noisy data; • Lack of clear biological association.

Table 1.4: Comparisons between parameters measured by DCE-MRI. Adapted from Cheng (2009).

There are several models that have been applied to clinical trial data to calculate K^{trans} and v_e. The exact meaning of K^{trans} depends on the kinetic model used for the analysis of the DCE-MRI data, and within the same patient cohort changes in K^{trans} may reflect different physiological processes in different individuals such as reduced blood flow, reduced permeability or a combination

of both. The analysis techniques chosen have to accommodate a compromise between relatively simple but unspecific or unstable models and physiologically congruency. Although DCE-MRI is more complex than simple anatomical imaging, T_1 weighted DCE-MRI provides very relevant information about tumour biology and response to treatment (O'Connor *et al.*, 2007).

1.4.2 Spectroscopy – ^{1}H/ ^{31}P

The frequency of nuclear spins is not only determined by the gyromagnetic ratio, and if this was the only differentiating factor nuclei of the same element or isotope would resonate at the same frequency in a homogeneous magnetic field, regardless of the molecule they were in. However, the resonance frequency of a nucleus is also influenced by the chemical environment surrounding it. The spinning nuclei are shielded by the electrons which surround them, and in an external magnetic field (B_0) the electrons rotate around B_0 in an opposite sense to the precession of the proton spin. Electrons are negatively charged particles, and hence their movement will create a magnetic field, μ_e, which opposes B_0. Consequently, the nucleus will sense a reduced external magnetic field and, therefore, have a different resonance frequency. This property is termed the chemical shift. The effective magnetic field, B, that the nucleus is exposed to can be expressed by the following equation:

$$B = B_0(1 - \sigma)$$

where B is the effective magnetic field to the nucleus, B_0 is the external magnetic field and σ is the shielding constant. This constant is dimensionless, and depends on the chemical environment of the nucleus. The chemical shift is also expressed in terms of ppm as the expression in Hertz units would make it dependant on the magnetic field strength. Chemical shift, δ, can be mathematically defined as:

$$\delta = \frac{\upsilon - \upsilon_{ref}}{\upsilon_{ref}} \times 10^6$$

where ν is the frequency of the investigated compound and ν_{ref} is the frequency of a reference compound. The ideal reference compound must be chemically inert and produce a strong (singlet) resonance signal in a region of the spectra away from all the other resonances. For proton (^{1}H) spectroscopy 3-(trimethylsilyl)propionic-2,2,3,3-d4 acid (TSP) is typically the reference used. In

phosphorus (^{31}P) spectroscopy methylenediphosphonic acid (MDP) is one of the compounds used as a reference (de Graad, 2007).

Magnetic resonance spectroscopy (MRS) is performed in the same scanner as standard magnetic resonance imaging. The technique exploits the absorption of electromagnetic radiation from RF pulses and data are presented as plots of absorption frequency *vs* peak intensities. The frequencies absorbed have their intensity modulated by the molecular composition of the sample. In theory MRS can be performed on any nuclei with an odd number of protons and neutrons, as in MRI. However, if the sum of the number of protons and neutrons is not an odd number, the SNR will be insufficient to achieve good quality data.

In MR spectra peak intensities correspond to the relative number of chemically equivalent protons or other magnetic nuclei. Any resonance frequency is represented in ppm. In the case of ^{1}H-MRS, protons in different local chemical environments will generate different resonance frequencies, providing spectroscopic differentiation of chemical compounds which can be very important physiologically.

Spectroscopic data can be acquired by single voxel or multi-voxel techniques (Reiser *et al.*, 2008). Three of the more commonly used sequences for single voxel spectroscopy are Stimulated Echo Acquisition Mode (STEAM), Point-Resolved Spectroscopy (PRESS) and Image Selected *in vivo* Spectroscopy (ISIS). PRESS uses three slice selective radiofrequency (RF) pulses. To avoid observing signals from spins that experience only one or two of the RF pulses this sequence incorporates spoiler gradients. It has a rather large TE. The STEAM sequence also has three slice-selective RF pulses and spoiler gradients as PRESS, however, the interval between the second and third pulses do not contribute to the effective echo time. Reducing TE results in a lower sensitivity when compared with PRESS but the ability to detect metabolites with short T_2 or complex coupling patterns. The ISIS sequence does not use echo formation. In this sequence a 180º slice-selective pulse is used to prepare the magnetization prior to the excitation of the entire magnetization of the object by a 90º non-selective pulse. Although the data acquisition is performed immediately after the 90º pulse allows the detection of

signals that decay rapidly, motion during the accumulation of data can result in severe localization errors. Also, localized shimming is not possible with ISIS, in contrast with PRESS and STEAM. ISIS is commonly used for 31P-MRS (Gadian, 1995). Multi-voxel techniques increase the volume that can be imaged, and allows a comparison between normal and abnormal tissue concurrently and also two and three dimensional chemical shift imaging (CSI). This multi-voxel data are acquired at the cost of the acquisition time which increases when compared with the single voxel techniques, and can be acquired using either PRESS or STEAM sequences (Reiser *et al.*, 2008).

As stated above, MRS can be performed on any nucleus with a magnetic moment. In an *in vivo* MRS experiment, metabolically and pharmacologically more relevant nuclei which have a magnetic moment are proton (^{1}H), carbon-13 (^{13}C), fluorine (^{19}F), sodium (^{23}Na) and phosphorus (^{31}P). Although it is a limited number, each of these nuclei can provide extensive information about a large number of metabolites or drugs. Glutamate, GABA and aspartate are examples of important neurotransmitters that can be detected by ^{1}H-MRS, and lactate is an important metabolite. Similarly, the tricarboxylic acid cycle can be studied *in vivo* and non-invasively by ^{13}C-MRS, and intracellular pH, magnesium concentrations and energetically important metabolites like ATP can be assessed by ^{31}P-MRS.

^{1}H-MRS

A high gyromagnetic ratio and high natural abundance makes the proton the most sensitive nucleus for magnetic resonance imaging, and ^{1}H-MRS can identify and quantify numerous biologically relevant compounds including cerebral metabolites. However, ^{1}H-MRS faces some limitations, even in the brain, where it has been widely used, notably that the water resonance signal is several fold larger than that of low concentration metabolites, and other extracranial signals can also dominate the smaller metabolite signals and the spectral resolution can be diminished by inhomogeneities in the magnetic field. The water signal can be suppressed using a 180° saturation pulse focused around 4.7ppm which is the resonance frequency for protons in the water molecule. Optimizing the spatial localization, better shimming and/or gradient pulses can increase the SNR for the relevant spectrum.

^{1}H-MRS has a further limitation; the chemical shift range is of 10ppm for non-exchangeable protons. Several metabolite resonances overlap because of this, and hence their separation and quantification becomes very difficult. Therefore several spectral editing techniques have been developed to separate overlapping resonances. Spectral editing includes techniques to discriminate scalar-coupled from uncoupled spins. Techniques used for spectral editing include two dimensional NMR, where two different nuclei, i.e. ^{1}H and ^{31}P present in the same sample, can be imaged, and the information is coupled to establish connections and identify atoms in molecules.

Absolute concentrations can, in principle, be calculated from spectra acquired by MRS, and expressed in mmol/L or mmol/g of tissue. Quantification is possible because the thermal equilibrium magnetization (M_0) is directly proportional to the number of spins (n) which is proportional to the molar concentration. However, in an NMR scan an induced current proportional to the transverse magnetization is measured, rather than the thermal equilibrium magnetization. From first principles, the following equation describes the signal that a metabolite M induces in a receiver coil after a specific NMR sequence:

$$S_M = NS \times RG \times \omega_0 \times [M] \times V \times f_{sequence} \times f_{coil} \times N_p$$

where NS is the number of scans, RG the receiver gain, ω_0 the Larmor frequency, [M] the molar concentration, V the volume size, $f_{sequence}$ and f_{coil} functions which describe the signal modulation induced by the NMR pulse sequence and the coil, and N_p the number of protons of the reference and the number of protons of the metabolite being studied. In these last elements, TR, TE, T_1 and T_2 number and type of RF pulses are included in the $f_{sequence}$ factor while the geometry and quality of the RF coil are elements of the f_{coil} factor. These last elements and factors are usually unknown making direct quantitation of the metabolite impossible. However, the concentration of the metabolite can be calculated by using a known concentration of a reference compound [R], and hence the concentration of metabolite M can be calculated by the equation:

$$[M] = [R]\frac{S_M}{S_R}C_{MR}$$

where S_R is the signal collected by the receiver coil from the reference compound and C_{MR} is a correction factor which arises from differences in T_1 and

T_2, diffusion, gyromagnetic ratio and several other differences between the reference compound and the studied metabolite. An alternative to this absolute quantitation is the expression of the metabolite level as a ratio to other metabolites. Although faster, metabolite ratios are ambiguous, and more generally, quantitation can be performed not only in ^{1}H-MRS but also with the other nuclei as long as a suitable reference is provided.

An important feature of ^{1}H-MRS and MRI in general is that numerous metabolites can be analysed in a single spectrum. Figure 1.15 shows an example of a ^{1}H-MRS spectrum acquired from an *in vivo* experiment using a rat brain in an 11.75T magnet (de Graaf, 2007).

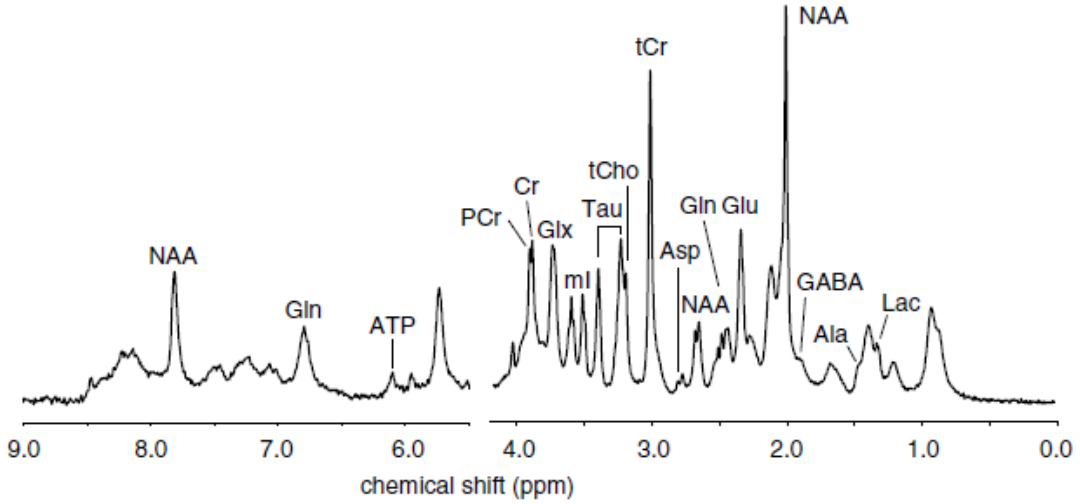

Figure 1.15: ^{1}H-MRS spectrum acquired from an *in vivo* experiment with a rat brain at 11.75T. Although water suppression has not being used, the water peak has been removed from the spectrum, hence the gap between 4 and 6ppm. 17 different metabolites can be discerned: NAA (N-acetyl Aspartate), Glu (Glutamine), ATP(Adenosine Triphosphate), PCr(Phosphocreatine), Cr(Creatine), Glx(Glutamate+ Glutamine), Tau(Taurine), tCho (total Choline), tCr(total Creatine), Asp (Aspartate), Gln (Glutamine), Glu(Glutamate), GABA(γ-Aminobutyric Acid), Ala(Alanine), Lac(Lactate). Copied from de Graaf (2007).

^{31}P-MRS

^{31}P-MRS, similarly to ^{1}H-MRS, has been widely used in pre-clinical and clinical research. Phosphorus has lower sensitivity when compared with ^{1}H-MRS and has a 100% natural abundance which coupled with relatively large chemical shift dispersion under *in vivo* conditions (~30ppm) allows the acquisition of high quality and well resolved spectra in short scan times even at lower (clinical) magnetic fields. ^{31}P-MRS can detect and quantify all the key metabolites involved in energy metabolism, and can also be used indirectly to measure intracellular pH. Due to its lower sensitivity, bigger voxels are required to

compensate losses in the SNR and only metabolites in reasonably high concentrations are detected. There are only a limited number of resonances in *in vivo* ^{31}P-MRS spectra and their chemical shift is sensitive to intracellular pH (and ionic strength, i.e. magnesium which complexes with phosphorus). Phosphocreatine (PCr) is by convention used as an internal chemical shift reference and assigned a chemical shift of 0.00ppm. ATP has chemical shifts of -2.48ppm (γ phosphorus), -7.52 ppm (α phosphorus) and -16.26ppm (β phosphorus) while inorganic phosphate has a chemical shift of 5.02ppm at a pH of 7.2 and with full magnesium complexation (Figure 1.16) (de Graaf, 2007).

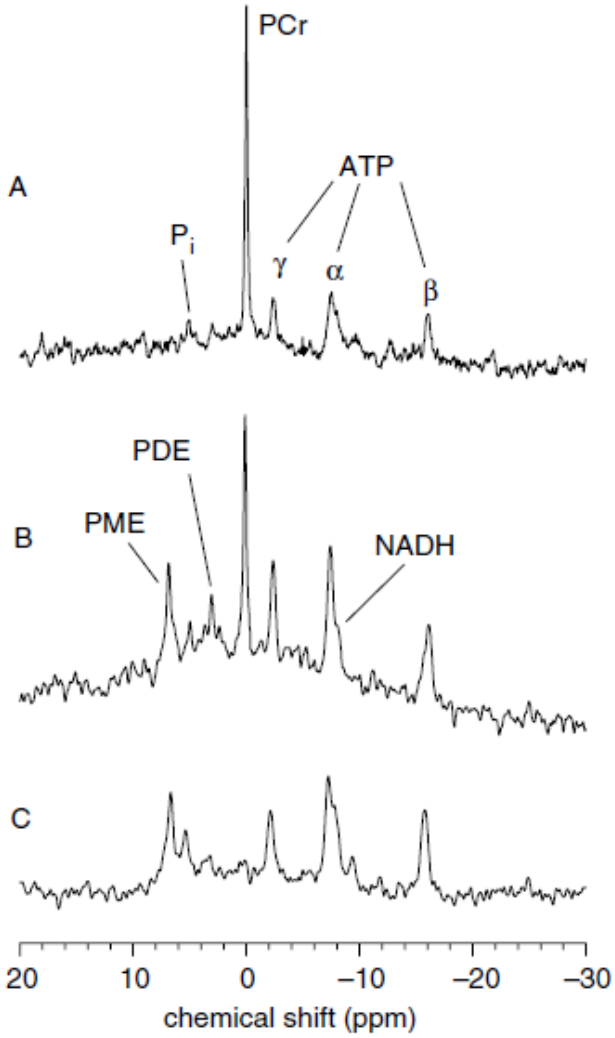

Figure 1.16: ^{31}P-MRS spectra from a *in vivo* scan of A) rat skeletal muscle, B) brain and C) liver. The metabolites identified are: inorganic phosphate (Pi), phosphocreatine (PCr), α,β and γ peaks of adenosine triphosphate (ATP), phosphomonoesters (PME), phosphodiesters (PD) and nicotinamide adenine dinucleotide (NADH). Copied from de Graaf (2007).

Figure 1.16 also shows that it is also possible to detect phosphomonoesters and diesters (PME and PD). In the liver PCr can be absent; however, its presence in some situations indicates that surrounding muscular tissue is contaminating to the spectrum.

A detailed study of artifacts encountered in the analysis of phosphorus metabolites by *in vivo* and *ex vivo* MRS has been published (Howe *et al.*, 1993).

As stated above, the chemical shift of compounds with phosphorus is affected by physiological parameters such as intracellular pH and magnesium concentration. When a phosphate containing compound complexes with magnesium the chemical environment of nearby nuclei is changed and hence its chemical shift changes. The pH can be described using a modified Henderson-Hasselbach relationship:

$$pH = pK_a + \log\left(\frac{\delta - \delta_{ha}}{\delta_a - \delta}\right)$$

where δ refers to observed chemical shift, δ_a and δ_{ha} are the chemical shifts of unprotonated and protonated forms of compound α and pK_a is the logarithm of the equilibrium constant for the acid-base equilibrium between ha and a.

Although almost all the resonances in ^{31}P-MRS spectra are pH dependent, the most common way to measure the pH is from the distance between inorganic phosphate and phosphocreatine. However, this measurement cannot be used in all situations. Phosphocreatine is not detectable in liver or kidney or under pathological conditions such as tumour ischemia, hypoxia and anoxia. Also, the inorganic phosphate might be very low or shadowed by more intense resonances (e.g. in the heart). If phosphocreatine and inorganic phosphate are detectable in the tissue, pH determination has an accuracy of 0.05 pH units. In a similar fashion, ATP chemical shifts provide information regarding the free magnesium concentration (de Graaf, 2007).

1.5 Positron Emission Tomography

Positron Emission Tomography (PET) is an imaging technique with an increasing role in the diagnosis and staging of malignant disease, and in monitoring therapy response.

The development and progress of PET imaging systems was originally limited by innate physics. However, the introduction of novel scintillation crystal technology and detector electronics combined with the widespread availability of fast, efficient and iterative image reconstruction algorithms has resulted in a dramatic reduction in clinical imaging times combined with the required resolution, sensitivity and signal-to-noise properties (Dresel, 2007). In addition, the combination of PET functional imaging with anatomical imaging techniques such as Computed Tomography (CT) or Magnetic Resonance Imaging (MRI) allows co-registration of anatomical/functional images, removing the need to transfer patients between equipment/facilities reducing greatly the time to perform multi-modal imaging scans.

Atoms are the central unit of matter. An atom (X) is composed of a nucleus encasing protons (Z) and neutrons (N) and orbiting electrons. The sum of protons and neutron in a nucleus is the mass number A and a unique combination of protons and neutrons in a nucleus form a nuclide which can be represented by: $^{A}_{Z}X_{N}$.

Radionuclides are unstable atoms due their nucleus being formed by an unstable composition of neutrons and protons or excess energy. These radionuclides decay into more stable configurations by the emission of radiation including α, β^- or β^+ particles, or by electron capture and isomeric transition.

The unstable radionuclides decay randomly and proportionally to the number of radioactive atoms in the sample. Activity is the measure of the rate of decay of unstable nuclei in a specific instant and can be translated in the following equation:

$$A_t = A_0 e^{-\lambda t}$$

where A_t is the activity of a nuclide after time t, A_0 is the amount of activity present initially and λ is the decay constant which is calculated by:

$$\lambda = \frac{\log_e(2)}{t_{\frac{1}{2}}}$$

where $t_{1/2}$ is the half-life for that radionuclide. Half-life is a unique characteristic of each radionuclide and is the time required to reduce to one half the initial activity. This physical half-life is for the free element and needs to be corrected for drug/tracer clearance when the radionuclide is in a pharmaceutical compound and has been delivered to a patient. In the setting of clinical imaging, the process of elimination of the radiolabelled drug by the body will characterize the biological half-life which is the time the biological system takes to eliminate half of the administered dose.

The decay process specific to PET is the positron decay whereby a radionuclide rich in protons will decays by the emission of a positron (β^+) along with a neutrino (v). The positron is a subatomic particle with an equivalent mass to an electron but with a positive charge while the neutrino is a particle, produced during the β^+ and electron capture decay of the radionuclide, with no charge or mass but variable energy. In simple terms, the excess proton in the nucleus is converted into a neutron plus a positron and a neutrino. This process is described by the following equation:

$$_1^1p^+ \rightarrow {}_0^1n + {}_1^0\beta^+ + \upsilon$$

where p stands for proton, n for neutron, β^+ for positron and v for neutrino. The neutron is one electron mass heavier than a proton and so the right hand side of the decay equation has two more electron mass units than the left side. In order to conserve the energy in both sides of the equation, the radionuclide must have transition energy of at least 1.022 MeV. This value comes from the application of Einstein's Special Theory of Relativity where it is established that there is an equivalency relationship between energy and mass. Applying this equation to one electron which has a rest mass (m) of 9.11×10^{-31} kg and the speed of light (c) that is 3×10^8 m/s we obtain:

$$E = mc^2 = 9.11 \times 10^{-31}\ kg \times (3 \times 10^8)^2\ m.s^{-1} = 8.2 \times 10^{-14}\ J$$

Using the conversion factor between energy in joules to energy in electron volts (eV):

$$\equiv \frac{8.2 \times 10^{-14}\ J}{1.6 \times 10^{-19}\ J.eV^{-1}} = 511\ keV$$

Hence the transition energy of a radionuclide in positron decay to be two times 511 keV.

Positrons are considered light charged particles and so move in a zigzag path, and their range is dependent on the density of the matter they pass through. The positron loses kinetic energy as it passes through matter by ionisation or by radiation after inelastic scattering which contributes to its zigzag path. The path length for the positron depends on the initial energy that the positron is emitting which is characteristic of the parent radionuclide.

As illustrated in Figure 1.17, once the positron is almost at rest it will interact with an electron, resulting in the annihilation of both particles with the emission of electromagnetic energy. The electromagnetic energy is released in the form of two photons of 511 keV emitted at 180° to each other. This annihilation occurs outside the nucleus of the atom and, depending on the parent radionuclide, several millimetres away from the emission nucleus, adding uncertainty to the localisation of the decaying atom. As an example, the maximum range for a positron emitted by an ^{18}F atom is 2.4 mm.

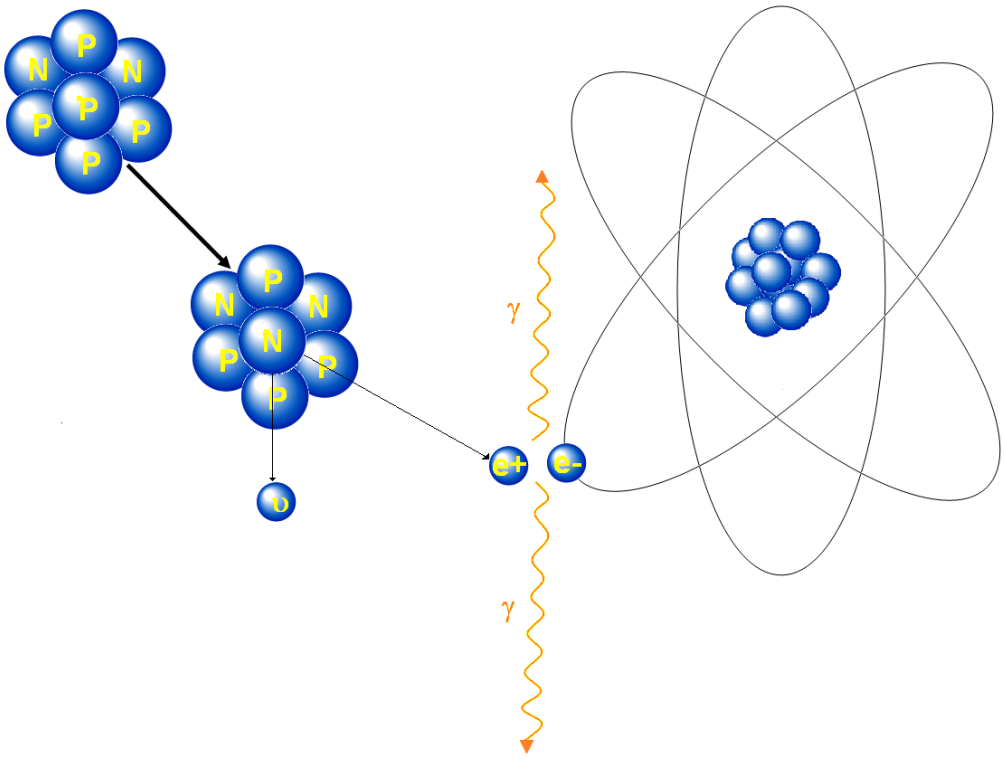

Figure 1.17: From left to right: a proton (P) in an unstable parent nucleus decays to a neutron (N) emitting a neutrino (ν) and a positron (e^+) which will annihilate with an electron (e^-) and emit two 511 keV gamma photons (γ).

The high energy photons emitted by the annihilation of the positron can interact with matter by 3 main mechanisms: photoelectric effect, Compton effect and pair production, depending on the energy of the electromagnetic radiation as briefly explained bellow.

The photoelectric process happens when γ radiation moving through an absorber transfers its entire energy to an electron from an inner shell of the atom causing the ejection of an electron. The vacancy in the shell will be filled by an electron transiting from an upper shell with the emission of the energy difference between both shells in the form of characteristic x-rays or by the Auger process. In the Compton scattering process the γ radiation transfers part of its energy to an electron in an outer shell of the absorbent atom. Due to its position in an outer shell, the binding energy of the electron is small and can be considered almost free, and this translates into the ejection of the electron from the outer shell while the γ radiation loses some energy and suffers a change in its path (scattering). Finally pair production happens when γ-rays with energy above 1.022 MeV interact with an absorber atom producing an electron and a positron. The combination of the three above mentioned processes creates a process of attenuation of the γ radiation. Attenuation can be expressed by a mono-exponential function when a well collimated source of photons and detector are considered:

$$I_x = I_0 e^{-\mu x}$$

where I_x refers to the beam intensity measured through a material of thickness x, I_0 the beam initial intensity and μ the attenuation coefficient of the material. In PET as well as in SPECT (Single Photon Emission Computed Tomography) the attenuation of the γ radiation is a critical factor to consider and attenuation correction is provided in some reconstruction algorithms.

Radiation detection exploits the interaction of ionising radiation with matter by detecting the energy lost or deposited by the radiation passing through the detector and converted into a measurable electrical signal or charge. Radiation detectors can be proportional (gas) chambers, semi-conductors or scintillation detectors. Gas chamber and semi-conductor detectors have low detection efficiency while scintillation detectors, due to their higher density, provide the highest stopping efficiency for 511 keV photons. Four main characteristics are

crucial in the selection of the PET detector: stopping power for 511 keV photons, scintillation decay time, light output per keV of photon energy and the energy resolution of the detector. The stopping power of the detector refers to the mean travelling distance of the photons, before they stop after complete energy deposition and is dependent on the density of the detector material. Scintillation decay time is the time interval between the γ ray interaction with an atom of the detector material (exciting it to a higher energy level), and the decay of that same atom to a ground state (of lower energy) emitting visible light (scintillation). Measured in nanoseconds, the scintillation time of the detector depends on the material which constitutes the detector and its efficiency is higher the shorter the scintillation decay time is. The energy resolution is improved not only by a higher light output but also by higher homogeneity in the crystal structure of the detector. Table 1.5 presents examples of crystals used in PET detectors and their properties.

Property	NaI(Tl)	BGO	LSO	YSO	GSO	BaF_2
Effective Z	50	74	66	34	59	52
Density (gm/cm^3)	3.7	7.1	7.4	4.5	6.7	4.9
Scintillation decay time (ns)	230	300	40	70	60	0.6
Photon yield per keV	38	6	29	46	10	2
Relative light output	100	15	75	118	25	5
Linear attenuation coefficient, μ (cm^{-1})	0.35	0.96	0.87	0.39	0.70	0.44
Energy resolution (% at 511keV)	6.6	20	10	12.5	8.5	11.4

Table 1.5: Properties of typical PET detector crystals. The crystal material acronyms stand for thallium-doped sodium iodide NaI(Tl), bismuth germinate (BGO), lutetium oxyorthosilicate (LSO), cerium-doped yttrium oxyorthosilicate (YSO), gadolinium oxyorthosilicate (GSO) and barium fluoride (BaF_2). Extracted from Saha (2005).

The crystals are disposed in a matrix in the detector. The visible light (scintillation) produced by the interaction between γ radiation and the detector material needs to be transformed into a measurable electrical pulse, and transfer is achieved by photomultiplier tubes (PMT) attached to the crystal detector matrix. The photomultiplier consists in a vacuum glass tube with a photocathode in the entrance window (usually an alloy of cesium and antimony), ten dynodes in the middle and an anode in the other end. There is a high voltage difference of -1000 volts between the photocathode and the anode split

into 100 volt increments between each dynode. A scintillation photon will deposit its energy in the photocathode triggering the release of a photo-electron. Due to the positive potential between the photocathode and the first dynode the photo-electron will accelerate to the first dynode with increased energy. The impact of the photo-electron with the first dynode will cause the release of multiple secondary electrons which will accelerate towards the second dynode due to the positive potential difference, and for each electron, several secondary electrons will be released at impact. As shown in Figure 1.18, this process is repeated until the last dynode releases a pulse of electrons towards the anode which transmits the signal to a preamplifier.

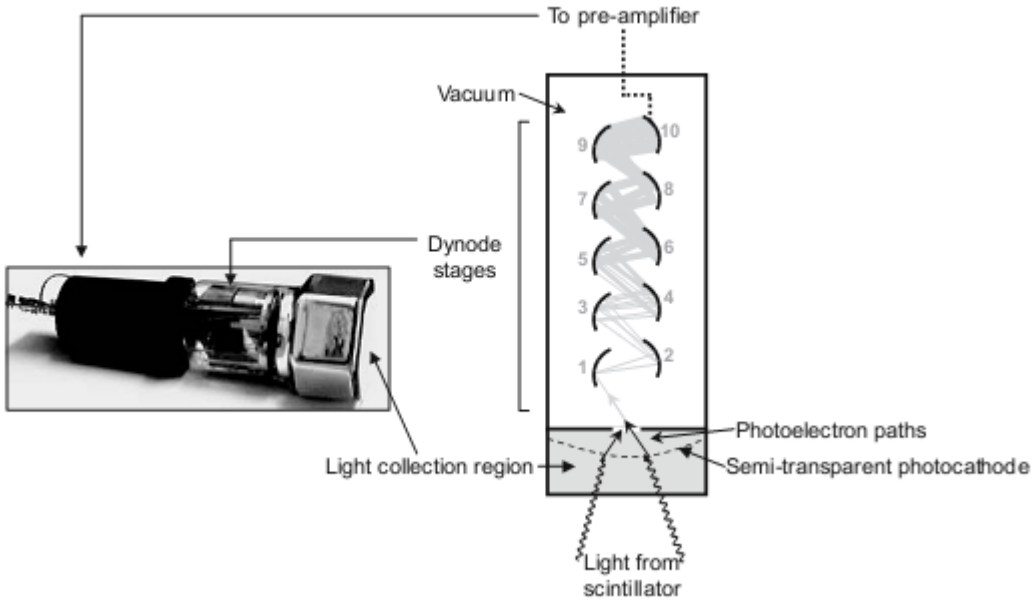

Figure 1.18: Schematic diagram of a photomultiplier tube and a photograph of a hexagonal 6 cm-diameter tube (inset). Seven to ten light photons cause the release of approximately one to three electrons approximately. Copied from Bailey and Towsend (2005).

The signal delivered to the preamplifier is then amplified to a detectable pulse, which is analysed by a pulse height analyser before reaching the computer. The pulse height analyser is responsible for separating the true coincidences (the ones which arise from a single positron-electron annihilation) from single events (single photons reaching the detector), randoms (two nuclei decay at approximately the same time but only two of the four photons reach the detectors causing a localisation error), multiple (three or more photons are detected in the same time window) and scattered events (due to Compton interaction one photon loses energy and changes direction). There are several detector conformations for PET scanners but the most usual is a ring of detectors which surround the patient bed.

The patient being scanned is injected with a PET tracer which has a positron emitting radionuclide incorporated in it. The two 511 keV photons resulting from the annihilation of the positron-electron interaction are detected within an electronic time window (in the order of 10 nanoseconds) and by a pair of opposite detectors (in a ring) when travelling along a straight line between the centres of the two detectors (line of response, LOR).

Figure 1.19 (copied from Saha, 2005) depicts the positron-electron annihilation, signalled as a *, and how the resulting photon detection generates a record in the sinogram.

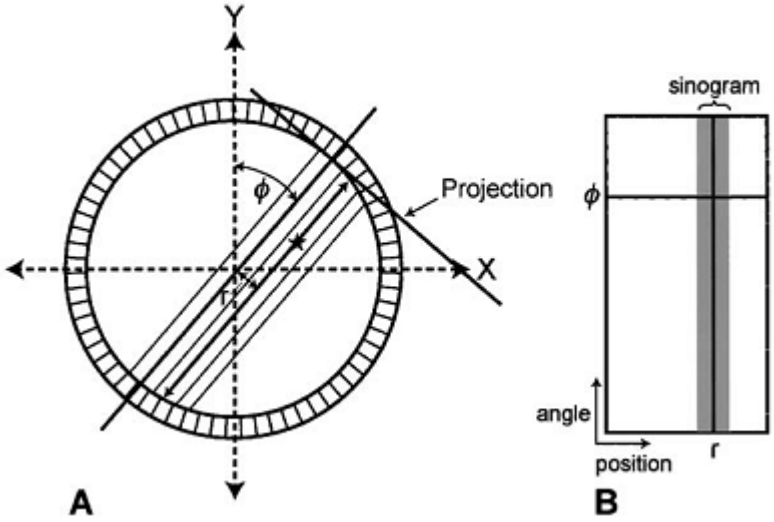

Figure 1.19: Representation of the detection of a true coincidence and its registration in a sinogram. Extracted from Saha (2005).

The resulting pair of 511 keV photons are emitted along the LOR and detected in the pair of opposite detectors within the time window. Because the time difference of the photons arrival is not measured, it is not possible to determine the exact annihilation point. However, the distance of the LOR from the centre of the scan field (r) and the angle between r and the vertical axis of the field (ϕ) are stored in sinograms. The sinogram is a two dimensional histogram of the coordinates of the LORs in a specific plane (events in the same LOR will add up in the same pixel of the sinogram), and the end of a PET scan acquisition, the sinogram is a composite of all the coordinates of all the LORs over the scan time.

The sinogram can be affected by several factors during data acquisition. PET scanners have a few thousand detectors coupled to hundreds of PMTs.

Normalization of the data allows the correction of variations in the gain of different PMTs, sensitivity of a detector pair and physical variation in the detector. Due to the fact that the radiation is emitted within a body, attenuation may occur. To compensate for that effect attenuation correction based on the knowledge of the attenuation coefficient and the thickness of the organ, tissue, body, that the radiation has to go through is applied. Random coincidences can also be minimized by the use of faster electronics, shorter time windows or a combination of standard time windows (which contain true and random events) and a delayed time window in the same energy window (which will only have the random events and will be subtracted from the acquisition in the standard time window). Scatter events are mainly discarded by the pulse height analyser due to energy differences in each detector. Another factor to be considered is the dead time, the time interval between a 511 keV photon interaction with the detector and the recording of a true coincidence event in the computer. At high count rates this is a serious problem which can be minimized by the use of faster electronic components and shorter scintillation decay time detectors.

Several methods of 2D and 3D data reconstruction are available, from simple or filtered backprojection to iterative reconstruction, and the method used will be defined by the acquisition method and the results sought. Figure 1.20, copied from Bailey and Towsend (2005), depicts a step by step reconstruction of a 2D PET image using filtered back projection.

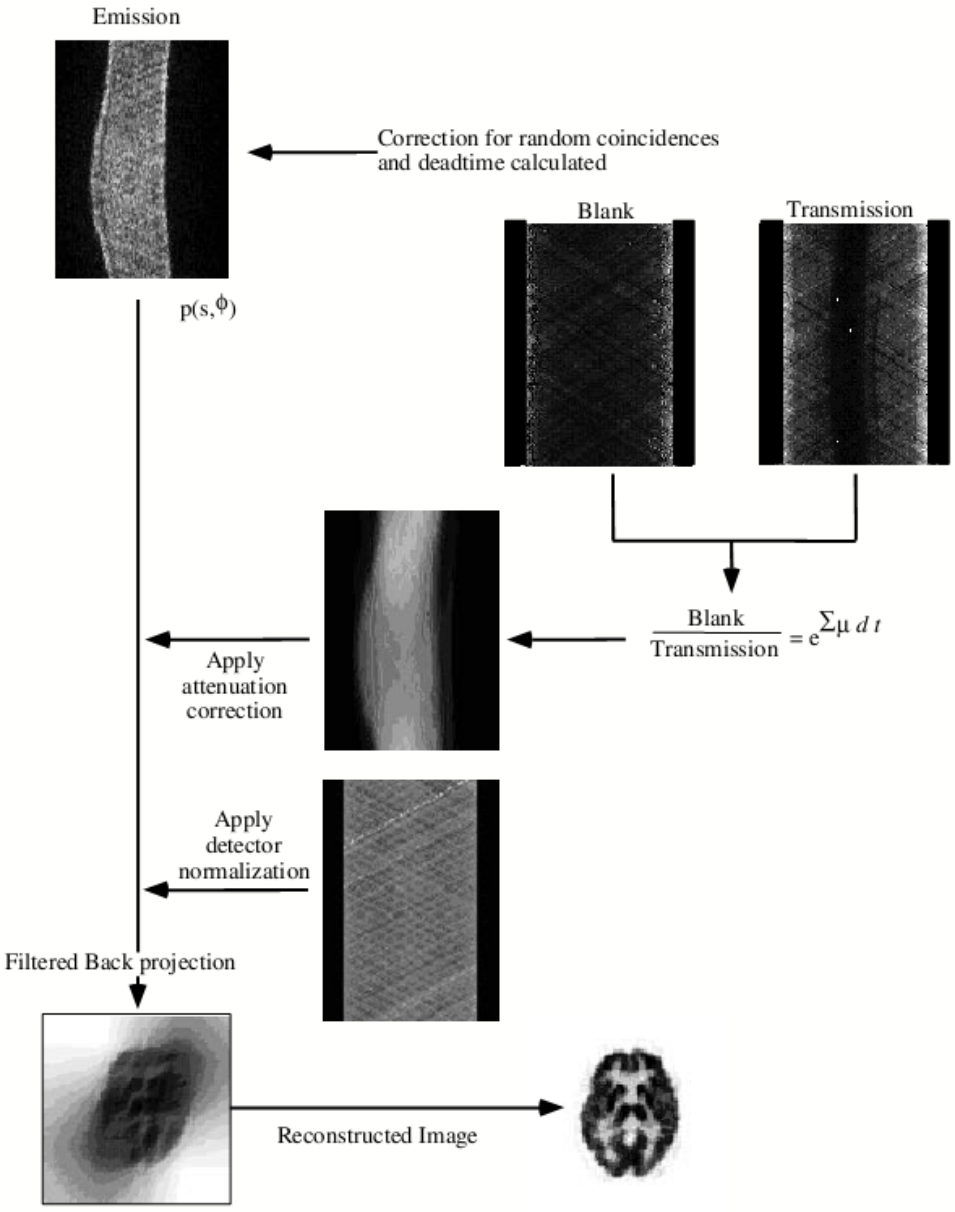

Figure 1.20: Representation of a step by step filtered back projection reconstruction, illustrating the several corrections applied over the process to obtain the best possible image. Copied from Bailey and Towsend (2005).

In this thesis the method of reconstruction used was 3D-OSEM which is an iterative reconstruction method. Iterative methods perform an initial estimate of an image and the projections of that estimated image are computed and compared with the measured projections in the sinogram. In the case of differences between both projections, corrections are made to improve the estimated image and further iteration takes place and another comparison is performed. This process is repeated until the differences between the estimated projections (of the estimated image) are negligible when compared with the measured projections (Bailey and Towsend, 2005; Saha, 2005).

In the specific case of Ordered Subset Expectation Maximization (OSEM) the projection data are grouped in ordered subsets. Each subset is subject to a standard Expectation Maximization algorithm using a matrix of weights (differences between the estimated image and the observed projections counts) which correspond to the ray sums. The resulting reconstruction is used as a starting value for the next subset. In the OSEM algorithm one iteration is a single pass through all the specified element subsets and each iteration starts with the reconstruction obtained in the previous iteration. This algorithm provides an accelerated reconstruction when compared with a standard Expectation Maximization (published by Hudson and Larkin, 1994, and reviewed by Beyer *et al.*, 2011).

1.5.1 PET tracers

The radioactive tracer principle is attributed to George Charles de Hevesy who in 1923 used small non-toxic amounts of ^{212}Pb to study the uptake of solutions in bean plants. A year later he performed the first pre-clinical experiment when he followed the circulation of antisyphilic drugs labelled with ^{210}Bi injected intra-muscularly in rabbits (Bailey and Towsend, 2005).

Positron emitter radionuclides which are the basis of PET can be produced in a cyclotron. In the cyclotron, charged particles are accelerated in circular paths under vacuum by the effect of a strong electromagnetic field. Targets are placed at the end of a window through which the accelerated particles will travel. The collision of the accelerated particles into the target promotes nuclear reactions and the production of the radionuclide. The material in the target and the energy of the accelerated particles will determine the radionuclide product.

For PET purposes, the radionuclides produced have to be positron emitting. For this project the most important is fluorine 18 (^{18}F). Fluorine 18 has a half-life of 109.8 minutes and can be produced by the bombardment of an 85 to 99% enriched $H_2{}^{18}O$ target with 11 to 18 MeV protons. The mixture resulting from the target is loaded into a carbonate ion exchange resin column where the parent $H_2{}^{18}O$ is forced out by neon gas and recovered for reuse. A potassium carbonate solution is then used to elute the $^{18}F^-$ ions from the column. This ion

can then be used for radiolabelling several tracers or pharmaceutical compounds (Saha, 2005).

Several other radionuclides can be produced in a radiochemistry facility and used in the labelling of PET tracers or pharmaceutical compounds depending on the nature of the study, the physiological process being studied and the radionuclide half-life required. Table 1.6 extracted from Aboagye *et al.* (2001) describes some radiotracers used in oncology and the processes they study.

Radiotracer	Process studied
6-[^{18}F]fluorodeoxyglucose	Tumour glucose utilization
2-[^{11}C]thymidine	Cell proliferation
3'-[^{18}F]fluorothymidine	Cell proliferation
[^{11}C]methionine	Protein synthesis
[^{15}O]H_2O	Tumour blood flow
[^{15}O]CO	Tumour blood volume
[^{11}C]HCO_3	pH (intra and extracellular)
[^{18}F]fluoromisonidazole	Tumour hypoxia
16α-[^{18}F]fluoro-17β-oestradiol	Oestrogen receptor status
5-[^{124}I]iodo-2'-fluoro-1β-$_D$-arabinofuranosyluracil	Gene expression (HSV1 tk reporter)
9-(1-[^{18}F]fluoro-3-hydroxy-2-propoxy)methylguanine	Gene expression (HSV1 tk reporter)
[^{11}C]daunorubicin	Multidrug resistance phenotype
[^{124}I]Annexin-V	Apoptosis
[^{124}I]VG76e	VEGF levels

Table 1.6: Ligands and tracers used in oncology and the corresponding physiological process they are designed to study. Extracted from Aboagye *et al.* (2001).

The method used for the synthesis of some radiotracers labelled with ^{18}F and commonly used in PET will be briefly explained.

Fluorine is widely used in the development of radiolabelled pharmaceutical compounds due to its electronegativity, the fact that it forms strong bonds with carbon atoms in organic chemistry and as ^{18}F is a positron emitter. As mentioned before, the half-life of ^{18}F is 109.8 minutes. The incorporation of radioactive fluorine into molecules has been subject to extensive study by

synthetic chemists, and elemental fluorine is used in electrophilic fluorination reactions, and arenes, alkenes and active methylenes can be selectively fluorinated by xenon fluorides. ^{18}F-F_2, a high polarized element with a partial positive charge is commonly used in electrophilic fluorination, in which electron rich substrates like alkenes or aromatic compounds act as nucleophiles and become fluorinated. One example in oncology is the electrophilic fluorination of uracil to generate the antitumour agent 5FU. Using ^{18}F-F_2, in the presence of acetic anhydride and a trace of acetic acid, 5-^{18}F-FU is synthetized. Nucleophilic fluorination occurs when inorganic and other ionic fluorides are used (reviewed by Alauddin, 2012).

[^{18}F]Fluoro-2-deoxy-2-D-glucose

[^{18}F]-Fluoro-2-deoxy-2-D-glucose (2-FDG) is one of the most commonly used radiotracers in PET. Its applications include the assessment of glucose metabolism in heart, lungs, brain, and in tumours. In the latter, it is used to acquire static or, in some research applications, dynamic data sets which assess Standardised Uptake Values (SUVs) over the scan time. This information is used in diagnosing, staging and monitoring cancer, and its treatment and response. [^{18}F]FDG is used is several tumours types, e.g. Hodgkin's disease, non-Hodgkin's lymphoma, colorectal, breast, skin and lung cancer, and has also been approved for use in Alzheimer disease diagnosis as reviewed by Alauddin (2012).

[^{18}F]FDG is an analogue of glucose in which an ^{18}F atom replaces the hydroxyl group at position 2 as illustrated in Figure 1.21. As summarized in Figure 1.22, in cancer cells, metabolism can be upregulated and these cells are glucose avid so the [^{18}F]FDG will be taken up by cells through facilitative glucose transporters. Once inside the cell [^{18}F]FDG is phosphorylated by hexokinase (in cancer cells hexokinase II is predominately expressed) to [^{18}F]FDG-6-phosphate which is not metabolised and is trapped in the cell. There can be dephosphorylation by glucose-6-phosphatase but this enzyme is often under expressed in cancer cells. Although widely used, [^{18}F]FDG-PET is not always specific for tumours and false positive results can be generated by inflammation and active muscles, as reviewed by He and Guo (2008).

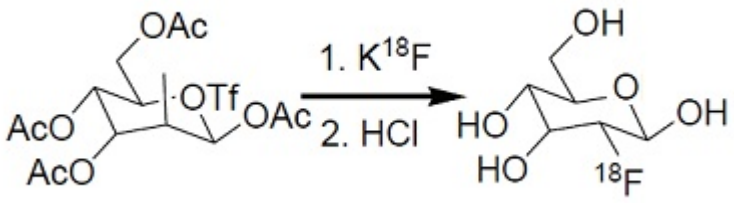

Figure 1.21: Nucleophilic fluorination in the synthesis of [^{18}F]FDG. Extracted from Alauddin (2012).

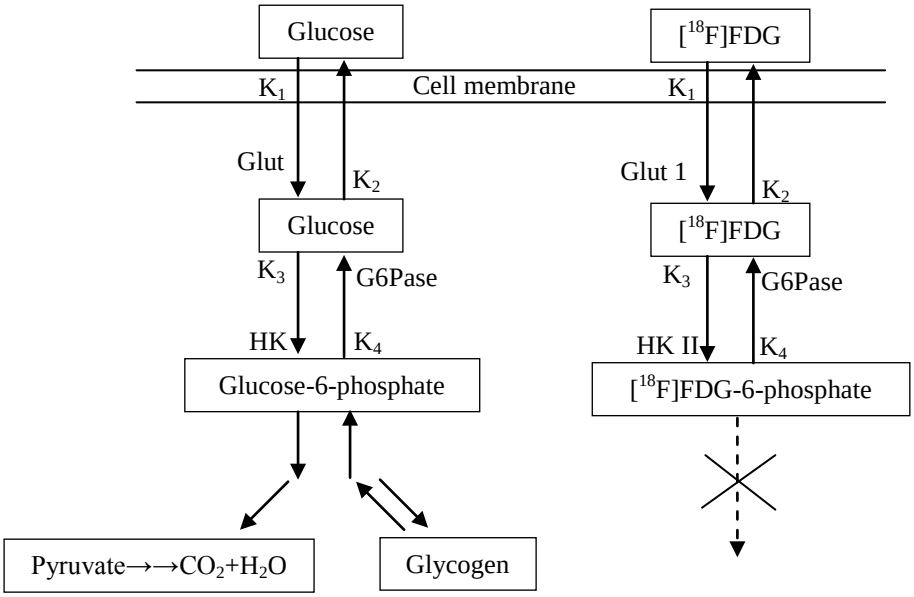

Figure 1.22: Schematic representation of the glucose and [^{18}F]FDG pathways in the cell. K_1, K_1, K_3, K_4 are rate constants while HK represents hexokinase and Glut stands for facilitative glucose transporters. Adapted from He and Guo (2008).

As shown in Figure 1.21, the reaction used for [^{18}F]FDG synthesis is nucleophilic displacement of an acetylated sugar derivative (glucose) by reaction with a fluoride ion followed by hydrolysis. The precursor for the nucleophilic reaction is a 2'-triflate of mannose acetate radiofluorinated with K^{18}F/Kryptofix 2.2.2. and hydrolysed by acid (HCl). The solution goes through a series of columns to purify it from free fluoride and other impurities, and a 0.22μm filter is used for sterilization of the final pure product (reviewed by Alauddin, 2012).

[^{18}F]FDG synthesis takes about 50 minutes and can achieve a yield of 60% (Saha, 2005).

[^{18}F]3'-Deoxy-3'-fluorothymidine

[^{18}F]-3'-Deoxy-3'-fluorothymidine ([^{18}F]FLT) is another PET tracer used for early detection and diagnosis of tumours, and treatment response assessment following therapy. [^{18}F]FLT is a proliferation marker, and brain tumours, malignant lymphomas, lung, colorectal and oesophageal cancer are some of the malignancies where [^{18}F]FLT PET has been investigated as reviewed by Alauddin (2012).

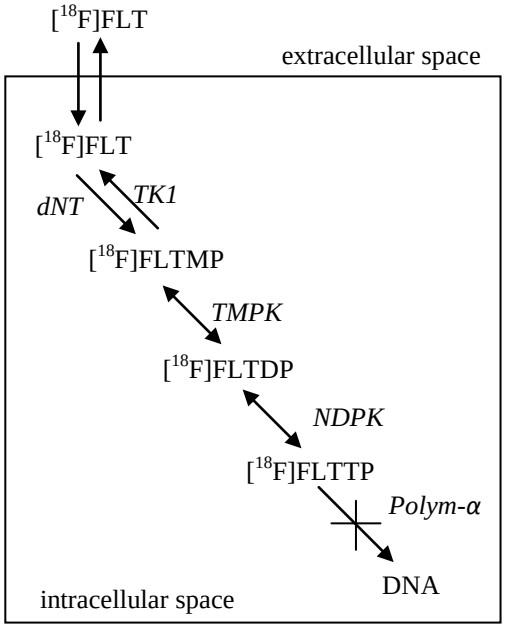

Figure 1.23: Schematic representation of the salvage DNA synthesis pathways imaged by [^{18}F]FLT in cells. TK1 stands for thymidine kinase-1, dNT deoxynucleotidase, TMPK for thymidylate kinase, NDPK nucleotide diphosphate kinase. FLTMP, FLTDP and FLTTP stand for fluorothymidine mono, di and triphosphate respectively. Adapted from Grierson *et al.* (2004).

In order to maintain intracellular nucleotide pools for DNA replication, proliferating cells utilize the DNA salvage pathway (Figure 1.23). [^{18}F]FLT entry into the pathway is controlled by the cytosolic enzyme thymidine kinase 1 (TK1). This enzyme is expressed during the S-phase of the cell cycle. Once inside the cytoplasm, [^{18}F]FLT is phosphorylated successively by TK1, thymidylate kinase (TMPK) and by nucleotide diphosphate kinase (NDPK) forming mono to triphosphates. Although there can be degradation of thymidine triphosphate, incorporation into DNA is rapid. In the case of [^{18}F]FLT, due to the fact it does not possess a 3'-hydroxyl on the deoxyribose ring, it cannot be incorporated in the DNA polymer (Grierson *et al.*, 2004).

[^{18}F]FLT is produced by the nucleophilic reaction of ^{18}F-sodium fluoride with the precursor 2,3'-anhydro-5'-0-benzoyl-2'-deoxythymidine (Figure 1.24). The

precursor preparation follows a standard organic synthesis and is described in Machulla *et al.*(2000). ^{18}F-Sodium fluoride forms a mixture with Kryptofix 2.2.2 and potassium carbonate in acetonitrile which is heated at 120°C for 5 minutes, followed by the addition of the precursor in dimethyl sulfoxide (DMSO) to the dried residue and drying for 10 minutes at 160°C. Sodium hydroxide is used to hydrolyse the 5'-0-protecting group, and finally the solution is filtered to isolate the [^{18}F]FLT which is further purified by HPLC (Saha, 2005).

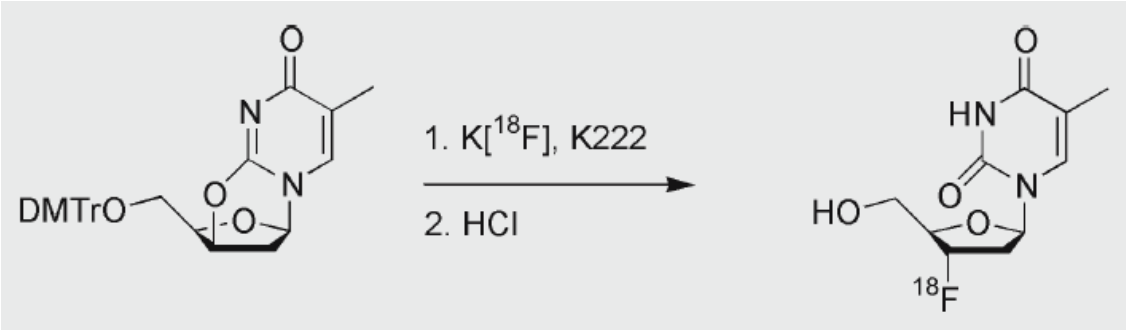

Figure 1.24: Preparation of [^{18}F]FLT. Copied from Bailey and Towsend, 2005.

[^{18}F]FLT is produced with an overall yield of approximately 45% and a radiochemical purity above 95% in a 60 minutes process (Saha, 2005). However, with [^{18}F]FLT this yield has been achieved only in recent years (Yun *et al.*, 2003; Oh *et al.,* 2004), as previously the yield was much lower, about 7% (Grierson and Shields, 2000; Machulla *et al.*, 2000). This latter value is a much lower yield when compared with [^{18}F]FDG and the complexity and price of the precursors make [^{18}F]FLT an expensive and less available tracer.

A number of studies have compared [^{18}F]FDG and [^{18}F]FLT scanning. In 2005 van Westreenen *et al.* published a study where [^{18}F]FLT-PET and [^{18}F]FDG-PET were performed in 10 patients with oesophageal cancer. [^{18}F]FDG-PET detected all oesophageal cancers while [^{18}F]FLT-PET failed to detect two. In comparison the median Standardized Uptake Value (SUV) for [^{18}F]FDG-PET was 6.0 while [^{18}F]FLT median SUV was 3.4 (van Westreenen *et al.*, 2005). In 2007, Yamamoto *et al.* published an article were they studied the relationship between [^{18}F]FDG and [^{18}F]FLT uptake, and Ki67 immunohistochemistry. This study in non-small cell lung cancer also demonstrated a mean [^{18}F]FLT SUV significantly lower than the [^{18}F]FDG value (Yamamoto *et al.*, 2007). In 2011 Mileshkin *et al.* also studied non-small cell lung cancer patients treated with

erlotinib (a tyrosine kinase inhibitor) to assess changes in [^{18}F]FDG and [^{18}F]FLT uptake in relation to clinical outcome. In this study patients had [^{18}F]FDG and [^{18}F]FLT scans at baseline (prior to treatment), at day 14 and at day 56. The median FDG uptake corrected for lean body mass (SUV max) was higher (approximately 5.63) than FLT uptake (SUVmax, 2.5) at baseline, and both [^{18}F]FDG- and [^{18}F]FLT-PET provided useful early information about erlotinib response (Mileshkin *et al.*, 2011).

1.5.2 Labelled Drugs in PET

PET can be a useful tool in drug development from early drug discovery to clinical trials by providing data relating to tumour pathophysiology, target selection and validation, lead generation and optimization as well as pre-clinical and clinical development. PET has the advantage of very high sensitivity coupled with being a non-invasive technology. During the drug development process, information regarding drug absorption, distribution, metabolism and excretion (i.e. pharmacokinetics) can influence decisions and PET can provide data that complement conventional plasma-derived pharmacokinetic results.

PET studies provide data on the kinetics, and distribution of drugs in healthy and diseased tissue, and drug clearance. Pharmacokinetic parameters that can be quantified by PET include peak radioactivity, time to reach peak radioactivity, standardised uptake value (SUV) as well as drug concentrations in tissues relative to that in the blood. Uptake and efflux-related kinetic parameters can also be inferred from the mathematical modelling of tissue PET data. Parameters include selective binding, distribution from plasma to tissue and from tissue to plasma, and the tissue volume of distribution (Aboagye *et al.*, 2001).

As referred to in the section 1.3, certain cancer drugs can be labelled with positron emitting isotopes in order to perform PET pharmacokinetic studies. An example of a tumour type where drugs have been labelled for PET studies is glioma.

Temozolomide is an alkylating agent of [5,1-d]-1,2,3,5-tetrazine series with good oral bioavailability and clinical activity in the treatment of malignant

melanomas and gliomas. Temozolomide has a pH dependent activation, i.e. it is stable at acid pH but the rate of activation increases rapidly on passing through neutral to basic pH. Temozolomide can be labelled with [^{11}C] in two sites, at the 4-carbonyl and 3-N-methyl positions of the molecule; the former generating [^{11}C]CO_2 during activation, and the latter being incorporated into DNA. The two [^{11}C]-labelled versions of temozolomide PET studies were used to demonstrate both biodistribution and activation (Saleem *et al.*, 2003).

5-Fluorouracil (5-FU) is an antitumour drug from the fluoroprymidine family which, following metabolism, inhibits thymidylate synthetase and is incorporated into DNA and RNA. Although it was first reported in 1958, 5-FU is still used in cancer therapy alone or in combination with other drugs for colorectal, gastric and advanced pancreatic cancer. [^{18}F] labelled 5-FU tumour uptake has been shown to be a positive predictive biomarker for patient selection, and the drug can also be labelled with [^{11}C] (Seki *et al.*, 2007).

As a final example, tamoxifen is an antiestrogen which binds to and primarily blocks the function of the estrogen receptor. Tamoxifen inhibits the growth of estrogen-dependent breast cancers, and can be labelled with [^{18}F] and used in the detection of primary and secondary estrogen receptor positive tumours, and in monitoring toxicity as described by Yang *et al.* (1993) and reviewed by Benard and Turcotte (2005).

1.6 Aims of the studies performed in this thesis

The overall aim of the project described in this thesis was to develop and optimize pharmacodynamic and surrogate response biomarkers for the PARP inhibitor rucaparib in pre-clinical models.

Based on previous experiments (Calabrese *et al.*, 2004; Ali *et al.*, 2009), it was hypothesised that the acute vascular effects of rucaparib could be measured by DCE-MRI. Experiments were performed in SW620 and A2780 human tumour xenograft bearing mice. Hydralazine was chosen as a positive control and treatment groups were rucaparib, temozolomide and the combination of rucaparib and temozolomide. Anticipating that acute effects on vasculature would influence tumour energy metabolism *in vivo* ^{31}P-MRS experiments were also performed and the ratio of the inorganic phosphate (Pi) and βNTP concentration was measured in each sample.

To allow comparison with the *in vivo* MRS data, absolute quantification and greater sensitivity and discrimination, *ex vivo* MRS experiments the A2780 tumour cell line were performed. Initially a protocol was developed for the quantification of relevant metabolites in cells and in tissues using the method of addition procedure. Tumour cells were again treated with rucaparib, temozolomide or the combination of rucaparib and temozolomide. To further validate *ex vivo* MRS as a biomarker for PARP1 activity and PARP inhibition, *ex vivo* MRS studies were performed on extracts of livers from WT and PARP1 KO mice treated with either rucaparib, temozolomide or the combination of rucaparib and temozolomide.

Lastly, a second imaging biomarker technique, PET, was evaluated as a potential surrogate response biomarker, using 2 tracers: [^{18}F]FDG and [^{18}F]FLT. The [^{18}F]FDG-PET studies were performed to determine the impact of 5 days treatment with rucaparib, temozolomide or rucaparib in combination with temozolomide, on glucose metabolism, and the relationship between tumour volume variation and [^{18}F]FDG uptake was evaluated. In similar studies with [^{18}F]FLT-PET the relationship between changes in [^{18}F]FLT uptake and the outcome of the treatment was evaluated.

Together, the studies described in this thesis represent the first comprehensive multimodality evaluation of imaging biomarkers for the investigation of PARP inhibitors.

Chapter 2. Materials and Methods

2.1 Materials

RPMI 1640, without L-glutamine, with Phenol Red, Foetal Bovine Serum Gold (EU Approved), 175 cm^2 cell culture flasks with filter caps and surface treated, trypsin EDTA (1:250), L-glutamine (200mM), penicillin/streptomycin (100x) and C-Chip disposable haemocytometers were purchased from PAA Laboratories Ltd., Termare Close, Houndstone Business Park, Yeovil, Somerset, BA22 8YG, United Kingdom (UK).

One ml, 5 ml, 10 ml, 25 ml pipettes individually wrapped, NMR tubes (economy standard borosilicate glass 0.020 mm concentricity, 0.070 mm camber, 178 mm length, 4.97 mm O.D. 4.20 mm I.D. Norell) and 5100 Cryo 1°C freezing container (“Mr. Frosty”) were purchased from Fisher Scientific UK Ltd., Bishop Meadow Road, Loughborough, LE11 5RG, UK.

Nineteen, 23, 25, and 30 gauge needles, 0.5 ml insulin, 1 ml, and 5 ml syringes, industrial methylated spirits (Denatured Alcohol), Decon 90, saline and water for injection were purchased from Nu-Care Products Ltd., Unit 21, Broadmead Business Park, Broadmead Road, Stewartby, Bedfordshire, MK43 9NX , UK.

3-(Trimethylsilyl)propionic-2,2,3,3-d4 acid sodium salt (TSP), methylenediphosphonic acid (MDP), adenosine 5'-triphosphate disodium salt hydrate (ATP), adenosine 5'-diphosphate sodium salt, from bacterial source (ADP), adenosine 5'-monophosphate sodium salt minimum 99% (AMP), adenosine 5'-diphosphoribose sodium salt (ADP ribose), β-nicotinamide adenine dinucleotide hydrate from yeast (NAD), dimethyl sulfoxide (DMSO), deuterium oxide (D_2O, 99.9% isotopic purity), phosphocholine chloride calcium salt tetrahydrate (PCh), Chelex® 100 sodium form, 50-100 mesh (dry) were purchased from Sigma-Aldrich Company Ltd., The Old Brickyard, New Road, Gillingham, Dorset, SP8 4XT, UK.

Eppendorf tubes (1.5 ml), 7 ml bijou containers, 15 ml centrifuge tubes, 20 ml universal containers, 50 ml Falcon tubes (skirted and non-skirted) were purchased from Scientific Laboratory Supplies Limited, Wilford Industrial Estate, Ruddington Lane, Wilford, Nottingham, NG11 7EP, UK.

Polyethelyne (PE) tubing for cannulation and contrast agent/radiotracer administration (BPTE-T10, 0.11” ID, 0.24” OD, non-sterile; BPTE-T10, 0.23” ID, 0.38” OD, non-sterile) were purchased from Linton instrumentation UK, Units 1-2, Forge Business Centre, Upper Rose Lane, IP22 1AP, Palgrave, Diss, Norfolk, UK.

Two hundred and 1000 µl pipettes, and 200 and 1000 µl pipettes tips loose were purchased from STARLAB (UK), Ltd, Unit 4 Tanners Drive, Blakelands, Milton Keynes, MK14 5NA, UK, and 20, 200 and 1000 µl pipettes were purchased from Gilson Scientific Ltd, 20 Charles Street, Luton, Bedfordshire LU2 0EB, UK.

Introcan Safety® 24G 0.7x19 mm catheter and Hystoacryl® were purchased from B. Braun Medical Ltd., Thorncliffe Park, Sheffield, S35 2PW, UK.

The Cryo-Cup Grinder for tissue grinding was purchased from BioSpec Products, PO Box 788, Bartlesville, OK 74005, USA.

Heparin sodium, 1000 units/ml for tail vein cannulation was purchased from Wockhardt UK Ltd, Ash Road North, Wrexham, LL13 9UF, United Kingdom.

The contrast agent used in the DCE-MRI experiments, gadoteridol, under the commercial name ProHance was purchased from Bracco International, Amsterdam, Netherlands.

The nude CD1 mice used to implant human tumour xenografts were purchased from Charles River UK Ltd., Manston Road, Margate, CT9 4LT, United Kingdom.

Temozolomide was a gift from the Cancer Research Campaign, UK and rucaparib was a gift from Pfizer UK; however, rucaparib has been licensed to Clovis Oncology, 2525, 28th Street, Suite 100, Boulder, CO 80301, United States of America (USA).

The [^{18}F]fluoro-2-deoxy-2-D-glucose and the 3'-deoxy-3'-[^{18}F]fluorothymidine used in the PET studies were purchased from PETNET Solutions, Heathfield Way, Nottingham City Hospital, Gate 1, Hucknall Road, Nottingham, NG5 1PB, UK.

2.2 Cell culture

Two cell lines were used to perform all the experiments: the colon cancer cell line SW620 (American Type Culture Collection, Manassas, VA, USA), and the ovarian cancer cell line, A2780 (Health Protection Agency, Porton Down, Salisbury, UK). These cell lines were provided in frozen vials stored in the NICR. Both cell lines were grown in monolayer culture in complete 1640 RPMI supplemented with 10% (v/v) foetal bovine serum (FBS), 2 mM L-glutamine, 100 units/ml penicillin and 100 µg/ml streptomycin. The cell lines were independently authenticated and shown to be mycoplasma free. These cells were chosen based in previous studies with PARP inhibitors (Calabrese *et al.*, 2003, Thomas *et al.*, 2007, and Ali *et al.*, 2009 for the SW620) and preliminary studies performed by Lan-zhen Whan (NICR, personal communication) in A2780 cells.

For every new culture started, the vial with frozen cells was defrosted in a water bath, the contents of the vial poured into a universal with 19 ml of media at 37ºC, centrifuged at 1000 rpm for 5 minutes and resuspended in an appropriate volume for transfer into a culture flask.

Cells were incubated in a humidified atmosphere of 20% O_2, 5% CO_2 and 75% N_2 (v/v/v) at 37ºC and kept in exponential growth phase by passage as soon as cultures reached 80-90% confluence. The passage method included a primary wash of the cells in 10 ml of PBS followed by the addition of 10 ml of trypsin-EDTA to harvest the cells, prior to centrifugation for 5 minutes at 1000 g, resuspension and dilution in an appropriate volume of fresh media.

Cell cultures were checked on a daily basis and media replaced every 2 days.
To freeze cells for storage, the contents of the flask were trypsinised, centrifuged and resuspended into media with 10% DMSO (v/v) and dispensed into several cryovials, frozen in a 5100 Cryo 1°C freezing container ("Mr. Frosty",) in a -80ºC freezer, and transferred to a liquid nitrogen tank.

Cells for implantation into nude CD1 mice were trypsinised, resuspended in fresh media at a density of 8-10x10^6 cells in 50µl.

2.3 Cell extract spectroscopy

Initially, a “methods of addition” approach was used to validate the protocol and quantify of the relevant cellular metabolite. Once the protocol was optimized, experiments were performed in which cells were treated with the relevant compounds and harvested. The cells were extracted using a perchloric acid extraction protocol and analysed as described under Nuclear Magnetic Resonance Spectroscopy (MRS).

2.3.1 Methods of addition

Modern chemical instruments, despite their high sensitivity and linearity, have output values which are still dependent on the conditions of the measurement and the response, R, of the equipment. The concentration of a compound in a sample can be estimated by the addition of known standards and the endogenous concentration calculated by the extrapolation of the calibration curve. In the experiments, known volumes (NV_s, where N is running multiple integer 0,1,2, etc.) of a standard of known concentration of standard (C_s) were added to sample aliquots of known volume, V_x, containing an unknown concentration, C_x, of the analyte and diluted to have a constant total volume across all the samples (V_t) (Figure 2.1).

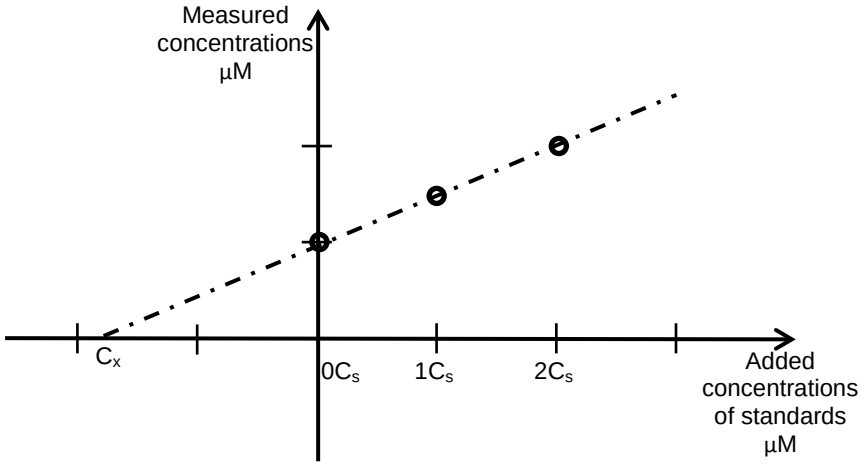

Figure 2.1: Calibration curve established from the addition and measurement of standards. Adapted from Bader (1980) and Schumann *et al.* (1992).

However, the absolute value is still dependent on the response so a suitable method of addition will provide a reduced standard error estimation of the unknown compound. The response of a linear instrument is directly proportional to the concentration of the compound by a constant of proportionality, k.

$$R = k \times C$$

In a series of additions R becomes

$$R_N = k\left[\frac{V_x C_x}{V_t} + \frac{N V_s C_s}{V_t}\right]$$

if the volumes are replaced by the volume fractions (quotient between volume of compound and total volume) for unknown (f_x) and standard (f_s) the equation becomes:

$$R_N = k(f_x C_x + N f_s C_s)$$

which represents a linear regression depicted by a straight line when plotted against N as in Figure 2.1, in which kf_sC_s is the slope, m, and kf_xC_x is the intercept. Hence the unknown concentration C_x can be calculated from

$$C_x = \frac{b V_s C_s}{m V_x}$$

(Bader, 1980; Schumann *et al.*, 1992)

This method has been used in a wide range of techniques namely high-performance liquid chromatography (HPLC) (Sakkiadi *et al.*, 2007), thin layer chromatography (TLC) (Shariatgorji *et al.*, 2009), spectrophotometry (Safavi and Tohidi, 2007), and magnetic resonance spectroscopy (MRS) (Talebpour *et al.*, 2004).

In the specific case of cell extract spectroscopy (and later in tissue extract spectroscopy) used in this thesis, known concentrations of each metabolite were added to aliquots of the sample, each being derived from 1.5×10^8 cells. To each aliquot was added a fixed volume of liquid either containing no metabolite (0 mM), or with metabolite at one of two different concentrations. All samples were then processed in an identical manner (subsection 2.3.3). Signals in the NMR spectrum were then quantified and the results plotted against the expected concentration of added metabolite. The slope of the fitted straight line provided an estimate of the recovery in the extraction procedure, and the interception of the fitted line with the x-axis provides the concentration of metabolite derived from the original cell sample. Ideally, a good linear fit is obtained with recovery of >50%.

2.3.2 Cell treatment and harvesting

The cells were cultured as described previously (section 2.2) and split into 12 175 cm² cell culture flasks at $5x10^7$ cells *per* flask for A2780 cells, and $4.5x10^7$ cells *per* flask for SW620 cells. The 12 flasks for each cell line were divided into 4 groups of 3 as each treatment required at least $1.5x10^8$ A2780 cells to start the experiment. The interval between the seeding of the cells and the treatment was 40 hours (with medium replacement 24 hours after seeding).

There were four treatment groups:

- Control;
- 0.1 μM rucaparib;
- 180 μM temozolomide;
- 0.1 μM rucaparib combined with 180 μM temozolomide.

Concentrations were based upon previous *in vitro* studies performed by Huw Thomas (Thomas *et al.*, 2007) and Lan-zhen Whan (NICR, personal communication), and where the GI_{50} concentration for temozolomide, and a rucaparib concentration that results in significant chemosensitization. On the day of treatment the media was replaced by 25 ml of fresh media (in the control group) or by 25 ml of the media with the appropriate concentrations of drugs added (remaining groups). The flasks were returned to the incubator for 6h.

Before the extraction procedure started it was necessary to harvest the cells and Figure 2.2 summarizes the harvesting protocol.

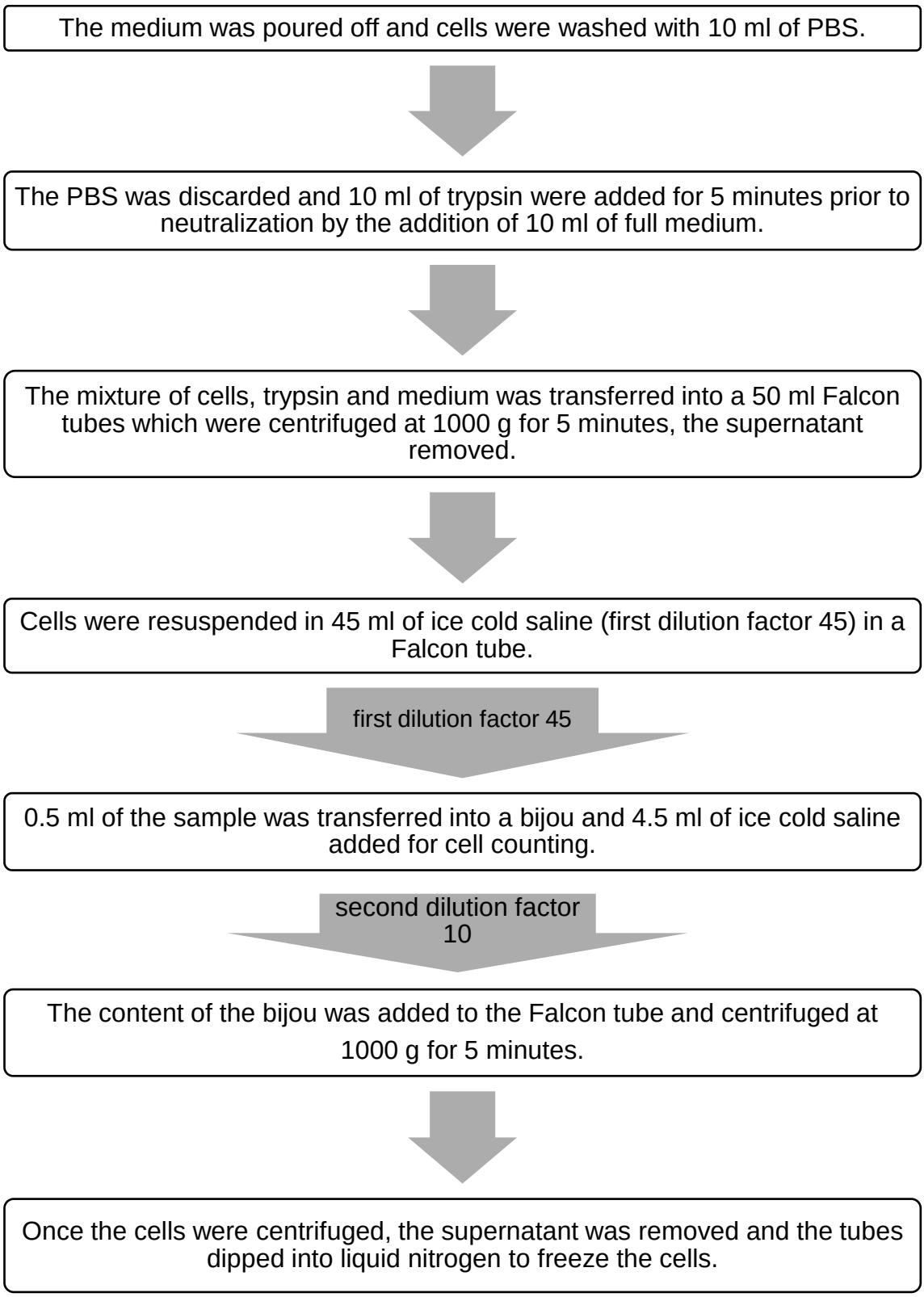

Figure 2.2: Flow chart summarizing the cell harvesting protocol.

Cells were counted using a disposable C-Chip haemocytometer and the tubes were kept in a -80°C freezer until extraction.

2.3.3 Extraction Procedure

This extraction procedure used was adapted from an existing protocol kindly supplied by Mrs Loreta Rodrigues from CR UK Cambridge Research Institute (Cambridge, UK).

The protocol is described in Figure 2.3.

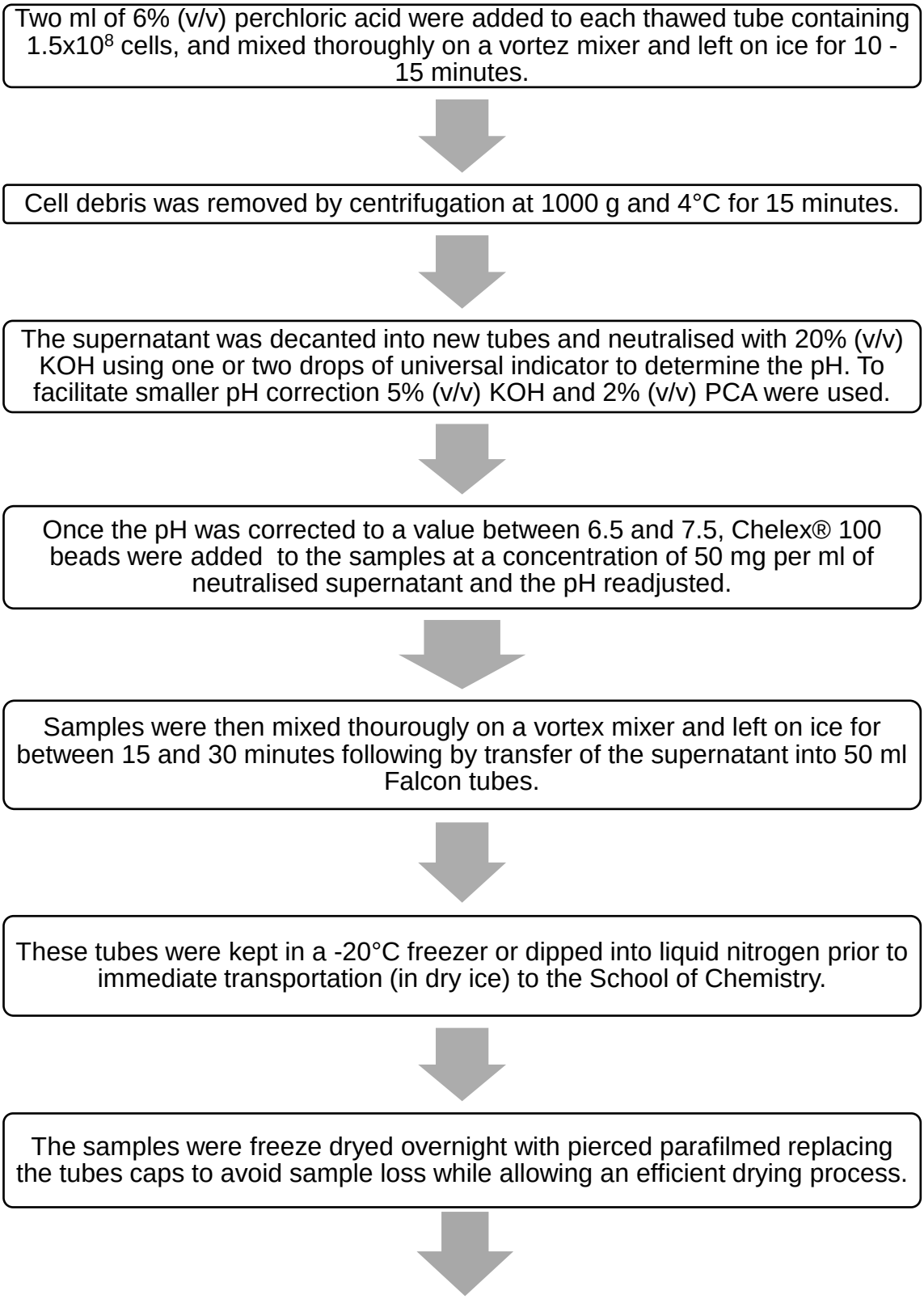

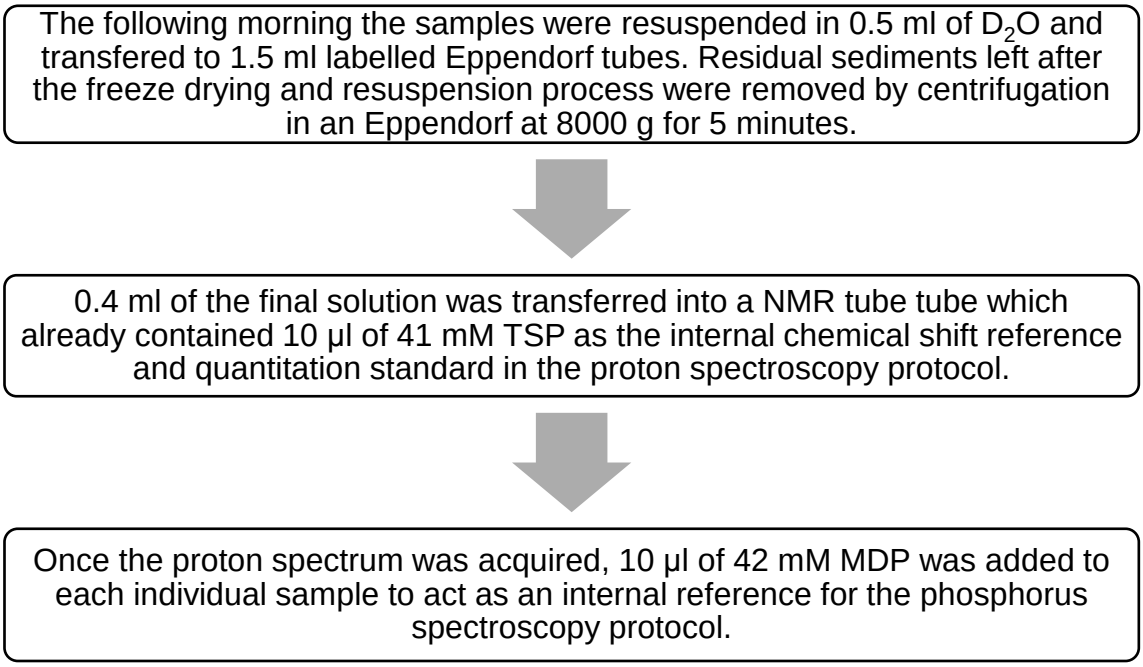

Figure 2.3: Flow chart summarizing the cell extraction protocol.

The dipping the tubes in liquid nitrogen mentioned in Figure 2.2 is intended to stop metabolism in the sample. To avoid the recovery of enzymatic activity the samples are always kept frozen in dry ice or in -80°C freezers. Perchloric acid addition to the sample enables metabolic fingerprinting studies by precipitating proteins in a solid phase and extracting hydrophilic metabolites in the liquid phase (Lin *et al.*, 2007). The Chelex® 100 beads complex with divalent ions in the sample which could affect the ^{31}P-MRS signal (Walsh *et al.*, 1991). The freeze drying step not only avoids metabolic activity taking place, but also enables the replacement of H_2O by D_2O to avoid contamination of proton MRS signal by the protons of the solvent.

2.3.4 Spectroscopy

All NMR spectroscopy experiments on the cell and tissue extracts were performed on an 11.4T Bruker Avance III 500MHz NMR spectrometer located in the Northern Institute for Cancer Research Laboratories, School of Chemistry, Newcastle University (Bedson Building). The samples were placed in the magnet tray and left to acquire proton spectra in daytime hours and the phosphorus spectra (with the MDP already added) overnight or during weekends.

The proton acquisition protocol included a standard single 90° pulse-acquire experiment with a water pre-saturation pulse at 4.7 ppm, delay time of 5 seconds, acquisition time of 2.34 seconds and 64 averages (total repetition time, TR, of 7.34 seconds) as represented in Figure 2.4. Overall the sequence would run for approximately 7 minutes and 45 seconds. In this ^{1}H sequence the TR is longer than expected T_1 values, giving minimal saturation effects about 95% signal recovery.

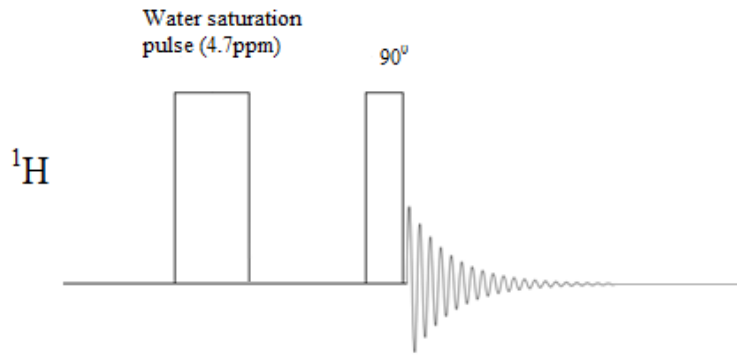

Figure 2.4: Design of the proton acquisition sequence. This sequence used a pre-saturation 180° pulse at 4.7 ppm to totally saturate the water signal, followed by a standard 90°pulse for the protons followed very closely by the FID signal acquisition. Figure kindly provided by Carlo Bawn.

For proton spectra acquisition, 1 mM TSP (the final concentration in the NMR tube) was used as the reference for quantification. After acquisition terminated, 10 µl of 42 mM MDP was added to the tube to give a final 1 mM concentration in the NMR tube, and allow quantification of the phosphorus spectrum.

The phosphorus spectra were acquired using a standard single 90° pulse-acquire experiment using inverse-gated decoupling of ^{1}H nuclei. The sequence had a delay time of 2 seconds, an acquisition time of 0.4 seconds and 4000 averages to improve the signal to noise ratio (SNR) as depicted in Figure 2.5.
In this ^{31}P sequence the TR being similar to expected T_1 values, there will be some partial saturation. This is a compromise due to limited SNR and scanning time constraints. In this sequence as well as for the ^{1}H spectra acquisition sequence, the flip angle used was 90°.

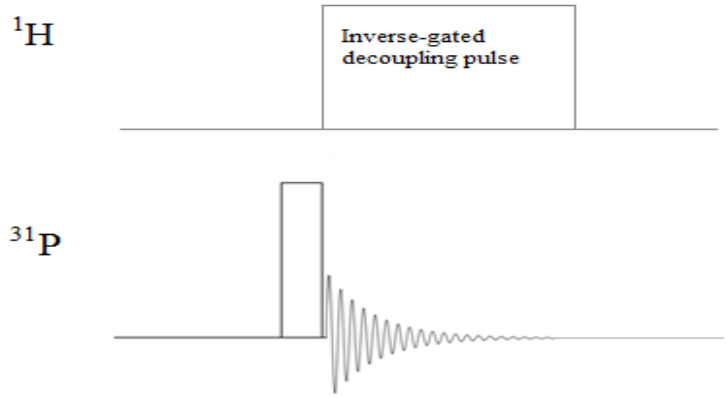

Figure 2.5: Design of the phosphorus acquisition sequence. This sequence used a standard single 90° pulse-acquire experiment using inverse-gated decoupling of ^{1}H nuclei. On the bottom half of the sequence, there is a 90°pulse for phosphorus followed by FID signal acquisition. At that same moment, as seen in the top half, a continuous wave starts which keeps the proton signal decoupled from the phosphorus signal to avoid the Nuclear Overhauser Effect (NOE) (Keepers and James, 1984), and make the quantification of the phosphorus data more accurate. Figure kindly provided by Carlo Bawn.

Data analysis

The results of the MRS experiments were analysed using the Bruker software package TopSpin™. Data were loaded into the software which applied a Fourier Transform, followed by a phasing step. After the phasing, the references peaks (TSP for proton and MDP for phosphorus) were set as zero order phases. The other peaks were phased in first and second order phasing steps based on the zero order phases of the references. After the phasing process, a baseline correction step was performed which was usually automatic but was performed manually if required (using a polynomial function correction). Finally, the individual peaks were defined manually and integrated for relative quantitation (by comparison with the internal reference).

2.4 DCE-MRI

All the *in vivo* experiments were reviewed and approved by the relevant Institutional Animal Welfare Committees and performed accordingly to national law under a UK Home Office license.

All the DCE-MRI experiments were performed in a Varian 7T horizontal bore preclinical MR system using human tumour xenografts grown in CD1 nude mice purchased from Charles Rivers. This specific strain is immunodeficient (a lack of thymus prevents the production of T-cells) and hairless (albino background) making it very well suited for xenografting and tumour biology research (Rice and O'Brien, 1980; Chia *et al.*, 2005).

For implantation, 6-8x10^6 cells *per* 50 µl of media were prepared and implanted. Each implant was performed under anaesthesia. The animals were returned to the animal housing facility and checked daily for tumour growth.

DCE-MRI experiment setup

When tumours reached an average size of 10x10 mm, mice were anaesthetized in a mixture of 2% isoflurane/oxygen (v/v). For DCE-MRI purposes, the tail vein was cannulated using a 30G needle attached to a 1 ml syringe containing 20 units/ml of heparin (100 µl of heparin diluted in 4.9 ml of saline) via a BPTE-T10, 0.28 mm ID, 0.61 mm OD tubing. Once the tail vein was successfully cannulated, the cannula was glued to the tail using Hystoacryl® and when the glue was dry the animal was transferred into the 7T scanner. The mouse was placed in a prone position and breathing monitored throughout the experiment by a breathing pillow placed under the abdomen. The temperature inside the magnet was also measured and controlled by a fibre-optic sensor. Both sensors were connected to a console which allowed regulation of the dose of anaesthetic as well as the temperature of the air propelled by the fan into the magnet (PC-sam software, SA Instruments, Inc., 65 Main Street, Stony Brook, NY 11790, USA). The cannula tubing was then cut and connected to a BPTE-T10, 0.58 mm ID, 0.97 mm OD tubing which was attached to a 1 ml syringe by a 23G needle which contained 25 mM gadoteridol.

A Rapid ^{1}H-^{31}P 12 mm surface coil (RAPID Biomedical GmbH, Technologiepark Wuerzburg-Rimpar, Kettelerstrasse 3-11, 97222 Rimpar, Germany) was placed over the tumour (i.e. the tumour was inserted into the coil lumen) and once secured in place the tray was inserted into the magnet ready for scanning.

DCE-MRI data acquisition protocol

This first part of the protocol was executed using the proton channel of the coil/receiver. Firstly a scout scan with 5 images over three planes was performed to confirm good positioning of the coil over the tumour and that the tumour was in the centre of the magnet. A proton power calibration was performed using a SPULS sequence, i.e. an array of 23 pulse width (pw) elements from 30 to 250 µs under a repetition time of 5 seconds and a transmitter pulse power (tpwr) of 45 decibels (dB). The pulse returning the biggest peak was used for the proton signal. When pulse width value was defined, the repetition time was reduced to 0.5 seconds and a manual global shim was performed to improve the magnetic field homogeneity for ^{1}H DCE-MRI and for ^{31}P-MRS. The shimming parameters were saved to allow them to be restored if the system required a reset. Another scout scan was then acquired, this time to allow the placement of a voxel over the tumour for localized shimming. The voxel size was dependant on the tumour size, and a PRESS sequence (represented in Figure 2.6) was used with a repetition time of approximately 1030 ms and without water suppression.

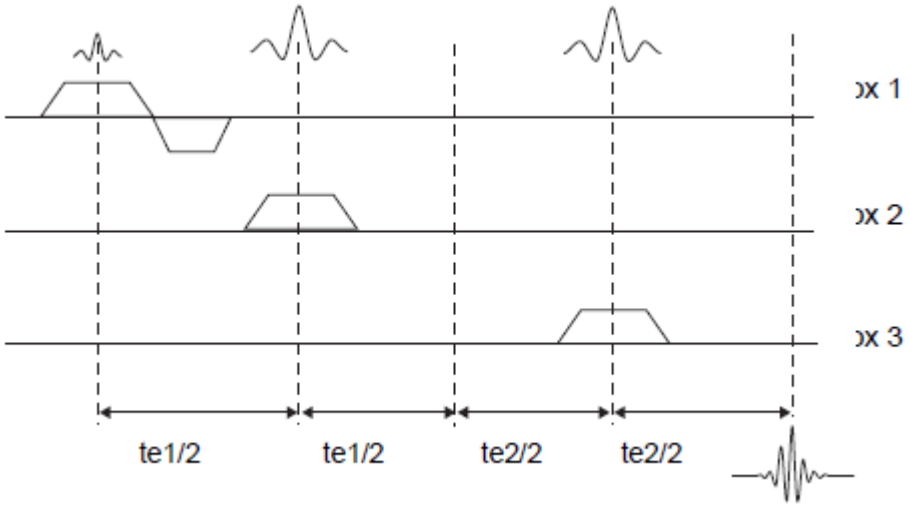

Figure 2.6: Design of a PRESS sequence. This sequence based in a double spin echo and allows the acquisition of 1D NMR spectra from a delimited area. Copied from Schreiber (2008).

This shimming enhancement was based on the global shimming previously performed and the shim settings were also saved. Once the shimming process was finished, the PRESS protocol was used to acquire a ^{1}H NMR spectrum of the tumour localized area and the water peak linewidth was recorded. A third scout scan was then performed for the selection of the 10 slices of 2 mm thickness (no gap) to be used in a GEMS sequence as depicted in Figure 2.7.

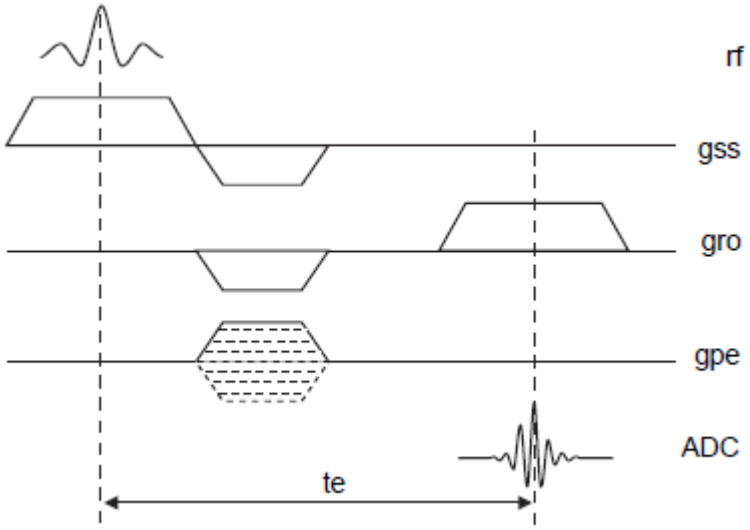

Figure 2.7: Design of a GEMS sequence. This gradient echo 2D multi slice sequence enables the use of shorter repetition time (tr) and a reduced flip angle. Copied from Schreiber (2008).

The parameters for the GEMS acquisition sequence included a repetition time of 100 ms, 2 averages, a 256x256 matrix, and a FOV of 35x40 mm. The slices were placed in order to be across the tumour in an axial direction, the middle slice in the centre of the tumour for later single slice acquisitions. For later gadolinium concentration calculations, a FSEMS sequence (depicted in Figure 2.8) was used to acquire T1 estimates. The parameters of this sequence included a repetition time of 1200 ms, one averaged, a 256x256 matrix and an array of inversion recovery (IR) pulses with 8 TI values starting at 10 ms and with a maximum values of 900 ms. This sequence uses sinc 90° excitation 180° refocusing pulses. The inversion pulse is adiabatic to try to provide a uniform response over the volume of interest, minimising flip angle variations occurring with the surface coil, the fact that it also uses sinc pulses makes it less effective and diminishes the quality of the T1 information and consequently the gadolinium concentration estimations.

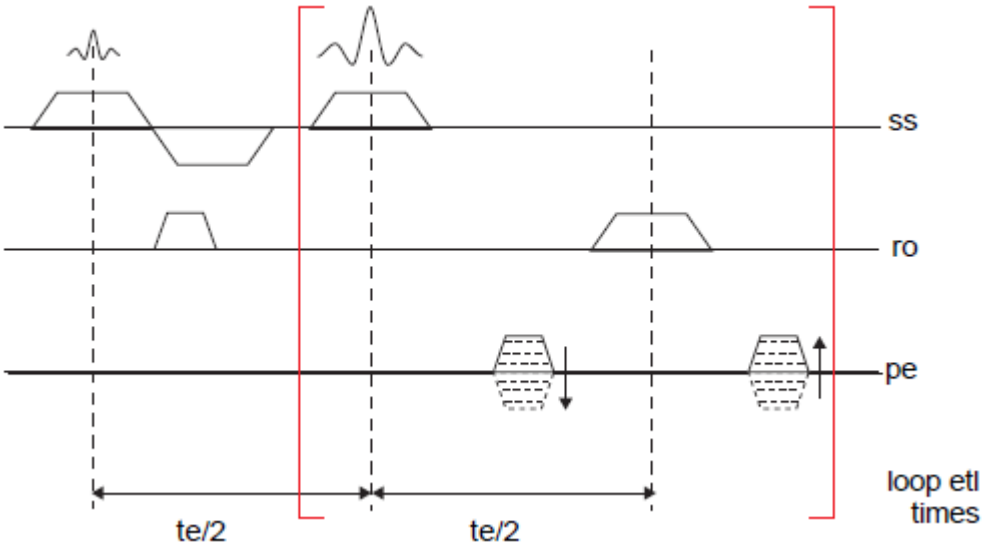

Figure 2.8: Design of a FSEMS sequence. This fast spin echo multi-slice sequence selects the number of echoes in an echo train and at the same time determines which echo will configure the centre of k-space. Copied from Schreiber (2008).

The previous GEMS sequence was used to acquire 100 images of the same central single slice of the tumour. Using the same 35x40 mm FOV, one 2 mm thick slice central in the tumour was selected. The repetition time was reduced to 23.44 ms and only one average acquired *per* image, which translates to a 10 minute scan time. Once the sequence started, approximately 0.1 mmoles/kg of gadoteridol in a volume of 200 µl was injected intravenously after block 6. The injection was given manually over the 6 seconds during the current block acquisition and constituted the pre-treatment injection of contrast agent for comparison with the post-treatment scan.

Thirty minutes after the first injection of gadoteridol, the mouse was treated as described below. For both tumour types the treatment groups were:

- Control (10µl of saline *per* g of body weight);
- 5 mg/kg of hydralazine (10 ml/kg of a 0.5 mg/ml solution in saline);
- 1 mg/kg of rucaparib (10 ml/kg of a 0.1 mg/ml solution in water for injection);
- 5 mg/kg of rucaparib (10 ml/kg of a 0.5 mg/ml solution in water for injection);
- 50 mg/kg of rucaparib (10 ml/kg of a 5 mg/ml solution in water for injection);
- 68 mg/kg of temozolomide (10 ml/kg of a 6.8 mg/ml solution in saline);

- 1 mg/kg of rucaparib combined with 68 mg/kg of temozolomide (10 ml/kg of a 0.1 mg/ml solution in water for injection with 10 ml/kg of a 6.8 mg/ml solution in saline);
- 5 mg/kg of rucaparib combined with 68 mg/kg of temozolomide (10 ml/kg of a 0.5 mg/ml solution in water for injection with 10 ml/kg of a 6.8 mg/ml solution in saline).

All the treatments were given manually by *i.p.* injection. The drug was in a 1 ml syringe connected to an *i.p.* cannula by an BPTE-T10, 0.58 mm ID, 0.97 mm OD tubing and a 23G needle. In the combination groups two *i.p.* cannulas were inserted in the mouse and glued with Hystoacryl® prior to its transfer to the magnet.

Approximately 80 minutes after the first contrast agent injection, a fourth scout scan was performed to confirm that there was no displacement in the mouse position which could affect the results. Another T1 dedicated FSEMS sequence was used to acquire T1 estimates of the tumour slice before a second injection of contrast agent during another dynamic GEMS sequence. All the parameters of the FSEMS (T1) and GEMS (dynamic) sequences were repeated as described for the first contrast agent injection. The second injection of contrast agent was then given 90 minutes after the first injection of gadoteridol, i.e. 60 minutes after the drug(s) treatment had been administered, using the same dose of approximately 0.1 mmoles/kg gadoteridol in a volume of 200 µl was given *i.v.*.

DCE-MRI data analysis

The data were analysed using ImageJ (v1.44) software, a freeware Java-based image processing program (Schneider *et al.*, 2012). The 100 images from each dynamic acquisition were gathered into one stack with 100 elements. One ROI around the tumour was drawn, which was automatically propagated to all the elements in the stack as exemplified in Figure 2.9 a). For each image the mean pixel intensity was measured inside the ROI, and the same ROI was used in the stack corresponding to the second injection of gadoteridol as represented in Figure 2.9 b) and c).

a)

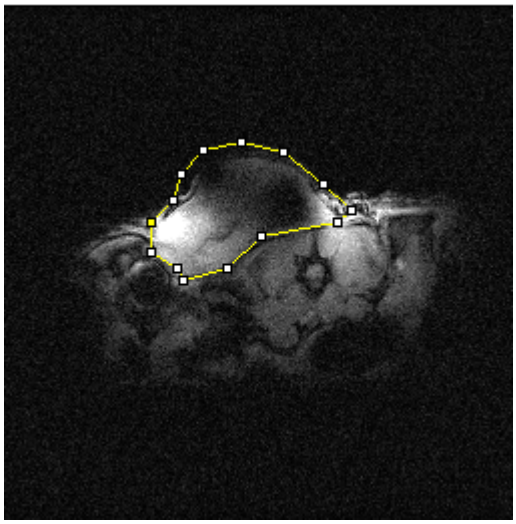

b)

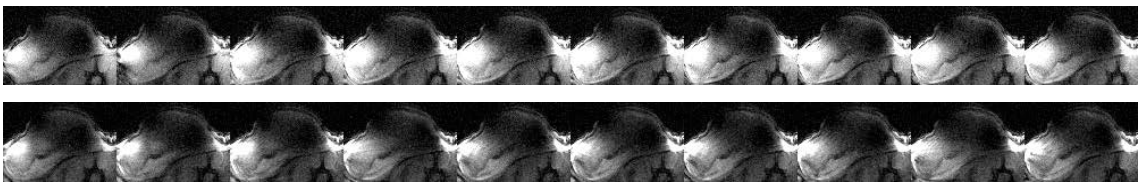

Figure 2.9: a) Proton image of an A2780 tumour with the ROI used in the DCE-MRI analysis drawn in it; b) Montage of 1 in every 10 of the 100 slices used in the dynamic DCE-MRI acquisition, *pre* (top) and *post* (bottom) the injection of hydralazine in the same tumour-bearing mouse.

This analysis provided a curve in a graph where time *versus* mean pixel intensity was plotted. The Area Under the Curve (AUC) for 120 seconds after the injection of the contrast agent of each curve was then calculated. This calculation was performed using Prism 5 for Windows (version 5.04, Graphpad). Setting the baseline as 1 (from the normalization), the software calculated the AUC for the defined region by the trapezoid rule (Atkinson, 1989).

2.5 *In vivo* ^{31}P spectroscopy

The *in vivo* ^{31}P spectroscopy of the human tumour xenografts implanted into the flanks of mice was performed in combination with the DCE-MRI protocol.

^{31}P-MRS data acquisition protocol

Once the first T1 FSEMS sequence was finished, the coil was programmed to the phosphorus channel. A phosphorus orientated SPULS sequence was used with the following parameters: a repetition time of 2 s, 64 averages, a pulse width of 7 μs, a transmitter pulse power of 45 dB, a transmitter offset (tof) of 3000 and the phosphorus offset frequency of transmitter (P31 offset) also of 3000. The parameters allowed calculation of the frequency offset of the centre of the phosphorus spectrum from the average of the frequency offsets of the peaks at the extremities of the spectrum (monophosphoesters on the left and βNTP on the right) as seen in Figure 2.10 as an example.

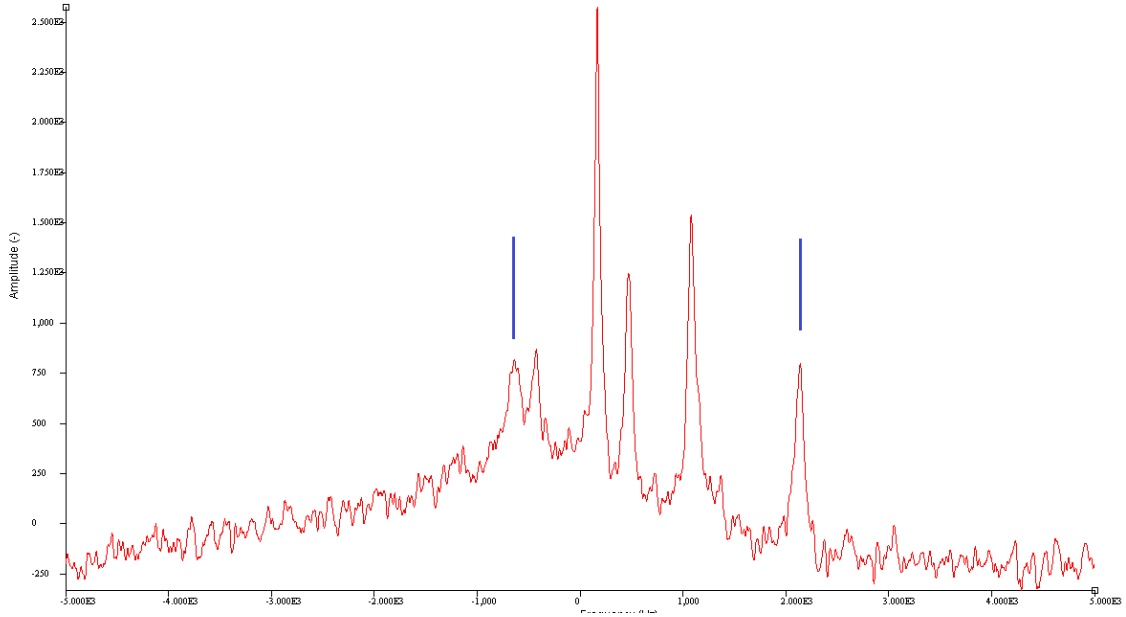

Figure 2.10: Example of an ^{31}P-SPULS spectrum acquired from an A2780 tumour-bearing mouse with the extremity peaks used in the calculation of the frequency offset of the centre of the phosphorus spectrum.

This sequence was also used every so often to test/calibrate the coil using a 1.5 ml Eppendorf tube with 100 mM of Phosphocholine as a phantom. With a repetition time of 2 s, 2 averages, the pulse width would be set in an array [1, 2, 3, 4, 5, 6, 7, 8, 9, 10, 12, 14, 16, 18, 20] to determine the best pulse width to use in the ^{31}P-MRS acquisition.

Once the phosphorus offset frequency of the transmitter was set to the centre of the spectrum, a phosphorus Image Selected In vivo Spectroscopy (ISIS)

sequence was used. This sequence uses HS-AFP pulses (hyperbolic secant adiabatic full passage, Silver *et al.*, 1984). The phosphorus signal was acquired from the same voxel where the local shim was previously performed, as exemplified in Figure 2.11, to verify the quality of the phosphorus spectrum, and assess the need to move the position of the acquisition voxel.

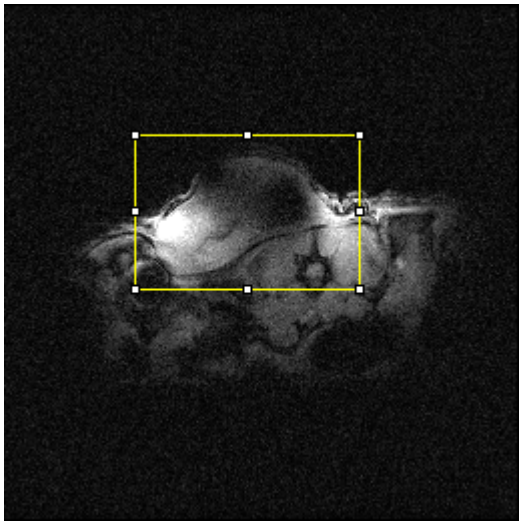

Figure 2.11: Example of a voxel used in the ^{31}P-MRS ISIS acquisition from an A2780 tumour-bearing mouse.

The chemical shift artefact affecting the spatial location of NTP voxels (gamma, alpha and/or beta are shifted compared to inorganic phosphate (Pi)) can be calculated. The gradient strength in ISIS was 50 mT/m which is equivalent to a ^{31}P shift of 865 kHz/m. The Pi and βNTP are approximately 23 ppm apart which corresponds to 2.783 kHz, while Pi to γNTP are approximately 8 ppm apart which corresponds to 0.968 kHz. The shift between Pi and βNTP is then 3.2 mm, while the shift between Pi and γNTP is 1.1 mm. If we compare this to an average voxel size of 10x 10x 10 mm, there is an overlap of 68% in each direction for the βNTP to Pi, and 89% overlap per dimension for the γNTP to Pi. The ratios between Pi and βNTP were compared to the ratios between Pi and γNTP (data not shown) without a relevant change in the profile over time, excluding the possibility systematic errors.

Two blocks of 120 averages were used. As soon as the first dynamic GEMS sequence (with the first injection of contrast agent) was over a dynamic ISIS sequence was initiated. This sequence had the same parameters as the previous test ISIS but 18 blocks of 120 averages, resulting in an 18 spectra

array acquired over 72 min (4 min *per* block). The drug or drug combination under study was injected during the 5th block of 120 averages.

^{31}P-MRS data analysis

For analysis purposes the individual spectra (i.e. for each block) were summed in pairs and the final analysis performed in 9 blocks which enclosed 8 minutes of acquisition. The data were analysed using jMRUI software (v4.0) with the AMARES algorithm (van den Boogaart *et al.*, 1996, van den Boogaart *et al.*, 1997). AMARES (Advanced Method for Accurate, Robust and Efficient Spectral fitting) performs parameter estimation of MRS signals using prior knowledge. This interactive time domain method relies on a sophisticated nonlinear least-squares algorithm. The setting of lower and upper boundaries also increases the robustness of this algorithm (Vanhamme *et al.*, 1997, Stefan *et al.*, 2009).

The first step involved the phasing of the spectrum, expansion of the line broadening to 75 Hz and setting of the reference frequency in the αNTP peak (-7.52 ppm). The starting values were defined according to the literature for 7 main peaks (de Graaf, 2007):

- AMP 6.33 ppm (representative of phosphomonoester signals);
- Inorganic phosphate 5.02 ppm;
- Phosphocreatine 0.00 ppm;
- γNTP -2.48 ppm;
- αNTP -7.52 ppm;
- NAD -8.30 ppm
- βNTP -16.26 ppm

Prior knowledge constrains were applied to the frequency of each peak defining them in an interval between -0.5 and +0.5 ppm of the reported frequency, and a first estimation performed. The damping values were averaged and divided by π to obtain the linewidth and applied during the second estimation in order to increase the robustness of the estimation and lower the mean error. An example of the jMRUI Graphical User Interface is presented in Figure 2.12.

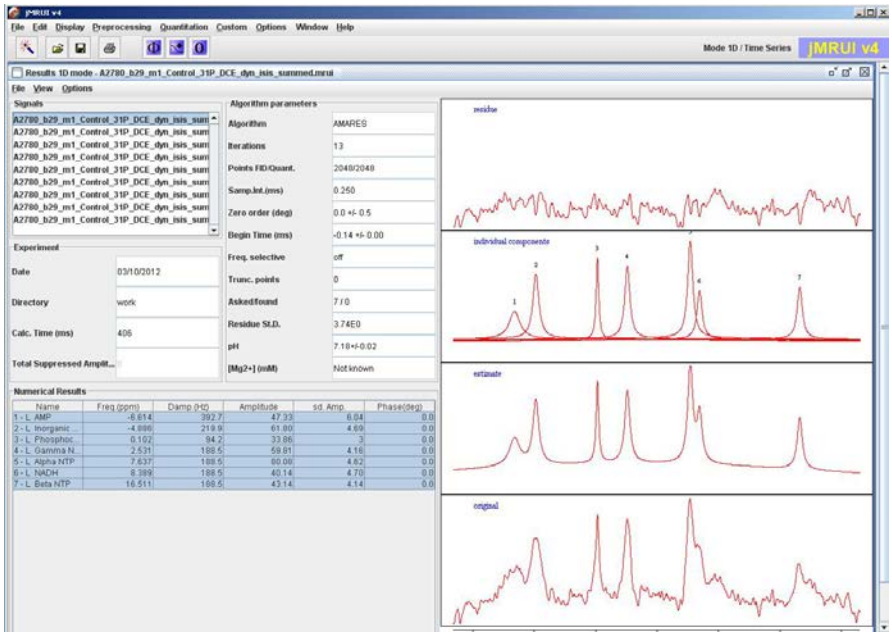

Figure 2.12: An example of the jMRUI user interface for one A2780 tumour AMARES final results. On the right hand side is, from bottom to top, the original spectrum, the estimated spectrum, the individual components of the spectrum and the residue of the estimation. On the left hand side are the numerical results including the amplitude and standard deviation of each peak.

Exclusion criteria for this analysis were:

- If the ratio between the inorganic phosphate peak amplitude and the inorganic phosphate peak amplitude standard deviation;
- or the ratio between the βNTP peak amplitude and βNTP peak amplitude standard deviation;

were below two, the data were excluded from analysis.

The lineshape was largely dominated by shimming. Therefore multiplet information was not used in the data fitting. That could only be achieved by improving the ^{31}P-MRS acquisition (increasing the gradient strength in ISIS to reduce chemical shifts artifacts) and/or include additional prior knowledge (e.g. ^{31}P multiplets) in the data fitting .

Using the dynamic phosphorus spectra analysis a real time evaluation of changes in the phosphorus spectrum profile was performed.

2.6 *Ex vivo* Tissue Spectroscopy

At the end of the MR scan (DCE-MRI and/or ^{31}P-MRS) the mouse was killed by cervical dislocation. Immediately the tumour was extracted and freeze-clamped in liquid nitrogen. Once the tumour was frozen, the liver was also removed and freeze clamped. The tissues were stored at -80°C until extraction.

2.6.1 Extraction Procedure

Figure 2.13 summarizes the tissue extraction procedure.

Frozen tumours and livers were ground to powder consistency by mortar and pestle in liquid nitrogen. Using a spatula precooled in the liquid nitrogen, the tissue powder was transferred to a pre-weighed 15 ml centrifuge tube. The difference in the tube weight measured the weight of tissue in the tube.

↓

Based on the weight and assuming 1 g tissue = 1 ml, 4x the volume of tissue of 6% (v/v) PCA was added and the content of the tube homogenized with a motor driven pestle and placed on ice for 15 minutes.

↓

The tube was centrifuged at 1000 g for 15 minutes in a refrigerated centrifuge at 4°C and the supernatant decanted into a pre-weighed 15 ml centrifuge tube.

↓

A few drops of universal indicator were added to the tube and the sample neutralised using 20% (v/v) potassium hydroxide (KOH), and 5% (v/v) KOH and 2%PCA (v/v) as required.

↓

When the samples were neutralized, Chelex® beads were added to the tube at a ratio of 50 mg of Chelex *per* ml of supernatant and the pH adjusted again.

↓

After the tube was thoroughly mixed, it was placed on ice for 15-30 minutes to allow full precipitation followed by centrifugation at 1000 g for 15 minutes at 4°C temperature.

↓

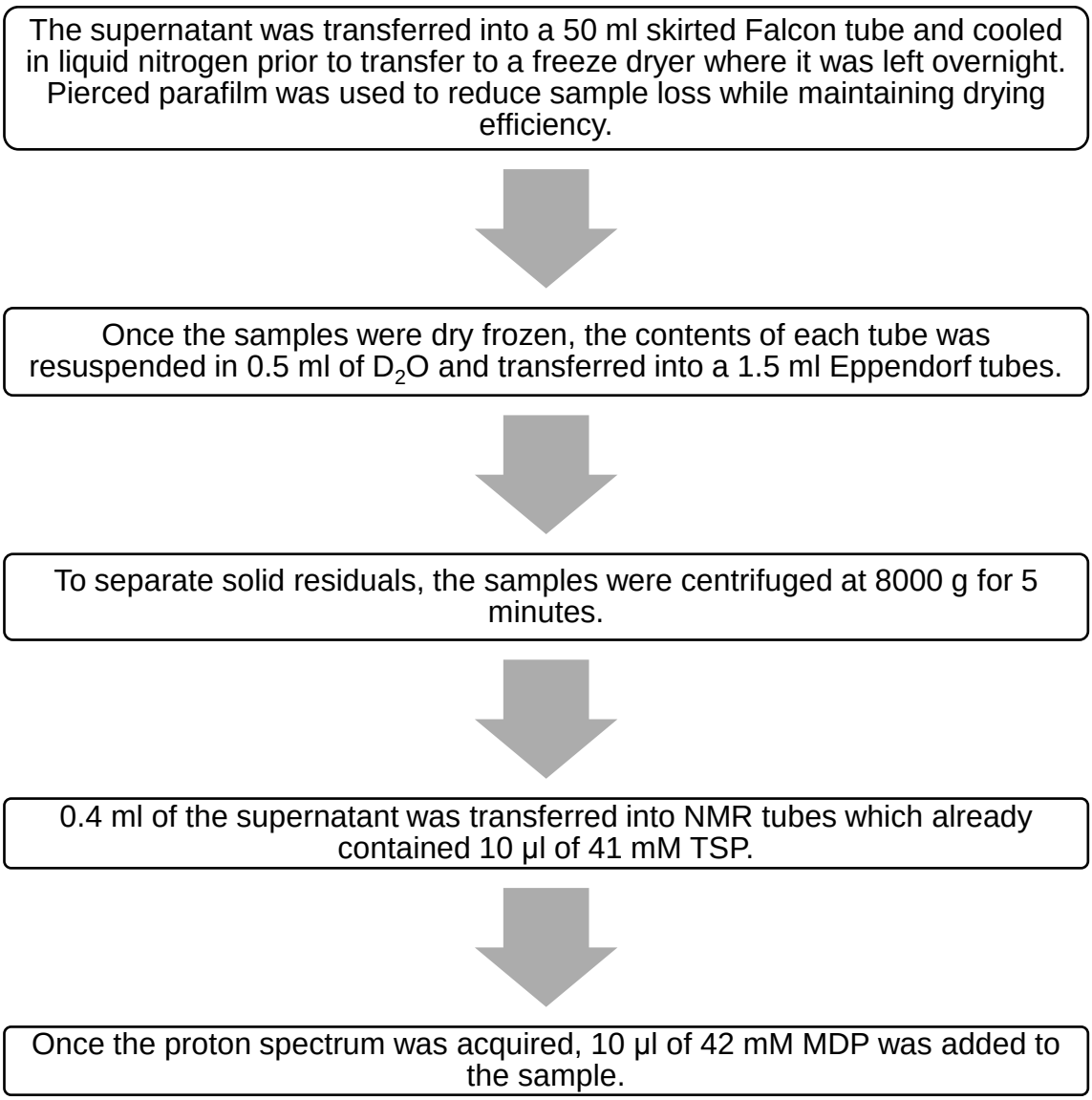

Figure 2.13: Flow chart summarizing the tissue extraction protocol.

2.6.2 Spectroscopy

Spectroscopy data acquisition was performed in an 11.4T Bruker Avance III 500MHz NMR spectrometer located in the Northern Institute for Cancer Research Laboratories, School of Chemistry, Newcastle University (Bedson Building). The same sequences used for the cell extract spectroscopy experiments were used for the tissue extract spectroscopy experiments, all the parameters were the same, and the data were analysed using TopSpin® software as described in subsection 2.3.4.

2.7 PARP1 KO mouse liver extract spectroscopy

PARP1 knock out (KO) mice used in this study were provided by the Comparative Biology Centre (Newcastle University) from an in-house colony originally developed by Professor Gilbert de Murcia. The development of a PARP1 KO colony was described by Ménissier de Murcia *et al.* (de Murcia *et al.*, 1997) Embryonic 129ySv mouse stem cells were used in which PARP1 was inactivated by homologous recombination through the insertion of a phosphoglycerate kinase promoter followed by the neo gene (PGK-neo) in the fourth exon. Southern blot analysis confirmed the gene targeting. Mutant mice were generated from one heterozygote embryonic clone using standard procedures. Disruption of both PARP1 alleles was confirmed by Southern blot analysis of DNA from tail biopsies. PARP1 was completely absent in mutant mice as shown by Western and activity analysis of spleen and testis isolated cells.

As with the *in vivo* ^{31}P-MRS experiments performed in tumour-bearing mice (section 2.5, data not shown), the *in vivo* ^{31}P-MRS study of livers of PARP1 KO and WT mice was performed in the Varian 7T horizontal bore preclinical MR system using the Rapid ^{1}H-^{31}P 12 mm surface coil. Mice were divided in two groups: KO and WT, and in each group there were four subgroups of mice treated with:

- Control (no treatment);
- 1 mg/kg of rucaparib (10 ml/kg of a 0.1 mg/ml solution in water for injection);
- 68 mg/kg of temozolomide (10 ml/kg of a 6.8 mg/ml solution in saline);
- 1 mg/kg of rucaparib combined with 68 mg/kg of temozolomide (10 ml/kg of a 0.1 mg/ml solution in water for injection with 10 ml/kg of a 6.8 mg/ml solution in saline);

Each animal was treated daily for 5 days and scanned on day 5, 30 minutes after the fifth treatment. ^{31}P-MRS acquisition was initiated approximately 1 hour after the treatment and 30 minutes after the imaging protocol started.

The setup for this experiment was marginally different from the one used for the tumour DCE-MRI/^{31}P-MRS protocol (section 2.5). Here, the mouse was placed

in a handmade polystyrene bed in which the coil was inserted in a position that allowed the mouse to lie in a prone position over it.
Because the PARP1 KO and WT mice have a C57 Black 6 background their abdomen was shaved under anaesthesia. The lower end of the sternum of the mouse was placed at the top limit of the coil to ensure that the liver was over the coil. The respiration pillow was attached to a platform taped onto the mouse back to monitor respiration. All the treatments were given before the mouse was placed into the magnet, hence no lines for injection were necessary.

Once the tray was placed in the magnet, the respiration and bore temperature were monitored and data acquisition initiated with a short scout scan of 5 images over 3 planes to confirm the positioning of the liver over the coil.

Data were then acquired as described in section 2.5 until the ISIS sequence. The first ISIS sequence had one block of 64 averages, and as the coil was positioned under the mouse ribcage, the sequence acquisition was gated with the respiration signal to avoid excessive movement of the mouse compared to the acquisition voxel. After verification of the signal quality a dynamic ISIS sequence was initiated. This sequence had the same parameters as the previous test ISIS for nine blocks of 64 averages, also gated. Depending on the breathing rate, the scan took on average 25 minutes. The 9 data blocks were summed into one single spectrum and the data analysed in jMRUI.

When the *in vivo* ^{31}P-MRS acquisition was finished, the mouse was removed from the magnet, kept under deep anaesthesia (4% (v/v) isoflurane/oxygen) and placed in a supine position on the bench. Abdominal surgery was performed to expose the liver which was freeze clamped *in situ* with tongs precooled in liquid nitrogen. The mouse was killed by cervical dislocation as the liver was frozen in the tongs and the frozen liver was detached, kept in liquid nitrogen and then stored in a -80°C freezer until extraction. The extraction protocol was exactly the same as the tissue extraction protocol (section 2.6.1) and the *ex vivo* ^{31}P-MRS acquisition was also performed in the 11.4T Bruker NMR spectrometer using the same protocols for proton and phosphorus spectroscopy as described in section 2.3.4.

2.8 PET studies

The PET studies were performed to assess changes in the mean Standardized Uptake Values (SUVs) for different tracers following drug treatment. [^{18}F]Fluoro-2-deoxy-2-D-glucose ([^{18}F]FDG) was used to assess metabolic changes in the tumour, while in the 3'-deoxy-3'-[^{18}F]-fluorothymidine ([^{18}F]FLT) was used to assess the proliferative status of the tumour. All the PET studies were carried out on a Philips Mosaic HP Small Animal imaging PET scanner (Philips Medical Systems, Global Information Center, P.O. Box 1168, 5602 BD Eindhoven, The Netherlands) with an Homeothermic Blanket System (Harvard Apparatus Ltd., Kent, TN8 6WF, UK) to maintain the body temperature. This particular PET scanner has a transverse FOV of 12.8 cm and an axial extent of 11.9 cm operating only in 3D mode. The coincidence timing window is 12 ns with a standard energy window between 410 and 665 KeV. The spatial resolution obtained is approximately 2 mm.

2.8.1 [^{18}F]FDG studies

Due to previous studies performed by Ian Wilson (personal communication) showing poor [^{18}F]-FDG uptake into SW620 tumours, only the A2780 cancer cell line was used to assess the effects of drug treatment on [^{18}F]-FDG uptake.

Nude CD1 mice were inoculated with 8-10x10^{6} A2780 cells *per* 50µl of media subcutaneously under anaesthesia. The tumours were allowed to grow until they have reached an approximate size of 5x5 mm and then randomized into four groups:

- Control (no treatment);
- 1 mg/kg of rucaparib (10 ml/kg of a 0.1 mg/ml solution in water for injection);
- 68 mg/kg of temozolomide (10 ml/kg of a 6.8 mg/ml solution in saline);
- 1 mg/kg of rucaparib combined with 68 mg/kg of temozolomide (10 ml/kg of a 0.1 mg/ml solution in water for injection with 10 ml/kg of a 6.8 mg/ml solution in saline);

Mice were treated for 5 days and rucaparib was administrated by *i.p.* injection while the temozolomide dose was given by oral gavage.

Data acquisition setup

On day 5, one hour after the treatment, the mice were anaesthetised with a cocktail of ketamine/medetomidine (ketamine 50-75 mg/kg *i.p.* and medetomidine 0.5-1.0 mg/kg *i.p.* in a volume of 0.1 ml/10 g). This cocktail was prepared and supplied by the Comparative Biology Centre, Newcastle University. The tail vein was cannulated using a 30G needle attached to a 1 ml syringe containing 20 units/ml of heparin by a BPTE-T10, 0.28 mm ID, 0.61 mm OD tubing as in the DCE-MRI protocol as described in section 2.4. Once the tail vein was successfully cannulated, the cannula was glued to the tail using Hystoacryl®. The mouse was then transferred into the PET scanner and placed on the heating blanket on the bed, and using an inbuilt laser marker the mouse was centred in the FOV of the scanner. The cannula tubing was then cut and a 1 ml syringe with a 30G needle which contained approximately 15 MBq of [^{18}F]FDG (prepared by dilution in saline) was connected.

As soon as the acquisition sequence was started in the scanner, the radiotracer was injected and the syringe and all the tubing removed from the mouse. Activity remaining in the syringe and tubing was measured in a scintillation well counter, and the difference between the activity in the syringe before and after the injection gave the amount of activity injected into the mouse for use with the mouse weight in the reconstruction algorithm. Due to the use of an injectable anaesthetic and a platform bed with a heating blanket it was possible to scan three mice at the same time in the same scan.

Data were acquired in dynamic mode with 10 one minute frames plus 6 five minutes frames plus 2 ten minutes frames (i.e. 10x 1 minute, 6x 5 minutes, 2x 10 minutes). Although reconstruction was concurrent with the data acquisition, the software can only have the activity and weight of one mouse at the time. Performing scans in 3 mice at a time translated into the repetition of the reconstructions with the individual values of activity and weight *per* mouse. This minimizes artifacts and maintains a good accuracy of the SUV measurements since the SUV calculation and reconstruction takes into account individual times of injection, individual injected doses and individual weights.

The reconstruction algorithm used was 3D-RAMLA (decay correction and SUV measurement) and the data analysis was performed using Philips Imalytics software with the Volume of Interest (VOI) drawn around the tumour and the mean SUV measured in the VOI. The variation in SUV was generally between 3 and 5%.

Data would be excluded from the study if the injection was poor (loss of the cannulation, detachment of the i.v. cannula during injection of radiotracer or vessel blockage during injection) leading to an injection of less than 5 MBq. During data analysis is the tumour did not have at least 6 voxels, it would be excluded too.

Once the acquisition terminated the mice were recovered by an *i.p.* injection of atipamezole (1-2.5 mg/kg), which reverses the medetomidine, and were left over a heating blanket until they were fully mobile.
The mice were then returned to the cage and taken back to the animal house.

The tumour volumes were measured until 100 days after treatment or until the tumour size reached 10x10 mm (or 15 mm in one direction), which was the maximum size allowed under animal welfare considerations. Also if the mouse showed signs of distress or poor health (e.g. a significant loss of body weight) it was killed. The tumour volume was calculated using the following equation:

$$Tumour\ Volume = \frac{long\ axis}{2} \times (short\ axis)^2$$

2.8.2 [^{18}F]-FLT studies

The [^{18}F]-FLT study was performed using the exactly same protocol as for the [^{18}F]-FDG study, the only difference being that both cancer cell lines, A2780 and SW620, were used (section 2.8.1).

Chapter 3. Results – Tumour vascular and metabolic changes due to hydralazine, rucaparib, temozolomide and combined rucaparib with temozolomide treatment as assessed by *in vivo* MR

The experiments described in this chapter were performed to test the hypothesis that PARP inhibition can modulate tumour vasculature, leading to an alteration in tumour energetics, and that the effect may contribute to the enhanced efficacy of PARP inhibitor/temozolomide combinations.

Calabrese *et al.* (2003) reported a statistically significant improvement of vascular perfusion in SW620 tumour xenografts treated with AG014361 (a forerunner of rucaparib). The Hoechst-stained vessel assay used showed that AG014361 had a vasoactive effect in the tumour. In the same study, SW620 tumour-bearing mice were injected with another PARP1 inhibitor, PD128763 which caused a drop in the mice body temperature while AG014361 had no such effect. This might indicate a direct vascular effect of AG014361 rather than an off-target effect. PARP inhibitors are analogues of nicotinamide and Horsman reviewed data showing that nicotinamide was able to reduce tumour hypoxia by preventing the transient cessation of blood flow in tumour microvasculature, a role that could sensitize to alkylating agent treatment (Horsman, 1995). Ali *et al.* (2009) reported that, although rucaparib failed to sensitize SW620 cells to the alkylating agent temozolomide *in vitro*, 1 mg/kg rucaparib improved tumour perfusion in SW620 tumours based on vessel mismatch studies and on real time observations of perfusion using SW620 tumours grown in dorsal window chambers. SW620 cells have low levels of ATases and mismatch repair proficiency making them hypersensitive to temozolomide. This already existing hypersensitivity is a likely explanation why a further potentiation of temozolomide with the treatment with PARP inhibitors is not observed in these cells (Calabrese *et al.*, 2004).

Ronen *et al.* (1999) published work where ^{31}P-MRS was used in SW620 cells treated with the anthracycline doxorubicin to assess metabolic changes due to chemotherapy-induced apoptosis. Cells treated for 24h with doxorubicin

showed a decrease of 30 to 40% in NTP concentration when compared to control cells (Ronen *et al.*, 1999).

To test the hypothesis that PARP inhibition induces vascular stabilization and metabolic deregulation both Dynamic Contrast Enhanced (DCE) MRI and ^{31}P-MRS studies were performed in A2780 and SW620 tumour-bearing mice.
In both experiments there were eight study groups:

- Control (10μl of saline *per* g of body weight);
- 5 mg/kg of hydralazine (10 ml/kg of a 0.5 mg/ml solution in saline);
- 1 mg/kg of rucaparib (10 ml/kg of a 0.1 mg/ml solution in water for injection);
- 5 mg/kg of rucaparib (10 ml/kg of a 0.5 mg/ml solution in water for injection);
- 50 mg/kg of rucaparib (10 ml/kg of a 5 mg/ml solution in water for injection);
- 68 mg/kg of temozolomide (10 ml/kg of a 6.8 mg/ml solution in saline);
- 1 mg/kg of rucaparib combined with 68 mg/kg of temozolomide (10 ml/kg of a 0.1 mg/ml solution in water for injection with 10 ml/kg of a 6.8 mg/ml solution in saline);
- 5 mg/kg of rucaparib combined with 68 mg/kg of temozolomide (10 ml/kg of a 0.5 mg/ml solution in water for injection with 10 ml/kg of a 6.8 mg/ml solution in saline).

These doses were chosen as being the standard clinical dose of temozolomide, when expressed as mg/m^2 (68 mg/kg ≈ 200 mg/m^2), and rucaparib doses which are known to potentiate temozolomide (Calabrese *et al.*, 2003; Thomas *et al.*, 2007; Ali *et al.*, 2011).

In all these experiments the mice received a single treatment, delivered by *intraperitoneal* (*i.p.*) injection during the course of the experiment.

3.1 Vascular effects of rucaparib, temozolomide or combined rucaparib and temozolomide treatment as assessed by DCE-MRI

Dynamic Contrast Enhanced MRI (DCE-MRI) was used to assess acute changes in the vascular state of tumours following drug administration. The principle underlying DCE-MRI is that drug-induced changes to the tumour vascular can be measured by alterations in MR contrast agent uptake. In the experiments described in this chapter drug-induced acute effects on the tumour vasculature were studied. To do so, a pre-treatment control DCE-MRI scan was performed following the injection of a contrast agent (gadoteridol), which was repeated 60 minutes after drug administration. Comparisons between the uptake curves at the two time points revealed the effect of the drug on the vasculature. MR signal intensity and quantitative analysis involving estimation of the gadolinium (Gd) concentration was undertaken, and the results presented focus on signal intensity before and after treatment. As mentioned in subsection 1.4.1, the use of a surface coil with variable flip angle across the tumour and the lack of arterial input function measurements did not allowed a simple extrapolation of Gd concentrations. The use of pre- and post-contrast agent injection DCE-MRI parameters has been widely used to assess vasculature response to treatment (Robinson *et al.*, 2003; McIntyre *et al.*, 2004).

The data were acquired using an Agilent 7T small bore MR scanner and analysed in imageJ, a freeware tool which can open multiple *.fdf (Agilent format image data) files at once and gather them into a stack. The dynamic acquisition was based on a gradient echo sequence, repeated 100 times over the same slice with a temporal resolution of 6 seconds. In the slice a Region Of Interest (ROI) was drawn and the average brightness intensity measured. Potentially, different ROIs can be drawn and compared, for example, vasculature changes in the centre of the tumour in comparison with the outer ring, although this was not performed in the current study.

The data analysis involved the definition of the ROI for each mouse and the measurement of the average brightness intensity over time in the ROI. Normalization to a background level (average of blocks 2-6 prior to contrast agent administration) was performed in order to compare the contrast agent uptake after both injections as shown in section 2.4.

Figure 3.1 (a) to d)) shows the normalized tumour DCE-MRI uptake curves, in pixel mean MR signal intensity for injections of gadoteridol (90 minutes apart) before and after the administration of saline (control), 5 mg/kg hydralazine, 1 mg/kg rucaparib or a combination of 1 mg/kg rucaparib with 68 mg/kg temozolomide to A2780 tumour-bearing mice.

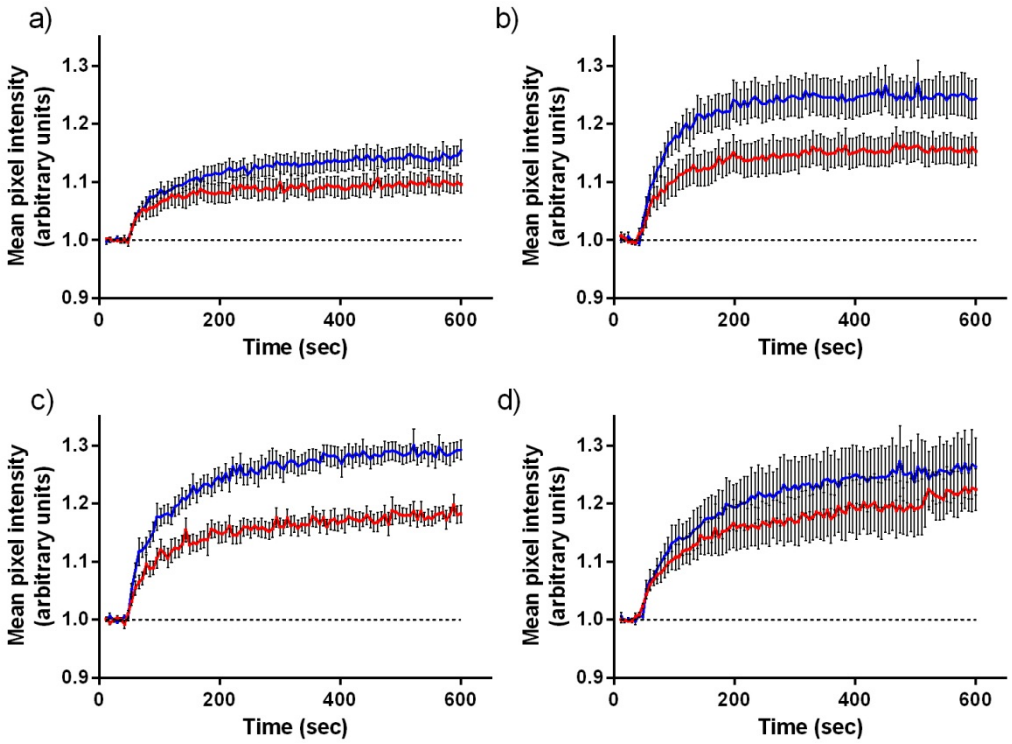

Figure 3.1: Normalized DCE-MRI uptake curves in A2780 tumours. In all graphs the uptake curve for the first gadoteridol injection is in blue and the uptake curve for the second injection of gadoteridol is in red. a) control group (n=8); b) 5 mg/kg hydralazine group (n=6); c) 1 mg/kg rucaparib group (n=8); d) 1 mg/kg rucaparib combined with 68 mg/kg temozolomide (n=4). Points are the mean and bars are the standard error.

The Area Under the Curve for MR signal intensity was calculated for the first 120 seconds after the injection of gadoteridol ($AUC_{MR,\ 120s}$) using Prism 5 for Windows as described in the Methods (section 2.4) and data are shown in Figures 3.2-3.4.

Figure 3.2 (a) and b)) shows the average (mean) A2780 tumour $AUC_{MR,\ 120s}$ for control and 5 mg/kg of hydralazine treated tumours with the corresponding standard error of the mean. In Figure 3.3 (a) to d)), A2780 tumour $AUC_{MR,\ 120s}$ data for control and 1, 5 and 50 mg/kg rucaparib-treated mice are depicted with the corresponding standard error of the mean. Figure 3.4 (a) to d)) shows the A2780 tumour $AUC_{MR,\ 120s}$ data for control, 68 mg/kg temozolomide and

rucaparib and temozolomide combination treated mice with the corresponding standard error.

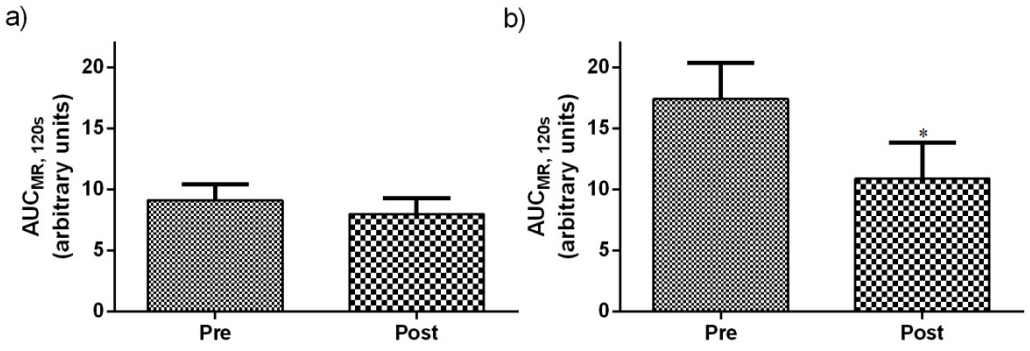

Figure 3.2: Average $AUC_{MR, 120s}$,with the corresponding standard error, pre and post drug injection for a) control group (n=8); b) 5 mg/kg hydralazine group (n=6) in A2780 tumours. In b) the star indicates a statistically significant reduction in AUC ($p \leq 0.05$).

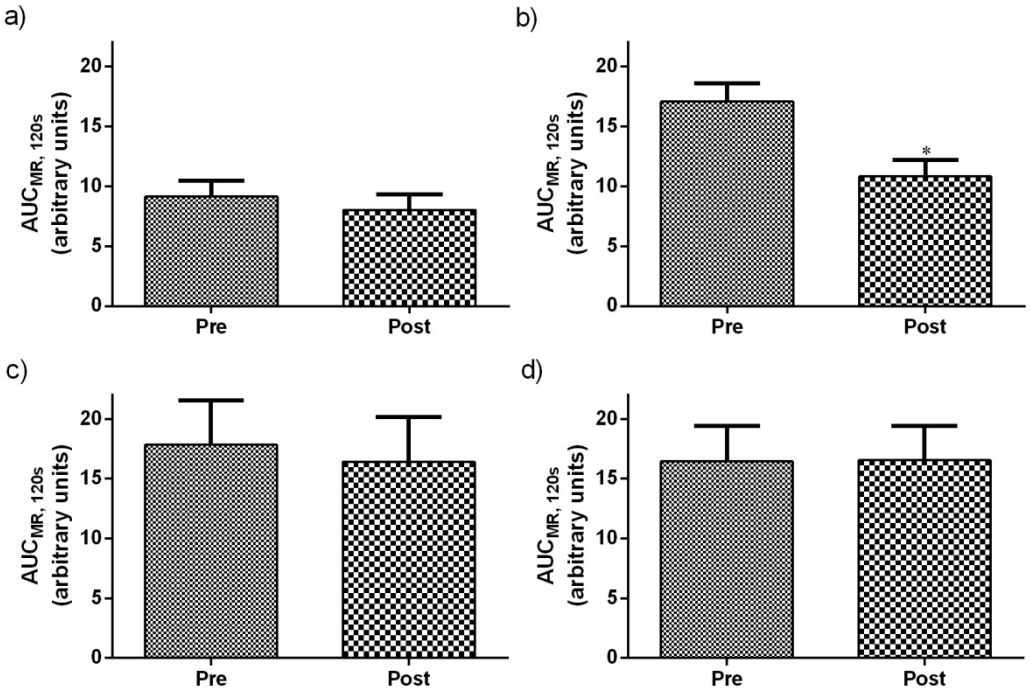

Figure 3.3: Average $AUC_{MR, 120s}$, with the corresponding standard error, pre and post drug injection for a) control group (n=8); b) 1 mg/kg rucaparib group (n=8); c) 5 mg/kg rucaparib group (n=4); d) 50 mg/kg rucaparib group (n=4) in A2780 tumours. In b) the star indicates a statistically significant reduction in AUC ($p \leq 0.05$).

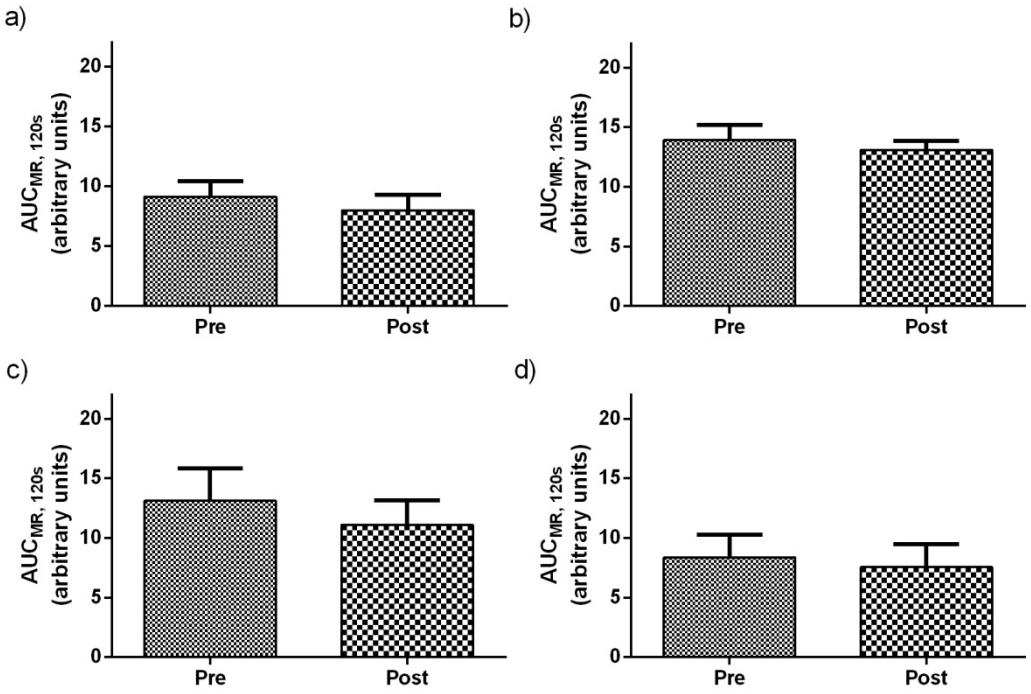

Figure 3.4: Average $AUC_{MR, 120s}$, with the corresponding standard error, pre and post drug injection for a) control group (n=8); b) 68 mg/kg temozolomide group (n=5); c) 1 mg/kg rucaparib combined with 68 mg/kg temozolomide group (n=4); d) 5 mg/kg rucaparib combined with 68 mg/kg temozolomide group (n=5) in A2780 tumours.

Figure 3.5 (a) to d)) shows the tumour DCE-MRI uptake curves (mean MR pixel signal intensity) for injections of gadoteridol (90 minutes apart) before and after the administration of saline, 5 mg/kg hydralazine, 5 mg/kg or 50 mg/kg rucaparib to SW620 tumour-bearing mice.

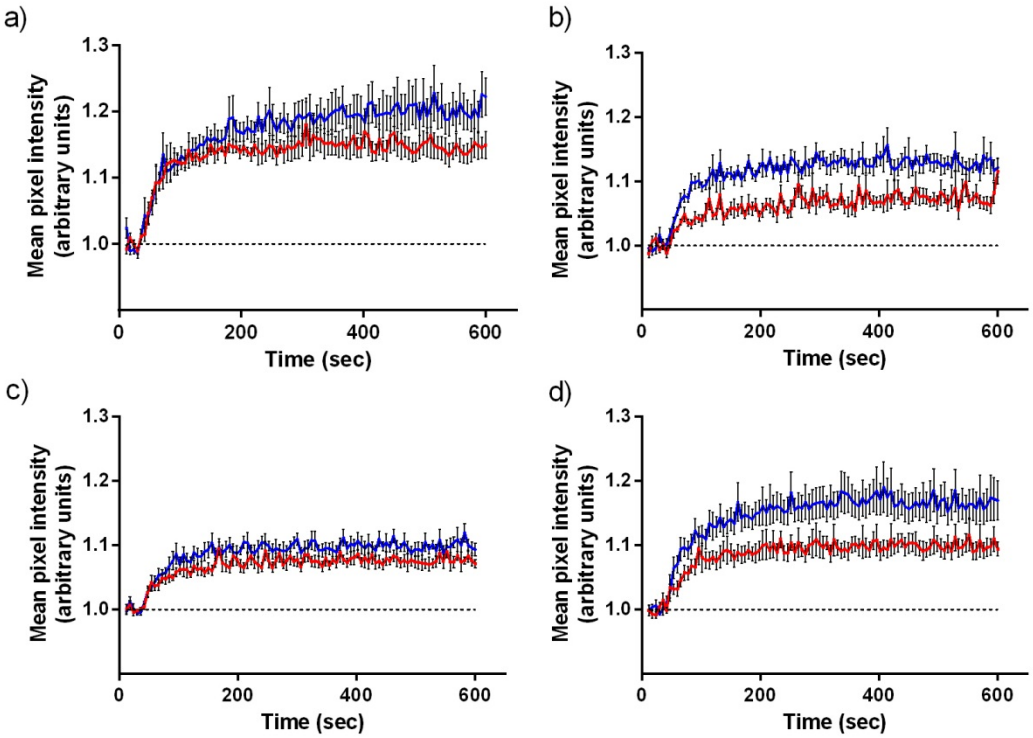

Figure 3.5: Normalized DCE-MRI uptake curves in SW620 tumours. In all graphs the uptake curve for the first gadoteridol injection is in blue and the uptake curve for the second injection of gadoteridol is in red. a) control group (n=6); b) 5 mg/kg hydralazine group (n=9); c) 5 mg/kg rucaparib group (n=6); d) 50 mg/kg rucaparib (n=7). Points are the mean and bars are the standard error.

The Area Under the Curve for the MR signal intensity in the first 120 seconds after the injection of gadoteridol was calculated, and the average $AUC_{MR,\ 120s}$ for SW620 tumour bearing-mice are shown in Figures 3.6-3.8.

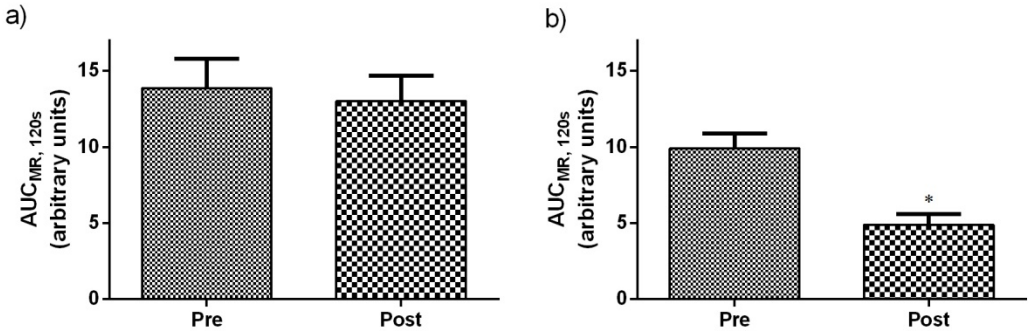

Figure 3.6: Average $AUC_{MR,\ 120s}$, with the corresponding standard error, pre and post drug injection for a) control group (n=6); b) 5 mg/kg hydralazine group (n=9) in SW620 tumours. In b) the star indicates a statistically significant reduction in AUC ($p \leq 0.05$).

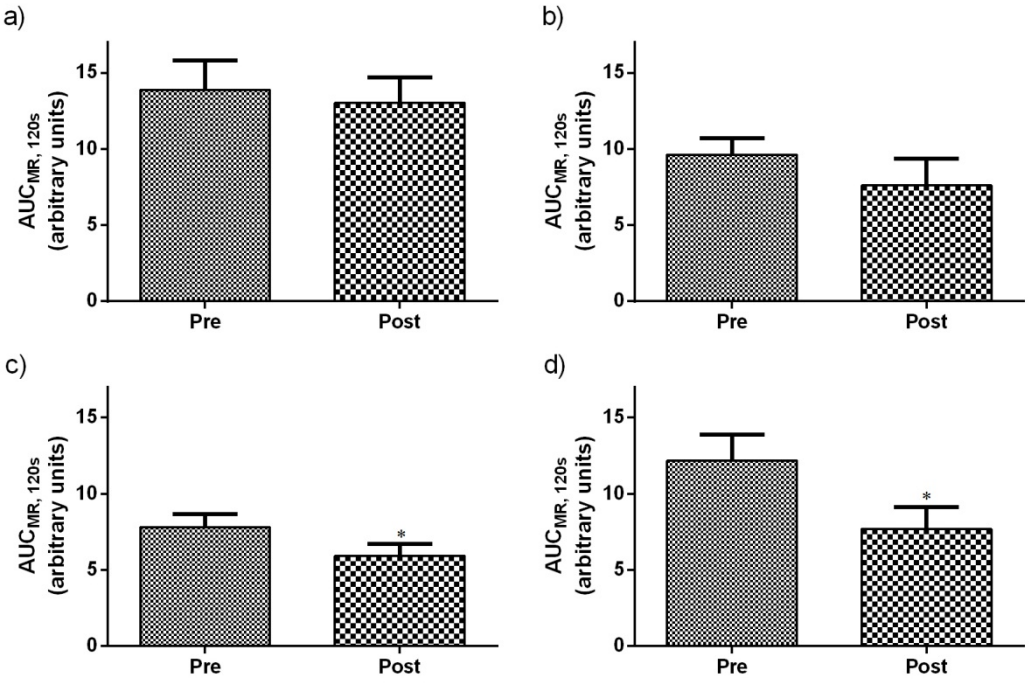

Figure 3.7: Average $AUC_{MR, 120s}$, with the corresponding standard error, pre and post drug injection for a) control group (n=6); b) 1 mg/kg rucaparib group (n=6); c) 5 mg/kg rucaparib group (n=6); d) 50 mg/kg rucaparib group (n=7) in SW620 tumours. In c) and d) the star indicates a statistically significant reduction in AUC following drug administration ($p \leq 0.05$).

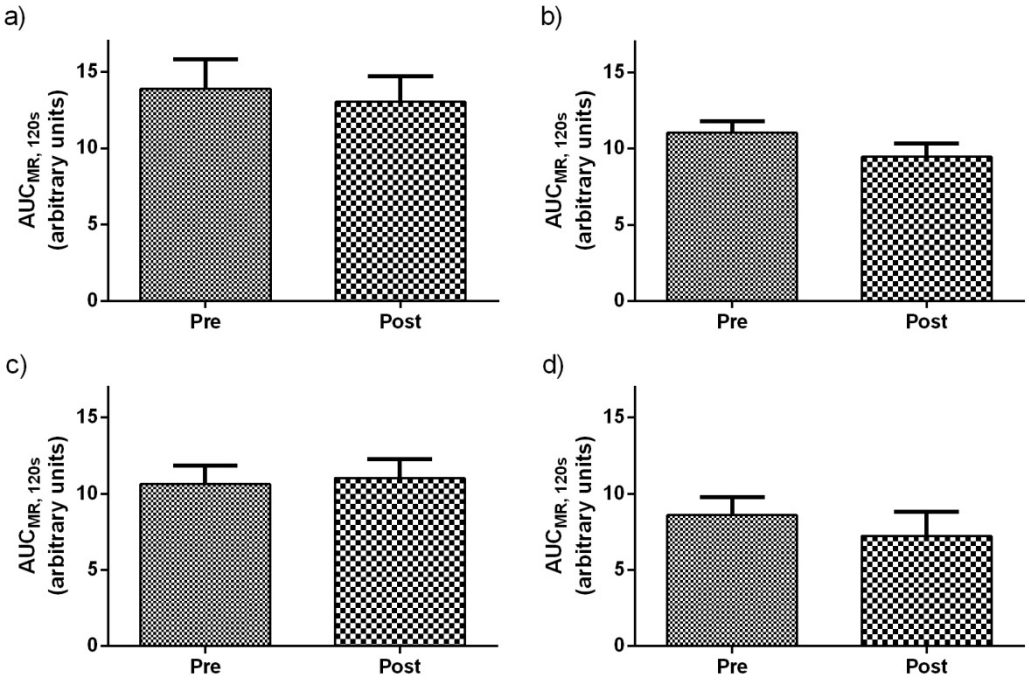

Figure 3.8: Average $AUC_{MR, 120s}$, with the corresponding standard error, pre and post drug injection for a) control group (n=6); b) 68 mg/kg temozolomide group (n=5); c) 1 mg/kg rucaparib combined with 68 mg/kg temozolomide group (n=5); d) 5 mg/kg rucaparib combined with 68 mg/kg temozolomide group (n=6) in SW620 tumours.

The data presented in Figures 3.2-3.4 and 3.6-3.8 are summarized in Table 3.1 and the results of a paired t test statistical analysis of the data are presented in Table 3.2.

Tumour treatment	**A2780**		**SW620**	
	$AUC_{MR, 120s}$ for first gadoteridol injection	$AUC_{MR, 120s}$ for second gadoteridol injection	$AUC_{MR, 120s}$ for first gadoteridol injection	$AUC_{MR, 120s}$ for second gadoteridol injection
Control	7.9±1.2	6.5±1.5	13.9±1.9	13.0±1.7
5 mg/kg hydralazine	17.4±2.4	10.5±2.5*	9.9±0.9	4.9±0.7*
1 mg/kg rucaparib	17.1±1.5	10.8±1.4*	9.6±1.1	7.6±1.7
5 mg/kg rucaparib	17.8±3.7	16.4±3.7	7.8±0.9	5.9±0.8*
50 mg/kg rucaparib	16.4±2.9	16.6±2.8	12.2±1.7	7.7±1.4*
68 mg/kg temozolomide	13.1±1.3	13.0±0.9	11.0±0.8	9.5±0.9
1 mg/kg rucaparib + 68 mg/kg temozolomide	13.1±2.7	11.1±2.1	10.6±1.2	11.0±1.3
5 mg/kg rucaparib + 68 mg/kg temozolomide	8.4±1.9	7.6±1.9	8.6±1.2	7.2±1.6

Table 3.1: Summary of the mean $AUC_{MR, 120s}$ data, with the correspondent standard error, from Figures 3.2-3.4 and 3.6-3.8 in A2780 and SW620 tumour-bearing mice. * Indicates that the values for the first and second gadoteridol injections were significantly different ($p<0.05$).

Tumour treatment	**A2780**	**SW620**
	p values for the difference between the $AUC_{MR, 120s}$ after the first and second contrast agent injection	p values for the difference between the $AUC_{MR, 120s}$ after the first and second contrast agent injection
Control	0.16	0.45
5 mg/kg hydralazine	0.029	0.000026
1 mg/kg rucaparib	0.00077	0.37
5 mg/kg rucaparib	0.18	0.020
50 mg/kg rucaparib	0.48	0.024
68 mg/kg temozolomide	0.94	0.18
1 mg/kg rucaparib + 68 mg/kg temozolomide	0.086	0.69
5 mg/kg rucaparib + 68 mg/kg temozolomide	0.063	0.25

Table 3.2: p Values generated using a paired t test analysis to evaluate the significance of the difference between pre- and post-treatment $AUC_{MR, 120s}$ values in A2780 and SW620 tumour-bearing mice (data from Table 3.1).

The results presented above show that in A2780 tumours the low dose (1 mg/kg) of rucaparib reduced the $AUC_{MR, 120s}$ whereas the higher doses (5 and

50 mg/kg) did not. In contrast, in SW620 tumours, the lower dose of rucaparib (1 mg/kg) did not alter $AUC_{MR,\ 120s}$ whilst the higher two doses (5 and 50 mg/kg) did. Neither temozolomide alone or in combination with rucaparib induced reductions in $AUC_{MR,\ 120s}$ at any of the doses studied at the 5% significance level. However, there was a trend to a reduced $AUC_{MR,\ 120s}$ for temozolomide in combination with both doses of rucaparib (1 mg/kg – p=0.086, 5 mg/kg – p=0.063) in A2780 tumours. In addition, the statistical analysis summarized in Table 3.2 demonstrated that hydralazine (5 mg/kg) induces a statistically significant decrease in the $AUC_{MR,\ 120s}$ in both A2780 and SW620 tumours. Rucaparib alone also produced a significant decrease in $AUC_{MR,\ 120s}$ which was dose dependent in both tumour types; however the dose dependency was inverse (the lower dose effecting A2780 tumours and the higher doses effecting SW620 tumours).

To allow the comparison between treatment groups it was necessary to normalize data and this was achieved by calculating the ratio between the $AUC_{MR,\ 120s}$ for the first injection (AUC_{120_1}) and for the second injection (AUC_{120_2}). This ratio will henceforth be termed the Anti-Vascular Index (AVI). An increase in this ratio corresponds to a decrease in the $AUC_{MR,\ 120s}$ for the second injection of contrast agent which is related to impairment of the vascular supply to the tumour.

Figures 3.9 and 3.10 present the DCE-MRI data as the AVI in A2780 and SW620 tumour-bearing mice.

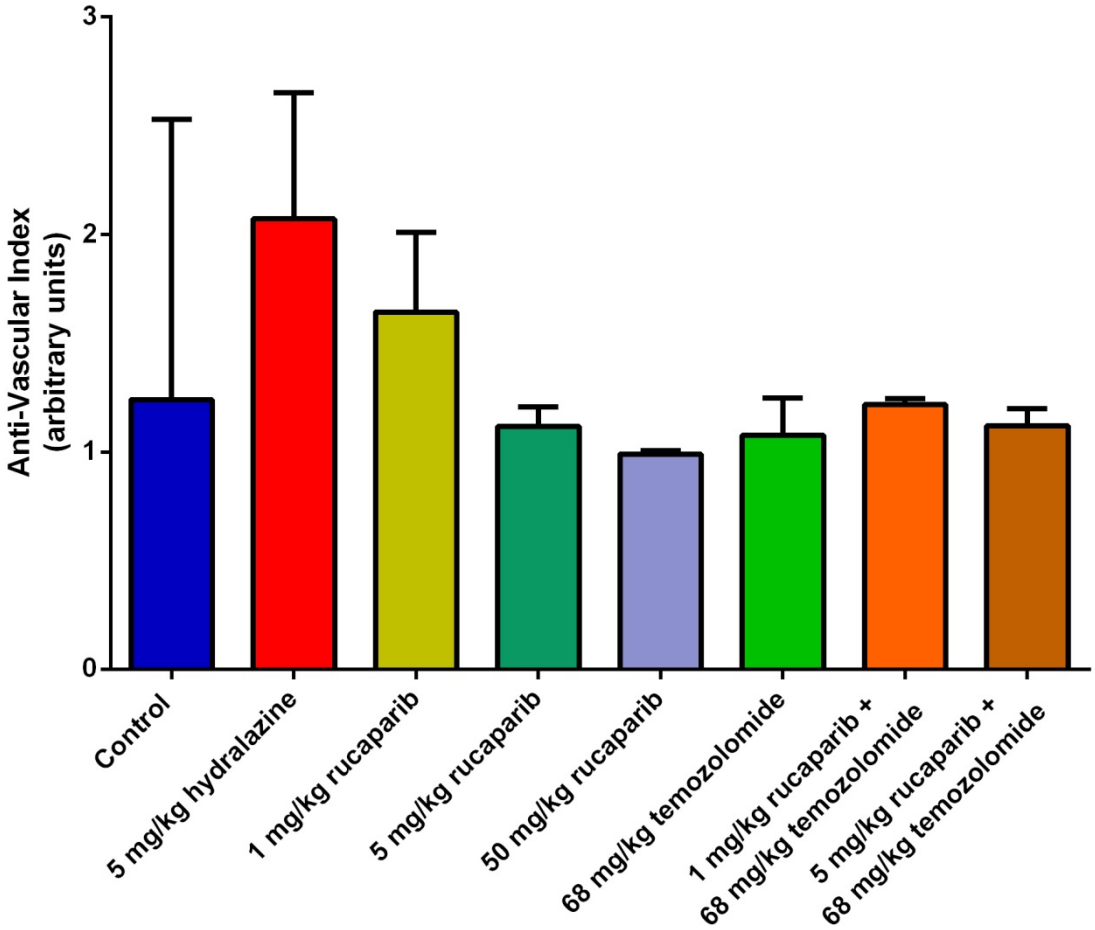

Figure 3.9: Median values and inter-quartile range (error bars) for the AVI in A2780 tumour-bearing mice.

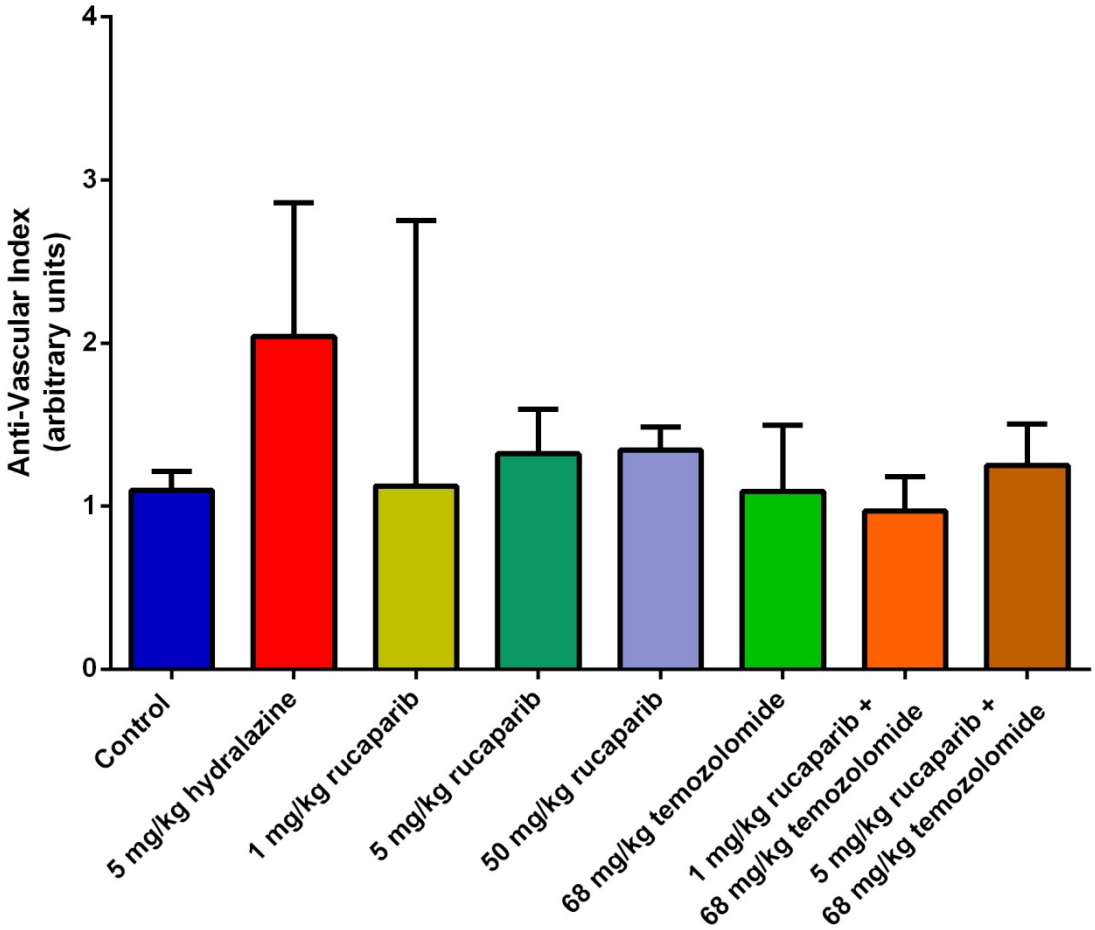

Figure 3.10: Median values and inter-quartile range (error bars) for the AVI in SW620 tumour-bearing mice.

Although a statistical analysis of the A2780 data using a one-way ANOVA with multiple comparisons between all the groups, and using each group as a reference, showed no significant differences for the AVI between different treatment groups in either tumour type, a Mann-Whitney non-paired t-test revealed significant differences between certain groups of A2780 tumour-bearing mice (Table 3.3). Thus for A2780 tumours the AVI for the 50 mg/kg rucaparib group was significantly lower than in controls and in the 1 mg/kg rucaparib combined with 68 mg/kg temozolomide group. Similarly, the AVI for the 1 mg/kg rucaparib group was significantly higher than all groups except for the control and 5 mg/kg hydralazine.

	5 mg/kg hydralazine		1 mg/kg rucaparib	5 mg/kg rucaparib
Control	0.65		0.28	0.26
5 mg/kg hydralazine			0.57	0.17
1 mg/kg rucaparib				0.028*
	50 mg/kg rucaparib	68 mg/kg temozolomide	1 mg/kg rucaparib + 68 mg/kg temozolomide	5 mg/kg rucaparib + 68 mg/kg temozolomide
Control	0.049*	0.22	0.74	0.22
5 mg/kg hydralazine	0.11	0.08	0.33	0.24
1 mg/kg rucaparib	0.0081*	0.0109*	0.049*	0.019*
5 mg/kg rucaparib	0.34	0.71	0.49	>0.99
50 mg/kg rucaparib		0.68	0.029*	0.064
68 mg/kg temozolomide			0.56	0.80
1 mg/kg rucaparib + 68 mg/kg temozolomide				0.19

Table 3.3: p Values generated using a Mann-Whitney (non-paired t test) to evaluate the significance of the effect of treatment on AVI in A2780 tumour bearing mice. The star indicates statistically significant values ($p<0.05$).

A corresponding statistical analysis was performed on data generated in SW620 tumour bearing mice. As shown in Table 3.4, the AVI for the 5 mg/kg hydralazine group was higher than all other groups except 1 mg/kg rucaparib. Similarly, the AVI for the 50 mg/kg rucaparib group was significantly higher than in controls and the 1 mg/kg rucaparib combined with 68 mg/kg temozolomide groups.

	5 mg/kg hydralazine		1 mg/kg rucaparib	5 mg/kg rucaparib
Control	0.0007*		0.79	0.09
5 mg/kg hydralazine			0.22	0.043*
1 mg/kg rucaparib				0.79
	50 mg/kg rucaparib	68 mg/kg temozolomide	1 mg/kg rucaparib + 68 mg/kg temozolomide	5 mg/kg rucaparib + 68 mg/kg temozolomide
Control	0.014*	0.65	0.52	0.26
5 mg/kg hydralazine	0.040*	0.0062*	0.0031*	0.0081*
1 mg/kg rucaparib	0.29	0.90	0.52	>0.99
5 mg/kg rucaparib	0.43	0.63	0.08	0.70
50 mg/kg rucaparib		0.33	0.03*	0.22
68 mg/kg temozolomide			0.15	0.71
1 mg/kg rucaparib + 68mg/kg temozolomide				0.29

Table 3.4: p Values generated using a Mann-Whitney (non-paired t test) to evaluate the significance of the effect of treatment on AVI in SW620 tumour bearing mice. The star indicates statistically significant values ($p<0.05$).

Consistently, the DCE-MRI data results demonstrate that hydralazine (5 mg/kg) strongly reduces the uptake of contrast agent, measured by the $AUC_{MR,\ 120s}$, after treatment in both A2780 and SW620 tumour-bearing mice.

3.2 Metabolic effects of rucaparib, temozolomide or rucaparib combined with temozolomide treatment as assessed by *in vivo* ^{31}P spectroscopy

In vivo ^{31}P MR spectroscopy was used to study metabolic changes in tumours following treatment. In theory, if a drug affects the tumour vasculature, tumour metabolism will also be affected and the ratio between inorganic phosphate (Pi) and beta-NTP (βNTP - primarily reflecting ATP) concentrations should change accordingly as the delivery of oxygen and nutrients is reduced. Although PARP inhibition could lead to an increase of cellular NAD, which could theoretically also be studied by ^{31}P-MRS, the coil used in this work was not sensitive enough to detect signals from NAD. Also, the protocol did not include an external reference, making absolute quantitation of NAD levels in the tumours impossible. Furthermore, there is partial overlap between the NAD and αNTP signals and, possibly, other signals in the diphosphodiester region of the ^{31}P spectrum, further compromising the analysis of NAD. There are numerous examples in the literature where *in vivo* ^{31}P-MRS has been performed to estimate absolute concentrations of metabolites (for example, Van Boogaart *et al.*, 1995).

In the experiments performed here, the Pi to βNTP ratio was measured and the data analysed in relation to the *in vivo* DCE-MRI results presented in section 3.1. The groups studied were the same as those described in section 3.1 and in some cases data were derived from the same individual mouse; the phosphorus spectra being acquired between the 2 injections of contrast agent in the DCE-MRI scan. Using a dynamic ISIS sequence, a phosphorus spectrum was acquired every 4 minutes, starting 11 minutes and 30 seconds after the first contrast injection and lasting for 72 minutes. The drug was injected during the acquisition of the phosphorus spectra to allow dynamic assessment of the changes in the tumour ^{31}P-MRS spectrum.

Analysis of the data was performed using jMRUI, a freeware software tool for MRS analysis (van den Boogaart *et al.*, 1996, van den Boogaart *et al.*, 1997). Using the AMARES algorithm within jMRUI, it was possible to estimate the amplitudes of several relevant peaks. In the analysis, the spectra were summed into 9 blocks of 8 minutes each and phased accordingly. Starting frequency

values for each peak, and a soft constraint of bounds for both frequency and damping, were used to facilitate the estimation.

Groups studied were: control, 5 mg/kg hydralazine, 1, 5 and 50 mg/kg rucaparib, 68 mg/kg temozolomide, 1 mg/kg rucaparib combined with 68 mg/kg temozolomide and 5 mg/kg rucaparib combined with 68 mg/kg of temozolomide. Treatment was given 30 minutes after the first injection of contrast agent, and 18.5 minutes after the ISIS sequence started, and for at least 45 minutes after the drug injection.

Figures 3.11 and 3.12 are examples of ^{31}P-MR spectra from A2780 and SW620 tumour-bearing mice. The original spectrum is shown in red and the AMARES estimation of the spectrum is shown in blue. Figure 3.11 depicts single spectra from individual a) control, b) 5 mg/kg hydralazine, c) 1 mg/kg rucaparib and d) 1 mg/kg rucaparib combined with 68 mg/kg temozolomide treated mice bearing A2780 tumours. Figure 3.12 depicts single spectra from individual a) control, b) 5 mg/kg hydralazine, c) 5 mg/kg rucaparib and d) 50 mg/kg rucaparib treated mice bearing SW620 tumours.

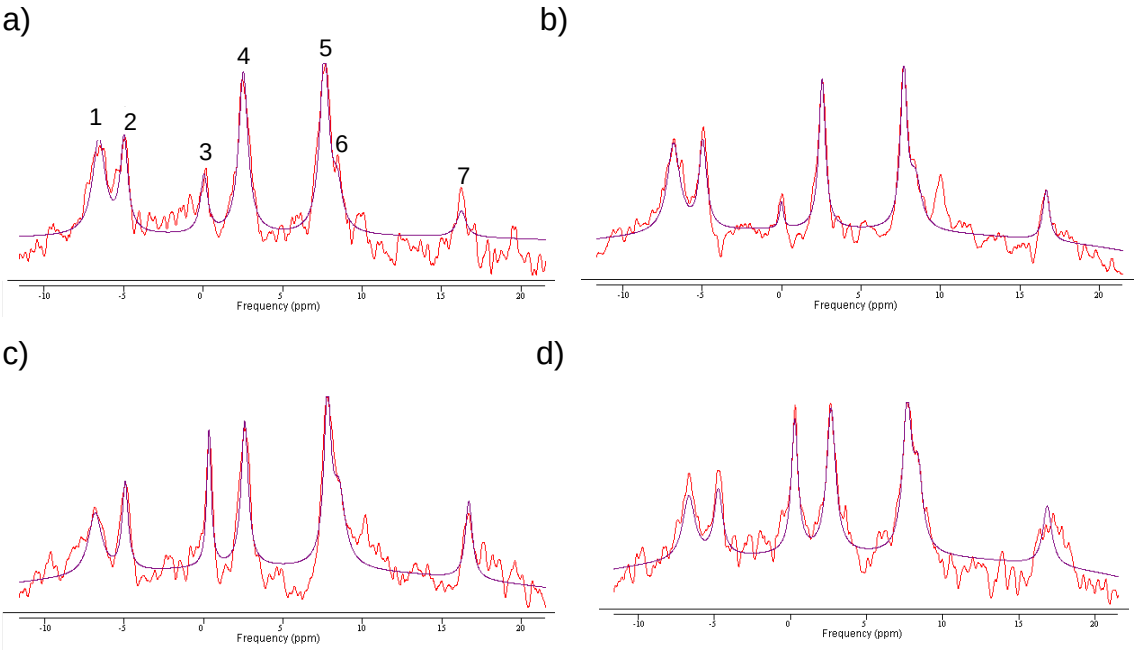

Figure 3.11: ^{31}P-MR spectra from A2780 tumour-bearing mice. a) Control, b) 5 mg/kg hydralazine, c) 1 mg/kg rucaparib and d) 1 mg/kg rucaparib combined with 68 mg/kg temozolomide. Peaks are labelled according to the following numbers: 1 – AMP; 2 – inorganic phosphate; 3 – phosphocreatine; 4 – γNTP; 5 – αNTP; 6 – NAD; 7 – βNTP.

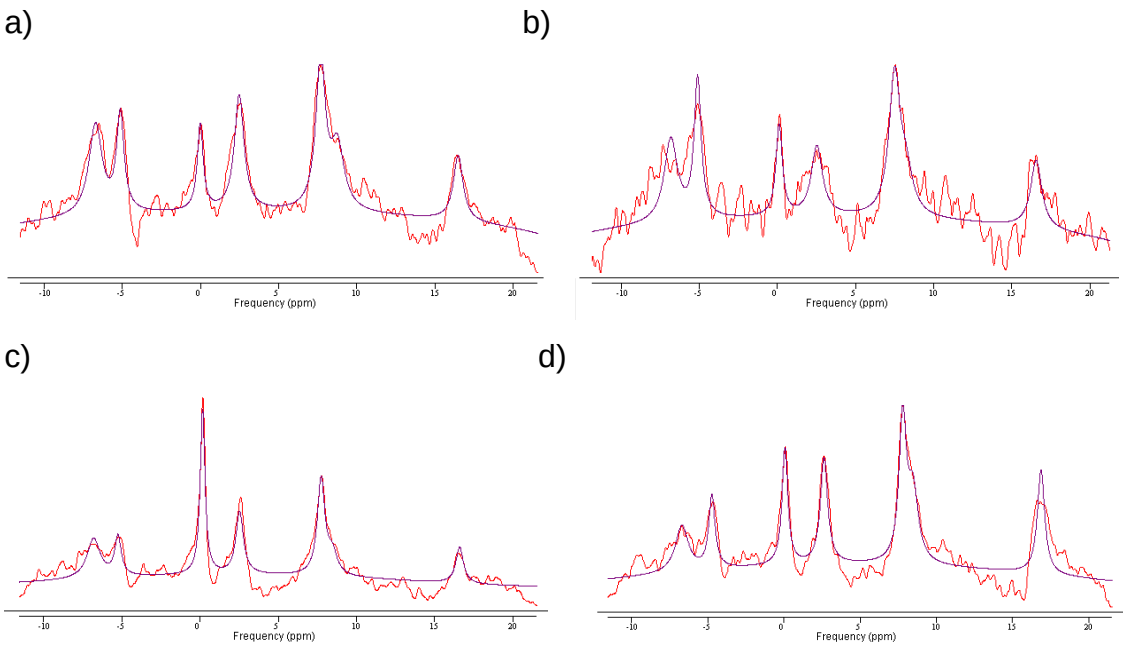

Figure 3.12: ^{31}P-MR spectra from SW620 tumour-bearing mice. a) Control, b) 5 mg/kg hydralazine, c) 5 mg/kg rucaparib and d) 50 mg/kg rucaparib.

For A2780 tumour-bearing mice Figure 3.13 (a) and b)) presents the normalised Pi to βNTP ratio as a percentage (%) of the pre-treatment value for the control and 5 mg/kg hydralazine groups, and Figure 3.14 (a) to d)), presents the A2780 data for the control and 1, 5 and 50 mg/kg rucaparib groups. Figure 3.15 (a) to d)) shows correspondent results for the control, 68mg/kg temozolomide, and the combination of 1 or 5 mg/kg rucaparib with 68 mg/kg temozolomide. All these Figures include the mean and standard error (error bars) and the fitted linear regression.

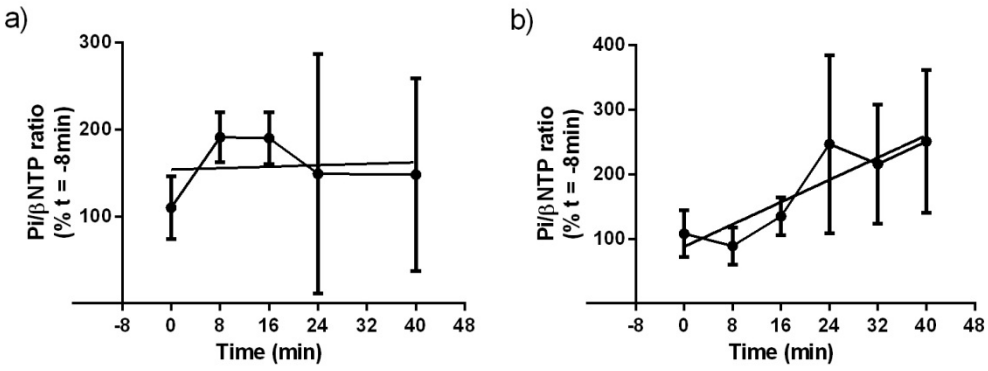

Figure 3.13: Change in the Pi to βNTP ratio and fitted linear regression for a) control (n=7), and b) 5 mg/kg hydralazine (n=4), treated A2780 tumour-bearing mice during the *in vivo* ^{31}P MRS acquisition. Points are the mean and bars are the standard error.

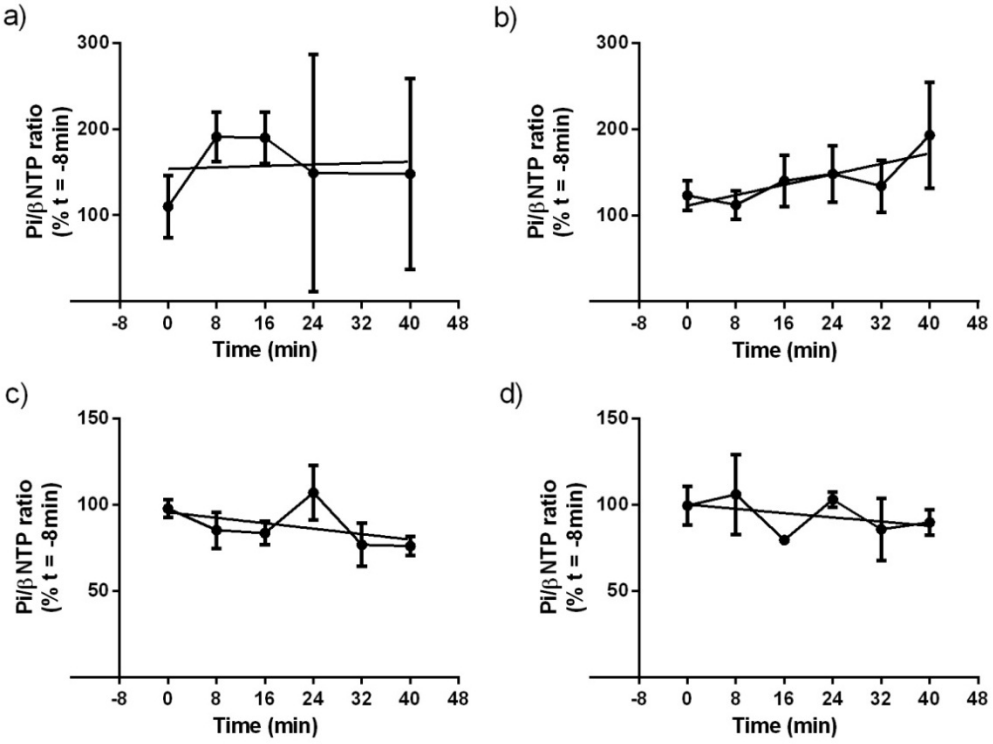

Figure 3.14: Change in the Pi to βNTP ratio and fitted linear regression for a) control (n=7), b) 1 mg/kg rucaparib (n=5), c) 5 mg/kg rucaparib (n=4), and d) 50 mg/kg rucaparib (n=3) treated A2780 tumour-bearing mice during the *in vivo* ^{31}P MRS acquisition. Points are the mean and bars are the standard error.

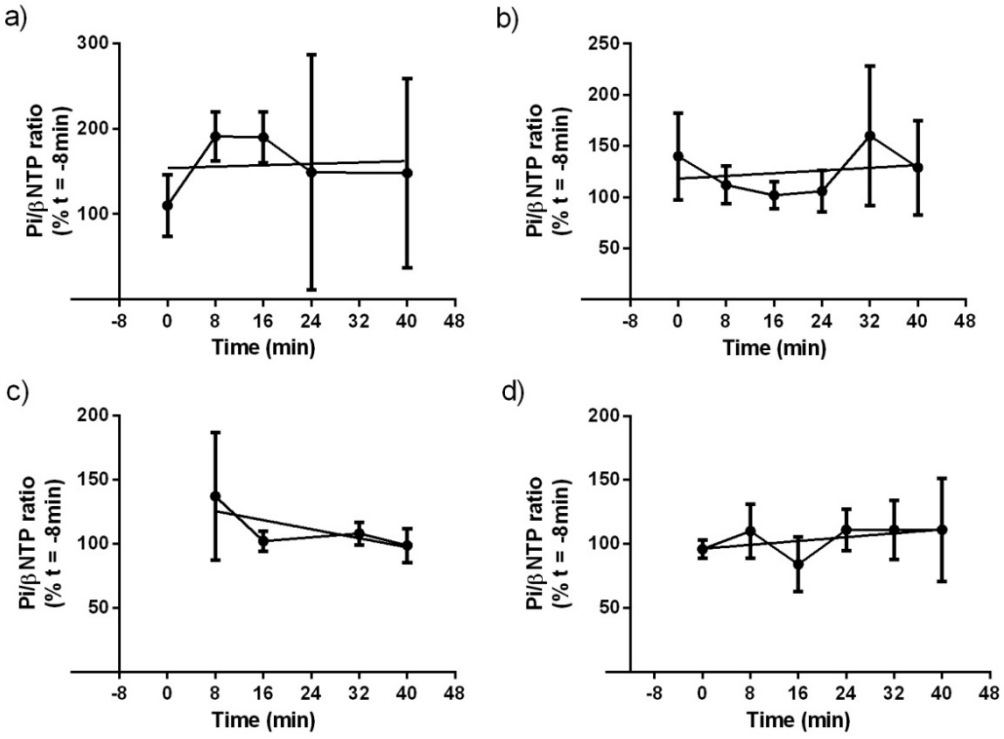

Figure 3.15: Change in the Pi to βNTP ratio and fitted linear regression for a) control (n=7), b) 68 mg/kg temozolomide (n=5), c) 1 mg/kg rucaparib plus 68 mg/kg temozolomide (n=4), and d) 5 mg/kg rucaparib plus 68 mg/kg (n=3), treated A2780 tumour-bearing mice during the *in vivo* ^{31}P MRS acquisition. Points are the mean and bars are the standard error.

Figures 3.16-3.18 show the corresponding Pi to βNTP ratio data for SW620 tumour-bearing mice.

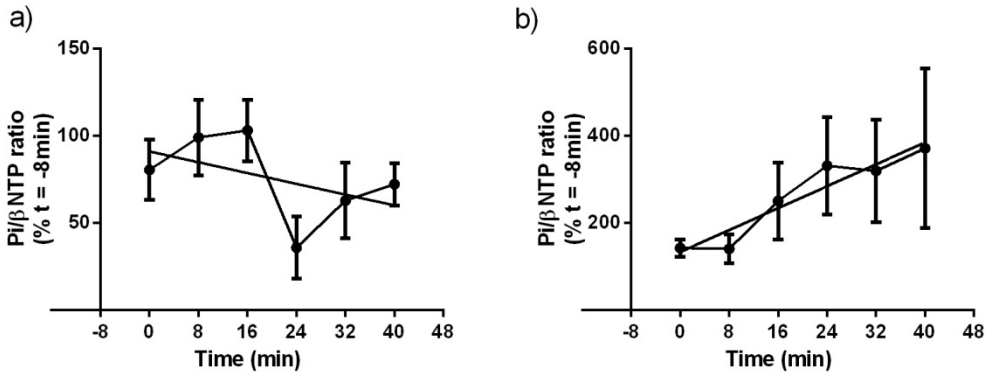

Figure 3.16: Change in the Pi to βNTP ratio and fitted linear regression for a) control (n=3), and b) 5 mg/kg hydralazine (n=6), treated SW620 tumour bearing mice during the *in vivo* ^{31}P MRS acquisition. Points are the mean and bars are the standard error.

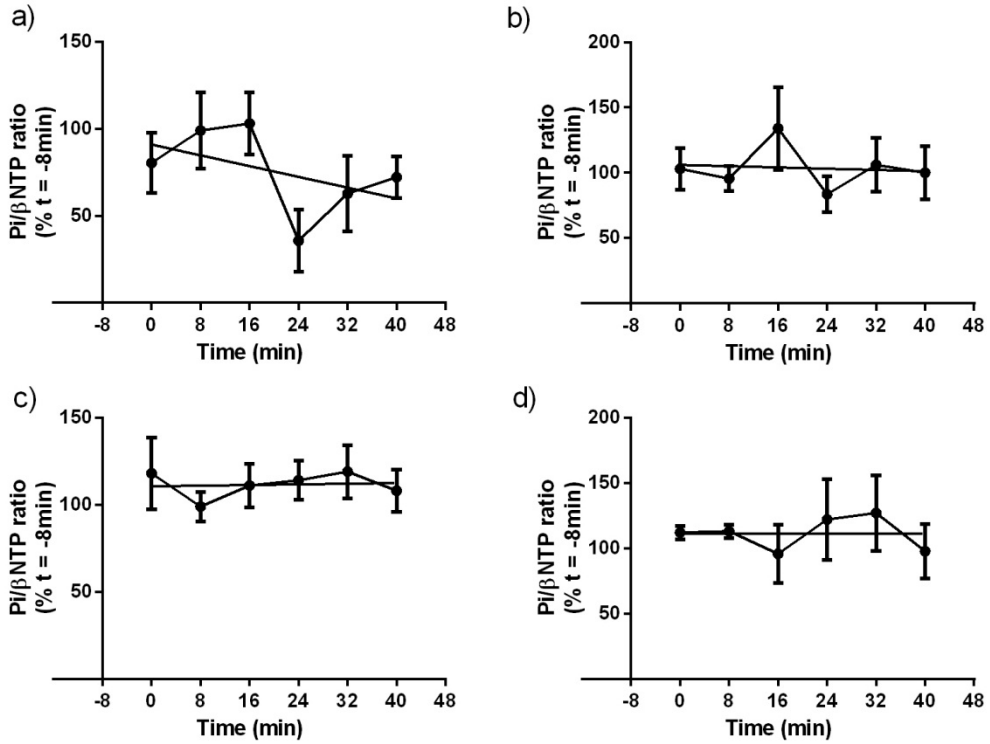

Figure 3.17: Change of Pi to βNTP ratio and fitted linear regression for a) control (n=3), b) 1 mg/kg rucaparib (n=10), c) 5 mg/kg rucaparib (n=6), and d) 50 mg/kg rucaparib (n=4), treated SW620 tumour-bearing mice during the *in vivo* ^{31P} MRS acquisition. Points are the mean and bars are the standard error.

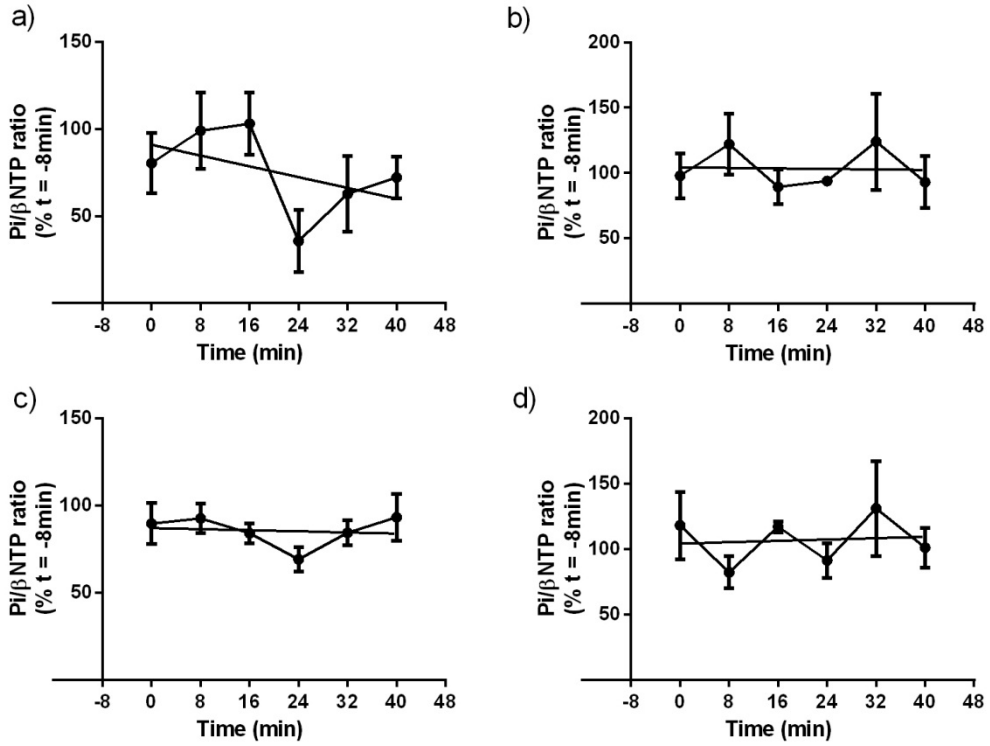

Figure 3.18: Change in the Pi to βNTP ratio and fitted linear regression for a) control (n=3), b) 68mg/kg temozolomide (n=4), c) 1mg/kg rucaparib plus 68mg/kg temozolomide (n=3), and d) 5mg/kg rucaparib plus 68mg/kg (n=3), treated SW620 tumour bearing-mice during the *in vivo* ^{31}P MRS acquisition. Points are the mean and bars are the standard error.

An alternative way to analyse these data is shown in Figures 3.19 and 3.20 where the percentage change in the Pi/βNTP ratio 8 minutes before drug administration (t = -8 min), 8 minutes after (t = 8 min) or 40 minutes (t = 40 min) after drug treatment for both tumour types is shown. These time points were chosen to assure a maximum total of data elements in all of them. The time point before injection was used as a background reading, the 8 minute after injection point was set as the earliest time where an acute affect might have occurred, and the 40 minute time point was used to as the latest time point and that with the maximum number of data elements to assure signal quality.

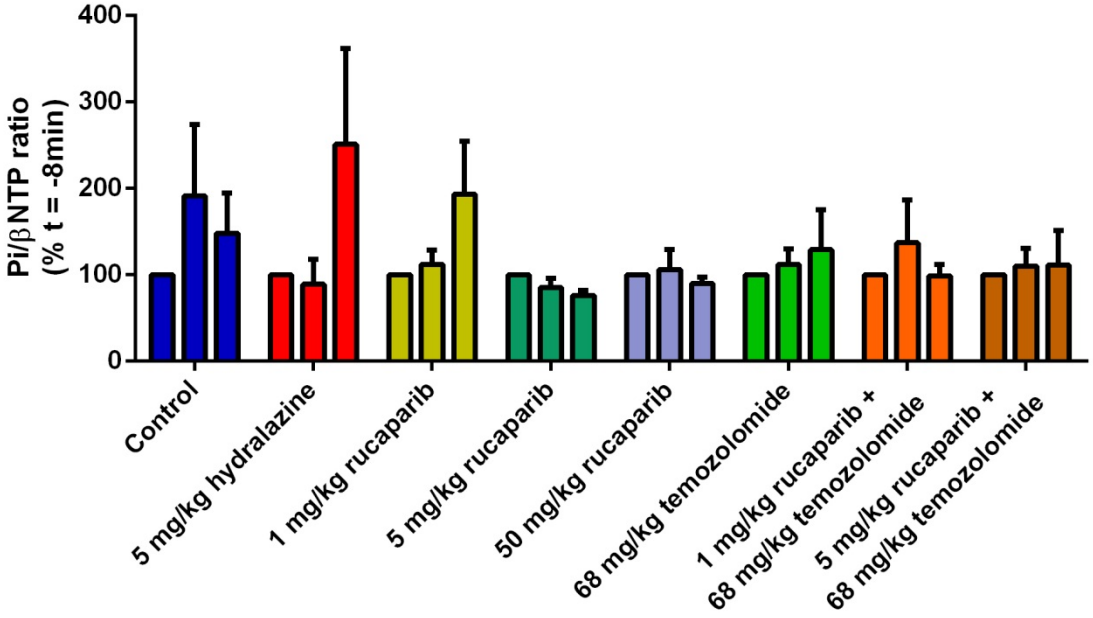

Figure 3.19: Change in Pi/βNTP ratios in A2780 tumour bearing-mice grouped between 8 minutes before injection of drug, 8 minutes and 40 minutes after drug injection. The mean ratio and standard error of the mean is shown on median and inter-quartile range.

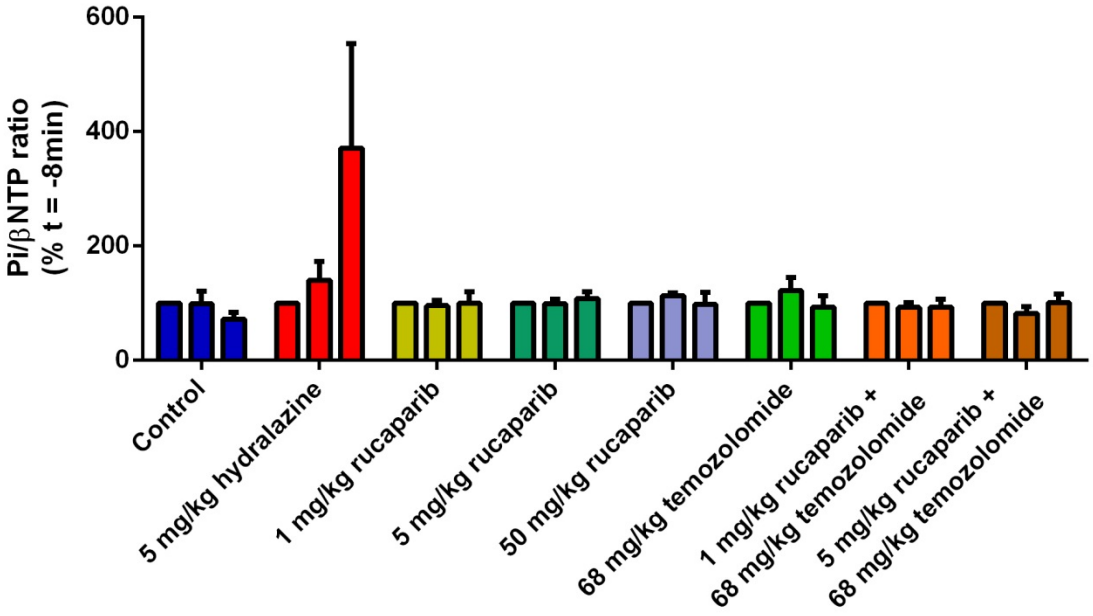

Figure 3.20: Change in Pi/βNTP ratios in SW620 tumour bearing-mice grouped between 8 minutes before injection of drug, 8 minutes and 40 minutes after drug injection. The mean ratio and standard error of the mean is shown on median and inter-quartile range.

The maximum change in the ratio Pi to βNTP in each group independent of the time point is shown in Figures 3.21 and 3.22 for A2780 and SW620 tumour-bearing mice, respectively.

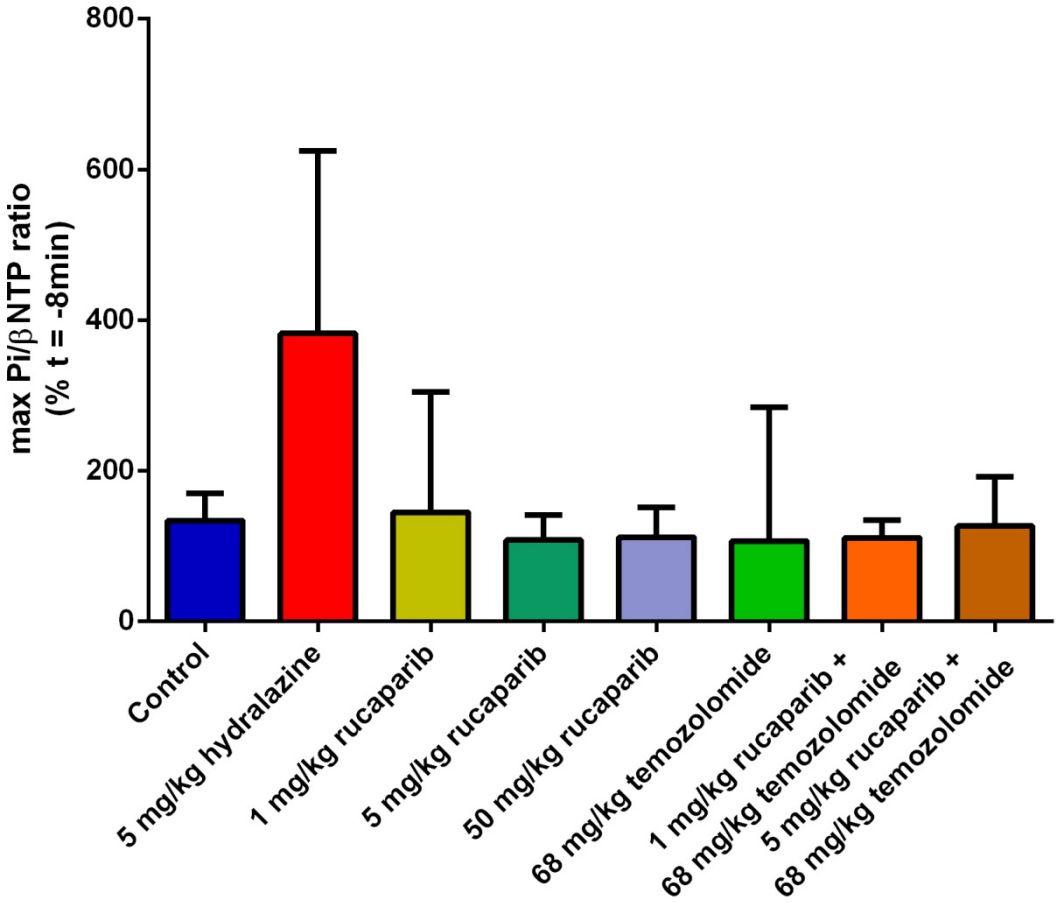

Figure 3.21: Median values and inter-quartile range (error bars) for the maximum change in Pi/βNTP ratios in each group of A2780 tumour-bearing mice.

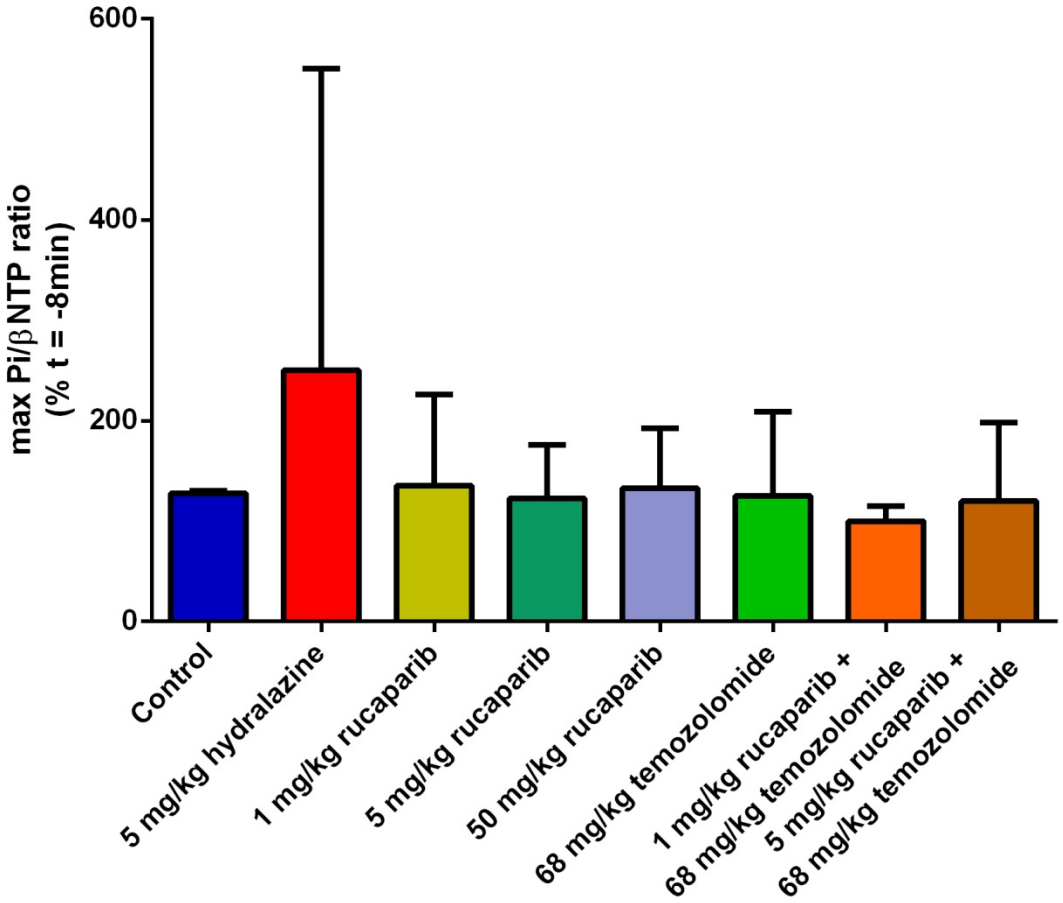

Figure 3.22: Median values and inter-quartile range (error bars) for the maximum change in Pi/βNTP ratios in each group of SW620 tumour-bearing mice.

Jones *et al.* (2008) have used ^{31}P-MRS to study muscle metabolic responses to exercise with linear regression analysis (slope) to define the highest constant work rate that can be sustained without a progressive loss of homeostasis (Jones *et al.*, 2008). In an analogous manner in the current study, linear regression was used to analyse the data depicted in Figures 3.9 to 3.14 and the slopes of each fitted line are presented in Table 3.5.

	Control	**5 mg/kg hydralazine**	**1 mg/kg rucaparib**	**5 mg/kg rucaparib**
A2780	0.2± 1.3	4.3±1.1	1.5±0.06	-0.4±0.4
SW620	-0.8±0.7	6.3±1.0	-0.1±0.6	0.05±0.3
	50 mg/kg rucaparib	**68 mg/kg temozolomide**	**1 mg/kg rucaparib + 68 mg/kg temozolomide**	**5 mg/kg rucaparib + 68 mg/kg temozolomide**
A2780	-0.3±0.3	0.3±0.7	-0.9±0.6	0.4±0.3
SW620	-0.01±0.4	-0.05±0.5	-0.08±0.3	0.1±0.6

Table 3.5: Slope and standard error for the linear regression analyses of the % change of Pi/βNTP ratio data presented in Figures 3.9 to 3.14.

The linear regression analysis of the data presented in Figures 3.9-3.14 generated p values (Table 3.6). Statistical analysis demonstrated that only 5 mg/kg hydralazine produced an effect where the slope was significantly different from zero. In A2780 tumour-bearing mice, 1 mg/kg rucaparib produced an effect that was on the borderline of significance at the 95% confidence level (p=0.053), suggesting an acute change in the ^{31}P-MR spectrum in this group.

	Control	**5 mg/kg hydralazine**	**1 mg/kg rucaparib**	**5 mg/kg rucaparib**
A2780	0.88	0.016*	0.053	0.33
SW620	0.35	0.0038*	0.84	0.86
	50 mg/kg rucaparib	**68 mg/kg temozolomide**	**1 mg/kg rucaparib + 68 mg/kg temozolomide**	**5 mg/kg rucaparib + 68 mg/kg temozolomide**
A2780	0.38	0.67	0.26	0.32
SW620	0.98	0.93	0.8	0.85

Table 3.6: p Values for the linear regression analyses of the % change of Pi/βNTP ratio data presented in Figures 3.9 to 3.14.

The maximum values for the change in Pi to βNTP ratio were also analysed statistically by using a one-way ANOVA and a Mann-Whitney non-paired t test. One-way ANOVA did not reveal any significant difference across groups nor across tumour type. Using a Mann-Whitney non-paired t test there were no statistically significant difference across treatment groups in A2780 tumour-bearing mice. In the SW620 tumour-bearing mice, however, the 5 mg/kg hydralazine group was significantly different from all the other treatment groups ($0.047 \leq p \leq 0.033$), and 1 mg/kg rucaparib alone group was significantly different from the combination of 1 mg/kg rucaparib with 68 mg/kg temozolomide (p=0.028).

Analysing the data by individual time point was also investigated, and 3 time points were chosen: 8 minutes before injection of the drug (t = -8min), 8 minutes after the injection of the drug (t = 8min) and 40 minutes after the injection of the drug (t = 40min). The change in the pre-treatment to post-treatment Pi to βNTP ratio as a percentage was analysed using paired t tests. Analysis of A2780 data identified statistically significant differences between pre-treatment and 40 minutes after drug injection in the 5 mg/kg rucaparib group (p=0.025) suggesting a fall in the Pi to βNTP ratio in this group due to treatment. Using the same analysis for data generated in SW620 tumour-bearing mice, no statistically significant effects at the 5% level of individual drugs or drug

combinations on Pi/βNTP ratios could be demonstrated. However, the 5 mg/kg hydralazine induced an increase in the Pi/βNTP ratio that was significant at the 10% level (p=0.082), consistent with a vascular effect.

3.3 Discussion

3.3.1 Vascular effects of rucaparib, temozolomide or combined rucaparib and temozolomide treatment as assessed by DCE-MRI

The vascular effects of hydralazine were described by Horsman *et al.* (1992) and have been reviewed by Gaya and Rustin (2005). In the original paper effects of doses between 0.1 and 5 mg/kg hydralazine were investigated, and the effect on mean arterial blood pressure studied. The authors found that after hydralazine administration the maximum changes in blood pressure were apparent within 10 to 15 minutes, and were still measurable at least 30 minutes after injection. They also found that a 2.5 mg/kg hydralazine dose caused a drop of 50% in the blood pressure, and that 80% - 90% reduction in blood pressure can be achieved with doses between 2.5 and 5 mg/kg hydralazine (Horsman *et al.*, 1992; Gaya and Rustin, 2005).

Bentzen *et al.* (2005) published work where DCE-MRI and susceptibility contrast MRI assays were used in C3H mouse mammary carcinoma-bearing mice to assess tumour blood volumes using a specific blood pool contrast agent (BPA NC100150). Changes in tumour blood volume were modulated by the use of perfusion reducing drugs: hydralazine and combretastatin A-4 disodium phosphate. In this study a reduction in the initial slope between the first and second post-contrast signal values of 78% of the tumour blood pool was found. Although the cause was unclear, the authors hypothesized that it was the result of antihypertensive effects causing a significant decrease in mean arterial blood pressure (Bentzen *et al.*, 2005). In the DCE-MRI study results presented in section 3.1, in both tumour types, 5 mg/kg hydralazine caused an acute decrease in the uptake of MR contrast agent in accordance with these previously published studies confirming that this agent is a good positive control.

As reviewed by Jagtap and Szabó (2005), there are several physiological processes where PARP deficiency is actually protective, including in vasculature. PJ-34 and INO-1001 are two PARP inhibitors which have been tested in the settings of diabetic endothelium dysfunction, balloon angioplasty and endothelial injury by homocysteine. The inhibition of PARP activity induced by these drugs had a protective effect, preventing or reversing the pathologies they were tested against (Jagtap and Szabo, 2005).

In 2009, Ali *et al.* published work where the vasoactivity of AG014699 (i.e. rucaparib) was studied. In this study, performed in SW620 tumour-bearing mice, the authors found that 1 mg/kg rucaparib reduced vessel mismatch in SW620 tumour xenografts *in vivo* and, using a dorsal window chamber technique, they demonstrated that 1 m/kg rucaparib enhanced tumour perfusion (Ali *et al.*, 2009). In 2011, the same authors published a further study using the same techniques, but with a higher dose of rucaparib (10 mg/kg), which showed that although rucaparib improved vessel perfusion in MDA-MB-231 and SW620 tumours, this effect did not enhance the antitumour activity of the chemotherapeutic agent doxorubicin (Ali *et al.*, 2011). The SW620 tumour cell line has been used in other vascular studies, and Bradley *et al.* (2008) has published experiments where the SW620 tumour model was used to assess the haemodynamic effects of vascular endothelial growth factors (VEGF) (Bradley *et al.*, 2008).

In A2780 human tumour xenografts antagonism of vascular endothelial growth factors and fibroblast growth factors (FGF) signalling has been studied using E-3810, a dual VEGFR and FGFR inhibitor. The authors reported a significant reduction in tumour vessel density in treated tumours, corroborated after 5 days of treatment by reduced tumour distribution of contrast agent during DCE-MRI (Bello *et al.*, 2011).

In work published by Zhang *et al.* (2011), DCE-MRI was used to assess the vascular effects of temozolomide on its own, or in combination with radiotherapy and/or combined with LY21009761 (a TGF-βRI kinase inhibitor) in glioblastomas. In this study, the amplitude parameter in DCE-MRI showed a significant decrease in the monotherapy groups, but no further decrease was observed with dual or triple combination therapy. The decrease in amplitude was thought to be a consequence of a reduction in the tumour relative blood volume (Zhang *et al.*, 2011).

As discussed above the PARP inhibitor rucaparib has been reported to have nicotinamide-like effects (i.e. as discussed in Horsman, 1995) in SW620 tumours, thus potentially improving the delivery of temozolomide to the tumour resulting in chemopotentiation *in vivo* (Ali *et al.*, 2009). However, the overall

result for the DCE-MRI experiments presented in section 3.1 in A2780 tumour-bearing mice, based on the $AUC_{MR,120}$, is that, although a significant change was observed in the hydralazine group and with the lowest dose (1 mg/kg) of the PARP inhibitor, no significant change was observed in any of the other groups.

In SW620 tumour-bearing mice, no significant change in $AUC_{MR,\ 120s}$ was observed in the control group. There were, however, significant differences in the uptake of contrast agent between injections of hydralazine and the higher doses of rucaparib (5 and 50 mg/kg). The Anti-Vascular Index (AVI, the ratio of $AUC_{MR,\ 120s}$ between contrast agent injections) is inverse to the AUC_{120_2} (second injection uptake). In the A2780 tumour-bearing mice in control mice there was a rather high AVI when compared with SW620 tumour-bearing mice. Nevertheless, the hydralazine group had the highest AVI followed by the 1 mg/kg rucaparib group in A2780 tumours. In SW620 tumours the hydralazine group and the 50 mg/kg rucaparib group had higher AVI values than control.

Although the results presented in this chapter are contrary to those published by Ali *et al.* (2009), the experimental conditions are different. While the published work reported an increase in the vascular perfusion, the results reported in this thesis show a decrease in the vascular function. In the published work a dorsal window chamber was applied to the mice and the tumour cell implanted in the opening while in the experiment here reported the tumours were implanted subcutaneously without further restraints. The solid and constricted nature of the dorsal window chamber can be one reason for the difference in the obtained results. Nevertheless, in subsection 5.3.1, data will be presented which demonstrate chemopotentiation by the use of rucaparib in combination with temozolomide in SW620 tumours, a result that is consistent with previous studies.

3.3.2 Metabolic effects of rucaparib, temozolomide or rucaparib combined with temozolomide treatment as assessed by in vivo ^{31}P spectroscopy

Thomas *et al.* in 1994 and Nordsmark *et al.* in 1997 have used the ratio between γ- or βNTP phosphates and inorganic phosphate as a bioenergetic indicator in mouse tumours. In the former study ^{31}P-MRS was used to detect

phosphomonoester signals from neoplastic and rapidly dividing normal tissues. Livers of lymphomatous mice and control mice were examined *in vivo* by ^{31}P-MRS 24 days after injection of the cancer cells. At this time point the lymphomatous infiltration was about 70% in the liver, and phosphomonoester and inorganic phosphate MRS signals had increased and shifted to the right (indicating a lower pH). The experiments were extended to liver extracts, where a positive correlation between hepatic phosphomonoesther and phosphodiester ratios, and the degree of lymphomatous infiltration quantified by histology, was observed. In the second paper, C3H mammary carcinoma-bearing mice were examined by ^{31}P-MRS, following exposure to atmospheric air or to air containing carbon monoxide. The authors concluded that the inhalation of carbon monoxide was associated with enhanced radiation resistance, decreased tumour oxygenation but an unchanged bioenergetic status expressed as the βNTP to Pi ratio (Thomas *et al.*, 1994; Nordsmark *et al.*, 1997). Madhu *et al.* (2008) have reported that the injection of different doses of Gd-DTPA-BMA caused an increase in the choline peak area (assessed by 1H-MRS in HT29 colon carcinomas) dependent on the concentration injected. However, Bauer *et al.* (1994) had investigated the changes in 31P-MRS caused by gadolinium chelates. In the study the signals intensities of the phosphorus metabolites were not influenced by GdCl3, slightly enhanced by Gd-DTPA and highly enhanced by Gd-EOB-DTPA (Madhu *et al.*, 2008; Bauer *et al.*, 1994).

In the current study, the inverse ratio (Pi/βNTP) was used, a higher ratio between inorganic phosphate and βNTP indicating a higher concentration of inorganic phosphate and/or a lower concentration of βNTP in tumours, due to reduced metabolism caused by an impaired blood supply. From Figures 3.19 and 3.20 it can be seen that by 40 minutes after administration, hydralazine treatment had an effect on tumour energy metabolism in both tumour types, consistent with previous ^{31}P-MRS studies (Bremner *et al.*, 1991; Wood *et al.*, 1992).

Although, overall, rucaparib with or without temozolomide did not produce marked changes in Pi/βNTP ratios, there was an increase in the Pi/βNTP ratio after 1 mg/kg rucaparib in A2780 tumours, based on the slope of the Pi/βNTP

ratio over time. This result was an unexpected observation and has no obvious explanation.

The results from the ^{31}P-MRS experiments in A2780 tumours show coherence with the DCE-MRI data, since the groups which showed a significant decrease in the uptake of contrast agent after drug treatment also showed an increase in the inorganic phosphate to βNTP ratio, i.e. in A2780 tumour-bearing mice with 5 mg/kg hydralazine or 1 mg/kg of rucaparib. Thus the effects of 1mg/kg rucaparib are consistent with an antivascular action, but there was no logical dose-dependence (i.e. no antivascular effect was seen at higher doses of rucaparib). To have a better understanding of the dose dependent effect, an intermediate dose of rucaparib between 1 and 5 mg/kg will be necessary.

In SW620 tumour-bearing mice, there is again coherence between the DCE-MRI and MRS results with an increase in the inorganic phosphate to βNTP ratio in the 5 mg/kg hydralazine group. These hydralazine results agree with work published by Robinson *et al.* (2000) where GH3 prolactinoma-bearing rats were treated with 5 mg/kg hydralazine administered with air breathing for 40 minutes, 1000 mg/kg nicotinamide and an initial 20 minutes carbogen breathing alone, resumption of air breathing for 40 minutes with administration of 1000 mg/kg nicotinamide, and finally 30 minutes carbogen breathing, all followed by MRI and ^{31}P-MRS. The results presented include a decrease of MR signal and βNTP/Pi ratio after hydralazine administration. However, an increase in βNTP/Pi ratio after nicotinamide administration was also reported (Robinson *et al.*, 2000).

Together, the results presented in this chapter demonstrate that rucaparib has no marked or consistent acute effect on tumour vasculature when given alone or in combination with temozolomide. In contrast, the positive control compound hydralazine induced a significant and consistent antivascular effect which resulted in an increased Pi/βNTP ratio, i.e., a decline in tumour energetics. The increase in this ratio is the result of a large increase in the Pi levels combined with a slight decrease of βNTP levels indicating the consumption without replacement of ATP.

Chapter 4. Results – The effects of rucaparib, temozolomide and rucaparib combined with temozolomide treatment on NAD and ATP concentrations as measured by *ex vivo* $^{1}H/^{31}P$ MRS

As described in section 1.2, PARP1 and PARP2 utilize NAD in single strand break DNA repair (Schreiber *et al.*, 2006). The results presented in this chapter relate to experiments performed to assess changes in ATP and NAD concentrations in cells and tissues following treatment with rucaparib, temozolomide or rucaparib combined with temozolomide.

In the previous chapter, effects on tumour vasculature and consequently tumour energetics in A2780 and SW620 tumour-models were studied. Evelhoch *et al.* (2000) have demonstrated that a drop in ATP is related to a reduction in cellular NAD following PARP activation, in apoptotic cells, a result confirmed by Ronen *et al.* (1999). Henning *et al.* (1997) estimated hepatic levels of PARP activity using the enzyme cycling method of Nisselbaum and Green to measure total amounts of NAD, and the results presented in this chapter have the additional goal of comparing NAD and ATP levels in cell and tissue extracts with the *in vivo* MR results.

To measure NAD and ATP in cell and tissue extracts, a method of addition assay was developed and then applied to tumour cells, tumours and to livers from PARP1 WT and KO mice treated with rucaparib, temozolomide and the combination of rucaparib with temozolomide. All the results in this section were obtained using the perchloric acid extraction method described in the sections 2.3 and 2.6. NMR spectroscopy was performed in the 11.4T Bruker Avance III 500MHz NMR spectrometer located in the School of Chemistry, Newcastle University (Bedson Building).

4.1 The effect of rucaparib, temozolomide and rucaparib combined with temozolomide treatment on NAD and ATP concentrations in tumour cells assessed by *in vitro* $^{1}H/^{31}P$ MRS

4.1.1 Methods of addition

As discussed in subsection 2.3.1, the method of addition can be used to generate quantitative data on analyte levels in a non-homogeneous sample. In particular, in a multi-step procedure, the method of addition provides data on analyte recovery and assay linearity as well as accounting for inter-sample variability.

A2780 cells

Experiments were performed as described in subsection 2.3.3. Aliquots of 5 mM ATP and 5 mM NAD were added to replicate samples of $1.50x10^{8}$ cells as indicated in Table 4.1.

	Volume added (µl)		Quantity added (nmoles/10^{6}cells)	
	5 mM ATP	5 mM NAD	ATP	NAD
Tube 1	0	0	0	0
Tube 2	75	30	2.5	1
Tube 3	150	60	5	2

Table 4.1: Volume of 5 mM ATP and 5 mM NAD added to $1.50x10^{8}$ A2780 cells in the methods of addition assay.

After the addition of ATP and NAD, the samples underwent PCA extraction, were freeze-dried overnight, and resuspended in 500 µl of D_2O prior to the transfer of 400 µl into the NMR tubes. Proton (^{1}H) and phosphorus (^{31}P) spectra were acquired and quantification was performed as described in subsection 2.3.4. TSP peaks were identified in the 0.064 ppm to -0.070 ppm region of the ^{1}H NMR spectra, and MDP peaks were identified in the 17.5 ppm to 15.12 ppm region of the ^{31}P NMR spectra. The NAD concentration was measured from the doublet at approximately 9.15 ppm in the spectrum and ATP was measured from the doublet at approximately -5.5 ppm in the ^{31}P spectra.

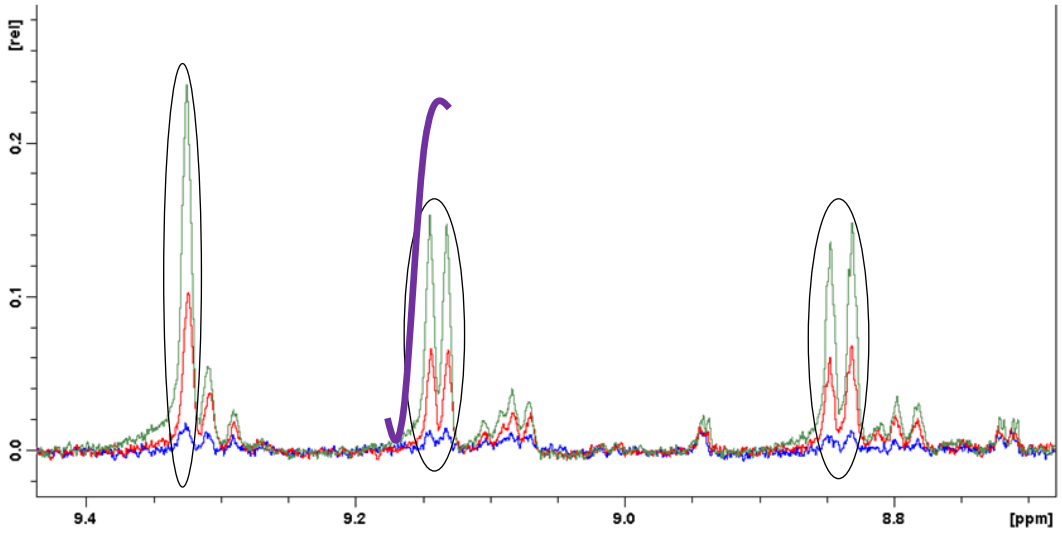

Figure 4.1: NAD region of 3 superimposed ^{1}H spectra of A2780 cell extracts (tube 1 in blue, tube 2 in red and tube 3 in green – see Table 4.1). The NAD peaks were assigned and the doublet at approximately 9.15 ppm was used for quantification as indicated by the purple integration curve.

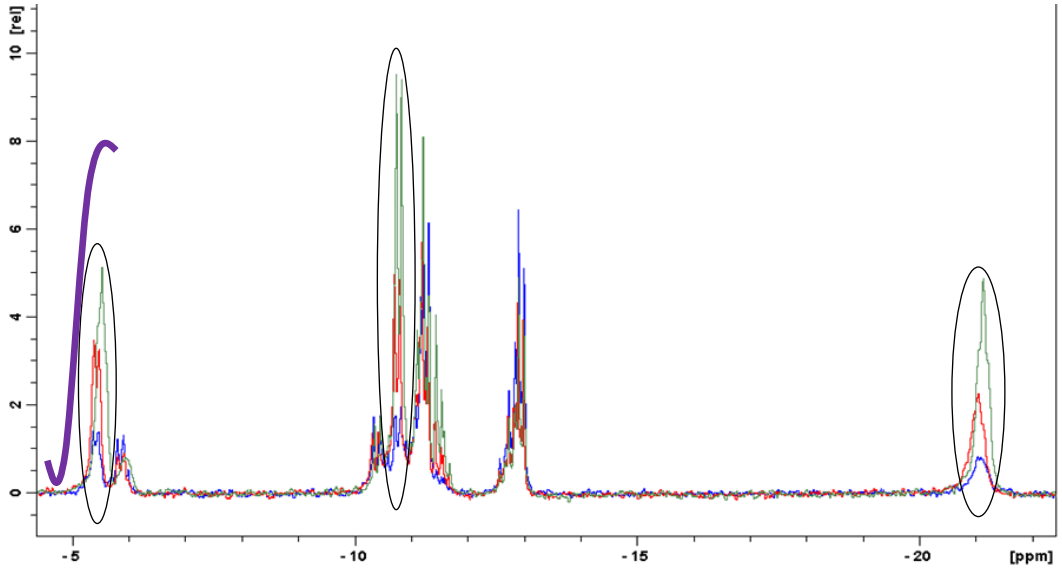

Figure 4.2: ATP region of 3 superimposed ^{31}P spectra of A2780 cell extracts (tube 1 in blue, tube 2 in red and tube 3 in green – see Table 4.1). γ-, α-, and β-ATP peaks were assigned and the doublet at approximately -5.5 ppm corresponding to γ-ATP was used to quantify ATP as indicated by the purple integration curve.

In Table 4.2 the results of the ATP and NAD concentrations measured are compared to those expected for the quantity of analyte added.

	Expected concentration of added analyte (nmoles/10^6cells)		Measured analyte concentration (nmoles/10^6cells)	
	ATP	NAD	ATP	NAD
Tube 1	0	0	0.67	0.04
Tube 2	2.5	1	1.7	0.93
Tube 3	5	2	3.1	1.83
Estimated concentration of endogenous analyte			1.25	0.043
Extraction efficiency			49%	90%

Table 4.2: Expected and measured ATP and NAD concentrations in A2780 cell extracts (samples prepared as shown in Table 4.1 and data produced from spectra in Figures 4.1 and 4.2)

Plotting these data and applying a linear regression analysis generated the results in Figure 4.3:

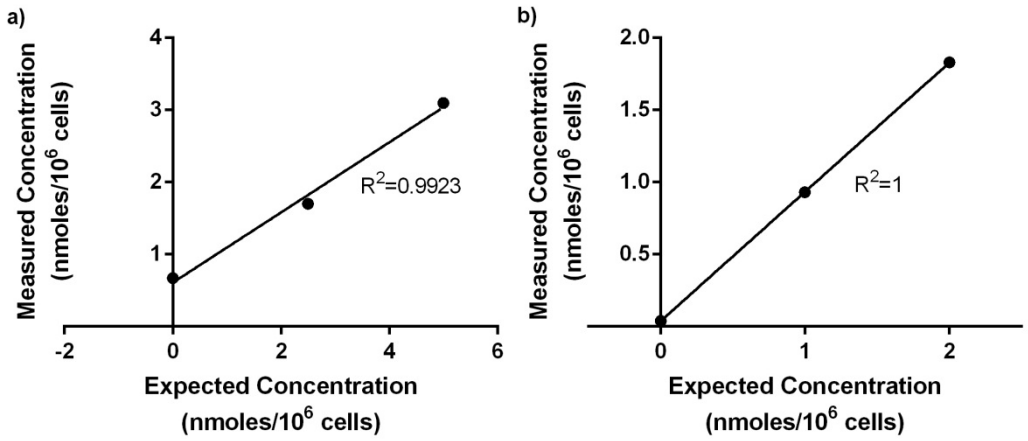

Figure 4.3: Linear regression analysis of expected and measured ATP (a) and NAD (b) concentrations in A2780 cell extracts. Data from Table 4.2.

From the linear regression analysis shown in Figure 4.3, the endogenous ATP concentration prior to addition of exogenous ATP was calculated to be 1.25 nmole/10^6 cells. In the case of NAD, the endogenous concentration was 0.043 nmoles/10^6 cells. The extraction efficiency or recovery, calculated by multiplying the slope of the regression line by 100, was 49% for ATP and 90% for NAD.

SW620 cells

Analogous experiments were performed to develop the method of addition assay for the measurement of ATP and NAD in SW620 cells (Table 4.3 and 4.4, and representative spectra in Figures 4.4 and 4.5).

	Volume added (µl) (50 mM ATP/NAD cocktail)	Quantity added (nmoles/10^6cells)	
		ATP	NAD
Tube 1	0	0	0
Tube 2	7.5	2.5	2.5
Tube 3	15	5	5

Table 4.3: Volume of 50 mM ATP/NAD cocktail added to $1.5x10^8$ SW620 cells in the method of addition assay.

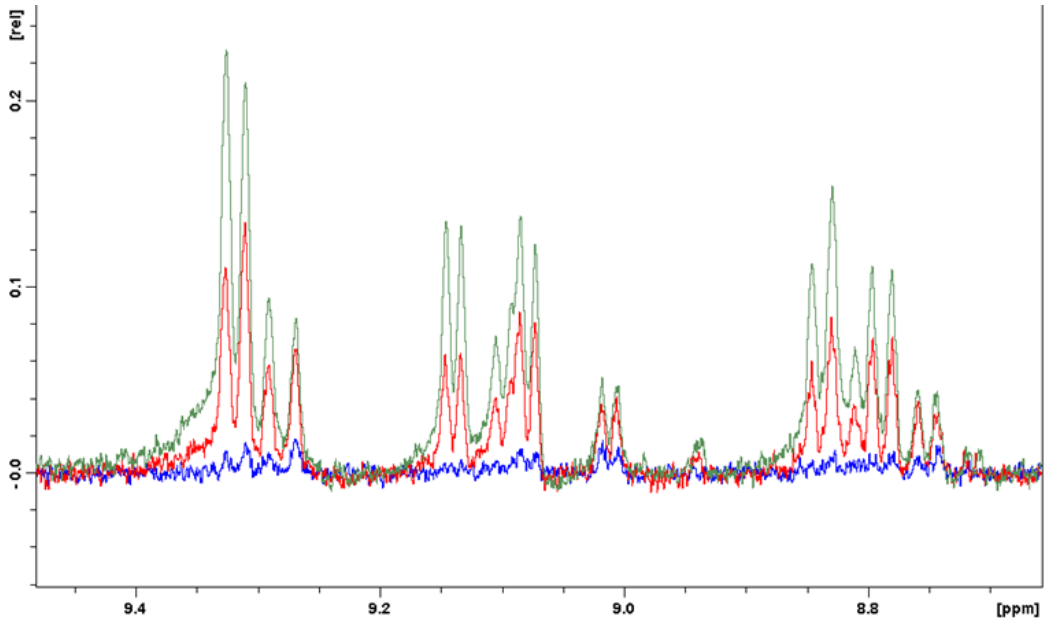

Figure 4.4: NAD region of 3 superimposed ^{1}H spectra of SW620 cell extracts (tube 1 in blue, tube 2 in red and tube 3 in green – see Table 4.3).

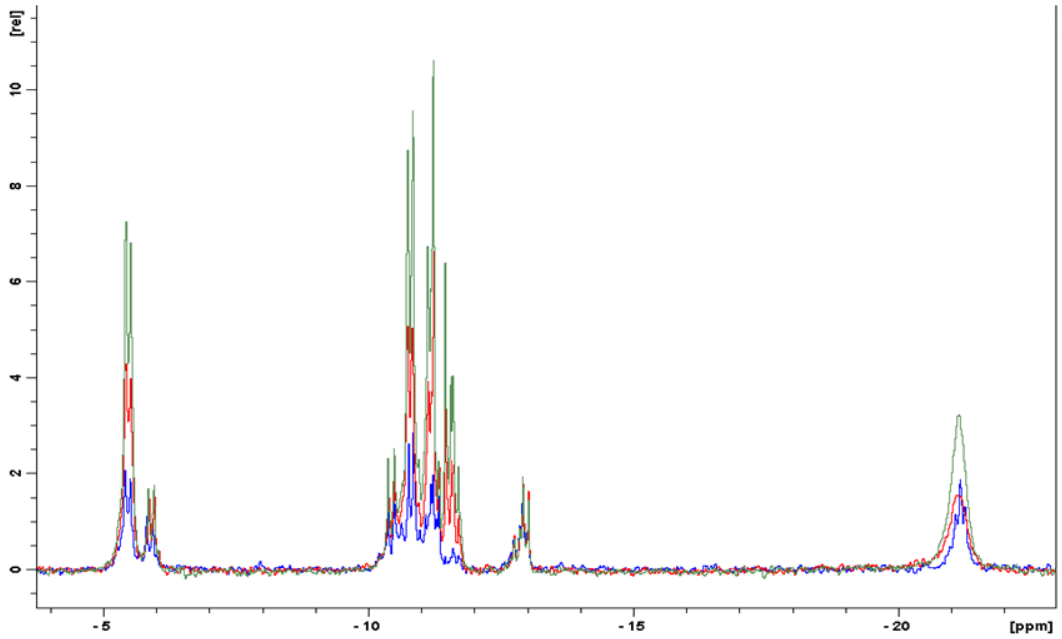

Figure 4.5: ATP region of 3 superimposed ^{31}P spectra of SW620 cell extracts (tube 1 in blue, tube 2 in red and tube 3 in green – see Table 4.3).

	Expected concentration of added analyte (nmoles/10^6cells)		Measured analyte concentration (nmoles/10^6cells)	
	ATP	NAD	ATP	NAD
Tube 1	0	0	1.07	0.27
Tube 2	2.5	2.5	1.83	2.27
Tube 3	5	5	2.87	4.13
Estimated concentration of endogenous analyte			2.84	0.38
Extraction efficiency			36%	77%

Table 4.4: Expected and measured ATP and NAD concentrations in SW620 cell extracts (samples prepared as shown in Table 4.3 and data produced from the spectra in Figures 4.4 and 4.5)

Plotting these data and applying a linear regression analysis generated the results shown in Figure 4.6.

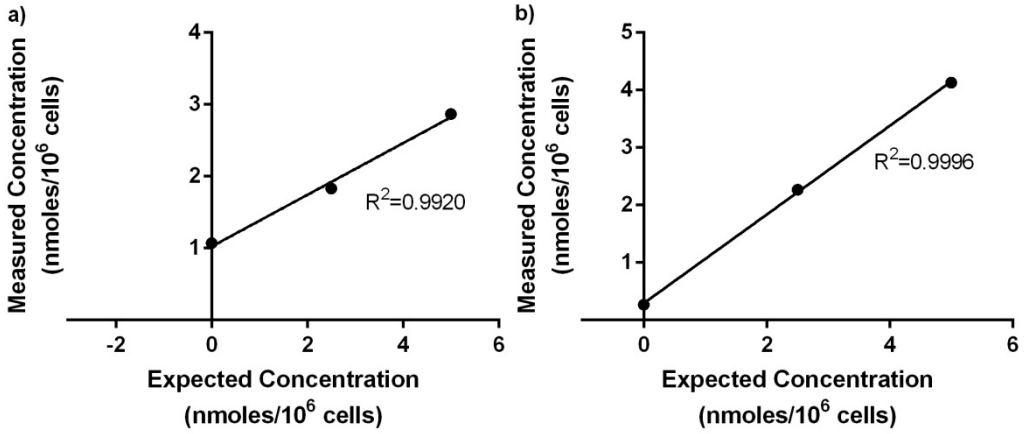

Figure 4.6: Linear regression analysis of expected and measured ATP (a) and NAD (b) concentrations in SW620 cell extracts. Data from Table 4.4.

From the linear regression analyse shown in Figure 4.6, the endogenous ATP concentration prior to addition of exogenous ATP was calculated to be 2.84 nmoles/10^6 cells. In the case of NAD, the endogenous concentration was 0.38 nmoles/10^6 cells, and the extraction efficiency was 36% for ATP and 77% for NAD.

4.1.2 NAD and ATP concentrations in drug treated cells

The effects of rucaparib, temozolomide and rucaparib/temozolomide combination treatments on ATP and NAD concentrations in A2780 cells were studied. Cell cultures were performed as described in section 2.2. Although Lutz *et al.* (1996) have demonstrated the feasibility of measuring individual purine and pyrimidine NDP and NTP concentrations by high resolution ^{31}P-NMR, several experimental conditions have to be met. In the results presented in this subsection, total nucleoside di- and triphosphate (NDP, NTP) levels, as opposed to specifically ADP and ATP, were measured (Lutz *et al.*, 1996).

A2780 cells

For the A2780 cell line, the drug treatments were:

- Control;
- 0.1 μM rucaparib;
- 180 μM temozolomide;
- 0.1 μM rucaparib combined with 180 μM temozolomide.

180 μM temozolomide corresponds to the GI_{50} of temozolomide alone in A2780 cells and it was combined with 0.1μM rucaparib. This combination has been shown to result in potentiation of growth inhibition in this cell line (personal communication from Lan-zhen Wang, NICR).

Cells were grown for 40 hours, incubated for 6 hours with the drugs as indicated above and then harvested. The number of cells harvested is shown in Table 4.5. Subsequently, NAD and ATP concentrations in the cell extracts were measure as described in subsection 2.3.4 and a representative spectrum is shown in Figure 4.7.

	Control	0.1 μM rucaparib	180 μM temozolomide	0.1 μM rucaparib + 180 μM temozolomide
Number of cells harvested ($x10^8$)	2.13	1.35	2.16	1.54

Table 4.5: Numbers of A2780 cells harvested for the analysis of the effects of rucaparib and temozolomide on ATP and NAD concentrations.

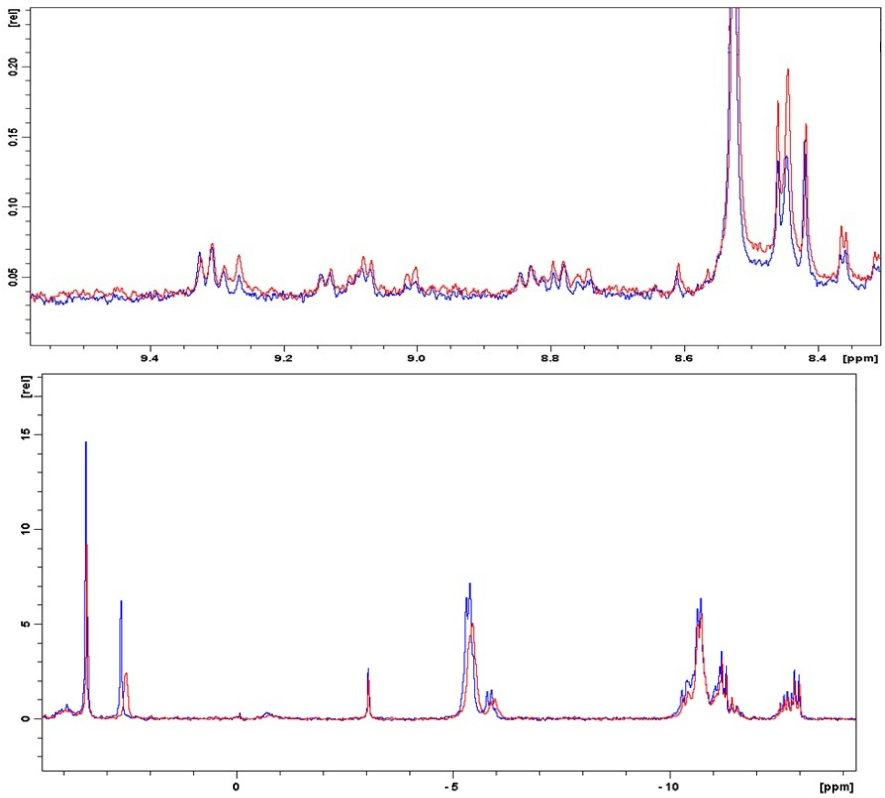

Figure 4.7: Top: NAD region of the ^{1}H spectra of A2780 in a cell extract of control (red) and following treatment with 0.1 μM rucaparib for 6h (blue). Bottom: ATP region of the ^{31}P spectrum in the same samples (control in red and following treatment with 0.1 μM rucaparib for 6h in blue).

Figures 4.8 and 4.9 depict the concentrations of NAD and NTP in each sample, and also the ratios between the NDP and NTP concentrations and the ratio between the inorganic phosphate (Pi) and NTP concentrations. The first parameter has been used by Bradbury *et al.* (2000) as an indicator of cell viability, necrosis and apoptosis, while the second parameter (inverted) has been used by Nordsmark *et al.* (1997) to assess the bioenergetic status of the tumour.

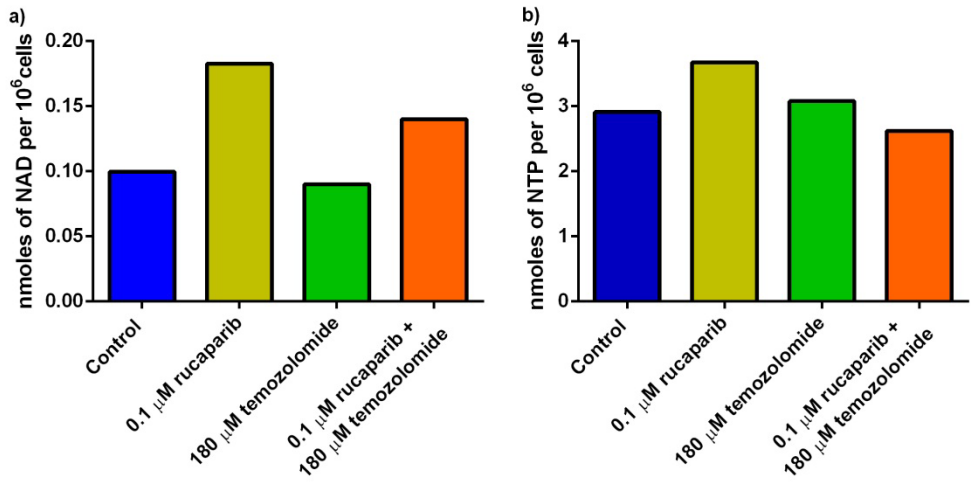

Figure 4.8: a) NAD and b) NTP concentrations in A2780 cells following treatment with 0.1 μM rucaparib, 180 μM temozolomide or 0.1 μM rucaparib combined with 180 μM temozolomide.

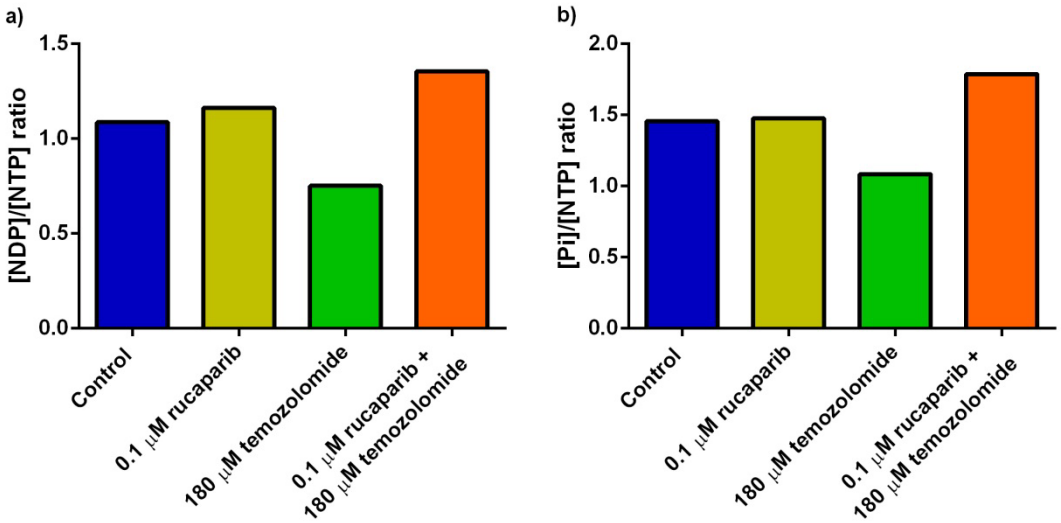

Figure 4.9: a) Ratio between the concentrations of NDP and NTP and b) ratio between Pi and NTP concentrations in A2780 cells treated with 0.1 μM rucaparib, 180 μM temozolomide or 0.1 μM rucaparib combined with 180 μM temozolomide. These results were not corrected for recovery rates due to the lack of information on the ADP recovery rate.

The data presented for A2780 cells are from a single experiment and hence primarily demonstrate the feasibility of the methodology.

4.2 The effect of rucaparib, temozolomide and rucaparib combined with temozolomide treatment on NAD and ATP concentrations assessed in mouse liver and human tumour xenografts by $^{1}H/^{31}P$ MRS

Bohndiek *et al.* (2010) studied tumour response to vascular disrupting agents by *in vivo* hyperpolarized ^{13}C-MRS, DCE- and DW-MRI. In addition, they performed PCA extraction to measure metabolite concentrations (Bohndiek *et al.*, 2010). Beloueche-Babari *et al.* (2010) investigated the metabolic effects of targeted cancer therapeutics by MRS and also compared *in vitro* ^{31}P-MRS of cell extracts with *in vivo* ^{31}P-MRS of human tumour xenografts in response of a histone deacetylase inhibitor treatment in HT29 cancer cells and tumours (Beloueche-Babari *et al.*, 2009). Similarly, Solanky *et al.* (2012) studied the metabolic profile of rat livers following hepatobiliary injury by using *in vivo* and *ex vivo* MRS (Solanky *et al.*, 2012).

4.2.1 Methods of addition

The methods of addition assay was performed to measure ATP and NAD concentrations in livers from CD1 nude mice and in A2780 and SW620 tumours grown subcutaneously.

Mouse Livers

Aliquots of 25 mM ATP and 25 mM NAD were added to replicate samples of 1 g wet weight of liver from SW620 tumour-bearing mice as indicated in Table 4.6 and as described in section 2.6.

	Volume added (µl)		Quantity added (µmoles/g of tissue)	
	25 mM ATP	25 mM NAD	ATP	NAD
Tube 1	0	0	0	0
Tube 2	100	40	2.5	1
Tube 3	200	80	5	2
Tube 4	400	160	10	4
Tube 5	800	320	20	8

Table 4.6: Volume of 25 mM ATP and 25 mM NAD added to 1 g of liver from SW620 tumour-bearing mice in the methods of addition assay.

The samples were then analysed as described in subsection 2.3.4 and representative spectra are shown in Figures 4.10 and 4.11.

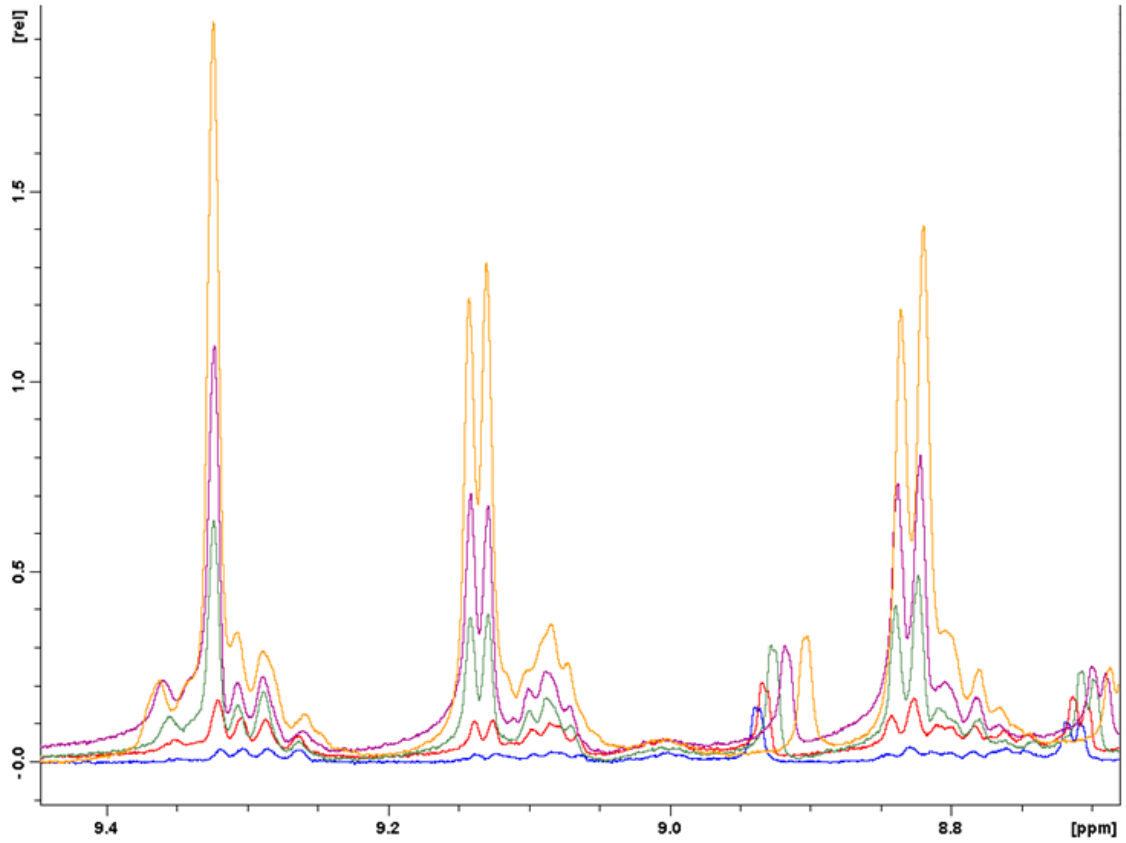

Figure 4.10: NAD region of 5 superimposed ^{1}H spectra of extracts of livers from SW620 tumour-bearing mice (tube 1 in blue, tube 2 in red, tube 3 in green, tube 4 in purple and tube 5 in yellow – see Table 4.6)

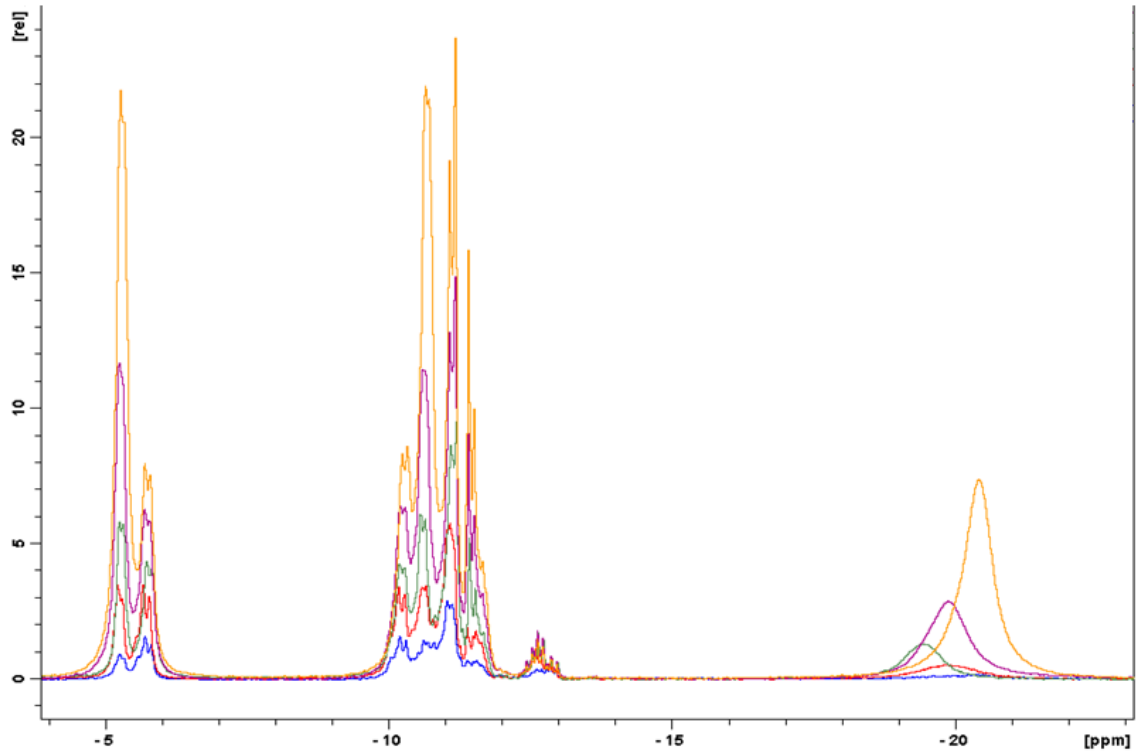

Figure 4.11: ATP region of 5 superimposed ^{31}P spectra of extracts of livers from SW620 tumour-bearing mice (tube 1 in blue, tube 2 in red, tube 3 in green, tube 4 in purple and tube 5 in yellow – see Table 4.6).

The results obtained are presented in Table 4.7 and linear regression analysis of the data in Figure 4.12.

	Expected concentration of added analyte (µmoles/g of tissue)		Measured analyte concentration(µmoles/g of tissue)	
	ATP	NAD	ATP	NAD
Tube 1	0	0	0.48	0.39
Tube 2	2.5	1	1.99	2.08
Tube 3	5	2	4.53	2.93
Tube 4	10	4	10.26	6.12
Tube 5	20	8	13.81	7.38
Estimated concentration of endogenous analyte			1.46	1.35
Extraction efficiency			69%	140%

Table 4.7: Expected and measured ATP and NAD concentrations in mouse liver samples from SW620 tumour-bearing mice.

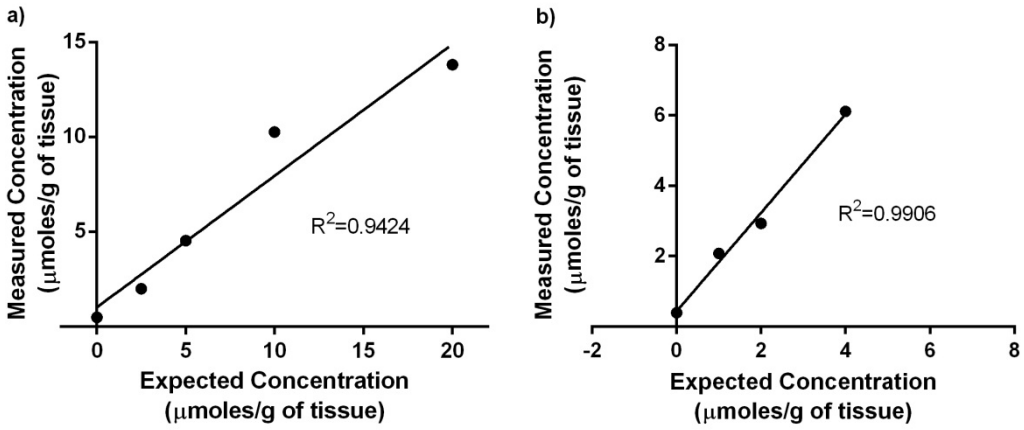

Figure 4.12: Linear regression analysis of expected and measured ATP (a) and NAD (b) concentrations in mouse liver samples from SW620 tumour-bearing mice. Data from Table 4.7.

From the linear regression analyses shown in Figure 4.12, the endogenous ATP concentration prior to addition of exogenous ATP was 1.46 µmoles/g of tissue (-2.48 to 10.06 within a 95% confidence interval). In the case of NAD, the endogenous concentration was 1.35 µmoles/g of tissue (-0.83 to 8.7 within a 95% confidence interval). The extraction efficiency or recovery was 69% for ATP and 140% for NAD.

SW620 Tumours

The methods of addition assay was also performed in replicates of 0.4 g wet weight of SW620 tumours to which aliquots of 25 mM ATP and 25 mM NAD were added as shown in Table 4.8.

	Volume added (µl)		Quantity added (µmoles/g of tissue)	
	25 mM ATP	25 mM NAD	ATP	NAD
Tube 1	0	0	0	0
Tube 2	40	16	2.5	1
Tube 3	80	32	5	2

Table 4.8: Volume of 25 mM ATP and 25 mM NAD added to 0.4g of SW620 tumour in the methods of addition assay.

The samples were then analysed as described in subsection 2.3.4, and representative spectra are shown in Figures 4.13 and 4.14

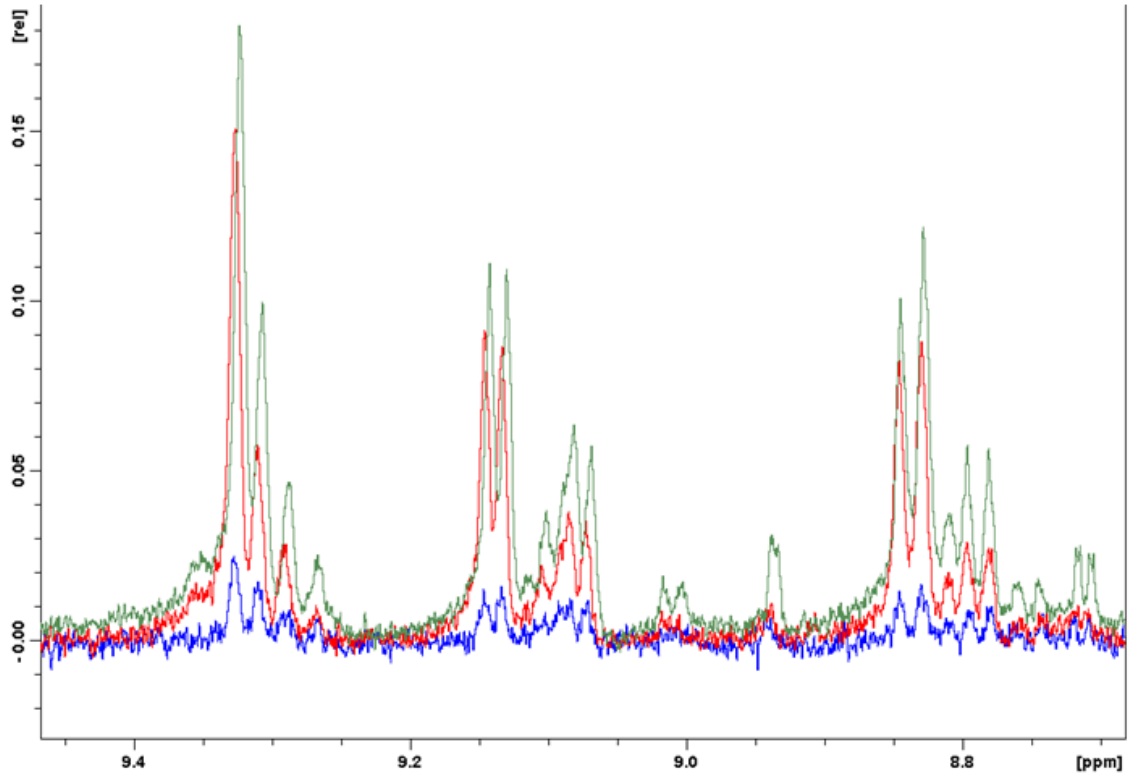

Figure 4.13: NAD region of 3 superimposed ^{1}H spectra of extracts of SW620 tumour (tube 1 in blue, tube 2 in red and tube 3 in green – see Table 4.8).

.

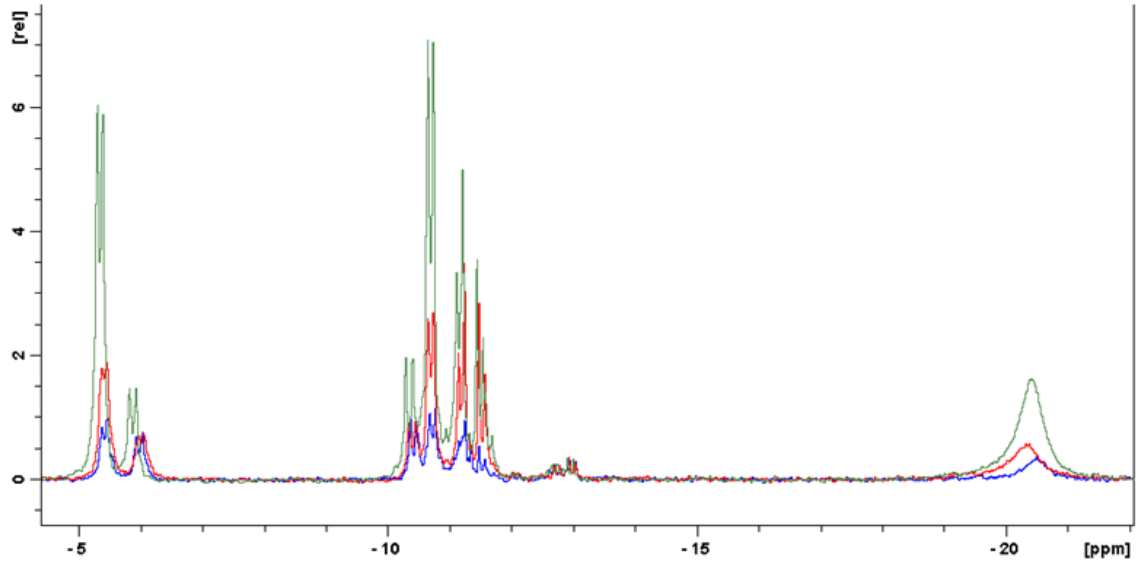

Figure 4.14: ATP region of 3 superimposed ^{31}P spectra of extracts of SW620 tumour (tube 1 in blue, tube 2 in red and tube 3 in green – see Table 4.8).

The results obtained for the method of addition assay in SW620 tumours are presented in Table 4.9 and linear regression analysis of the data in Figure 4.15.

	Expected concentration of added analyte (µmoles/g of tissue)		Measured analyte concentration (µmoles/g of tissue)	
	ATP	NAD	ATP	NAD
Tube 1	0	0	0.63	0.13
Tube 2	2.5	1	1.58	1.07
Tube 3	5	2	4.24	1.98
Estimated concentration of endogenous analyte			0.48	0.14
Extraction efficiency			72%	93%

Table 4.9: Expected and measured ATP and NAD concentrations in SW620 tumour extracts (samples prepared as shown in Table 4.10 and data derived from the spectra in Figures 4.13 and 4.14.

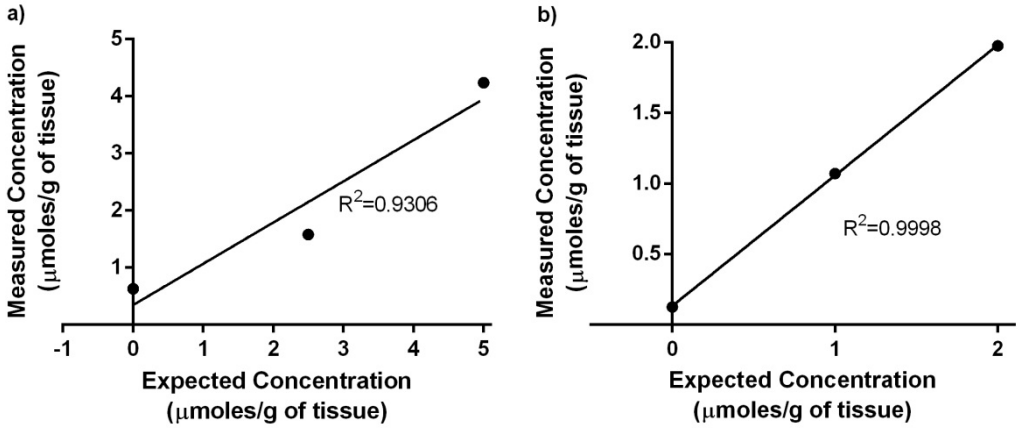

Figure 4.15: Linear regression analysis of expected and measured ATP (a) and NAD (b) concentrations in SW620 tumour extracts (data from Table 4.9).

From the linear regression analyses shown in Figure 4.18, the endogenous ATP concentration prior to addition of exogenous ATP was 0.48 µmoles/g of tissue.

In the case of NAD, the endogenous concentration was 0.14 µmoles/g of tissue (-0.05 to 0.4 within a 95% confidence interval). The extraction efficiency or recovery was 72% for ATP and 93% for NAD.

A2780 tumours

A procedure similar to that described in subsection 2.3.1 was followed using 0.3 g wet weight of A2780 tumour material. The standards used were a 25 mM solution of ATP and 2 mM NAD solution, and the volumes of the standard solutions used are presented in Table 4.10.

	Volume added (µl)		Quantity added (µmoles/g of tissue)	
	25 mM ATP	2 mM NAD	ATP	NAD
Tube 1	0	0	0	0
Tube 2	30	37.5	2.5	0.25
Tube 3	120	150	10	1

Table 4.10: Volume of 25 mM ATP and 2 mM NAD added to 0.3 g of A2780 tumour in the methods of addition assay.

The samples were analysed as described in subsection 2.3.4, and representative spectra are shown in Figures 4.16-4.17

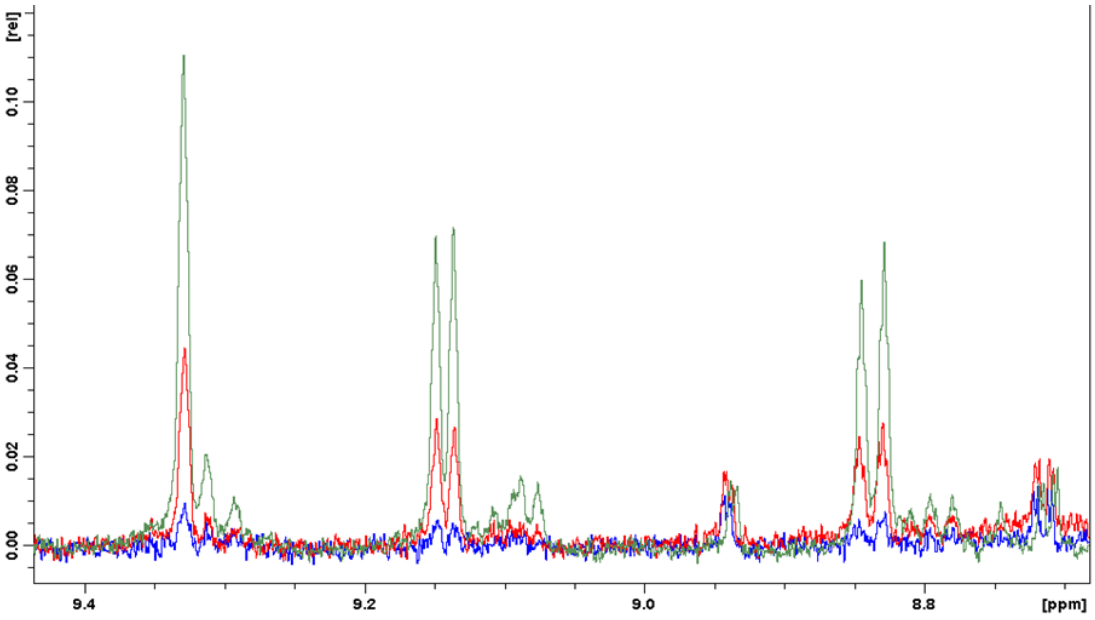

Figure 4.16: NAD region of 3 superimposed ^{1}H spectra of extracts of A2780 tumours (tube 1 in blue, tube 2 in red and tube 3 in green – see Table 4.10).

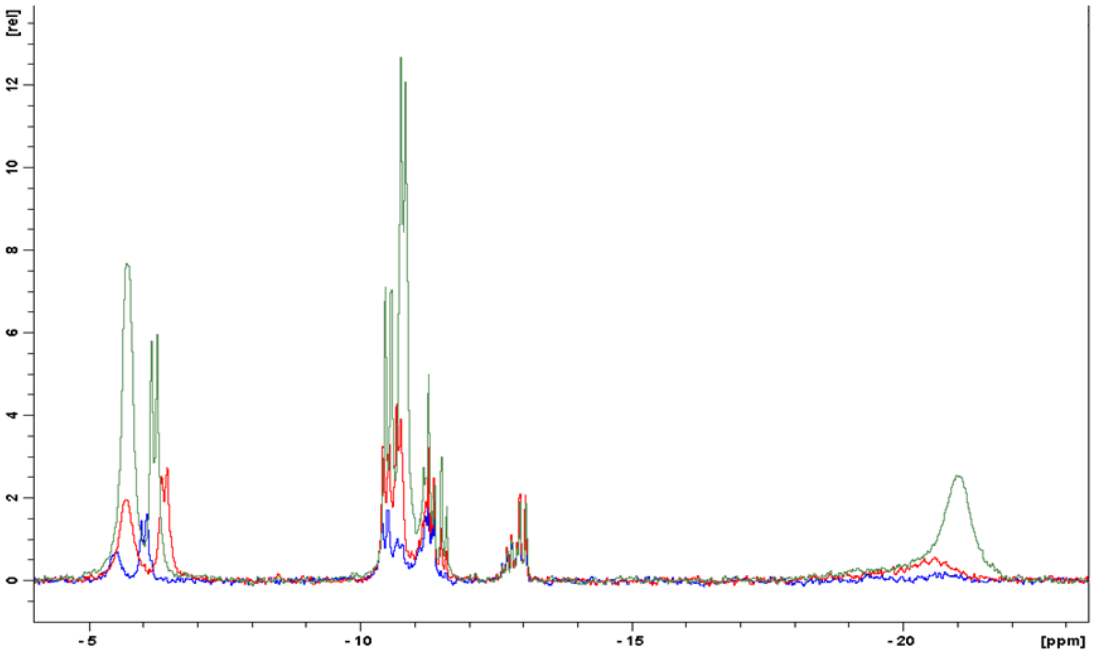

Figure 4.17: ATP region of 3 superimposed ^{31}P spectra of extracts of A2780 tumours (tube 1 in blue, tube 2 in red and tube 3 in green – see Table 4.10) from A2780 tumours in the methods of addition.

The results obtained are presented in Table 4.11 and linear regression analysis of the data in Figure 4.18.

	Expected concentration of added analyte (µmoles/g of tissue)		Measured analyte concentration (µmoles/g of tissue)	
	ATP	NAD	ATP	NAD
Tube 1	0	0	0.34	0.02
Tube 2	2.5	0.25	1.35	0.2
Tube 3	10	1	4.62	0.55
Estimated concentration of endogenous analyte			0.73	0.081
Extraction efficiency			43%	51%

Table 4.11: Expected and measured ATP and NAD concentrations in A2780 tumour extracts (samples prepared as shown in Table 4.8 and data produced from the spectra in Figures 4.13 and 4.14).

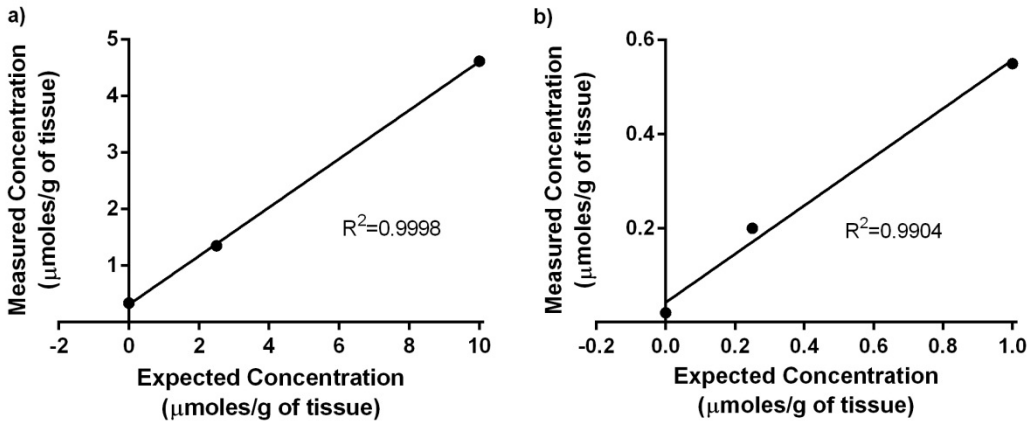

Figure 4.18: Linear regression analysis of expected and measured ATP (a) and NAD (b) concentrations in A2780 tumour extracts (data from Table 4.11).

From the linear regression analyses shown in Figure 4.18, the endogenous ATP concentration prior to addition of exogenous ATP was 0.73 μmoles/g of tissue (-0.35 to 2.17 within a 95% confidence interval). In the case of NAD, the endogenous concentration was 0.081 μmoles/g of tissue, and the extraction efficiency or recovery was 43% for ATP and 51% for NAD.

4.2.2 The effect of rucaparib, temozolomide and rucaparib combined with temozolomide treatment on NAD and ATP concentrations in the liver of PARP1 WT and PARP1 KO mice assessed by $^{1}H/^{31}P$-MRS

Experiments were performed as described in section 2.7, to identify the impact of PARP1 expression on NAD and NTP concentrations in the liver of mice by comparison of data from PARP1 WT and KO (i.e. null) mice.

The hypothesis is that PARP inhibition will cause a rise in NAD levels, temozolomide action will lead to a PARP activation, hence a decrease in NAD levels and the combination will have a balancing effect in NAD levels. Whether the NAD changes depend on the mice genotype is also an object of the study.

Groups of PARP1 WT and PARP1 KO mice were treated as summarized in Table 4.12.

Treatment groups and route of administration	PARP1 WT (n)	PARP1 KO (n)
Control	7	5
1 mg/kg rucaparib (*i.p.*)	6	4
68 mg/kg temozolomide (orally)	5	5
1 mg/kg rucaparib (*i.p.*) + 68mg/kg temozolomide (orally)	6	4

Table 4.12: Treatment groups and the number (n) of PARP1 WT and PARP1 KO mice studied.

Mice were treated daily for 5 days, and 1 hour after treatment on day 5 an *in vivo* liver MRS study was performed as described in section 2.7. However, the resulting data are not shown due to the poor quality of the spectra. Possible reasons for the poor quality and poor SNR are that the coil was optimized for tumour not liver imaging and that it was not tunable (no variable capacitors). ISIS uses adiabatic pulses, however the pulse width was not calibrated using tumours and the surface of the coil is limited, reducing quality of the acquired spectra. Following MRS, livers were then freeze-clamped, removed and placed

in liquid nitrogen, prior to PCA extraction and analysis by high resolution ^{1}H and ^{31}P spectroscopy as described in subsection 2.3.4.

Figure 4.19 shows the NAD concentrations per gram of liver wet weight for control and rucaparib, temozolomide and rucaparib combined with temozolomide treated PARP1 WT and KO mice.

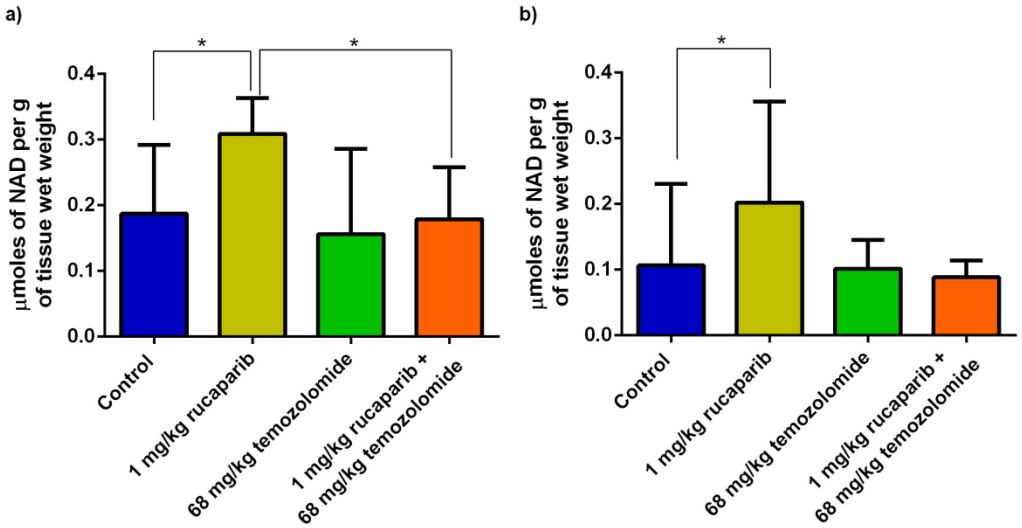

Figure 4.19: Effect of daily x5 treatment with 1 mg/kg rucaparib, 68 mg/kg temozolomide, or 1 mg/kg rucaparib combined with 68 mg/kg temozolomide on the concentration of NAD in the livers of a) PARP1 WT and b) PARP1 KO mice. The median with inter-quartile range of concentrations is shown and the groups sizes are given in Table 4.12. The * indicate a statistically significant difference.

Performing a Mann-Whitney (non-paired) t-test on the data for the PARP1 WT mice, generated a p value of 0.065 for the difference between the control and 1 mg/kg rucaparib treated mice. The p value for the difference between the NAD concentrations in the livers of the 1 mg/kg rucaparib and 1 mg/kg rucaparib combined with 68 mg/kg temozolomide treated mice is 0.03, i.e. a statistically significant difference at the 5% level. None of the other differences between the groups were statistically significant. Furthermore, there were no statistically significant differences when the data for the PARP1 WT mouse livers were analysed using a one-way ANOVA analysis.

Applying the Mann-Whitney (non-paired) t-test to the data from PARP1 KO mice, the only statistically significant difference was between 1 mg/kg rucaparib and 1 mg/kg rucaparib combined with 68 mg/kg temozolomide (p value 0.032). A one-way ANOVA evaluation of the data from the livers of PARP1 KO mice demonstrated statistically significant differences between the 1 mg/kg rucaparib

and 68 mg/kg temozolomide groups, and between 1 mg/kg rucaparib and 68 mg/kg temozolomide treated groups, both with a p value of 0.043.

These experiments demonstrated that there are higher levels of NAD in the livers of mice after 1mg/kg rucaparib treatment regardless of PARP1 gene status and higher baseline concentrations of NAD in the livers of PARP1 WT mice than in the livers of PARP1 knockout mice.

Figure 4.20 shows the NDP to NTP concentration ratios for extracts of both PARP1 WT and KO livers.

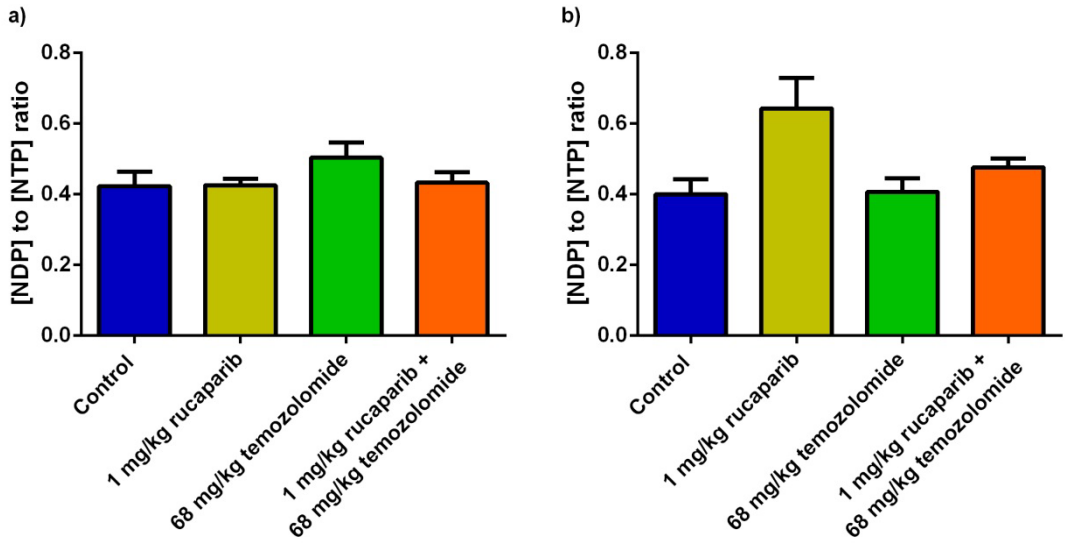

Figure 4.20: Effect of 1 mg/kg rucaparib, 68 mg/kg temozolomide and 1 mg/kg rucaparib plus 68 mg/kg temozolomide treatment on the ratio of NDP to NTP concentrations in a) PARP1 WT livers and b) PARP1 KO livers. The median with inter-quartile range of concentrations is shown.

Statistical analysis (Mann-Whitney non-paired t-test or one-way ANOVA) of the NDP to NTP concentration ratios in the livers of PARP1 WT mice showed that there is not a statistically significant difference between the treatment groups. In the extracts of livers from PARP1 KO mice one-way ANOVA demonstrated significant differences between the NDP/NTP ratio in control and 1 mg/kg rucaparib; between 1 mg/kg rucaparib and 68 mg/kg temozolomide, and between 1 mg/kg rucaparib and 1 mg/kg rucaparib combined with 68 mg/kg temozolomide treatments (one-way ANOVA p=0.019). The difference between the 1 mg/kg rucaparib and 68 mg/kg temozolomide groups was confirmed using the Mann-Whitney test (p=0.03).

Thus the NDP/NTP ratio is higher following treatment with 1 mg/kg rucaparib in the livers of PARP1 KO but not PARP1 WT mice.

In Figure 4.21, the ratio between the Pi and NTP concentrations in extracts of livers from PARP1 WT and PARP1 KO mice is depicted.

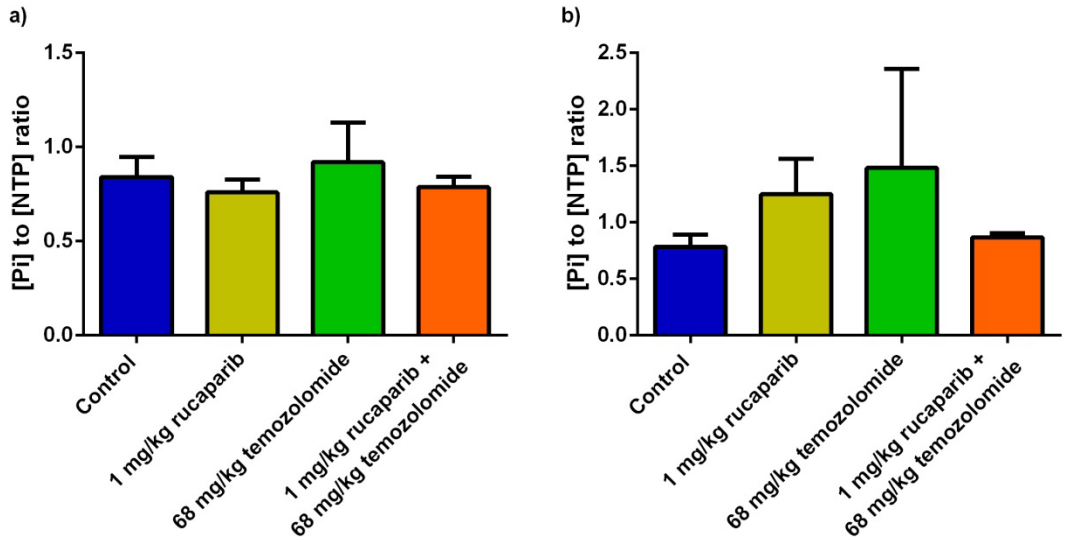

Figure 4.21: Effect of 1 mg/kg rucaparib, 68 mg/kg temozolomide and 1 mg/kg rucaparib plus 68 mg/kg temozolomide treatment on the ratio of Pi /NTP concentrations in liver extracts of a) PARP1 WT and b) PARP1 KO mice. The median with inter-quartile range of concentrations is shown.

Statistical analysis of the data did not reveal any significant differences between the Pi to NTP ratios following treatment with rucaparib, temozolomide or a combination of rucaparib and temozolomide in extracts of livers regardless of PARP1 gene status.

According to Nijsten and van Dam (2009) elevated lactate levels and local acidosis are characteristic of many tumours and more pronounced acidosis is associated with invasive potential, as it believed that the local lactic acidosis degrades the stroma surrounding the cancer by inducing apoptosis and necrosis in the non-malignant cells (Nijsten and van Dam, 2009).

Figure 4.22 summarizes lactate concentrations, an anaerobic by-product of glycolysis, in the extracts of livers from PARP1 WT or KO mice after 5 days treatment with 1 mg/kg rucaparib, 68 mg/kg temozolomide or the combination of 1 mg/kg rucaparib and 68 mg/kg temozolomide.

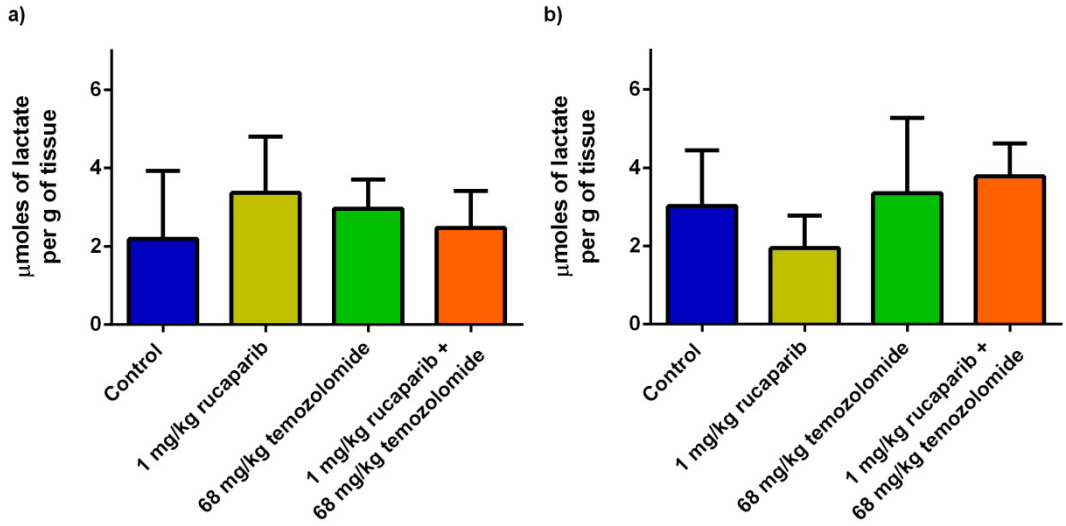

Figure 4.22: Effect of 1 mg/kg rucaparib, 68 mg/kg temozolomide and 1 mg/kg rucaparib plus 68 mg/kg temozolomide treatment on the concentration of lactate per gram of tissue in extracts of liver from a) PARP1 WT and b) PARP1 KO mice. The median with inter-quartile range of concentrations is shown.

Mann-Whitney (non-paired) t test and one-way ANOVA analysis of the data from the PARP1 WT mice did not reveal any statistically significant differences in lactate concentration. In the PARP1 KO mice, although one-way ANOVA did not demonstrate any statistically significant differences, the Mann-Whitney test showed that liver extracts from 1 mg/kg rucaparib-treated mice had significantly lower lactate concentrations than the 68 mg/kg temozolomide treated mice ($p=0.03$).

4.3 Discussion

4.3.1 The effect of rucaparib, temozolomide and rucaparib combined with temozolomide treatment on NAD and ATP concentrations assessed by in vitro $^{1}H/^{31}P$ MRS

The methods of addition procedure developed demonstrated higher recovery of NAD (77-90%) than for ATP (36-49%), in the two cell lines studied. Assuming that 10^6 cells have a volume of 1µl the concentrations of ATP and NAD produced from the methods of addition in SW620 cell extracts can be converted from 2.8 nmoles/10^6 cells and 0.38 nmoles/10^6 cells into approximately 2.8 mM ATP and 0.38 mM NAD. These values are consistent with the literature where ATP concentrations in cells are reported to range from 1-10 mM (Beis and Newsholme, 1975), and NAD concentration in cells to be around 0.3 mM (Yamada *et al.*, 2006; Yang *et al.*, 2007).

For the treatment of cells with rucaparib, temozolomide, or rucaparib and temozolomide, the concentrations used were based on previous data and were GI_{50} (concentration to produce 50% growth inhibition) values for temozolomide and a concentration of rucaparib (0.1 µM) known to produce temozolomide sensitization (Huw Thomas, Lan-zhen Wang, NICR, personal communication). In the A2780 cell line treatment of the cells with rucaparib appeared to increase the NAD levels. However, although treatment with temozolomide would be expected to create DNA damage and activate PARP thereby utilising NAD, there was no obvious change in cellular NAD concentration following temozolomide treatment. The combination treatment appeared to produce an intermediate effect on the NAD concentration. However, replicate experiments were not performed in A2780 cells and hence statistical analysis could not be performed. Furthermore, studies should be extended to SW620 cells.

4.3.2 The effect of rucaparib, temozolomide and rucaparib combined with temozolomide treatment on NAD and ATP concentrations in mouse liver and human tumour xenografts assessed by $^{1}H/^{31}P$ MRS

The methods of addition procedure was also successfully applied to mouse liver with recovery rates of 69% for ATP and 140% for NAD. For ATP, the estimated amount of ATP in the liver was 1.46 µmoles/g of tissue. Considering that 1g tissue wet weight is approximately equivalent to 1ml, then 1.46 µmoles/g of

tissue ATP concentration is equivalent to 1.46 mM. Iles *et al.* (1985) studied phosphorylation status of liver by ^{31}P-MRS in rats and reported a concentration of 2.80 mM ATP (Iles *et al.*, 1985). Similar experiments have been published by Corbin *et al.* (2003) and hepatic ATP concentrations of 3.04 mM reported (Corbin *et al.*, 2003). The estimated NAD concentration in the liver was 1.35 μmoles/g of tissue which equates to 1.35 mM NAD. There must be some uncertainty about the absolute concentration in the current assay, given the calculated extraction efficiency is not feasible, at 140%. According to Brosnan *et al.* (1970), in studies performed to assess effects of ischaemia on metabolite concentrations in rat liver the NAD concentration was 0.83 μmoles/g wet weight (Brosnan *et al.*, 1970).

Application of the assay to the analysis of extracts of livers of PARP1 WT or PARP1 KO mice removed after 5 daily treatments with rucaparib, temozolomide or a combination of rucaparib and temozolomide demonstrated that rucaparib treatment increases NAD concentrations presumably due to reduced utilization; however the effect was only significant in the PARP1 KO mouse liver extracts.

The ADP to ATP ratio has been reported to be an indicator of cell viability (Bradbury *et al.*, 2000), and the ratio between inorganic phosphate and NTP used to measure the metabolic status in the livers (Kimura *et al.*, 1994). However, in the current study none of the treatments investigated affected the Pi/βNTP ratio or the NDP/NTP ratio in either PARP1 WT or PARP1 KO mouse liver extracts.

The lactate results show a lactate level in the 1 mg/kg rucaparib group that was 45% lower than in the 68 mg/kg temozolomide group in PARP1 KO mice, but no significant differences in the PARP1 WT group.

The methods of addition for the analysis of NAD and ATP concentrations was also successfully applied to the analysis of concentrations in A2780 and SW620 human tumour xenografts grown in immune-deprived mice. In the literature, ATP concentrations in viable (non-necrotic) tumour is 1.9 mM (Walenta *et al.*, 1992) while the values from the experiment described in this chapter were 0.73 μmoles/g of tissue and 0.48 μmoles/g of tissue for A2780 and SW620 tumours,

respectively. Regarding the NAD concentrations in the tumours, the values of the experiment described in this chapter were 0.081 μmoles/g of tissue and 0.14 μmoles/g of tissue for A2780 and SW620 tumours respectively which is different from the average 206 μM NAD concentration reported for A12B3 sarcoma tumours, measured by HPLC (Ohlson *et al.*, 1995). The difference in the tumour type could be the reason for that discrepancy.

Unfortunately, there was insufficient time to investigate the effect of rucaparib, temozolomide and rucaparib plus temozolomide combination treatment on tumour NAD and ATP concentration, although a some preliminary results will be presented in chapter 6 in relation to the *in vivo* MRS data.

Overall, the method of addition has been proven feasible, however the recovery rates were variable depending on the sample. Application of the assay to study the effects of treatment with rucaparib, temozolomide, and rucaparib combined with temozolomide in cells has been proven not only feasible, but a preliminary experiment also generated results consistent with NAD elevation due to PARP inhibition.

Studies in PARP1 WT and KO mouse liver extracts again demonstrated that the assay methodology was applicable, generating results consistent with the literature, and suggestive that NAD levels are influenced by PARP1 genotype and rucaparib administration, although further experiments are required.

Chapter 5. Results – An evaluation of the utility of [^{18}F]FDG- and [^{18}F]FLT-PET as surrogate response biomarkers for PARP inhibitors

There are several examples in the literature of PET studies where both [^{18}F]FDG and [^{18}F]FLT have been used in the assessment of post-treatment changes in the glycolytic and proliferative status of tumours. In 2010, Honer *et al.* published data for several tumour models where [^{18}F]FDG and [^{18}F]FLT uptake changes induced by the rapamycin-based mTOR inhibitor everolimus were studied. The results of this study showed that the allosteric mTOR inhibitor everolimus decreased the [^{18}F]FDG and [^{18}F]FLT uptake in tumours after treatment (Honer *et al.*, 2010).

Munk Jensen *et al.* (2010) also used [^{18}F]FDG and [^{18}F]FLT for the early detection of response to the mTOR inhibitor Top216 in A2780 human ovary cancer xenografts grown in mice (A2780). In this study mice underwent [^{18}F]FDG- or [^{18}F]FLT-PET scanning 18 hours before treatment (baseline), 6 hours after treatment (t = 6h), 24 hours (t = 24h) after a second treatment on day 2 and at 72 hours (t = 5 days). The results of this experiment showed a rapid and significant decrease in cell proliferation at early time points. However, on day 5 the [^{18}F]FLT uptake in the treated group was comparable to the control group suggesting that the proliferative capacity of the tumour had recovered. Since the [^{18}F]FLT uptake did not change over the 5 days in the control group the anti-proliferative effect of Top216 was established. There was a small but significant decrease in [^{18}F]FDG uptake at 6 hours, and on day 1 and day 5, i.e. in the treated groups the [^{18}F]FDG uptake remained lower than in the control group where the [^{18}F]FDG uptake increased over the experiment. Overall, this study concluded that [^{18}F]FLT is superior to [^{18}F]FDG in the assessment of early response to treatment with the mTOR inhibitor Top216 (Munk Jensen *et al.*, 2010).

Moroz *et al.* (2011) followed a similar approach by using [^{18}F]FDG and [^{18}F]FLT to study the response of colon cancer xenografts to treatment with the aurora B kinase inhibitor AZD1152. In this study HCT116 and SW620 tumours were used. HCT116 xenografts responded more rapidly and to a greater extent with marked decreases in [^{18}F]FDG and [^{18}F]FLT uptake in the treated groups

associated with decreases in tumour volumes over time. In contrast SW620 xenografts continued to grow during treatment, and the growth rate only decreased after three cycles of treatment. The authors reported that sequential [^{18}F]FDG-PET showed no significant difference between treated and untreated mice throughout the experiment in SW620 tumours, suggesting that the treatment did not interfere with glucose utilization, whereas SW620 xenografts showed very little or no accumulation of [^{18}F]FLT above background levels. The authors concluded that [^{18}F]FLT-PET can be used as a surrogate response biomarker in HCT116 xenografts but not in SW620 tumours, suggesting that SW620 cells predominantly use the *de novo* rather than the salvage pathway to generate thymidine nucleotides for DNA synthesis (Moroz *et al.*, 2011).

One final example, published by Corroyer-Dulmont *et al.* (2012), involved DCE-MRI, [^{18}F]FDG- and [^{18}F]FLT-PET studies to investigate tumour response to the anti-angiogenic drug bevacizumab, the alkylating agent temozolomide, and a combination of bevacizumab with temozolomide in glioblastoma xenografts. The use of a cytotoxic treatment with a vascular targeting molecule resulted in both anti-vasculature and direct anti-tumour effects. The results of this study, once more, showed that [^{18}F]FLT-PET was a superior surrogate response biomarker to [^{18}F]FDG-PET (Corroyer-Dulmont *et al.*, 2012). The use of [^{18}F]FDG- and [^{18}F]FLT-PET has been reviewed by Perumal *et al.* (2012).

The preclinical Positron Emission Tomography (PET) studies described in this chapter were performed to examine the potential value of PET as a surrogate response biomarker following treatment with rucaparib and/or temozolomide. The tracers used were [^{18}F]FDG, an indicator of tumour metabolism, and [^{18}F]FLT as a measure of proliferation.

5.1Treatment groups and imaging protocol

The treatment groups and the imaging protocols were the same for both the [^{18}F]FDG and [^{18}F]FLT experiments and the studies were performed as described in section 2.8.

Once tumours had grown to approximately 5 by 5 millimetres the mice were randomly assigned to four treatment groups:

- Control (no injection);
- 1 mg/kg of rucaparib (10 ml/kg of a 0.1 mg/ml solution in water for injection);
- 68 mg/kg of temozolomide (10 ml/kg of a 6.8 mg/ml solution in saline);
- 1 mg/kg of rucaparib combined with 68 mg/kg of temozolomide (10 ml/kg of a 0.1 mg/ml solution in water for injection with 10 ml/kg of a 6.8 mg/ml solution in saline).

The mice were treated and tumour volumes were measured once a day for five days. On day five the mice were treated and the PET scan performed one hour later. The PET scan lasted for one hour, after which mice recovered and were monitored for up to 100 days, or until the tumours reached a size that required killing on the basis of animal welfare considerations. All the PET image analysis was performed by Ian Wilson using the Imalytics software package from Philips, as described in section 2.8.

As in previous chapters, the dose of rucaparib (1 mg/kg) used in this experiment has previously been shown to result in extensive PARP inhibition and, when used in combination with temozolomide, marked chemopotentiation. The dose of temozolomide used (68 mg/kg) equates to the routine daily dose of the drug in patients (~ 200 mg/m^2) (Calabrese *et al.*, 2003; Thomas *et al.*, 2007).

5.2 Metabolic changes in A2780 human tumour xenografts following treatment with rucaparib, temozolomide or rucaparib combined with temozolomide as assessed with [^{18}F]FDG-PET

Only A2780 tumour bearing mice were scanned using [^{18}F]FDG because preliminary tests in SW620 tumours showed very limited uptake of the tracer (Ian Wilson, personal communication).

Mice were injected with an average of 10 MBq (range of activities from 9 MBq to 16 MBq) of [^{18}F]FDG and scanned for one hour. The number of imaged mice, n, per group was:

- Control: n=3;
- 1 mg/kg rucaparib: n = 3
- 68 mg/kg temozolomide: n = 3
- 1 mg/kg rucaparib combined with 68 mg/kg temozolomide: n = 5.

5.2.1 Effect of drug treatment on A2780 tumour growth

Tumour volumes were measured before and after the PET scan (see section 2.8), and tumour growth data from both the [^{18}F]FDG- and [^{18}F]FLT-PET studies were combined. In both experiments the treatment procedure was exactly the same, and the total number of treated and measured mice in each group was :

- Control n = 8;
- 1 mg/kg rucaparib n = 8;
- 68 mg/kg temozolomide n = 8;
- 1 mg/kg rucaparib combined with 68 mg/kg temozolomide n = 10.

The time taken for individual tumours to reach a relative tumour volume 4 times that of the volume on the day of the first treatment (time to RTV4) is shown in Figure 5.1 and the data are presented in detail in Table 5.1.

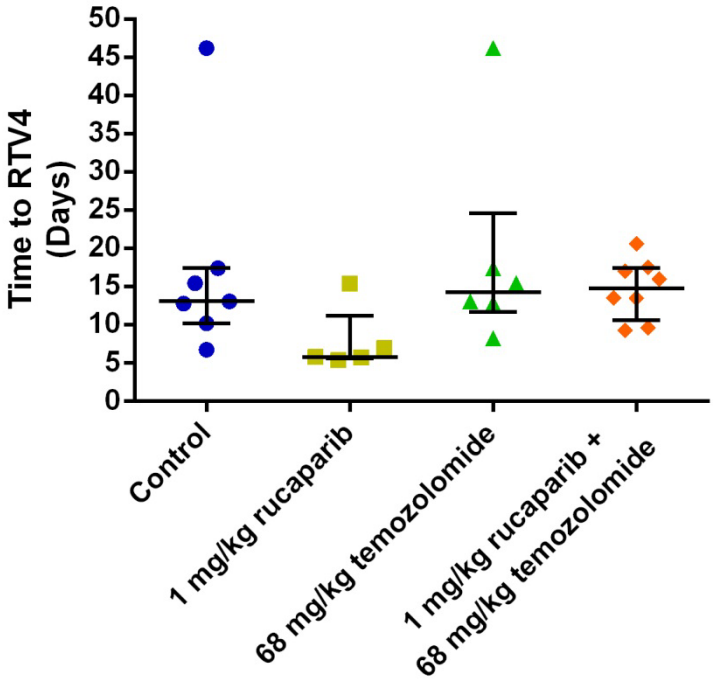

Figure 5.1: Effect of 1 mg/kg rucaparib, 68 mg/kg temozolomide or 1 mg/kg rucaparib plus 68 mg/kg temozolomide on A2780 tumour growth. Points are the individual mice, lines are the median and the error bars the inter-quartile range.

Group	Median time to RTV4 (range) in days	Tumour growth delay (days)
Control	13 (7-46)	–
1 mg/kg rucaparib	6 (5-15)	-7
68 mg/kg temozolomide	14 (8-46)	+1
1 mg/kg rucaparib + 68 mg/kg temozolomide	15 (9-21)	+2

Table 5.1: Median time to reach a tumour volume of RTV4 and tumour growth delay in A2780 tumour-growth following daily x5 treatment with rucaparib, temozolomide or rucaparib plus temozolomide.

The time to RTV4 data presented in Figure 5.1 and Table 5.1 were subjected to statistical evaluation using one-way ANOVA and Mann-Whitney (non-parametric t test) analyses. The one-way ANOVA did not demonstrate any significant differences between the groups ($p > 0.05$). The Mann-Whitney test did reveal significant differences and the p values are presented in Table 5.2. Thus treatment with 1 mg/kg rucaparib appears to result in accelerated tumour growth, while neither temozolomide alone or in combination with rucaparib had significant activity.

	1 mg/kg rucaparib	68 mg/kg temozolomide	1 mg/kg rucaparib + 68 mg/kg temozolomide
Control	0.048	0.77	0.67
1 mg/kg rucaparib		0.030	0.019
68 mg/kg temozolomide			0.81

Table 5.2: Mann-Whitney (non-paired t test) statistical analysis of the time to RTV4 data for A2780 tumour-bearing mice presented in Figure 5.1 and Table 5.1.

5.2.2 [^{18}F]FDG-PET images in A2780 tumour bearing mice

Figure 5.2 shows representative [^{18}F]FDG-PET images (axial slices through the animal) of a control A2780 tumour-bearing mouse compared with an A2780 tumour-bearing mouse treated with rucaparib. These images are from 60 minutes after [^{18}F]FDG injection and a lower uptake in the 1 mg/kg rucaparib treated tumour is suggested.

a) b)

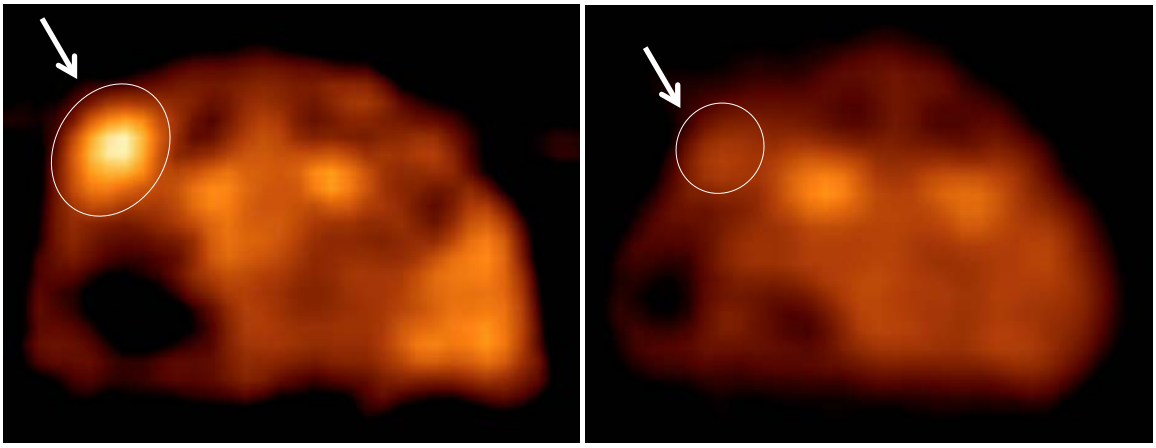

Figure 5.2: [^{18}F]FDG-PET scans of a) a control A2780 tumour bearing mouse, b) a A2780 tumour-bearing mouse treated with 1 mg/kg rucaparib daily x5. In both images the arrow indicates the tumour.

5.2.3 Effects of rucaparib, temozolomide and rucaparib combined with temozolomide treatment on [^{18}F]-FDG uptake in A2780 tumour-bearing mice

Mean Standardised Uptake Values [^{18}F]-FDG (SUV) were calculated as described in section 2.8 for A2780 tumours after 5x daily treatment with 1 mg/kg rucaparib, 68 mg/kg temozolomide or 1 mg/kg rucaparib and 68 mg/kg temozolomide. Figure 5.3 shows the dynamic SUV_{mean} data and Figure 5.4 the SUV_{mean} data from the 1 hour time point in the scan ($SUV_{mean@1h}$).

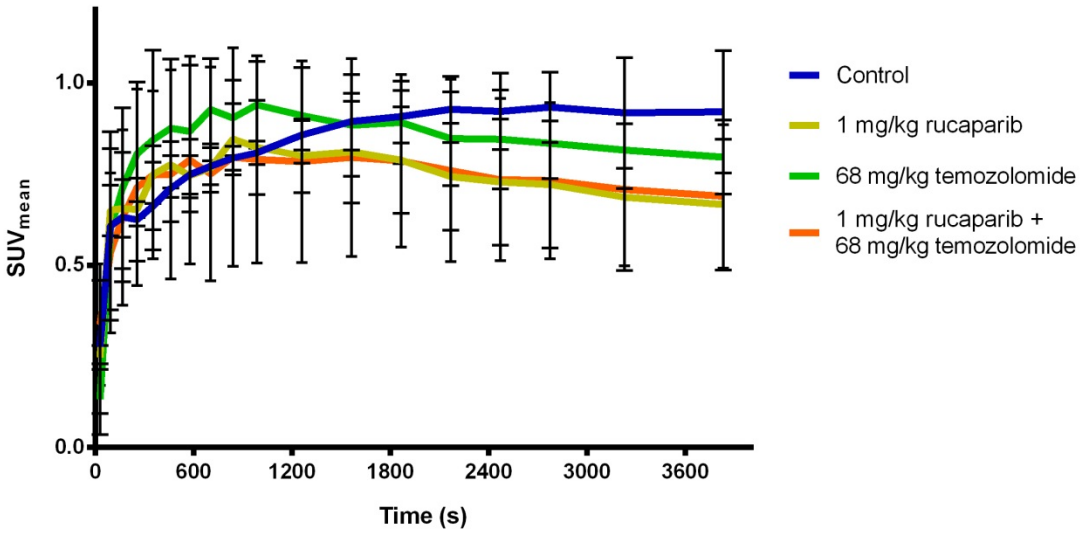

Figure 5.3: Mean tumour [^{18}F]FDG SUV *vs* time in A2780 tumour-bearing mice following 5 daily treatments with 1 mg/kg rucaparib, 68 mg/kg temozolomide or the combination of 1 mg/kg rucaparib with 68 mg/kg temozolomide. Points are the mean and the bars are the standard error.

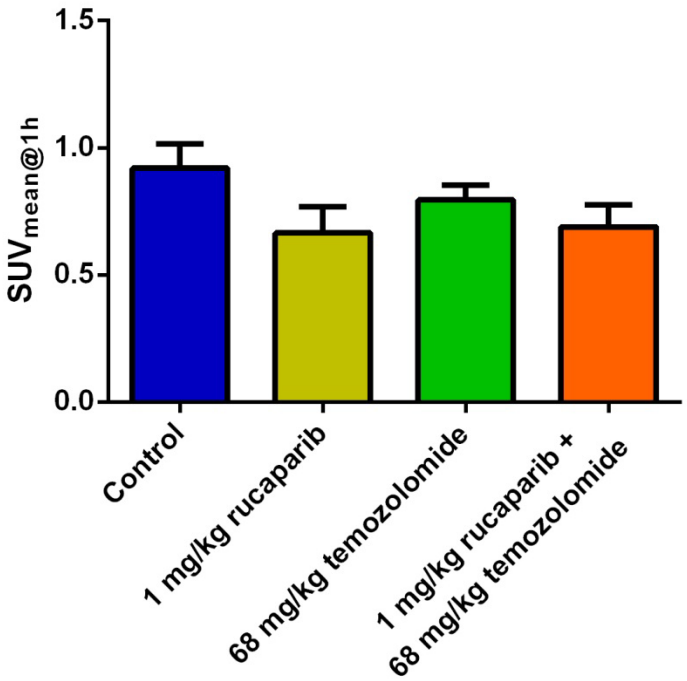

Figure 5.4: Mean tumour [^{18}F]FDG SUV with standard error (bars) one hour after tracer administration in A2780 tumour-bearing mice following 5 daily treatments with 1 mg/kg rucaparib, 68 mg/kg temozolomide or the combination of 1 mg/kg rucaparib with 68 mg/kg temozolomide.

In addition to the mean [^{18}F]FDG SUV in each tumour at each time point, the 0-60minute area under the mean SUV versus time curve was calculated and the data are presented in Figure 5.5 normalized to the mean SUV AUC_{1h} in the control untreated tumours.

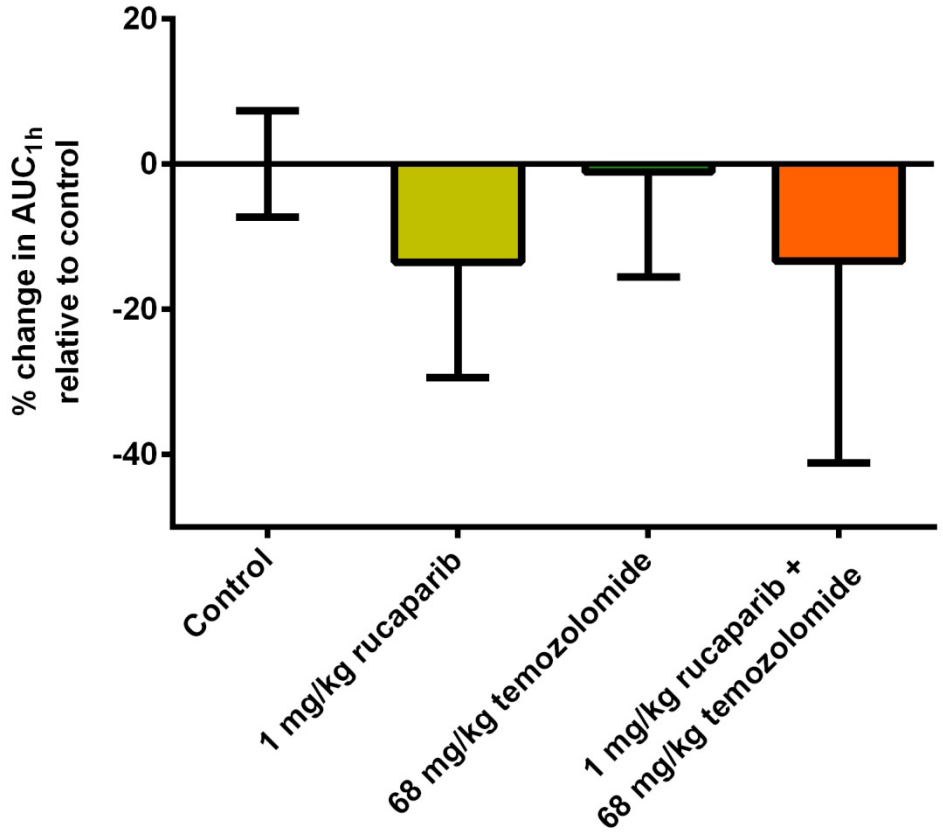

Figure 5.5: Percentage change with standard error (bars) relative to control in [^{18}F]FDG SUV AUC_{1h} following daily x5 treatment with 1 mg/kg rucaparib, 68 mg/kg temozolomide or the combination of 1 mg/kg rucaparib with 68 mg/kg temozolomide relative to control.

Table 5.3 presents results of a Mann-Whitney (non-paired t test) statistical analysis of the [^{18}F]FDG mean SUV values (data presented in Figure 5.3). There was a significant difference in the mean SUV between the 1 mg/kg rucaparib and 68 mg/kg temozolomide (p=0.0008) groups and between the 68 mg/kg temozolomide and the combination of 1mg/kg rucaparib with 68 mg/kg temozolomide groups. Thus rucaparib alone or in combination with temozolomide, reduced [^{18}F]FDG uptake whereas temozolomide alone did not.

	1 mg/kg rucaparib	68 mg/kg temozolomide	1 mg/kg rucaparib + 68 mg/kg temozolomide
Control	p=0.14	p=0.62	p=0.10
1 mg/kg rucaparib		p=0.0008	p> 0.99
68 mg/kg temozolomide			p=0.0001

Table 5.3 Statistical analysis (Mann-Whitney non-paired t test) of the [^{18}F]FDG SUV data presented in Figure 5.3 assessing the effect of rucaparib, temozolomide and rucaparib plus temozolomide treatment on the mean in A2780 tumour-bearing mice.

However, performing a one-way ANOVA with multiple comparisons between all the groups and using each group as a reference, no significant differences are found between the SUV_{mean} of any groups.

Applying the same statistical tests (one-way ANOVA and Mann-Whitney) to the $SUV_{mean@1h}$ data (for the one hour time point, i.e. static data only) there were also no significant differences between groups.

Overall, the groups treated with rucaparib appeared to show a small decrease in the uptake of the tracer [^{18}F]FDG when compared with the control and temozolomide alone groups. However, the analysis of data using the last time point ($SUV_{mean@1h}$) only generated different results from to those generated from the overall SUV_{mean} (0-1 hour period). Furthermore, the significance of the small effect of rucaparib on [^{18}F]FDG uptake that was observed was not demonstrated in all of the statistical analysis undertaken.
The uptake of [^{18}F]FDG was lower in the treated groups. However, it should be noted that in the 1 mg/kg rucaparib treated group, tumour growth was accelerated but the [^{18}F]FDG did not reflect that fact.

5.3 Proliferation changes in A2780 and SW620 human tumour xenografts following treatment with rucaparib, temozolomide or rucaparib combined with temozolomide as assessed with [^{18}F]FLT-PET

The [^{18}F]FLT-PET studies were performed to evaluate the potential of [^{18}F]FLT as a surrogate response imaging biomarker. [^{18}F]FLT-PET was performed after treatment with rucaparib, temozolomide or with a rucaparib and temozolomide in combination in both A2780 and SW620 tumour-bearing mice. The number of mice per group and the average and range of injected [^{18}F]FLT doses are summarized in Table 5.4

	Number of mice per treatment group		Average [^{18}F]FLT activity injected (range, MBq)	
	A2780	SW620	A2780	SW620
Control	3	3	10 (8-12)	11 (8-13)
1 mg/kg rucaparib	3	5		
68 mg/kg temozolomide	2	3		
1 mg/kg rucaparib + 68 mg/kg temozolomide	3	3		

Table 5.4: Number of mice *per* treatment group and [^{18}F]FLT activities injected in A2780 and SW620 tumour-bearing mice.

[^{18}F]FLT-PET scanning was performed 1 hour after the last one of a daily x5 treatment protocol as described in section 2.8.

The amount of activity injected is variable due to factors such as initial activity in the syringe prior to injection and length of the cannulation tube.

5.3.1 Effects of drug treatment on tumour growth

The effects of treatment with 1 mg/kg rucaparib, 68 mg/kg temozolomide or 1 mg/kg rucaparib and 68 mg/kg temozolomide on the tumour growth of A2780 tumours was presented in subsection 5.2.1. For the tumour growth study in SW620 tumours, all the groups had 18 mice apart from the control group which contained 20 mice.

The time taken for individual tumours to reach a relative tumour volume 4 times that of the volume on the day of the first treatment volume (time to RTV4) is shown in Figure 5.6 and the data are presented in detail in Table 5.5.

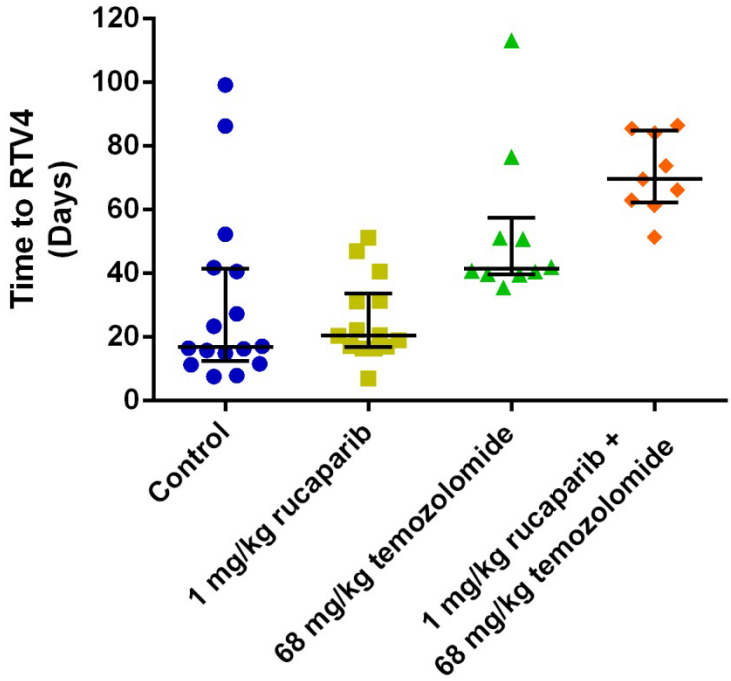

Figure 5.6: Effect of 1 mg/kg rucaparib, 68 mg/kg temozolomide or 1 mg/kg rucaparib plus 68 mg/kg temozolomide on SW620 tumour growth. Points are the individual mice, lines are the median and the error bars the inter-quartile range.

Group	Median time to RTV4 (range) in days	Tumour growth delay (days)
Control	17 (8-99)	–
1 mg/kg rucaparib	21 (7-51)	+4
68 mg/kg temozolomide	41 (36-113)	+24
1 mg/kg rucaparib + 68 mg/kg temozolomide	70 (51-87)	+53

Table 5.5: Median time to reach a tumour volume of RTV4 and tumour growth delay in SW620 tumour-bearing mice following daily x5 treatment with rucaparib, temozolomide or rucaparib plus temozolomide.

Analysis of the data in Figure 5.6 (Mann-Whitney non-paired t test) demonstrated a statistically significant difference between all the groups apart from the between control and 1mg/kg rucaparib treated animals (Table 5.6). A one-way ANOVA with multi-comparisons between all groups also demonstrated a statistical difference between all groups apart from the control and 1mg/kg rucaparib groups, and the 68mg/kg temozolomide and 1mg/kg rucaparib plus 68mg/kg temozolomide groups. In all the other comparisons the p value was < 0.0001.

	1 mg/kg rucaparib	68 mg/kg temozolomide	1 mg/kg rucaparib + 68 mg/kg temozolomide
Control	p = 0.602	p = 0.017	p = 0.0014
1 mg/kg rucaparib		p = 0.0015	p < 0.0001
68 mg/kg temozolomide			p = 0.0133

Table 5.6: Statistical analysis (Mann-Whitney non-paired t test) of the effect of rucaparib, temozolomide or rucaparib plus temozolomide treatment on tumour growth in SW620 tumour-bearing mice. Data analysed and the time to RTV4 values are from Figure 5.6 and Table 5.5.

5.3.2 [^{18}F]-FLT images

Figure 5.7 shows [^{18}F]FLT-PET scan images of a control A2780 tumour-bearing animal in comparison with an A2780 tumour-bearing mouse treated with temozolomide. Three time points are shown: 1, 10 and 60 minutes after [^{18}F]FLT injection. The top row, Figure 5.9 a), b) and c), shows the distribution of [^{18}F]FLT in the control mouse, while in the second row, Figure 5.9 d), e) and f), scans at the same time points are shown for a mouse treated with 68 mg/kg temozolomide daily for 5 days. For the first time point (Figure 5.7, a and d) the image reveals [^{18}F]FLT in the heart and kidneys. At 10 minutes the [^{18}F]FLT is distributed throughout the body and starting to accumulate in the bladder. By 60 minutes the tumour has retained more radioactivity than normal tissues, with the bladder the main site of FLT accumulation. Comparing Figure 5.9 c) and f) there is less [^{18}F]FLT uptake in tumour of the temozolomide-treated mouse when compared with the control mouse.

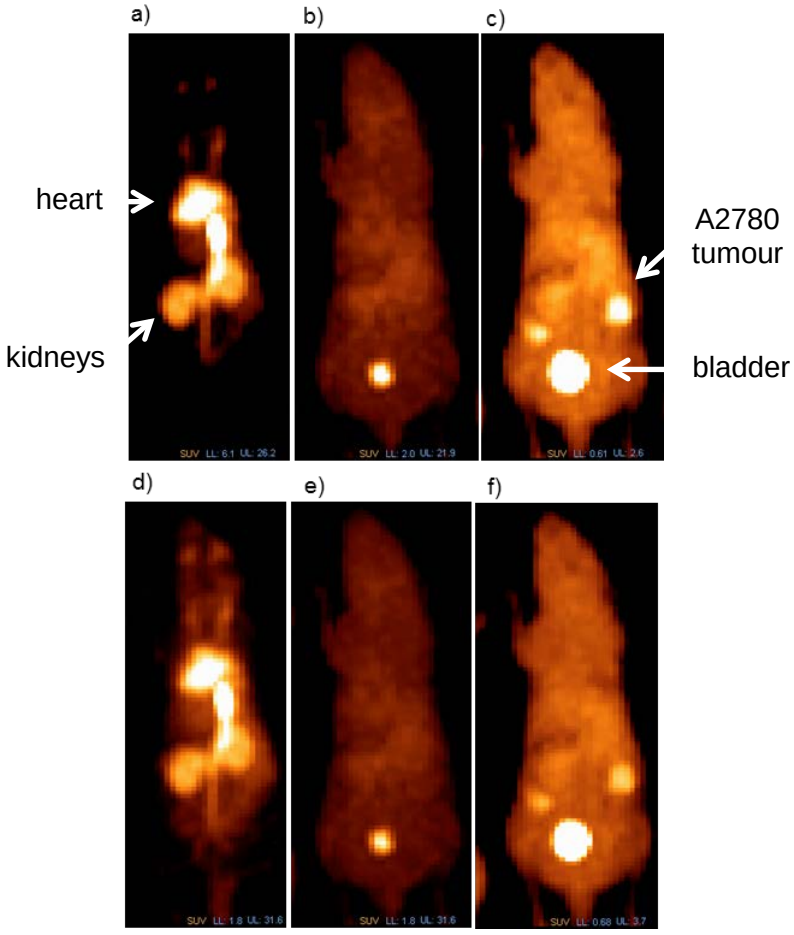

Figure 5.7: Representative images of an [^{18}F]FLT PET acquisition. Images a), b) and c) are from a mouse implanted with an A2780 tumour (control) and injected with 8.18 MBq of [^{18}F]FLT and collected 1, 10 and 60 minutes after [^{18}F]FLT injection. Images d), e) and f) are from a mouse implanted with an A2780 tumour and treated for 5 days with 68 mg/kg temozolomide, injected with 10.38 MBq of [^{18}F]FLT and collected 1, 10 and 60 minutes after [^{18}F]FLT injection.

Figure 5.8 shows [^{18}F]FLT-PET images of a control SW620 tumour-bearing animal in comparison with an SW620 tumour-bearing mouse treated with 1 mg/kg rucaparib combined with 68 mg/kg temozolomide. These images are from 60 minutes after the [^{18}F]FLT injection and the non-tumour tissue background in the control image does not allow the ready visualization of any differences. However, these images only show one slice of the tumour and hence have a merely illustrative role. The SUV is calculated over all the volume of the tumour and not only in the central slice.

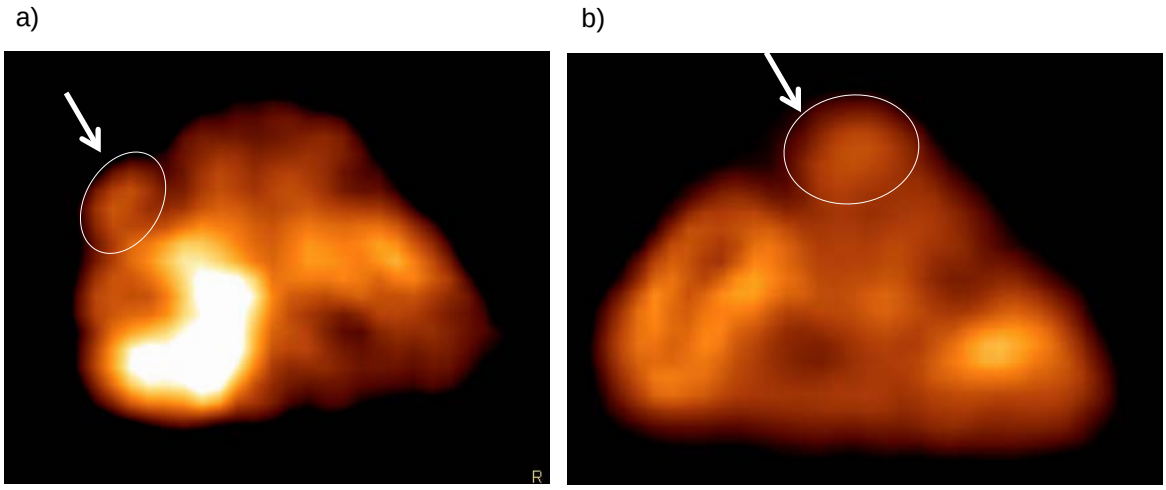

Figure 5.8: Representative images of an [^{18}F]FLT-PET acquisition scans of a) a control SW620 tumour-bearing mouse, b) A2780 tumour-bearing mouse treated daily x5 with 1 mg/kg rucaparib combined with 68 mg/kg temozolomide. In both images the arrow indicates the tumour.

5.3.3 Effects of rucaparib, temozolomide or rucaparib plus temozolomide treatment on [^{18}F]-FLT uptake in A2780 and SW620 tumour-bearing mice

Mean Standardised [^{18}F]-FLT Uptake Values (SUV) were calculated as described in section 2.8 for A2780 and SW620 tumours after 5x daily treatment with 1 mg/kg rucaparib, 68 mg/kg temozolomide or 1 mg/kg rucaparib combined with 68 mg/kg temozolomide. These calculations are performed by the software taking into account the injected activity, time of injection and the animal weight. The intended injectable activity (10 MBq) was general for all the treatment groups.

Figures 5.9 and 5.10 shows the dynamic SUV_{mean} data for A2780 and SW620 tumour-bearing mice, respectively, and Figures 5.11 and 5.12 the SUV_{mean} data for the 1 hour timepoint only ($SUV_{mean@1h}$).

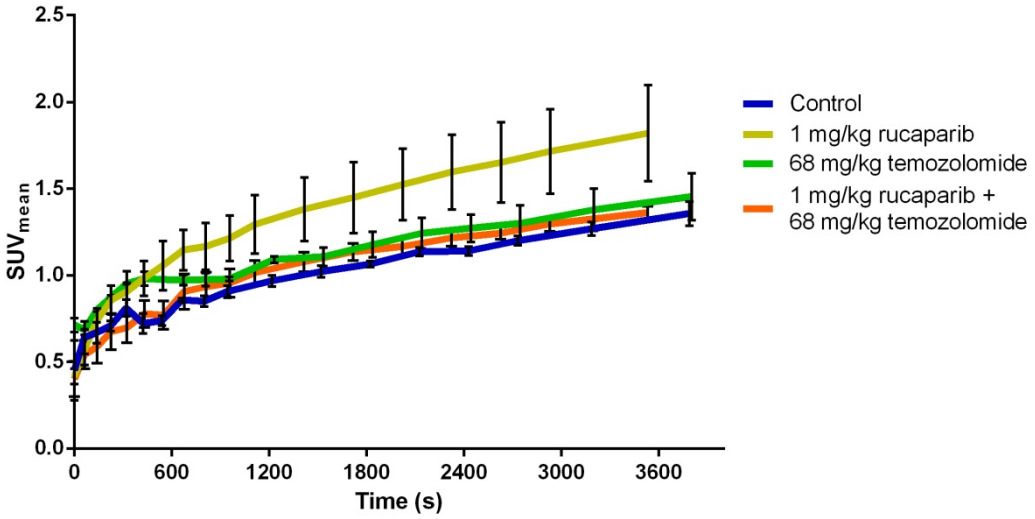

Figure 5.9: Mean tumour [^{18}F]FLT SUV *vs* time in A2780 tumour-bearing mice following 5 daily treatments with 1 mg/kg rucaparib, 68 mg/kg temozolomide or the combination of 1 mg/kg rucaparib with 68 mg/kg temozolomide. Points are the mean and the bars are the standard error.

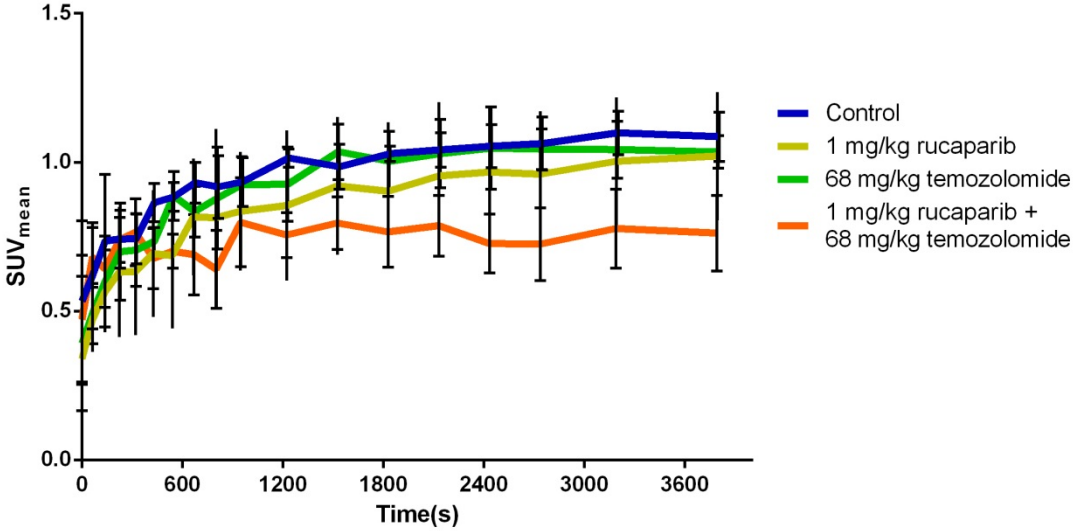

Figure 5.10: Mean tumour [^{18}F]FLT SUV *vs* time in SW620 tumour-bearing mice following 5 daily treatments with 1 mg/kg rucaparib, 68 mg/kg temozolomide or the combination of 1 mg/kg rucaparib with 68 mg/kg temozolomide. Points are the mean and bars are the standard error.

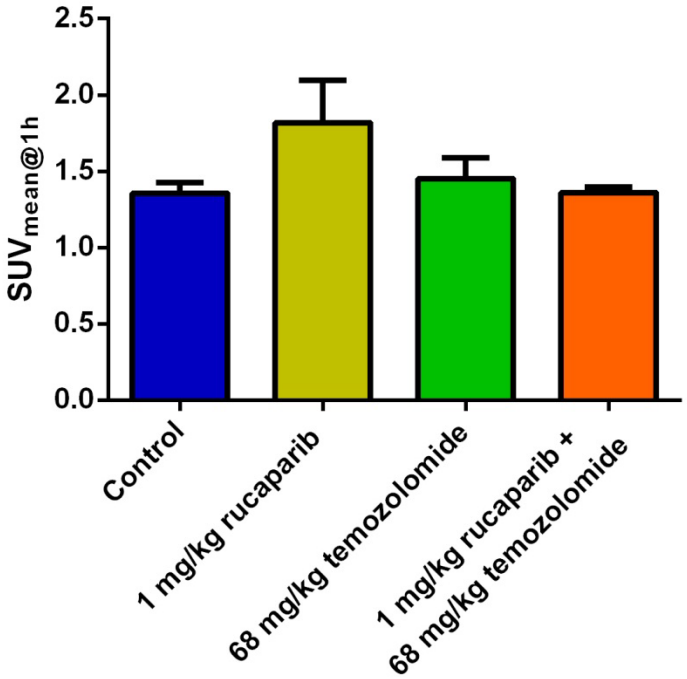

Figure 5.11: Mean tumour [^{18}F]FLT SUV with standard error (bars) at one hour after tracer injection in A2780 tumour-bearing mice following 5 daily treatments with 1 mg/kg rucaparib, 68 mg/kg temozolomide or the combination of 1 mg/kg rucaparib with 68 mg/kg temozolomide.

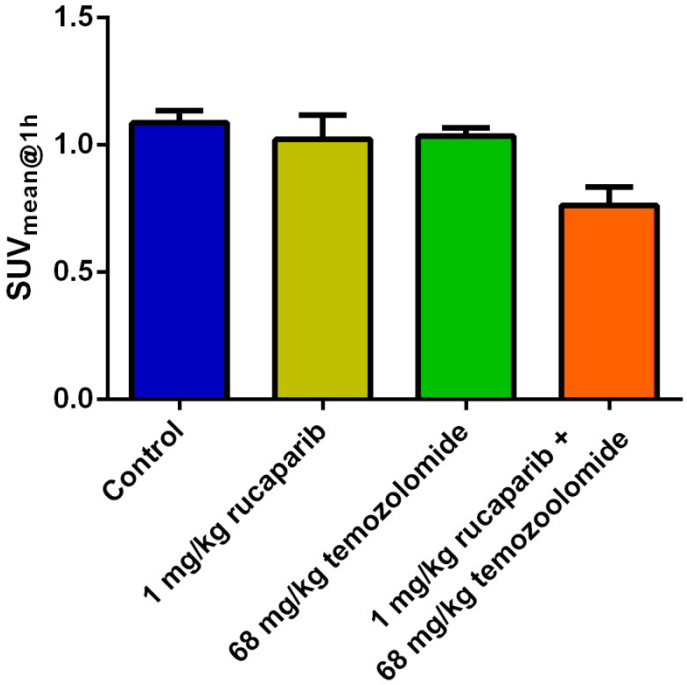

Figure 5.12: Mean tumour [^{18}F]FLT SUV with standard error (bars) at one hour after tracer injection in SW620 tumour-bearing mice following 5 daily treatments with 1 mg/kg rucaparib, 68 mg/kg temozolomide or the combination of 1 mg/kg rucaparib with 68 mg/kg temozolomide.

Figures 5.13 and 5.14 present the 0-60minute area under the mean SUV versus time curve calculated from the data presented in Figures 5.9 and 5.10, and normalized to the mean SUV AUC_{1h} in the control untreated tumours.

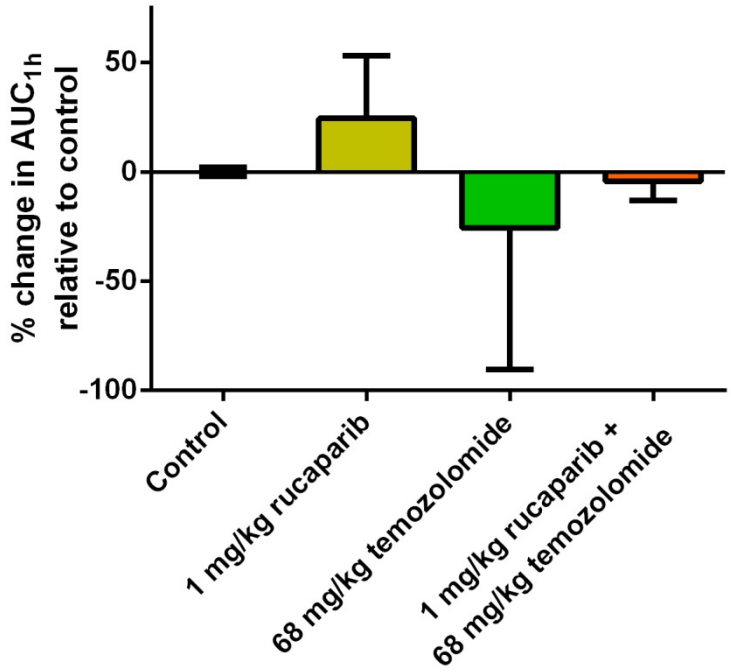

Figure 5.13: Percentage change with standard error (bars) relative to control in [^{18}F]FLT SUV AUC_{1h} following daily x5 treatment with 1 mg/kg rucaparib, 68 mg/kg temozolomide or the combination of 1 mg/kg rucaparib with 68 mg/kg temozolomide relative to control in the A2780 tumours.

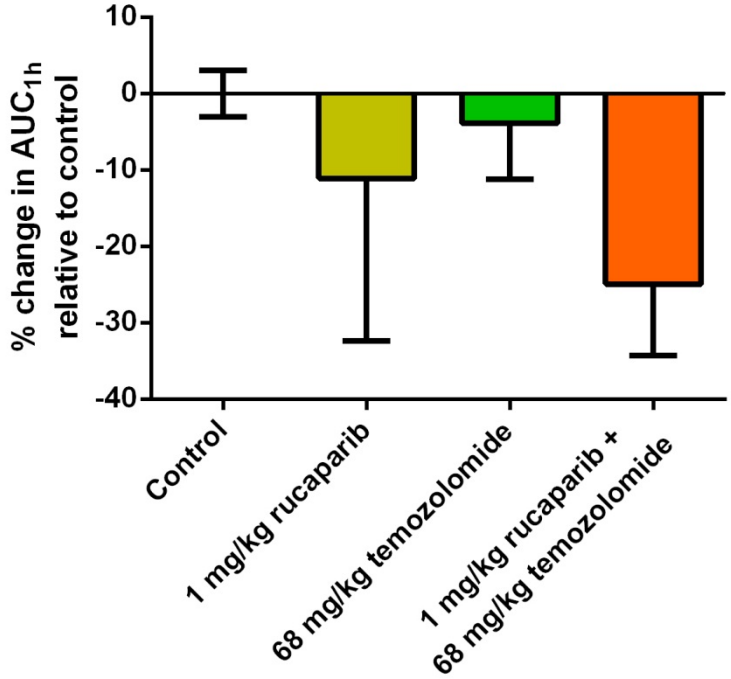

Figure 5.14: Percentage change with standard error (bars) relative to control in [^{18}F]FLT SUV AUC_{1h} following daily x5 treatment with 1 mg/kg rucaparib, 68 mg/kg temozolomide or the combination of 1 mg/kg rucaparib with 68 mg/kg temozolomide relative to control in the SW620 tumours.

Statistical analysis of the [^{18}F]FLT SUV AUC_{1h} data for A2780 human tumour xenografts presented in Figure 5.13 demonstrated that 1 mg/kg rucaparib alone

increases [^{18}F]FLT uptake in comparison to both control and 1 mg/kg rucaparib plus 68 mg/kg temozolomide treated mice (Table 5.7). A one-way ANOVA statistical analysis with multiple comparisons confirms that there is a statistically significant difference between the control and the 1 mg/kg rucaparib groups (p = 0.022), and between the 1 mg/kg rucaparib and the 1 mg/kg rucaparib plus 68 mg/kg temozolomide (p = 0.022) treatment groups.

	1 mg/kg rucaparib	68 mg/kg temozolomide	1 mg/kg rucaparib + 68 mg/kg temozolomide
Control	p = 0.019	p = 0.103	p = 0.103
1 mg/kg rucaparib		p = 0.103	p = 0.047
68 mg/kg temozolomide			p = 0.18

Table 5.7: Statistical analysis (Mann-Whitney non-paired t test) of the [^{18}F]-FLT PET data presented in Figure 5.13 assessing the effect of rucaparib, temozolomide and rucaparib plus temozolomide treatment on the SUV_{mean} values over an hour in A2780 tumour-bearing mice.

Statistical analysis of the [^{18}F]FLT SUV AUC_{1h} data for SW620 human tumour xenografts presented in Figure 5.14 demonstrated that 1 mg/kg rucaparib alone or in combination with 68 mg/kg temozolomide decreased [^{18}F]FLT uptake in comparison to both control and 68 mg/kg temozolomide alone treated mice (Table 5.8). A one-way ANOVA statistical analysis with multiple comparisons only confirms that there is a statistically significant difference between the control and 1mg/kg rucaparib plus 68mg/kg temozolomide combination treatment groups (p=0.0087).

	1mg/kg rucaparib	68mg/kg temozolomide	1mg/kg rucaparib + 68mg/kg temozolomide
Control	p=0.040	p=0.37	p=0.0008
1mg/kg rucaparib		p=0.14	p=0.11
68mg/kg temozolomide			p=0.013

Table 5.8: Statistical analysis (Mann-Whitney non-paired t test) of the [^{18}F]-FLT PET data presented in Figure 5.3 assessing the effect of rucaparib, temozolomide and rucaparib plus temozolomide treatment in the SUV_{mean} values over an hour in SW620 tumour-bearing mice experiment.

5.4 Discussion

5.4.1 The effect of rucaparib, temozolomide and rucaparib plus temozolomide on tumour growth and [^{18}F]FLT uptake in SW620 human tumour xenografts

Tumour growth

In the experiments described in this chapter, rucaparib was shown to enhance the anti-tumour activity of temozolomide in the SW620 human tumour xenografts model (Figure 5.6). Temozolomide alone at a dose equivalent to the standard clinical dose (68 mg/kg/day ~ 200mg/m^2) was active; however, rucaparib at 1 mg/kg was not.

These results are consistent with previously published studies. Calabrese *et al.*, in 2004 published a study in which chemosensitization and radiosensitization by the PARP inhibitor AG14361 (a precursor of rucaparib) was demonstrated. Temozolomide administered as a single agent or in combination with the PARP inhibitor resulted in a delay in SW620 tumour growth similar to that observed in the current studies (Calabrese *et al.*, 2004). Subsequently, Thomas *et al.* in 2007 demonstrated that AG14447, the phosphate salt equivalent to rucaparib, also resulted in chemosensitization in combination with temozolomide in SW620 xenografts, of a similar magnitude to the effect reported in this chapter (Thomas *et al.*, 2007).

[^{18}F]FLT PET

In SW620 tumours, [^{18}F]FLT uptake was unchanged following temozolomide treatment; however, [^{18}F]FLT uptake was reduced by the combination of rucaparib and temozolomide (Figures 5.10, 5.12 and 5.14). The effect on [^{18}F]FLT uptake correlates closely with the effects on tumour growth (Figure 5.6), and these data support the use of [^{18}F]FLT-PET as a surrogate response biomarker for rucaparib/temozolomide combination treatment.

5.4.2 The effect of rucaparib, temozolomide and rucaparib plus temozolomide on tumour growth and [^{18}F]FLT and [^{18}F]FDG uptake in A2780 human tumour xenografts

Tumour growth

In contrast to the data from the SW620 human tumour model temozolomide alone or rucaparib combined with temozolomide did not inhibit A2780 tumour growth. *In vitro* data show that A2780 cells are markedly less sensitive to temozolomide treatment than SW620 cells (see Chapter 4). However, higher temozolomide doses could not be given to mice bearing A2780 tumours because of toxicity limitations. Unexpectedly, rucaparib alone may have increased tumour growth rate (Figure 5.1 and Table 5.1). A2780 cells have a doubling time of 26.3h which is very similar to the 24h doubling time of SW620 cells (Li and Lin, 1995; Maybaum *et al.*, 1991). This similarity in growth time *in vitro* suggests a physiological mechanism to explain the difference in tumour growth rates.

[^{18}F]FLT-PET

Consistent with the results of the tumour growth delay studies, neither temozolomide alone or in combination with rucaparib reduced [^{18}F]FLT uptake in A2780 tumour after 5 daily dosing (Figure 5.13, Table 5.7). Again unexpectedly, but consistent with the tumour growth data, rucaparib alone increased [^{18}F]FLT uptake (Figure 5.13, Table 5.7). The correlation of the tumour growth (Figure 5.1, Table 5.1 and 5.2) and [^{18}F]FLT uptake data (Figure 5.13 and Table 5.7) suggest that PARP inhibition may have accelerated tumour growth in this model and this possibility requires confirmation and extension to other pre-clinical models.

[^{18}F]FDG-PET

Although [^{18}F]FDG studies could not be performed in SW620 tumour-bearing mice, tracer uptake in A2780 tumours was sufficient to evaluate the effect of rucaparib, temozolomide and rucaparib/temozolomide combination therapy. Although there was a suggestion that rucaparib either alone or in combination with temozolomide reduced [^{18}F]FDG uptake (Figure 5.5 and Table 5.3), the

effect was not statistically significant in all the tests performed, consistent with the lack of any antitumour effects in the growth delay studies.

In an article published by Ebenhan *et al.* (2009) several PET tracers were used in various tumour models to assess the suitability of each tracer as a surrogate response PET biomarker. Several important conclusions were drawn by these authors, notably that [^{18}F]FDG-PET in preclinical human tumour models has low tracer uptake, [^{18}F]FDG SUV does not correlate with tumour volume and that the tracer accumulates more in the tumour periphery than the central area, which may be due to a dependence on the vasculature of the tumour for tracer access. In contrast, [^{18}F]FLT uptake was less heterogeneous and gave good visualization in all the models studied suggesting that [^{18}F]FLT uptake is less dependent upon the tumour blood supply (Ebenhan *et al.*, 2009).

Overall, the results presented in this chapter demonstrate that [^{18}F]FLT-PET can be used as a surrogate response imaging biomarker for temozolomide/rucaparib combinations. Thus in a model where there was significant chemosensitization (SW620) increased activity (chemosensitization) was predicted by a significant decrease in [^{18}F]FLT uptake, whereas in a model where there was no chemosensitization (A2780) there was no significant change in [^{18}F]FLT uptake.

Chapter 6. General discussion

This chapter considers how the potential biomarkers explored in earlier chapters may be used to provide greater insights into the biological effects of PARP inhibitors such as rucaparib and their interaction with DNA damaging agents such as temozolomide.

6.1 The relationship between changes in tumour vasculature and tumour energetics

As introduced in subsection 1.5.1 DCE-MRI can be used to predict the outcome of a specific treatment by the characterization of changes to tumour vasculature prior to tumour volume changes (Reiser *et al.*, 2008), and ^{31}P-MRS can be used to assess changes in metabolic status as reflected by changes in NTP levels (Ronen *et al.*, 1999). The ratio between the $AUC_{MR,120}$ for the first injection ($AUC_{MR,120\_1}$) of contrast agent and for the second injection (AUC_{MR120_2}) has been termed the Anti-Vascular Index (AVI). An increase in this ratio corresponds to a decrease in the $AUC_{MR,\ 120s}$ for the second injection of contrast agent which can be due to an impairment in the vascular supply to the tumour, while the ratio between the inorganic phosphate (Pi) and beta-NTP (βNTP) (primarily reflecting ATP) concentrations change in relation to the supply of oxygen and nutrients. The study of both biomarkers in the same experiment has been widely published in the literature in the study of anti-vascular agents such as combretastatin A4 phosphate (anti-tubulin agent), DMXAA (tumour necrosis stimulator), docetaxel (anti-mitotic agent) (Beauregard *et al.*, 2001; Beauregard *et al.*, 2002; Maxwell *et al.*, 2002; Jensen *et al.*, 2010). Bevacizumab is an anti-VEGF agent which has been studied with DCE-MRI and ^{1}H/^{31}P-MRS (Hattingen *et al.*, 2011).

In Figure 6.1, the AVI in both tumour types (A2780 and SW620) is compared with the percentage change in the inorganic phosphate to βNTP ratio following treatment with rucaparib, temozolomide, or rucaparib/temozolomide combinations.

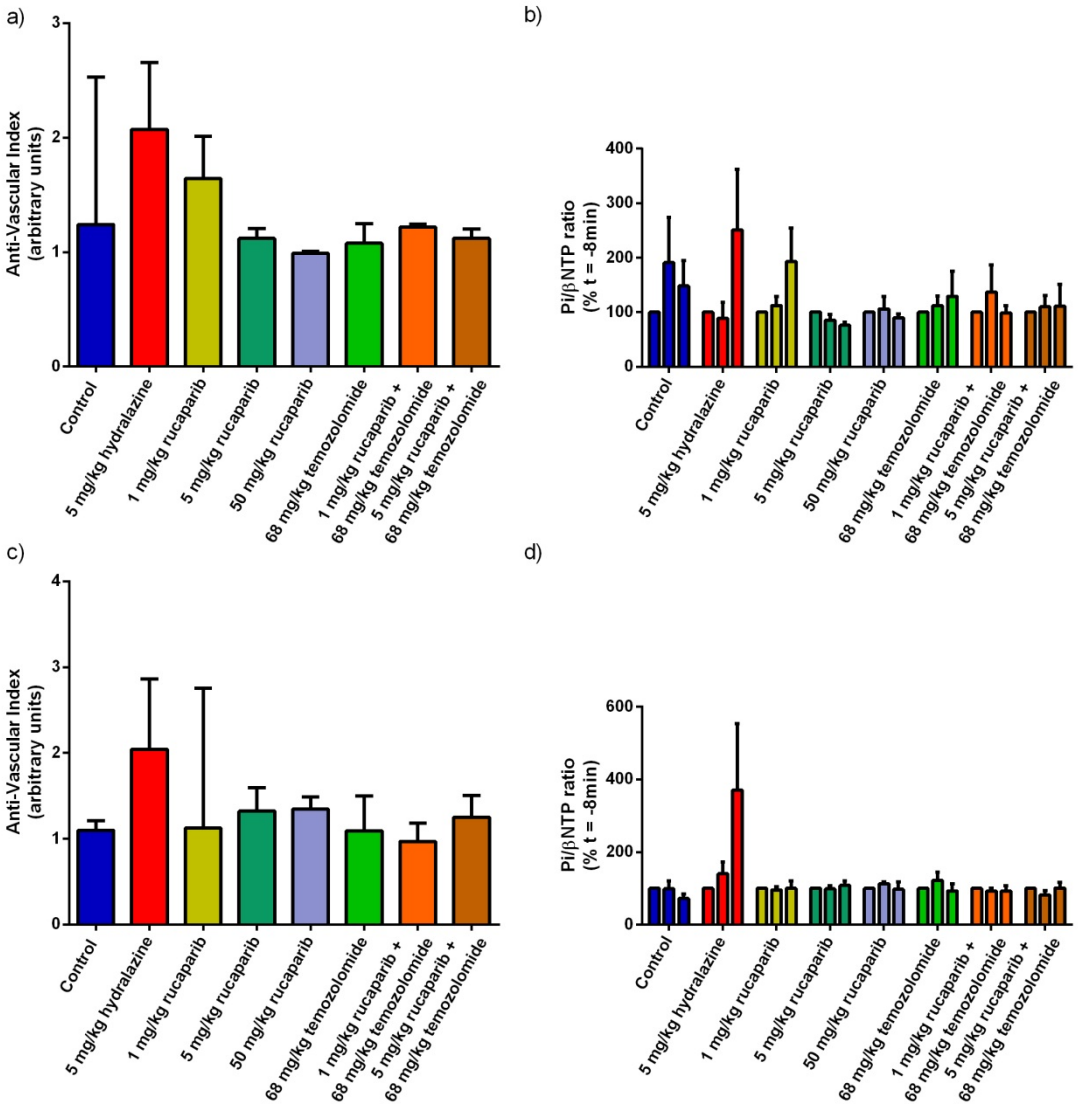

Figure 6.1: Effect of hydralazine, rucaparib, temozolomide and rucaparib/temozolomide combinations on a) median values and inter-quartile range (error bars) for the AVI in A2780 tumour-bearing mice; b) mean change with standard error (bars) in Pi/βNTP ratios in A2780 tumour bearing-mice grouped between 8 minutes before injection of drug, 8 minutes and 40 minutes after drug injection; c) median values and inter-quartile range (error bars) for the AVI in SW620 tumour-bearing mice; d) mean change with standard error (bars) in Pi/βNTP ratios in SW620 tumour bearing-mice grouped between 8 minutes before injection of drug, 8 minutes and 40 minutes after drug injection.

Figure 6.1 (a)-(d)) shows that in the groups where the treatment caused a reduction of contrast agent uptake after the second injection, there was also an increase in the inorganic phosphate (Pi) to βNTP ratio. This relationship is clearly observed following hydralazine which causes vessel collapse preventing the tumour from obtaining oxygen and nutrients, resulting in metabolic stress and an increase in inorganic phosphate and decrease in βNTP. This effect is seen in A2780 tumours in mice treated with 5 mg/kg hydralazine and with 1 mg/kg rucaparib, and possibly with the combination of 1 mg/kg rucaparib with 68 mg/kg temozolomide. In SW620 tumours in mice treated with 5 mg/kg

hydralazine the dual increase in AVI and associated increase in Pi/βNTP ratio is again observed. There is a less prominent effect at the higher doses of rucaparib given alone (5 and 50 mg/kg). The fact that the hydralazine effects are replicated in tumours derived from two different cell lines increases the confidence in the techniques used and results obtained. However, the fact that the Pi/βNTP ratio is measured before the second contrast agent injection might be sub-optimal, and longer acquisition period for the phosphorus spectra could provide different results.

In Figures 6.2 and 6.3 AVI is plotted against the ratio of inorganic phosphate to βNTP ratio 40 minutes after the drug injection (Pi/βNTP@40') to the same ratio 8 minutes before the drug injection (Pi/βNTP@-8'), for both tumour types in individual animals. A higher ratio between Pi/βNTP@40' and Pi/βNTP@-8' indicates metabolic stress and an increased AVI indicates that the uptake of contrast agent after the second injection was lower, therefore the vasculature of the tumour has been compromised. In these figures, the data presented relates only to animals which underwent both imaging protocols (and passed signal-noise criteria for ^{31}P-MRS analysis), DCE-MRI and ^{31}P-MRS. The resulting graphs were analysed to determine if the change in Pi/βNTP ratio was related to AVI (nonparametric Spearman correlation analysis).

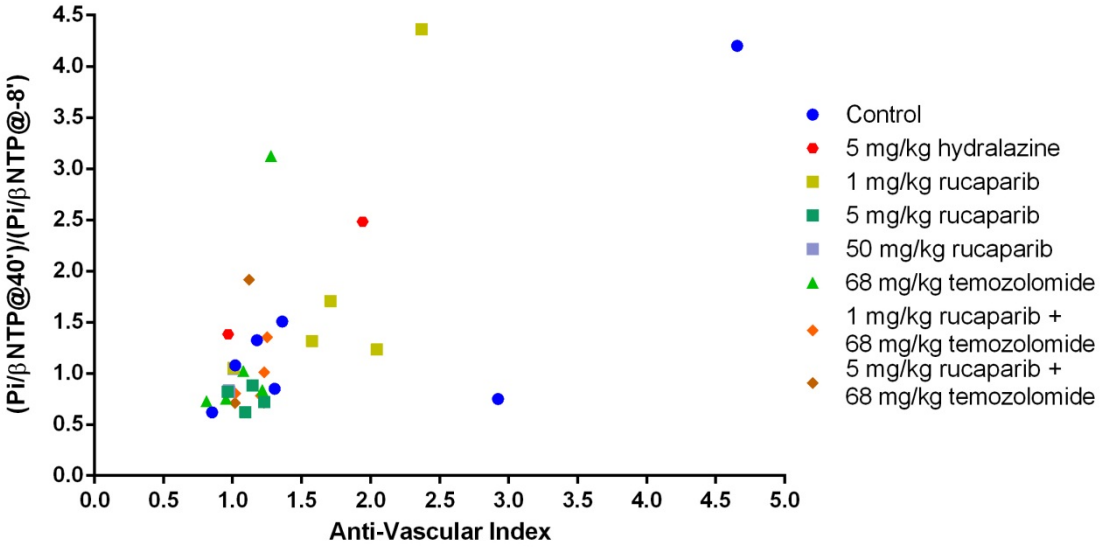

Figure 6.2: Ratio of Pi to βNTP ratios at 40min after and 8min before drug injection versus the anti-vascular index in A2780 tumour-bearing mice following treatment as indicated in the figure key. Each point is the AVI and corresponding Pi/ βNTP value for each individual mouse.

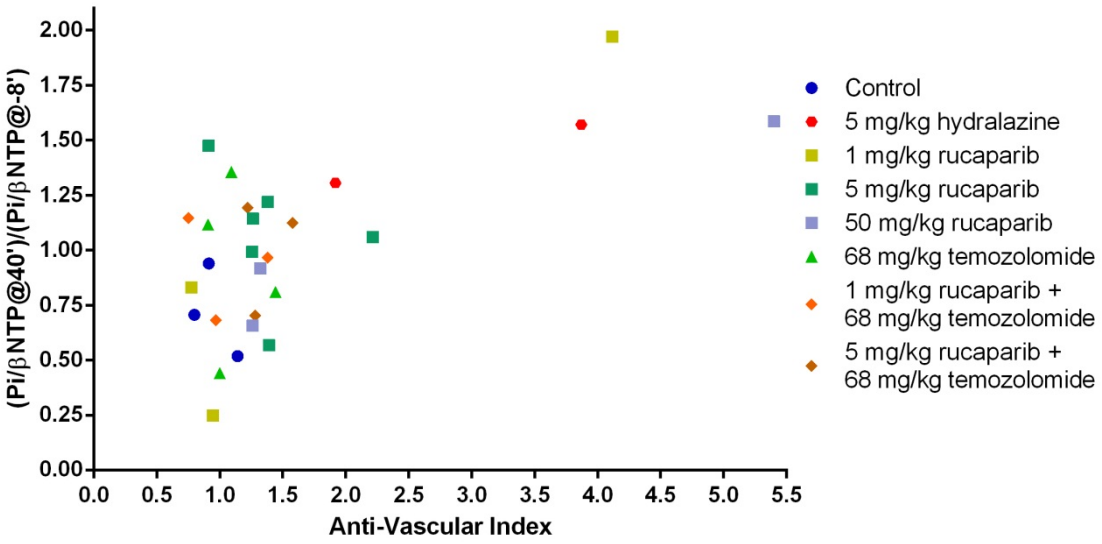

Figure 6.3: Ratio of Pi to βNTP ratios at 40min after and 8min before drug injection versus the anti-vascular index in SW620 tumour-bearing mice following treatment as indicated in the figure key. Each point is the AVI and corresponding Pi/ βNTP value for each individual mouse.

In A2780 tumours the nonparametric Spearman correlation coefficient, r, was 0.505 with a p value of 0.003 (statistically significant). This r value indicates a correlation between the two variables. For SW620 tumours the correlation coefficient was 0.36 with a p value of 0.06 (not statistically significant at the 95% level). However, the r value for the SW620 results indicates a similar trend to the data for A2780 tumours. It is important to note that these low p values in the correlation might be somehow forced by the some extreme or “outliers” values. In the absence of a valid reason for exclusion, these “outliers” have to be included. These relationships indicate a likely link between drug effects on tumour vasculature and tumour energetics.

Some of the tumours examined in the *in vivo* MR studies were harvested and freeze clamped after the DCE-MRI, and *ex vivo* ^{31}P-MRS analysis performed as reported in chapter 4. Samples were extracted according to the PCA protocol and the results obtained were compared with the AVI data from the *in vivo* experiments. Due to limited time available on the high resolution NMR only a few samples were selected to provide preliminary results. This cross analysis is important to assess if the *in vivo* results are coherent with the *ex vivo* results and if the vascular and metabolic effects can be seen in the extracted tissues.

Figures 6.4 and 6.5 show the amount of NTP (primarily reflecting ATP in μmoles per gram of tissue wet weight) measured from the *ex vivo* analysis against the AVI in A2780 and SW620 tumours, respectively, where both *in vivo* DCE-MRI and *ex vivo* ^{31}P-MRS analyses were performed.

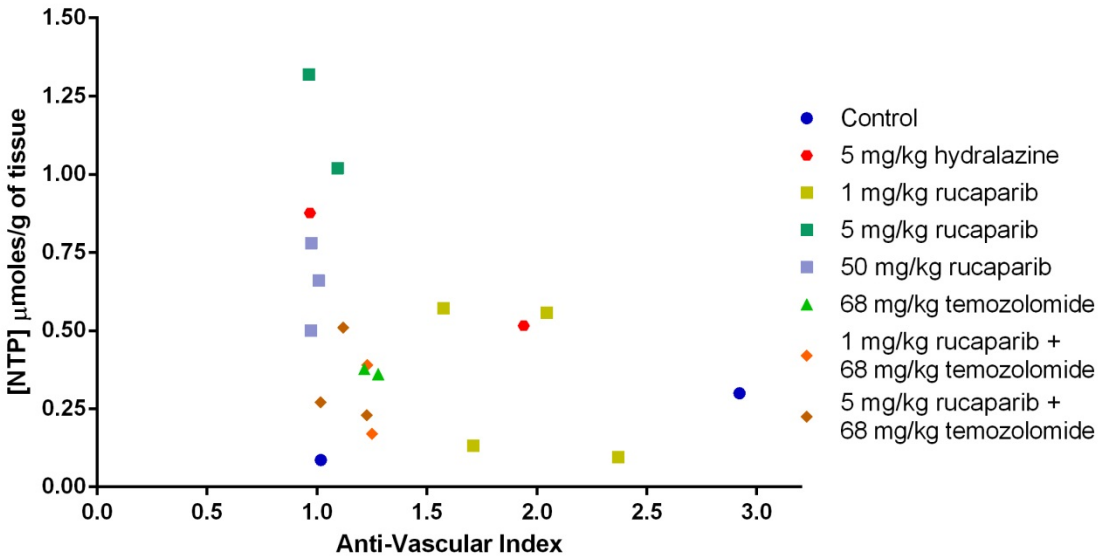

Figure 6.4: Relationship between NTP concentration measured *ex vivo* in A2780 tumour extracts and the AVI in individual mice. Treatments are as indicated in the figure key.

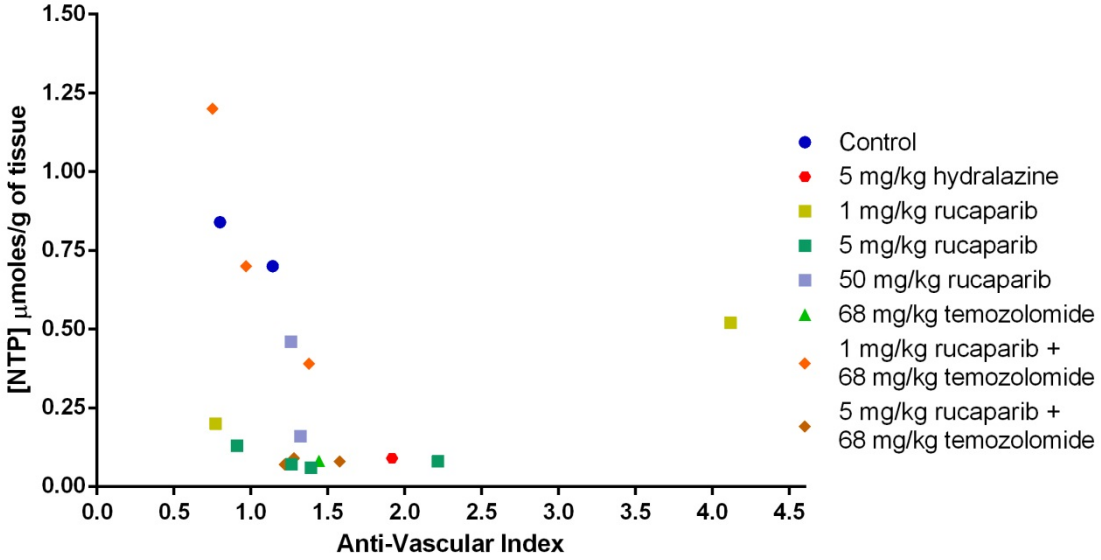

Figure 6.5: Relationship between NTP concentration measured *ex vivo* in SW620 tumour extracts and the AVI in individual mice. Treatments are as indicated in the figure key.

Spearman rank correlation analysis demonstrated that there was a significant negative correlation in both tumour types between tumour AVI and tumour NTP concentration (A2780: $r = -0.47$, $p = 0.04$; SW620: $r = -0.5$, $p = 0.035$). Thus a high AVI has associated reduced tumour NTP concentrations when measured *ex vivo* in tumour extracts. The mechanism underlying the relationship is most probably that vasculature damage results in a reduced oxygen and nutrient supply which in turn decreases tumour ATP production.

6.2 The relation between *in vivo* and *ex vivo* measurements of NTP

Figures 6.6 and Figure 6.7 compare NTP levels measured by MRS in tumour extracts *ex vivo* with the ratio between βNTP 40 minutes after drug injection (βNTP@40) and βNTP 8 minutes before the drug injection (βNTP@-8) measured *in vivo* in A2780 and SW620 tumours, respectively.

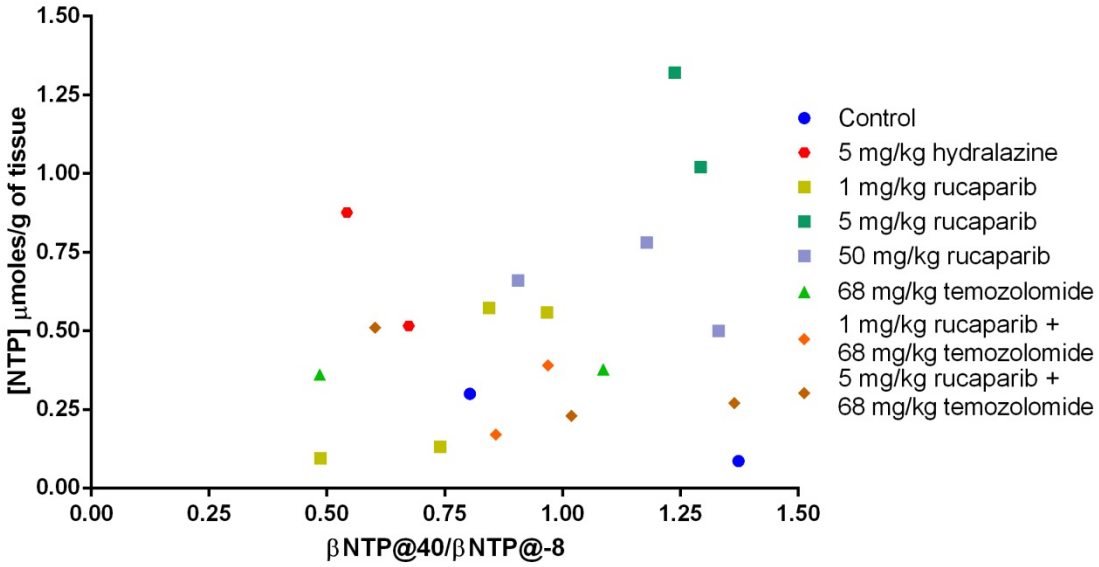

Figure 6.6: Amount of NTP in *ex vivo* A2780 tumour extracts in relation to the ratio between βNTP@40' and βNTP@-8' *in vivo* in individual mice. Treatments are as indicated in the figure key.

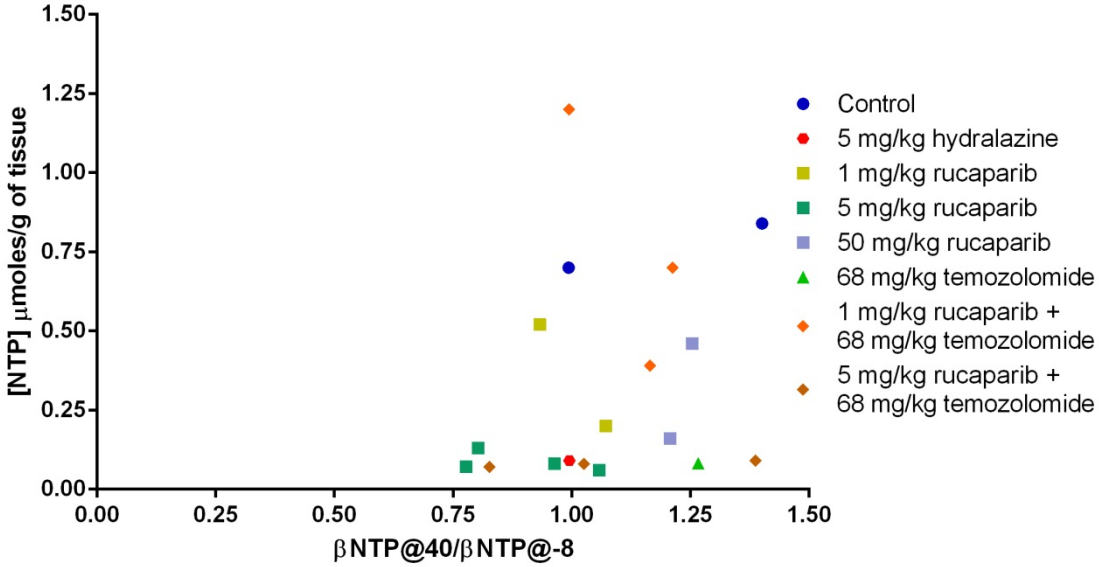

Figure 6.7: Amount of NTP in *ex vivo* SW620 tumour extracts in relation to the ratio between βNTP@40' and βNTP@-8' *in vivo* in individual mice. Treatments are as indicated in the figure key.

For data in Figures 6.6 and 6.7, the Spearman correlation coefficients, r, were 0.078 with a p value of 0.74 (not significant) for the A2780 tumours and 0.31 with p value of 0.22 (not significant) for SW620 tumours, and hence there was no significant relationship between the two parameters.

The studies described in this thesis also allow a comparison of tumour energetics measured non-invasively by single voxel *in vivo* MRS and *ex vivo* using MRS to study tumour extracts. In Figures 6.8 and 6.9 NTP levels measured by *ex* vivo MRS in tumours extracts are compared with the Pi/βNTP ratio 40 minutes after drug injection as measured by *in vivo* ^{31}P-MRS.

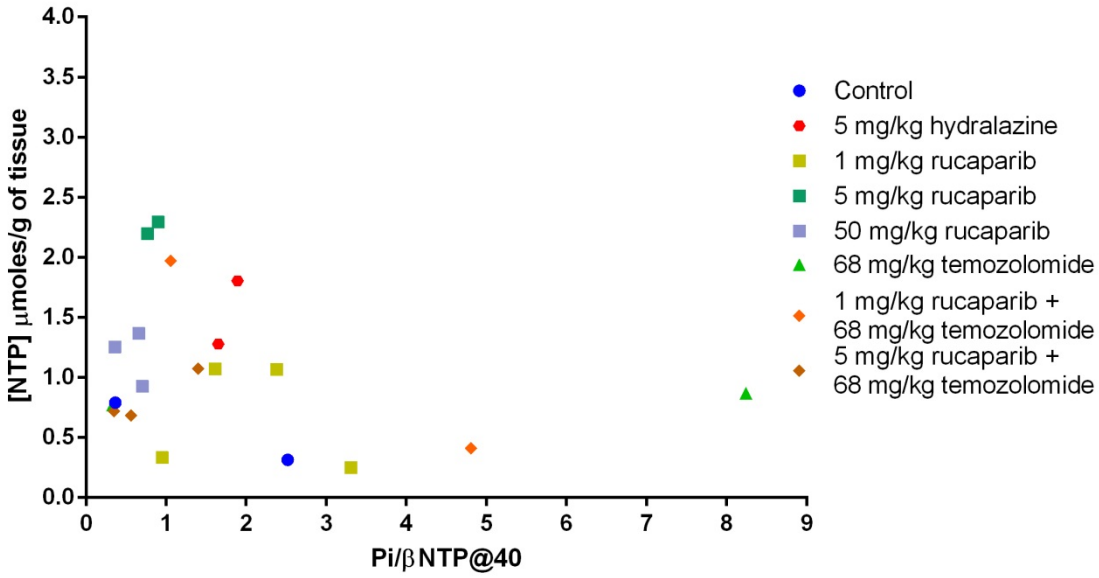

Figure 6.8: Relationship between NTP concentrations measured *ex vivo* in A2780 tumour extracts and Pi/βNTP@40'ratio *in vivo* in the same mouse. Treatments are as indicated in the figure key.

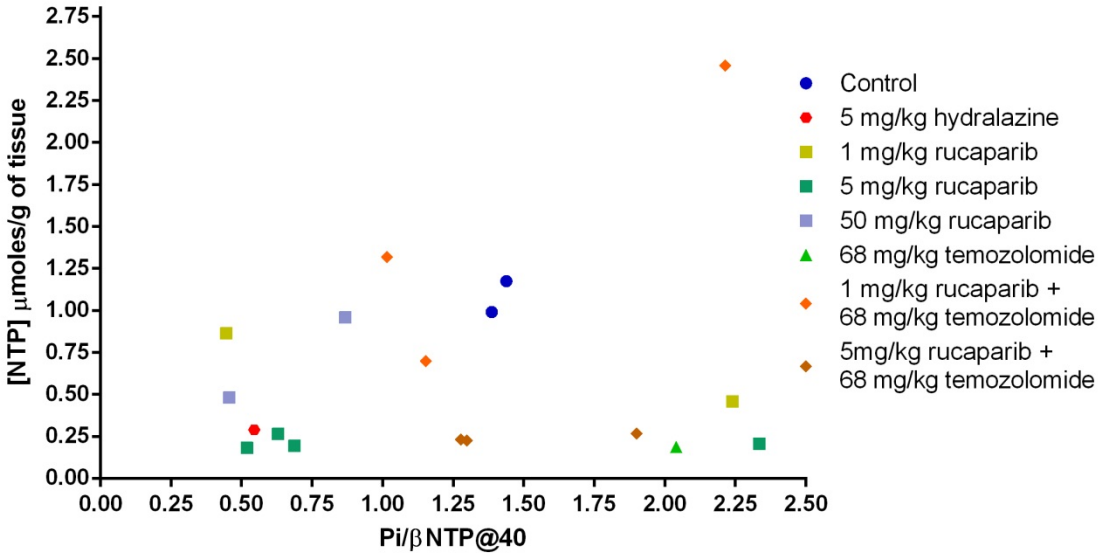

Figure 6.9: Relationship between NTP concentrations measured *ex vivo* in SW620 tumour extracts and Pi/βNTP@40'ratio *in vivo* in the same mouse. Treatments are as indicated in the figure key.

The Spearman correlation coefficient for the data for A2780 tumours was -0.15 ($p = 0.53$), and for SW620 tumours 0.04 ($p = 0.87$). Thus there was no

significant relationship between the parameters, perhaps reflecting the fact that the Pi/βNTP ratio, and not the actual NTP level, was measured *in vivo*.

6.3 Comparison of drug treatment-induced changes in MR and PET biomarkers

Figure 6.10 compares the results of all the techniques applied to A2780 tumours or cells (DCE-MRI, ^{31}P-MRS and [^{18}F]FDG and [^{18}F]FLT PET), where only the treatments used in all experiments are shown.

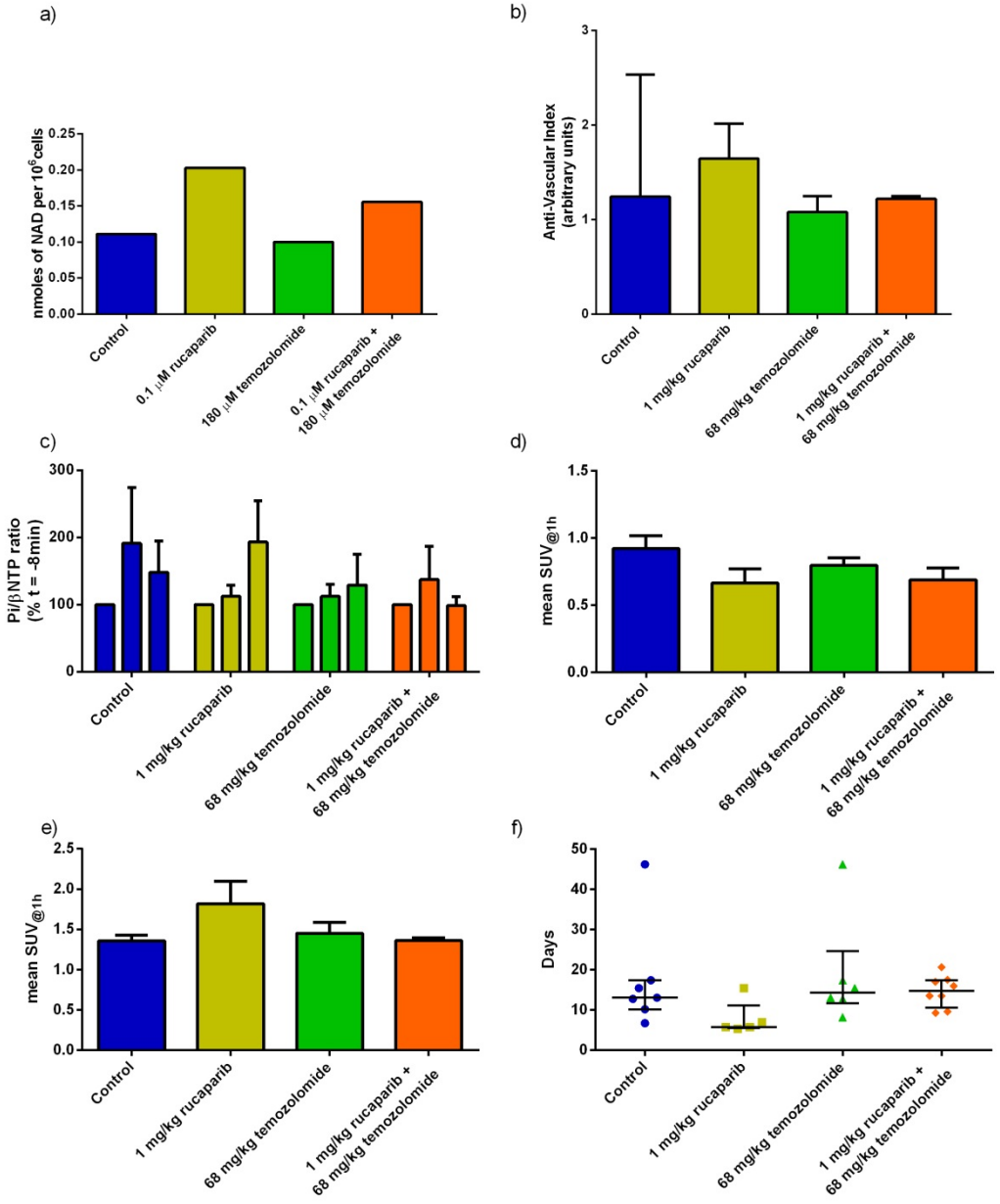

Figure 6.10: Comparison of MR and PET biomarker data in A2780 tumours and cells. a) NAD concentration in nanomoles per million cells in the four different groups of A2780 treated cells; b) Median and inter-quartile range for the AVI in A2780 tumour-bearing mice; c) Percentage change of Pi/βNTP ratios in A2780 tumour-bearing mice grouped between 8 minutes before injection of drug, 8 minutes after drug injection and 40 minutes after drug injection; d) Mean [^{18}F]FDG SUV for each treatment group at the one hour time point in A2780 tumour-bearing mice; e) Mean [^{18}F]FLT SUV for each treatment group at the one hour time point in A2780 tumour-bearing mice; f) Median time in days for A2780 tumours to reach four times their initial volume and inter-quartile range. Treatments were as indicated in each figure.

From data in Figure 6.10 several comparisons can be made. In doing so, it is important to note that the DCE-MRI and ^{31}P-MRS results relate to an acute experiment with a single treatment while the PET and growth delay experiments involve a 5 day treatment schedule, and cells were treated *in vitro* for 6 hours. The different experiments had different time points regarding the acute or prolonged effected of drugs. Still it is worth of comparison as the it might indicate if prolonged effects can be identified earlier in the acute studies.

In addition to the DCE-MRI and ^{31}P-MRS comparisons discussed above, the results from these two techniques can be compared with the [^{18}F]FDG-PET results, and the decrease of contrast agent uptake in the second injection may possibly be reflected in a lower uptake of [^{18}F]FDG, potentially due to damage to the tumour vasculature. In contrast, from the [^{18}F]FLT-PET and tumour growth results, it appears that there is an increase in the growth and proliferative status of A2780 tumours when treated with 1mg/kg rucaparib.

Although preliminary, the results from A2780 cells treated *in vitro* are consistent with data presented by Sims et al. (1981) and more recently by Bai et al. (2011). In both papers, inhibition of PARP lead to an increase of NAD levels, dose dependant and of 50% in the Bai *et al.* paper (Sims *et al.*, 1981; Bai *et al.*, 2011). However, the results presented here are limited and further experiments are required.

Figure 6.11 presents the comparative DCE-MRI, ^{31}P-MRS and [^{18}F]FLT-PET data for SW620 tumours in rucaparib, temozolomide and rucaparib plus temozolomide treated mice.

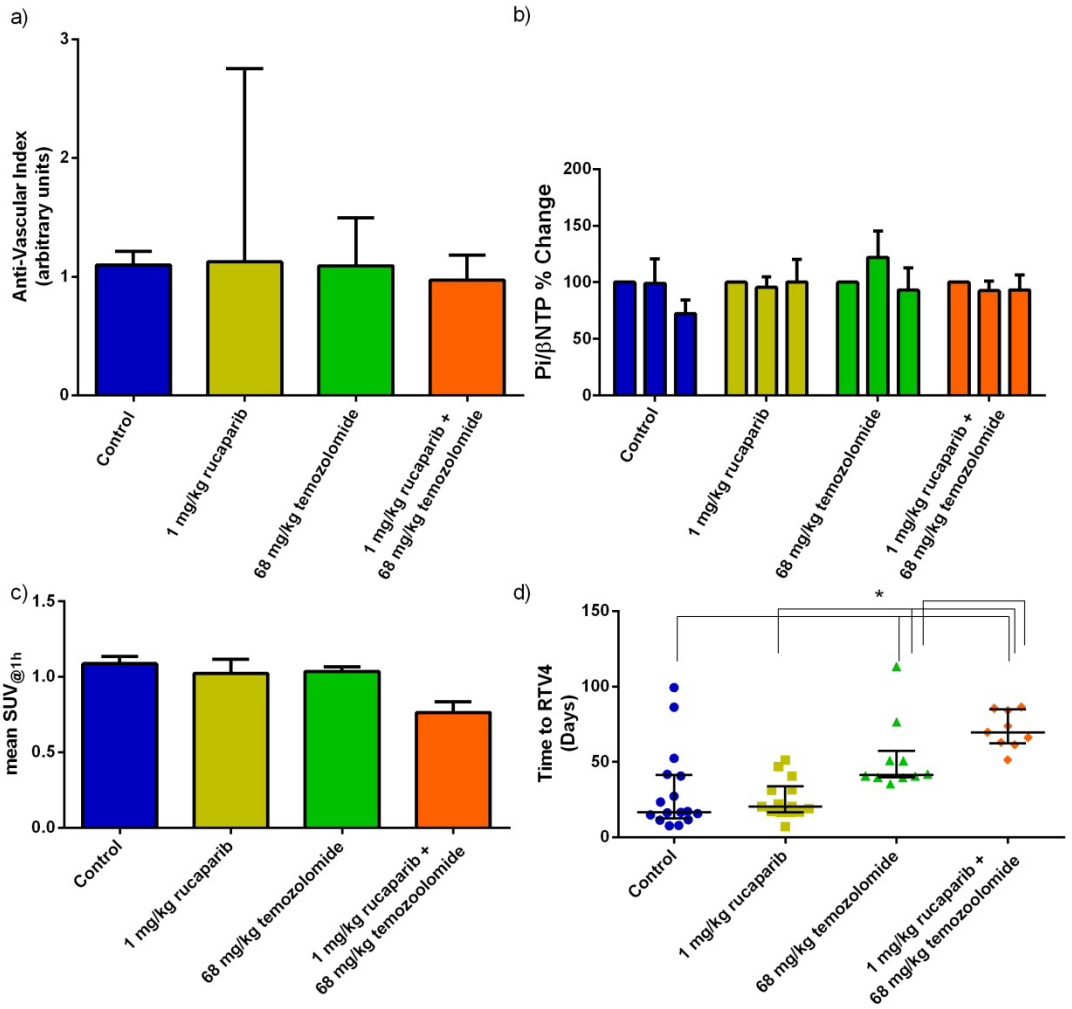

Figure 6.11: Comparison of MR and PET biomarkers data in SW620 tumours. a) AVI (median and inter-quartile range); b) Percentage change in Pi/βNTP ratios 8 minutes before drug injection, 8 minutes after drug injection and 40 minutes after drug injection; c) Mean [^{18}F]FLT SUV for each treatment group at the one hour time point in A2780 tumour-bearing mice; d) Median time in days for A2780 tumours to reach four times their initial volume and inter-quartile range with the star indicating statistically significant difference between all the groups apart from between control and 1 mg/kg rucaparib groups. Treatments were as indicated in each figure.

The DCE-MRI and ^{31}P-MRS data have been compared previously and no significant changes were produced by drug treatment in the SW620 tumour model. As previously discussed, chapter 5, the most notable result in the SW620 tumour model was the prediction of chemosensitization in the rucaparib plus temozolomide combination group by the [^{18}F]FLT-PET scan.

Although only studied in one tumour cell line and the data are preliminary, the increase in NAD levels in A2780 cells treated with rucaparib is consistent with PARP inhibition, as is the decrease in NAD when A2780 cells are treated with temozolomide, potentially due to hyperactivation of PARP. In work by Horsman

et al. C3H mouse mammary carcinoma growth inhibition after administration of a high dose of nicotinamide (1000 mg/kg) resulted in a similar level of growth inhibition to that caused by fumagillin (angiogenesis inhibitor). However, the mechanism underlying the nicotinamide effect was not established (Horsman *et al.*, 1995).

Overall, the imaging biomarker studies have shown that [^{18}F]FLT-PET can be used as a surrogate response biomarker for PARP inhibitor-temozolomide combination. Intriguingly, data generated in A2780 tumour model suggest that [^{18}F]FLT-PET may also be able to predict enhanced tumour growth following single agent rucaparib administration, although further experiments are needed to confirm this unexpected observation.

6.4 The effect of rucaparib, temozolomide, and rucaparib plus temozolomide on NAD concentrations in the livers of PARP1 WT and KO mice

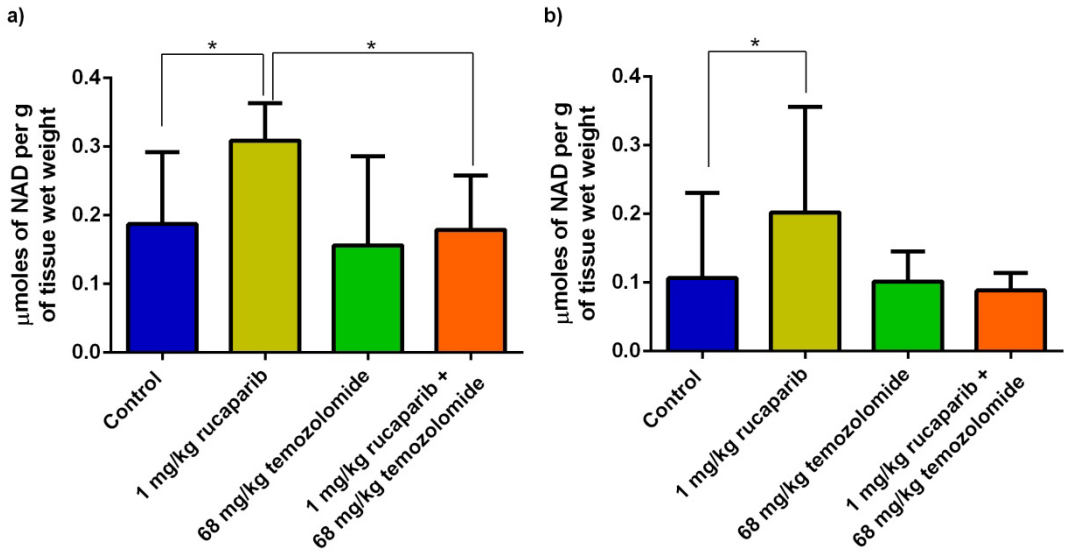

Figure 6.12: Effect of daily x5 treatment with rucaparib, temozolomide, or rucaparib combined with temozolomide on the concentration of NAD in the livers of a) PARP1 WT and b) PARP1 KO mice. The median with inter-quartile range of concentrations is shown and the stars indicate the statistically significant differences.

The studies in PARP1 WT and PARP1 KO mice were performed to determine whether PARP1 status influenced the impact of rucaparib, temozolomide or rucaparib plus temozolomide combination treatment on NAD levels. The liver was chosen as a large-volume relatively homogeneous organ that is amenable to non-invasive *in vivo* MRS. However, satisfactory *in vivo* MRS data could not be obtained and hence studies were performed *ex vivo* on liver extracts. Dual *in vivo*/*ex vivo* liver ^{31}P-MRS study can be found in the literature, and Sevastianova *et al.* (2010) described *in vivo* clinical MRS measurements of nicotinamide adenine dinucleotide phosphate (NADP) in human liver and *ex vivo* analysis of biopsies (Sevastianova *et al.*, 2010).

As expected, in the PARP1 WT mice, PARP inhibition lead to an increase in liver NAD. The PARP1 KO mouse livers had a lower endogenous NAD concentration, and again rucaparib treatment increased NAD levels potentially as a result of PARP2 inhibition.

Other NAD^+-dependent enzymes that might be affected by a PARP inhibitor such as rucaparib include mono-ADP- ribosyltransferases (reviewed by Hassa *et al.*, 2006) and sirtuins (Benavente *et al.*, 2012). However, the real effects of PARP inhibitors in the catalytic activity of these enzymes are not fully understood (reviewed by Rouleau *et al.*, 2010).

6.5 Future work

Reviewing the work developed in this thesis, some methodological alterations should be implemented. In the DCE-MRI/^{31}P-MRS studies it would be worthwhile to perform the scans with the surface coil but the inside the 72mm volume coil to optimize the proton imaging. The possible loss of SNR in the ^{31}P-MRS could be compensated with the built of a more sensitive and/or tunable coil.

The extraction protocol for tissues and cells could and should be optimized in order to provide clearer spectra. Also the use of different doses and different incubation times in the cell treatment protocol could provide valuable extra information.

Regarding the PET experiments, instead of having a separate control group, it would be more robust to have each mouse scanned prior to treatment so each individual can be its own control.

In addition, several questions regarding the effects of rucaparib, temozolomide or rucaparib combined with temozolomide remain unanswered.

Firstly the studies described in this thesis have not addressed the impact of rucaparib delivery to the tumour on the pharmacodynamics of the drug, and PET can be used to assess the penetration of drugs into the tumours by using a PET isotope labelled version. For PARP inhibitors Tu *et al.* (2005) have described experiments where a phenanthridinone derivative, PJ34, which has high affinity for PARP1, was labelled with [^{11}C]methyl iodide ([^{11}C]MeI). The compound production had a yield of 60% based on the starting amount of [^{11}C]MeI, and a radiochemistry purity of 99%. Rats were injected with streptozocin, an alkylating agent which causes damage to the beta cells of the pancreas and consequent activation of PARP activity. One week after treatment the streptozocin treated rats had developed diabetes and were injected with [^{11}C]PJ34 followed by tissue removal for radioactivity measurements 5 and 30 minutes after tracer injection. The results of the experiment revealed higher uptake of the radiotracer in the pancreas and liver of the streptozocin-treated rats relative to control rats suggesting higher levels of PARP enzyme(s) (Tu *et*

al., 2005). Similarly, Reiner *et al.* (2011) described experiments where the PARP inhibitor olaparib was radiolabelled with [^{18}F], using rapid orthogonal conjugation chemistry, and used to measure PARP levels in tumours. It was shown that co-administration of non-radioactive olaparib reduced the tumour [^{18}F]-olaparib uptake, demonstrating that drug-target (PARP) interaction could be measured by PET (Reiner *et al.*, 2011).

For the PARP inhibitor rucaparib, an [^{18}F] labelled version could be generated using an ^{18}F/^{19}F exchange strategy. As shown in Figure 6.13, rucaparib possesses a fluorine atom making it suitable for fluorine substitution by exchange with [^{18}F]. Studies to produce [^{18}F]-rucaparib are ongoing.

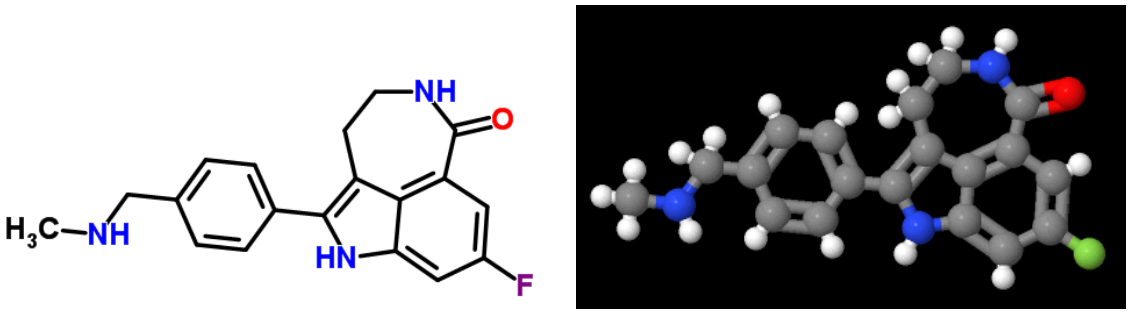

Figure 6.13: Chemical structure of the PARP inhibitor rucaparib in two dimensions on the left and in three dimensions on the right. In the 3D picture, the carbon atoms are depicted in grey, the nitrogen atoms in blue, the oxygen atom in red, the fluorine atom in green and the hydrogen atoms in white. The fluorine present in the structure is the best candidate to be replaced by ^{18}F in the radiolabelling process. Copied from (ChemSpider; ChemSpider).

Once delivery of rucaparib to the tumour has been established, the proof of PARP inhibition should be demonstrated. As indicated above Reiner *et al.* (2011) have demonstrated that a PET isotope-labelled PARP inhibitor can be used to determine whether PARP has been saturated with an inhibitor, and hence would in theory be inactive. To measure the biochemical impact of PARP inhibition, determination of the NAD (substrate) to ADP-ribose (breakdown product of poly(ADP)ribose) ratio may be informative, and it may be possible to use MRS to do so.

Data presented in this thesis on the impact of rucaparib on tumour vasculature are not consistent with those reported by Ali *et al.* (2009). However, longer treatment duration may be required to study effects, and further studies are warranted. To aid these studies, histological studies and other vascular

measurements (i.e. Time Of Flight angiography) would be extremely helpful to clarify the data here presented. A comparative study between the implanted xenografts as described here with naturally arising tumour could also provide more information between an atypical vascular supply (subcutaneous xenografts) and the resort to an already established one (naturally arising tumours.

With regards to imaging biomarker techniques, in addition to the MR and PET methods used in these studies, diffusion-weighted MR, hyperpolarized MR, and PET using alternative tracers (e.g. labelled amino acids) could be investigated and these methods are being implemented more widely in pre-clinical and clinical studies (Hara, 2001; Thoeny *et al.*, 2005; Langen *et al.*, 2006; Jamin *et al.*, 2009).

In conclusion, the work developed and presented in this thesis demonstrates that [^{18}F]FLT-PET can be used as a surrogate response biomarker for rucaparib and temozolomide combination. DCE-MRI and ^{31}P-MRS to measure effects on tumour vasculature and the impact on tumour energetics have been validated using hydralazine treatment. However, neither rucaparib nor temozolomide alone or in combination had a marked or consistent effect on tumour vasculature. Multiple imaging techniques were used and provided consistent results, and these studies have shown that multimodality imaging can be used in the assessment of novel anticancer therapies in preclinical investigations. This information should help in the design of *in vivo* biomarker measurements for clinical trials.

Chapter 7. References

Aboagye, E.O., Price, P.M. and Jones, T. (2001) 'In vivo pharmacokinetics and pharmacodynamics in drug development using positron-emission tomography', Drug Discovery Today, 6(6), pp. 293-302.

Ackerstaff, E., Pflug, B.R., Nelson, J.B. and Bhujwalla, Z.M. (2001) 'Detection of Increased Choline Compounds with Proton Nuclear Magnetic Resonance Spectroscopy Subsequent to Malignant Transformation of Human Prostatic Epithelial Cells', Cancer Research, 61(9), pp. 3599-3603.

Alauddin, M.M. (2012) 'Positron emission tomography (PET) imaging with 18F-based radiotracers', American Journal of Nuclear Medicine and Molecular Imaging, 2(1), pp. 55-76.

Alban, A., David, S.O., Bjorkesten, L., Andersson, C., Sloge, E., Lewis, S. and Currie, I. (2003) 'A novel experimental design for comparative two-dimensional gel analysis: Two-dimensional difference gel electrophoresis incorporating a pooled internal standard', PROTEOMICS, 3(1), pp. 36-44.

Ali, M., Kamjoo, M., Thomas, H.D., Kyle, S., Pavlovska, I., Babur, M., Telfer, B.A., Curtin, N.J. and Williams, K.J. (2011) 'The Clinically Active PARP Inhibitor AG014699 Ameliorates Cardiotoxicity but Does Not Enhance the Efficacy of Doxorubicin, despite Improving Tumor Perfusion and Radiation Response in Mice', Molecular Cancer Therapeutics, 10(12), pp. 2320-2329.

Ali, M., Telfer, B.A., McCrudden, C., O'Rourke, M., Thomas, H.D., Kamjoo, M., Kyle, S., Robson, T., Shaw, C., Hirst, D.G., Curtin, N.J. and Williams, K.J. (2009) 'Vasoactivity of AG014699, a Clinically Active Small Molecule Inhibitor of Poly(ADP-ribose) Polymerase: a Contributory Factor to Chemopotentiation In vivo?', Clinical Cancer Research, 15(19), pp. 6106-6112.

Alley, W.R., Madera, M., Mechref, Y. and Novotny, M.V. (2010) 'Chip-based Reversed-phase Liquid Chromatography−Mass Spectrometry of Permethylated N-Linked Glycans: A Potential Methodology for Cancer-biomarker Discovery', Analytical Chemistry, 82(12), pp. 5095-5106.

An, H.J., Miyamoto, S., Lancaster, K.S., Kirmiz, C., Li, B., Lam, K.S., Leiserowitz, G.S. and Lebrilla, C.B. (2006) 'Profiling of Glycans in Serum for the Discovery of Potential Biomarkers for Ovarian Cancer', Journal of Proteome Research, 5(7), pp. 1626-1635.

Anker, P., Lefort, F., Vasioukhin, V., Lyautey, J., Lederrey, C., Chen, X.Q., Stroun, M., Mulcahy, H.E. and Farthing, M.J. (1997) 'K-ras mutations are found in DNA extracted from the plasma of patients with colorectal cancer', Gastroenterology, 112(4), pp. 1114-1120.

Atkinson, K.E. (1989) An introduction to numerical analysis. 2nd edn. New York: Wiley.

Aung, K.L., Board, R.E., Ellison, G., Donald, E., Ward, T., Clack, G., Ranson, M., Hughes, A., Newman, W. and Dive, C. (2010) 'Current status and future potential of somatic mutation testing from circulating free DNA in patients with solid tumours', The HUGO Journal, 4(1-4), pp. 11-21.

Bader, M. (1980) 'A systematic approach to standard addition methods in instrumental analysis', Journal of Chemical Education, 57(10), pp. 703-706.

Bai, P., Cantó, C., Oudart, H., Brunyánszki, A., Cen, Y., Thomas, C., Yamamoto, H., Huber, A., Kiss, B., Houtkooper, Riekelt H., Schoonjans, K., Schreiber, V., Sauve, Anthony A., Menissier-de Murcia, J. and Auwerx, J. (2011) 'PARP-1 Inhibition Increases Mitochondrial Metabolism through SIRT1 Activation', Cell Metabolism, 13(4), pp. 461-468.

Bailey, D.L. and Towsend, D.W. (2005) Positron Emission Tomography Basic Sciences. Springer.

Banasik, M., Komura, H., M., S. and K., U. (1992) 'Specific inhibitors of poly(ADP-ribose) synthetase and mono(ADP-ribosyl) transferase', Journal of Biological Chemistry, 267(3), pp. 1569-1575.

Bauer, H., Negishi, C., Weinmann, H.J. (1994) ‘Influence of gadolinium chelates on phosphorus-31 magnetic resonance spectroscopy of the liver’, Investigative Radiology, 29(8), pp. 752-757.

Beauregard, D.A., Hill, S.A., Chaplin, D.J. and Brindle, K.M. (2001) 'The Susceptibility of Tumors to the Antivascular Drug Combretastatin A4 Phosphate Correlates with Vascular Permeability', Cancer Research, 61(18), pp. 6811-6815.

Beauregard, D.A., Pedley, R.B., Hill, S.A. and Brindle, K.M. (2002) 'Differential sensitivity of two adenocarcinoma xenografts to the anti-vascular drugs combretastatin A4 phosphate and 5,6-dimethylxanthenone-4-acetic acid, assessed using MRI and MRS', NMR in Biomedicine, 15(2), pp. 99-105.

Beis, I. and Newsholme, E.A. (1975) 'The contents of adenine nucleotides, phosphagens and some glycolytic intermediates in resting muscles from vertebrates and invertebrates.', Biochemistry Journal, 152(1), pp. 23-32.

Bello, E., Colella, G., Scarlato, V., Oliva, P., Berndt, A., Valbusa, G., Serra, S.C., D'Incalci, M., Cavalletti, E., Giavazzi, R., Damia, G. and Camboni, G. (2011) 'E-3810 Is a Potent Dual Inhibitor of VEGFR and FGFR that Exerts Antitumor Activity in Multiple Preclinical Models', Cancer Research, 71(4), pp. 1396-1405.

Beloueche-Babari, M., Chung, Y.L., Al-Saffar, N.M.S., Falck-Miniotis, M. and Leach, M.O. (2009) 'Metabolic assessment of the action of targeted cancer therapeutics using magnetic resonance spectroscopy', British Journal of Cancer, 102(1), pp. 1-7.

Benard, F. and Turcotte, E. (2005) 'Imaging in breast cancer: Single-photon computed tomography and positron-emission tomography', Breast Cancer Research, 7(4), pp. 153 - 162.

Benavente, C.A., Schnell, S.A. and Jacobson, E.L. (2012), 'Effects of Niacin Restriction on Sirtuin and PARP Responses to Photodamage in Human Skin', PLOS One, 7(7), e42276.

Bentzen, L., Vestergaard-Poulsen, P., Nielsen, T., Overgaard, J., Bjørnerud, A., Briley-Sæbø, K., Horsman, M.R. and Østergaard, L. (2005) 'Intravascular contrast agent–enhanced MRI measuring contrast clearance and tumor blood volume and the effects of vascular modifiers in an experimental tumor', International Journal of Radiation Oncology Biology Physics, 61(4), pp. 1208-1215.

Benveniste, H., Zhang, S., Reinsel, R.A., Li, H., Lee, H., Rebecchi, M., Moore, W., Johansen, C., Rothman, D.L. and Bilfinger, T.V. (2012) 'Brain metabolomic profiles of lung cancer patients prior to treatment characterized by proton magnetic resonance spectroscopy', International Journal of Clinical and Experimental Medicine, 5(2), pp. 154-164.

Bergström, M., Collins, V.P., Ehrin, E., Ericson, K., Eriksson, L., Greitz, T., Halldin, C., von Holst, H., Långström, B. and Lilja, A. (1983) 'Discrepancies in brain tumor extent as shown by computed tomography and positron emission tomography using [68Ga]EDTA, [11C]glucose, and [11C]methionine', Journal of computer assisted tomography, 7(6), pp. 1062-1066.

Beyer, T., Townsend, D., Czernin, J. and Freudenberg, L. (2011) 'The future of hybrid imaging—part 2: PET/CT', Insights into Imaging, 2(3), pp. 225-234.

Bohndiek, S.E., Kettunen, M.I., Hu, D.-e., Witney, T.H., Kennedy, B.W.C., Gallagher, F.A. and Brindle, K.M. (2010) 'Detection of Tumor Response to a Vascular Disrupting Agent by Hyperpolarized 13C Magnetic Resonance Spectroscopy', Molecular Cancer Therapeutics, 9(12), pp. 3278-3288.

Bradbury, D.A., Simmons, T.D., Slater, K.J. and Crouch, S.P.M. (2000) 'Measurement of the ADP:ATP ratio in human leukaemic cell lines can be used as an indicator of cell viability, necrosis and apoptosis', Journal of Immunological Methods, 240(1–2), pp. 79-92.

Bradley, D.P., Tessier, J.L., Checkley, D., Kuribayashi, H., Waterton, J.C., Kendrew, J. and Wedge, S.R. (2008) 'Effects of AZD2171 and vandetanib (ZD6474, Zactima) on haemodynamic variables in an SW620 human colon tumour model: an investigation using dynamic contrast-enhanced MRI and the rapid clearance blood pool contrast agent, P792 (gadomelitol)', NMR in Biomedicine, 21(1), pp. 42-52.

Bremner, J.C.M., Counsell, C.J.R., Adams, G.E., Stratford, I.J., Wood, P.J., Dunn, J.F. and Radda, G.K. (1991) 'In vivo 31P nuclear magnetic resonance spectroscopy of experimental murine tumours and human tumour xenografts: effects of blood flow modification', British Journal of Cancer, 64(5), pp. 862-866.

Brosnan, J.T., Krebs, H.A. and Williamson, D.H. (1970) 'Effects of ischaemia on metabolite concentrations in rat liver', Biochemistry Journal, 117(1), pp. 91-96.
Brown, J.M. (1973) 'A Study of the Mechanism by Which Anticoagulation with Warfarin Inhibits Blood-borne Metastases', Cancer Research, 33(6), pp. 1217-1224.

Bryant, H.E., Schultz, N., Thomas, H.D., Parker, K.M., Flower, D., Lopez, E., Kyle, S., Meuth, M., Curtin, N.J. and Helleday, T. (2005) 'Specific killing of BRCA2-deficient tumours with inhibitors of poly(ADP-ribose) polymerase', Nature, 434(7035), pp. 913-917.

Buxton, R.B. (2002) Introduction to Functional Magnetic Resonance Imaging Principles and Techniques. Cambridge University Press.

Calabrese, C.R., Almassy, R., Barton, S., Batey, M.A., Calvert, A.H., Canan-Koch, S., Durkaz, B.W., Hostomsky, Z., A. Kumpf, R., Kyle, S., Li, J., Maegley, K., Newell, D.R., Notarianni, E., Stratford, I.J., Skalitzky, D., Thomas, H.D., Wang, L.-Z., Webber, S.E., Williams, K.J. and Curtin, N.J. (2004) 'Anticancer Chemosensitization and Radiosensitization by the Novel Poly(ADP-ribose) Polymerase-1 Inhibitor AG014361', Journal of the National Cancer Institute, 96(1), pp. 56-67.

Calabrese, C.R., Batey, M.A., Thomas, H.D., Durkacz, B., Wang, L.-Z., Kyle, S., Skalitzky, D., Li, J., Zhang, C., Boritzki, T., Maegley, K., Calvert, A.H., Hostomsky, Z., Newell, D.R. and Curtin, N.J. (2003) 'Identification of Potent Nontoxic Poly(ADP-Ribose) Polymerase-1 inhibitors: Chemopotentiation and Pharmacological Studies', Clinical Cancer Research, 9(7), pp. 2711-2718.

Calvert, H. and Azzariti, A. (2011) 'The clinical development of inhibitors of poly(ADP-ribose) polymerase', Annals of Oncology, 22(suppl 1), pp. i53-i59.

Carlin, S., Pugachev, A., Sun, X., Burke, S., Claus, F., O'Donoghue, J., Ling, C.C. and Humm, J.L. (2009) 'In vivo characterization of a reporter gene system for imaging hypoxia-induced gene expression', Nuclear Medicine and Biology, 36(7), pp. 821-831.

Castellani, U., Cristani, M., Daducci, A., Farace, P., Marzola, P., Murino, V. and Sbarbati, A. (2009) 'DCE-MRI Data Analysis for Cancer Area Classification', Methods of Information in Medicine, 48(3), pp. 248-253.

Cavone, L. and Chiarugi, A. (2012) 'Targeting poly(ADP-ribose) polymerase-1 as a promising approach for immunomodulation in multiple sclerosis?', Trends in Molecular Medicine, 18(2), pp. 92-100.

Chambon, P., Weill, J.D. and Mandel, P. (1963) 'Nicotinamide mononucleotide activation of a new DNA-dependent polyadenylic acid synthesizing nuclear enzyme', Biochemical and Biophysical Research Communications, 11(1), pp. 39-43.

ChemSpider rucaparib 2D. http://www.chemspider.com/ImageView.aspx?id=8107584&mode=2d http://www.chemspider.com/Chemical-Structure.8107584.html ChemSpider, CSID:8107584, png.

ChemSpider rucaparib 3D. http://www.chemspider.com/ImageView.aspx?id=8107584&mode=3d http://www.chemspider.com/Chemical-Structure.8107584.html ChemSpider, CSID:8107584, png.

Chen, R., Brentnall, T.A., Pan, S., Cooke, K., Moyes, K.W., Lane, Z., Crispin, D.A., Goodlett, D.R., Aebersold, R. and Bronner, M.P. (2007) 'Quantitative Proteomics Analysis Reveals That Proteins Differentially Expressed in Chronic Pancreatitis Are Also Frequently Involved in Pancreatic Cancer', Molecular & Cellular Proteomics, 6(8), pp. 1331-1342.

Cheng, H.L.M. (2009) ‘Improved Correlation to Quantitative DCE-MRI Pharmacokinetic Parameters Using a Modified Initial Area Under the Uptake Curve (mIAUC) Approach’, Journal of Magnetic Resonance Imaging, 30(4), pp. 864-872.

Chia, R., Achilli, F., Festing, M.F.W. and Fisher, E.M.C. (2005) 'The origins and uses of mouse outbred stocks', Nature Genetics, 37(11), pp. 1181-1186.

Cohen, E., Ophir, I. and Shaul, Y.B. (1999) 'Induced differentiation in HT29, a human colon adenocarcinoma cell line', Journal of Cell Science, 112(16), pp. 2657-2666.

Corbin, I.R., Buist, R., Peeling, J., Zhang, M., Uhanova, J. and Minuk, G.Y. (2003) 'Hepatic 31P MRS in rat models of chronic liver disease: assessing the extent and progression of disease', International Journal of Gastroenterology and Hepatology, 52(7), pp. 1046-1053.

Corroyer-Dulmont, A., Pérès, E.A., Petit, E., Guillamo, J.-S., Varoqueaux, N., Roussel, S., Toutain, J., Divoux, D., MacKenzie, E.T., Delamare, J., Ibazizène, M., Lecocq, M., Jacobs, A.H., Barré, L., Bernaudin, M. and Valable, S. (2013) 'Detection of glioblastoma response to temozolomide combined with bevacizumab based on µMRI and µPET imaging reveals [18F]-fluoro-l-thymidine as an early and robust predictive marker for treatment efficacy', Neuro Oncology, 15(1) 41-56 (published online October 2012).

Cristofanilli, M., Budd, G.T., Ellis, M.J., Stopeck, A., Matera, J., Miller, M.C., Reuben, J.M., Doyle, G.V., Allard, W.J., Terstappen, L.W.M.M. and Hayes, D.F. (2004) 'Circulating Tumor Cells, Disease Progression, and Survival in Metastatic Breast Cancer', New England Journal of Medicine, 351(8), pp. 781-791.

Curtin, N.J. (2005) 'PARP inhibitors for cancer therapy', Expert Reviews in Molecular Medicine, 7(4), pp. 1-20.

Daniel, R.A., Rozanska, A.L., Thomas, H.D., Mulligan, E.A., Drew, Y., Castelbuono, D.J., Hostomsky, Z., Plummer, E.R., Boddy, A.V., Tweeddle, D.A., Curtin, N.J. and Clifford, S.C. (2009) 'Inhibition of Poly(ADP-Ribose) Polymerase-1 Enhances Temozolomide and Topotecan Activity against Childhood Neuroblastoma', Clinical Cancer Research, 15(4), pp. 1241-1249.

de Graaf, R.A. (2007) in vivo NMR Spectroscopy: Principles and Techniques. 2nd Edition edn. John Wiley & Sons, Ltd.

de Murcia, J.M., Niedergang, C., Trucco, C., Ricoul, M., Dutrillaux, B., Mark, M., Oliver, F.J., Masson, M., Dierich, A., LeMeur, M., Walztinger, C., Chambon, P. and de Murcia, G. (1997) 'Requirement of poly(ADP-ribose) polymerase in recovery from DNA damage in mice and in cells', Proceedings of the National Academy of Sciences, 94(14), pp. 7303-7307.

de Murcia, J.M., Ricoul, M. Tartier, L., Niedergang, C., Huber, A., Dantzer, F., Schreiber, V., Amé, J.C., Dierich, A., LeMeur, M., Sabatier, L., Chambon, P. and de Murcia, G. (2003) ‘Functional interaction between PARP-1 and PARP-2 in chromosome stability and embryonic development in mouse’, The EMBO Journal, 22(9), pp. 2255-2263

De Soto, J.A. and Deng, C.X. (2006) ‘PARP-1 inhibitors: are they the long-sought genetically specific drugs for BRCA1/2-associated breast cancers?’, International Journal of Medical Sciences, 3(4), pp. 117-123.

De Vos, M., Schreiber, V. and Dantzer, F. (2012) 'The diverse roles and clinical relevance of PARPs in DNA damage repair: Current state of the art', Biochemical Pharmacology, 84(2), pp. 134-146.

Drabovich, A.P., Pavlou, M.P., Dimitromanolakis, A. and Diamandis, E.P. (2012) 'Quantitative analysis of energy metabolic pathways in MCF-7 breast cancer cells by selected reaction monitoring assay', Molecular & Cellular Proteomics, 11, pp. 422-434.

Dresel, S. (2007) PET in oncology. Springer.

Dumas, S., Jacques, V., Sun, W.C., Troughton, J.S., Welch, J.T., Chasse, J.M., Schmitt-Willich, H. and Caravan, P. (2010) 'High relaxivity MRI contrast agents part 1: Impact of single donor atom substitution on relaxivity of serum albumin-bound gadolinium complexes', Investigative Radiology, 45(10), pp. 600-612.

Durkacz, B., Omidiji, O., Gray, D.A. and Shall, S. (1980) '(ADP-ribose)n participates in DNA excision repair', Nature, 283, pp. 593-596.

Ebenhan, T., Honer, M., Ametamey, S.M., Schubiger, P.A., Becquet, M., Ferretti, S., Cannet, C., Rausch, M. and McSheehy, P.M.J. (2009) 'Comparison of [18F]-Tracers in Various Experimental Tumor Models by PET Imaging and Identification of an Early Response Biomarker for the Novel Microtubule Stabilizer Patupilone', Molecular Imaging and Biology, 11(5), pp. 308-321.

Farmer, H., McCabe, N., Lord, C.J., Tutt, A.N.J., Johnson, D.A., Richardson, T.B., Santarosa, M., Dillon, K.J., Hickson, I., Knights, C., Martin, N.M.B., Jackson, S.P., Smith, G.C.M. and Ashworth, A. (2005) 'Targeting the DNA repair defect in BRCA mutant cells as a therapeutic strategy', Nature, 434(7035), pp. 917-921.

Feinberg, A.P., Ohlsson, R. and Henikoff, S. (2006) 'The epigenetic progenitor origin of human cancer', Nature Reviews Genetics, 7(1), pp. 21-33.

Foerster, A. (1865) Handbuch der Allgemeinen Pathologischen Anatomie. Voss.

Gadian, D.G. (1995) NMR and its application to living systems, Oxford Science Publications, Second Edition.

Gaya, A.M. and Rustin, G.J.S. (2005) 'Vascular disrupting agents: a new class of drug in cancer therapy', Clinical Oncology, 17(4), pp. 277-290.

Ginos, J.Z., Cooper, A.J.L., Dhawan, V., Lai, J.C.K., Strother, S.C., Alcock, N. and Rottenberg, D.A. (1987) '[13N]Cisplatin PET to Assess Pharmacokinetics of Intra-Arterial versus Intravenous Chemotherapy for Malignant Brain Tumors', Journal of Nuclear Medicine, 28(12), pp. 1844-1852.

Greaves, M. (2010) 'Cancer stem cells: Back to Darwin?', Seminars in Cancer Biology, 20(2), pp. 65-70.

Grierson, J.R., Schwartz, J.L., Muzi, M., Jordan, R. and Krohn, K.A. (2004) 'Metabolism of 3'-deoxy-3'-[F-18]fluorothymidine in proliferating A549 cells: Validations for positron emission tomography', Nuclear Medicine and Biology, 31(7), pp. 829-837.

Grierson, J.R. and Shields, A.F. (2000) 'Radiosynthesis of 3′-deoxy-3′-[18F]fluorothymidine: [18F]FLT for imaging of cellular proliferation in vivo', Nuclear Medicine and Biology, 27(2), pp. 143-156.

Haider, M.A., van der Kwast, T.H., Tanguay, J., Evans, A.J., Hashmi, A.-T., Lockwood, G. and Trachtenberg, J. (2007) 'Combined T2-Weighted and Diffusion-Weighted MRI for Localization of Prostate Cancer', American Journal of Roentgenology, 189(2), pp. 323-328.

Hanahan, D. and Coussens, L.M. (2012) 'Acessories to the Crime: Functions of cells Recruited to the Tumor Microenvironment', Cancer Cell, 21(3), pp. 309-322.

Hanahan, D. and Weinberg, R.A. (2011) 'Hallmarks of Cancer: The Next Generation', Cell, 144(5), pp. 646-674.

Hara, T. (2001) '18F-Fluorocholine: A New Oncologic PET Tracer', Journal of Nuclear Medicine, 42(12), pp. 1815-1817.

Harlow, E., Crawford, L.V., Pim, D.C. and Williamson, N.M. (1981) 'Monoclonal antibodies specific for simian virus 40 tumor antigens', Journal of Virology, 39(3), pp. 861-869.

Hashemi, R.H., Bradley Jr., W.G. and Lisanti, C.J. (2003) MRI The Basics. Lippincott Williams & Wilkins.

Hassa, P.O., Haenni, S.S., Elser, M. and Hottiger, M.O. (2006), ‘Nuclear ADP-Ribosylation Reactions in Mammalian Cells: Where Are We Today and Where Are We Going?’ Microbiology and Molecular Biology Reviews, 70(3), pp. 789-829.

Hattingen, E., Jurcoane, A., Bähr, O., Rieger, J., Magerkurth, J., Anti, S., Steinbach, J.S. and Pilatus, U. (2011), ‘Bevacizumab impairs oxidative energy metabolism and shows antitumoral effects in recurrent glioblastomas: a 31P/1H MRSI and quantitative magnetic resonance imaging study’, Neuro-Oncology, 13(12), pp. 1349-1363.

Hay, T., Jenkins, H., Sansom, O.J., Martin, N.M.B., Smith, G.C.M. and Clarke, A.R. (2005) 'Efficient Deletion of Normal *Brca2*-Deficient Intestinal Epithelium by Poly(ADP-Ribose) Polymerase Inhibition Models Potential Prophylactic Therapy', Cancer Research, 65(22), pp. 10145-10148.

He, Y.-x. and Guo, Q.-y. (2008) 'Clinical applications and advances of positron emission tomography with fluorine-18-fluorodeoxyglucose (18F-FDG) in the diagnosis of liver neoplasms', Postgraduate Medical Journal, 84(991), pp. 246-251.

Ho, C.-L., Yu, S.C.H. and Yeung, D.W.C. (2003) '11C-Acetate PET Imaging in Hepatocellular Carcinoma and Other Liver Masses', Journal of Nuclear Medicine, 44(2), pp. 213-221.

Honer, M., Ebenhan, T., Allegrini, P.R., Ametamey, S.M., Becquet, M., Cannet, C., Lane, H.A., O'Reilly, T.M., Schubiger, P.A., Sticker-Jantscheff, M., Stumm, M. and McSheehy, P.M. (2010) 'Anti-Angiogenic/Vascular Effects of the mTOR Inhibitor Everolimus Are Not Detectable by FDG/FLT-PET', Translational Oncology, 3(4), pp. 264-275.

Horsman, M.R. (1995) 'Nicotinamide and Other Benzamide Analogs as Agents for Overcoming Hypoxic Cell Radiation Resistance in Tumours', Acta Oncologica, 34(5), pp. 571-587.

Horsman, M.R., Christensen, K.L. and Overgaard, J. (1992) 'Relationship between the hydralazine-induced changes in murine tumor blood supply and mouse blood pressure', International Journal of Radiation Oncology*Biology*Physics, 22(3), pp. 455-458.

Horsman, M.R., Khalil, A.A., Chaplin, D.J. and Overgaard, J. (1995) 'The Ability of Nicotinamide to Inhibit the Growth of a C3H Mouse Mammary Carcinoma', Acta Oncologica, 34(3), pp. 443-446.

Hottiger, M.O. (2011) 'ADP-ribosylation of histones by ARTD1: An additional module of the histone code?', FEBS Letters, 585(11), pp. 1595-1599.

Howe, F.A., Stubbs, M., Rodrigues, L.M. and Griffiths, J.R. (1993) 'An assessment of artifacts in localized and non-localized 31P MRS studies of phosphate metabolites and pH in rat tumours', NMR in Biomedicine, 6(1), pp. 43-52.

Hudson, H.M. and Larkin, R.S. (1994) 'Accelerated Image Reconstruction Using Ordered Subsets of Projection Data', IEEE Transaction on Medical Imaging, 13(4), pp. 601-609.

Iles, R.A., Stevens, A.N., Griffiths, J.R. and Morris, P.G. (1985) 'Phosphorylation status of liver by 31P-n.m.r. spectroscopy, and its implications for metabolic control. A comparison of 31P-n.m.r. spectroscopy (in vivo and in vitro) with chemical and enzymic determinations of ATP, ADP and Pi.', Biochemistry Journal, 229(1), pp. 141-151.

Inoue, T., Kim, E.E., Wallace, S., Yang, D.J., Wong, F.C.L., Bassa, P., Cherif, A., Delpassand, E., Buzdar, A. and Podoloff, D.A. (2009) 'Positron Emission Tomography using [18F]fluorotamoxifen to Evaluate Therapeutic Responses in Patients with Breast Cancer: Preliminary Study', Cancer Biotherapy & Radiopharmaceuticals, 11(4), pp. 235-245.

Jackson, A., Buckley, D.L. and Parker, G.J.M. (2005) Dynamic Contrast-Enhanced Magnetic Resonance Imaging in Oncology. Springer.

Jackson, S.P. and Bartek, J. (2009) 'The DNA-damage response in human biology and disease', Nature, 461(7267), pp. 1071-1078.

Jagtap, P. and Szabo, C. (2005) 'Poly(ADP-ribose) polymerase and the therapeutic effects of its inhibitors', Nature Reviews Drug Discovery, 4(5), pp. 421-440.

Jamin, Y., Gabellieri, C., Smyth, L., Reynolds, S., Robinson, S.P., Springer, C.J., Leach, M.O., Payne, G.S. and Eykyn, T.R. (2009) 'Hyperpolarized 13C magnetic resonance detection of carboxypeptidase G2 activity', Magnetic Resonance in Medicine, 62(5), pp. 1300-1304.

Jensen, L.R., Huuse, E.M., Bathen, T.F., Goa, P.E., Bofin, A.M., Pedersen, T.B., Lundgren, S. and Gribbestad, I.S. (2010) 'Assessment of early docetaxel response in an experimental model of human breast cancer using DCE-MRI, ex vivo HR MAS, and in vivo1H MRS', NMR in Biomedicine, 23(1), pp. 56-65.

Jeswani, T. and Padhani, A.R. (2005) 'Imaging tumour angiogenesis', Cancer Imaging 5(1), pp. 131-138.

Jones, A.M., Wilkerson, D.P., DiMenna, F., Fulford, J. and Poole, D.C. (2008) 'Muscle metabolic responses to exercise above and below the “critical power” assessed using 31P-MRS', American Journal of Physiology - Regulatory, Integrative and Comparative Physiology, 294(2), pp. R585-R593.

Jones, H.B. (1848) 'On a New Substance Occuring in the Urine of a Patient with Mollities Ossium', Philosophical Transactions of the Royal Society 138, pp. 55-62.

Keepers, J.W. and James, T.L. (1984) 'A theoretical study of distance determinations from NMR. Two-dimensional nuclear overhauser effect spectra', Journal of Magnetic Resonance (1969), 57(3), pp. 404-426.

Kimura, H., Itoh, S., Kawamura, Y., Nakatsugawa, S. and Ishii, Y. (1994) 'Metabolic alterations in implanted human tumors after combined radiation and hyperthermia therapy measured by in vivo 31P MRS', Magnetic Resonance Imaging, 12(1), pp. 109-119.

Kirkland, J.B. (2010) 'Poly ADP-ribose polymerase-1 and health', Experimental Biology and Medicine, 235(5), pp. 561-568.

Kluetz, P.G., Figg, W.D. and Dahut, W.L. (2010) 'Angiogenesis inhibitors in the treatment of prostate cancer', Expert Opinion on Pharmacotherapy, 11(2), pp. 233-247.

Kummar, S., Chen, A., Parchment, R., Kinders, R., Ji, J., Tomaszewski, J. and Doroshow, J. (2012) 'Advances in using PARP inhibitors to treat cancer', BMC Medicine, 10(1), p. 25.

Kurdziel, K., Figg, W., Carrasquillo, J., Huebsch, S., Whatley, M., Sellers, D., Libutti, S., Pluda, J., Dahut, W., Reed, E. and Bacharach, S. (2003) 'Using positron emission tomography 2-deoxy-2-[18F]fluoro-D-glucose, 11CO, and 15O-water for monitoring androgen independent prostate cancer', Molecular Imaging and Biology, 5(2), pp. 86-93.

Langen, K.-J., Hamacher, K., Weckesser, M., Floeth, F., Stoffels, G., Bauer, D., Coenen, H.H. and Pauleit, D. (2006) 'O-(2-[18F]fluoroethyl)-l-tyrosine: uptake mechanisms and clinical applications', Nuclear Medicine and Biology, 33(3), pp. 287-294.

Langen, K.-J., Tatsch, K., Grosu, A.-L., Jacobs, A.H., Weckesser, M. and Sabri, O. (2008) 'Diagnostics of Cerebral Gliomas With Radiolabeled Amino Acids', Deutsches Ärzteblatt International, 105(4), pp. 55-61.

Lankester, K.J., Taylor, N.J., Stirling, J.J., Boxall, J., D'Arcy, J.A., Leach, M.O., Rustin, G.J.S. and Padhani, A.R. (2005) 'Effects of platinum/taxane based chemotherapy on acute perfusion in human pelvic tumour measured by dynamic MRI', British Journal of Cancer, 93(9), pp. 979-985.

Leung, M., Rosen, D., Fields, S., Cesano, A. and Budman, D.R. (2011) 'Poly(ADP-Ribose) Polymerase-1 Inhibition: Preclinical and Clinical Development of Synthetic Lethality', Molecular Medicine, 17(7-8), pp. 854-862.

Leach, M.O., Brindle, K.M., Evelhoch, J.L., Griffiths, J.R., Horsman, M.R., Jackson, A., Jayson, G., Judson, I.R., Knopp, M.V., Maxwell, R.J., McIntyre, D.,

Padhani, A.R., Price, P., Rathbone, R., Rustin, G., Tofts, P.S., Tozer, G.M., Vennart, W., Waterton, J.C., Williams, S.R., and Workman, P. (2003) ‘Assessment of antiangiogenic and antivascular therapeutics using MRI: recommendations for appropriate methodology for clinical trials’, The British Journal of Radiology, 76 (special number 1) pp. S87-S91.

Li, P.Y. and Lin, C. (1995) ‘Establishment of Adriamycin-resistant human ovarian carcinoma cell line and its mechanism of multidrug resistance’, Acta Pharmaceutica Sinica, 30(4), pp. 258-262.

Li, J., Zhang, Z., Rosenzweig, J., Wang, Y.Y. and Chan, D.W. (2002) 'Proteomics and Bioinformatics Approaches for Identification of Serum Biomarkers to Detect Breast Cancer', Clinical Chemistry, 48(8), pp. 1296-1304.

Lin, C.Y., Wu, H., Tjeerdema, R.S. and Viant, M.R. (2007) ‘Evaluation of metabolite extraction strategies from tissue samples using NMR metabolomics’. Metabolomics, 3(1), pp. 55-67.

Lindhal, T. (1993) 'Instability and decay of the primary structure of DNA', Nature, 362(6422), pp. 709-715.

Lutz, N.W., Yahi, N., Fantini, J. and Cozzone, P.J. (1996) 'Analysis of individual purine and pyrimidine nucleoside di- and triphosphates and other cellular metabolites in PCA extracts by using multinuclear high resolution NMR spectroscopy', Magnetic Resonance in Medicine, 36(5), pp. 788-795.

Machulla, H.-J., Blocher, A., Kuntzsch, M., Piert, M., Wei, R. and Grierson, J.R. (2000) 'Simplified labelling approach for synthesizing 3'-deoxy-3'-[18F]fluorothymidine ([18F]FLT)', Journal of Radioanalytical and Nuclear Chemistry, 243(3), pp. 843-846.

Mani, V., Chikkaveeraiah, B.V. and Rusling, J.F. (2011) 'Magnetic particles in ultrasensitive biomarker protein measurements for cancer detection and monitoring', Expert Opinion on Medical Diagnostics, 5(5), pp. 381-391.

Maxwell, R.J., Wilson, J., Prise, V.E., Vojnovic, B., Rustin, G.J., Lodge, M.A. and Tozer, G.M. (2002) 'Evaluation of the anti-vascular effects of combretastatin in rodent tumours by dynamic contrast enhanced MRI', NMR in Biomedicine, 15(2), pp. 89-98.

Maybaum, J., Burton, E.C., Shelton, D.A., Jing, H.W., Dusenbury, C.E., Ensminger, W.D. and Stetson, P.L. (1991), ‘Divergent patterns of incorporation of Bromodeoxyuridine and iododeoxyuridine in human colorectal tumor cell lines’, Biochemical Pharmacology, 42(1), pp. 131-137.

McIntyre, D.J.O., Robinson, S.P., Howe, F.A., Griffiths, J.R., Ryan, A.J., Blakey, D.C., Peers, I.S. and Waterton, J.C. (2004) 'Single Dose of the Antivascular Agent, ZD6126 (N-Acetylcolchinol-O-Phosphate), Reduces Perfusion for at Least 96 Hours in the GH3 Prolactinoma Rat Tumor Model', Neoplasia, 6(2), pp. 150-157.

Mileshkin, L., Hicks, R.J., Hughes, B.G.M., Mitchell, P., Charu, V., Gitlitz, B.J., Macfarlane, D., Solomon, B., Amler, L., Yu, W., Pirzkall, A. and Fine, B.M. (2011) 'Changes in FDG- and FLT-PET Imaging in Patients with Non-Small Cell Lung Cancer Treated with Erlotinib', Clinical Cancer Research, 17, pp. 3304-3315.

Mishra, A. and Verma, M. (2010) 'Cancer Biomarkers: Are We Ready for the Prime Time?', Cancers, 2(1), pp. 190-208.

Moroz, M.A., Kochetkov, T., Cai, S., Wu, J., Shamis, M., Nair, J., de Stanchina, E., Serganova, I., Schwartz, G.K., Banerjee, D., Bertino, J.R. and Blasberg, R.G. (2011) 'Imaging Colon Cancer Response Following Treatment with AZD1152: A Preclinical Analysis of [18F]Fluoro-2-deoxyglucose and 3′-deoxy-3′-[18F]Fluorothymidine Imaging', Clinical Cancer Research, 17(5), pp. 1099-1110.

Munk Jensen, M., Erichsen, K.D., Björkling, F., Madsen, J., Jensen, P.B., Højgaard, L., Sehested, M. and Kjær, A. (2010) 'Early Detection of Response to Experimental Chemotherapeutic Top216 with [18F]FLT and [18F]FDG PET in Human Ovary Cancer Xenografts in Mice', PLoS ONE, 5(9), p. e12965.

Nath, K., Nelson, D.S., Ho, A.M., Lee, S.-C., Darpolor, M.M., Pickup, S., Zhou, R., Heitjan, D.F., Leeper, D.B. and Glickson, J.D. (2012) '31P and 1H MRS of DB-1 melanoma xenografts: lonidamine selectively decreases tumor intracellular pH and energy status and sensitizes tumors to melphalan', NMR in Biomedicine, pp. n/a-n/a.

Neumann, F., Borchert, S., Schmidt, C., Reimer, R., Hohenberg, H., Fischer, N. and Grundhoff, A. (2011) 'Replication, Gene Expression and Particle Production by a Consensus Merkel Cell Polyomavirus (MCPyV) Genome', PLoS ONE, 6(12), p. e29112.

Newton, K.F., Newman, W. and Hill, J. (2011) 'Review of biomarkers in colorectal cancer', Colorectal Disease, 14(1), pp. 3-17.

Nijsten, M.W.N. and van Dam, G.M. (2009) 'Hypothesis: Using the Warburg effect against cancer by reducing glucose and providing lactate', Medical Hypotheses, 73(1), pp. 48-51.

Nordsmark, M., Maxwell, R.J., Horsman, M.R., Bentzen, S.M. and Overgaard, J. (1997) 'The effect of hypoxia and hyperoxia on nucleoside triphosphate/inorganic phosphate, pO2 and radiation response in an experimental tumour model.', British Journal of Cancer, 76(11), pp. 1432-1439.

Nordsmark, M., Maxwell, R.J., Wood, P.J., Stratford, I.J., Adams, G.E., Overgaard, J. and Horsman, M.R. (1996) 'Effect of hydralazine in spontaneous tumours assessed by oxygen electrodes and 31P-magnetic resonance spectroscopy', British Journal of Cancer, 74(Supplement XXVII), pp. S232-S235.

Nowell, P.C. (1976) 'The clonal evolution of tumour cell populations', Science, 194(4260), pp. 23-28.

O'Connor, J.P.B., Jackson, A., Parker, G.J.M. and Jayson, G.C. (2007) 'DCE-MRI biomarker in the clinical evaluation of antiangiogenic and vascular disrupting agents', British Journal of Cancer, 96(2), pp. 189-195.

Oh, S.J., Mosdzianowski, C., Chi, D.Y., Kim, J.Y., Kang, S.H., Ryu, J.S., Yeo, J.S. and Moon, D.H. (2004) 'Fully automated synthesis system of 3′-deoxy-3′-[18F]fluorothymidine', Nuclear Medicine and Biology, 31(6), pp. 803-809.

Olsson, A., Sheng, Y., Kjellén, E. and Pero, R.W. (1995) 'In vivo tumor measurement of DNA damage, DNA repair and NAD pools as indicators of radiosensitization by metoclopramide', Carcinogenesis, 16(5), pp. 1029-1035.

Orlando, L., Schiavone, P., Fedele, P., Calvani, N., Nacci, A., Cinefra, M., D'Amico, M., Mazzoni, E., Marino, A., Sponziello, F., Morelli, F., Lombardi, L., Silvestris, N. and Cinieri, S. (2012) 'Poly (ADP-ribose) polymerase (PARP): rationale, preclinical and clinical evidences of its inhibition as breast cancer treatment', Expert Opinion on Therapeutic Targets, 16(Supplement 2), pp. S83-S89.

Payne, J.F. and Bal, A.K. (1976) 'Cytological detection of poly (ADP-ribose) polymerase', Experimental Cell Research, 99(2), pp. 428-432.

Perumal, M., Stronach, E., Gabra, H. and Aboagye, E. (2012) 'Evaluation of 2-Deoxy-2-[18F]Fluoro-D-glucose- and 3′-Deoxy-3′-[18F]Fluorothymidine–Positron Emission Tomography as Biomarkers of Therapy Response in Platinum-Resistant Ovarian Cancer', Molecular Imaging and Biology, 14(6), pp. 753-761.

Pietras, R.J., Pegram, M.D., Finn, R.S., Maneval, D.A. and Slamon, D.J. (1998) 'Remission of human breast cancer xenografts on therapy with humanized monoclonal antibody to HER-2 receptor and DNA-reactive drugs', Oncogene, 17(17), pp. 2235-2249.

Piskunova, T.S., Yurova, M.N., Ovsyannikov, A.I., Semenchenko, A.V., Zabezhinski, M.A., Popovich, I.G., Wang, Z.Q. and Anisimov, V.N., (2008), 'Deficiency in Poly(ADP-ribose) Polymerase-1 (PARP-1) Accelerates Aging and Spontaneous Carcinogenesis in Mice', Current Gerontology and Geriatrics Research, 2008, Article ID 754190, 11 pages.

Rather, L.J. (1978) ‘The genesis of cancer: a study in the history of ideas’, Johns Hopkins University Press.

Rebollo Aguirre, Á.C., Ramos-Font, C., Villegas Portero, R., Cook, G.J.R., Llamas Elvira, J.M. and Tabares, A.R. (2009) '18F-Fluorodeoxiglucose Positron Emission Tomography for the Evaluation of Neoadjuvant Therapy Response in Esophageal Cancer: Systematic Review of the Literature', Annals of Surgery, 250(2), pp. 247-254

Reiner, T., J. Keliher, E., Earley, S., Marinelli, B. and Weissleder, R. (2011) 'Synthesis and In Vivo Imaging of a 18F-Labeled PARP1 Inhibitor Using a Chemically Orthogonal Scavenger-Assisted High-Performance Method', Angewandte Chemie International Edition, 50(8), pp. 1922-1925.

Reiser, M.F., Semmler, W. and Hricak, H. (2008) Magnetic Resonance Tomography. Springer.

Rice, M.C. and O'Brien, S.J. (1980) 'Genetic variance of laboratory outbred Swiss mice', Nature, 283(5743), pp. 157-161.

Robinson, S.P., Howe, F.A., Stubbs, M. and Griffiths, J.R. (2000) 'Effects of nicotinamide and carbogen on tumour oxygenation, blood flow, energetics and blood glucose levels', British Journal of Cancer, 82(12), pp. 2007-2014.

Robinson, S.P., McIntyre, D.J.O., Checkley, D., Tessier, J.J., Howe, F.A., Griffiths, J.R., Ashton, S.E., Ryan, A.J., Blakey, D.C. and Waterton, J.C. (2003) 'Tumour dose response to the antivascular agent ZD6126 assessed by magnetic resonance imaging', British Journal of Cancer, 88(10), pp. 1592-1597.

Rodon, J., Iniesta, M.D. and Papadopoulos, K. (2009) 'Development of PARP inhibitors in oncology', Expert Opinion on Investigational Drugs, 18(1), pp. 31-43.

Ronen, S.M., DiStefano, F., McCoy, C.L., Robertson, D., Smith, T.A.D., Al-Saffar, N.M., Titley, J., Cunningham, D.C., Griffiths, J.R., Leach, M.O. and Clarke, P.A. (1999) 'Magnetic resonance detects metabolic changes associated with chemotherapy-induced apoptosis', British Journal of Cancer, 80(7), pp. 1035-1041.

Rooney, S., Alt, F.W., Lombard, D., Whitlow, S., Eckersdorff, M., Fleming, J., Fugmann, S., Ferguson, D.O., Schatz, D.G. and Sekiguchi, J. (2003) 'Defective DNA Repair and Increased Genomic Instability in Artemis-deficient Murine Cells', The Journal of Experimental Medicine, 197(5), pp. 553-565.

Rouleau, M., Patel, A., Hendzel, M.J., Kaufmann, S.H. and Poirier, G.G. (2010), 'PARP inhibition: PARP1 and beyond', Nature Reviews Cancer, 10(4), pp. 293-301.

Safavi, A. and Tohidi, M. (2007) 'Simultaneous kinetic determination of levodopa and carbidopa by H-point standard addition method', Journal of Pharmaceutical and Biomedical Analysis, 44(1), pp. 313-318.

Saha, G.B. (2005) 'Basics of PET Imaging
Physics, Chemistry, and Regulations', p. 206.

Sakkiadi, A.-V., Georgiou, C.A. and Haroutounian, S.A. (2007) 'A Standard Addition Method to Assay the Concentration of Biologically Interesting Polyphenols in Grape Berries by Reversed-Phase HPLC', Molecules, 12(9), pp. 2259-2269.

Saleem, A., Brown, G.D., Brady, F., Aboagye, E.O., Osman, S., Luthra, S.K., Ranicar, A.S.O., Brock, C.S., Stevens, M.F.G., Newlands, E., Jones, T. and Price, P. (2003) 'Metabolic Activation of Temozolomide Measured in vivo Using Positron Emission Tomography.', Cancer Research, 63(10), pp. 2409-2415.

Sawyers, C.L. (2008) 'The cancer biomarker problem', Nature, 452(7187), pp. 548-552.

Schneider, C.A., Rasband, W.S. and Eliceiri, K.W. (2012), 'NIH Image to ImageJ: 25 years of image analysis', Nature Methods, 9, pp. 671-675.

Schreiber, E. (2008) VnmrJ Imaging User's Guide. Varian, Inc.

Schreiber, V., Dantzer, F., Amé , J.-C. and de Murcia, G. (2006) 'Poly(ADP-ribose): novel functions for an old molecule', Nature Reviews Molecular Cell Biology, 7(7), pp. 517-528.

Schreiber, V., Hunting, D., Trucco, C., Gowans, B., Grunwald, D., De Murcia, G. and De Murcia, J.M. (1995) 'A dominant-negative mutant of human poly(ADP-ribose) polymerase affects cell recovery, apoptosis, and sister chromatid exchange following DNA damage', Proceedings of the National Academy of Sciences, 92(11), pp. 4753-4757.

Schumann, G., Klauke, R. and Büttner, J. (1992) '036 Standard addition in HPLC: A calibration method for the determination of reference method values', Fresenius' Journal of Analytical Chemistry, 343(1), pp. 89-90.

Schwann, T. (1847) Microscopical researches into the accordance in the strcture and growth of animals and plants.

Seki, K.-i., Nishijima, K.-i., Kuge, Y., Tamaki, N., Wiebe, L.I. and Ohkura, K. (2007) 'A novel and efficient synthesis of [2-11C]5-fluorouracil for prognosis of cancer chemotherapy', Journal of Pharmacy & Pharmaceutical Sciences, 10(2), pp. 212-216.

Semmes, O.J., Feng, Z., Adam, B.-L., Banez, L.L., Bigbee, W.L., Campos, D., Cazares, L.H., Chan, D.W., Grizzle, W.E., Izbicka, E., Kagan, J., Malik, G., McLerran, D., Moul, J.W., Partin, A., Prasanna, P., Rosenzweig, J., Sokoll, L.J., Srivastava, S., Srivastava, S., Thompson, I., Welsh, M.J., White, N., Winget, M., Yasui, Y., Zhang, Z. and Zhu, L. (2005) 'Evaluation of Serum Protein Profiling by Surface-Enhanced Laser Desorption/Ionization Time-of-Flight Mass Spectrometry for the Detection of Prostate Cancer: I. Assessment of Platform Reproducibility', Clinical Chemistry, 51(1), pp. 102-112.

Sevastianova, K., Hakkarainen, A., Kotronen, A., Cornér, A., Arkkila, P., Arola, J., Westerbacka, J., Bergholm, R., Lundbom, J., Lundbom, N. and Yki-Järvinen, H. (2010) 'Nonalcoholic Fatty Liver Disease: Detection of Elevated Nicotinamide Adenine Dinucleotide Phosphate with in Vivo 3.0-T 31P MR Spectroscopy with Proton Decoupling1', Radiology, 256(2), pp. 466-473.

Shariatgorji, M., Spacil, Z., Maddalo, G., Cardenas, L.B. and Ilag, L.L. (2009) 'Matrix-free thin-layer chromatography/laser desorption ionization mass spectrometry for facile separation and identification of medicinal alkaloids', Rapid Communications in Mass Spectrometry, 23(23), pp. 3655-3660.

Sharma, S., Kelly, T.K. and Jones, P.A. (2010) 'Epigenetics in cancer', Carcinogenesis, 31(1), pp. 27-36.

Shen, Z. (2011) 'Genomic instability and cancer: an introduction', Journal of Molecular Cell Biology, 3(1), pp. 1-3.

Shi, K., Souvatzoglou, M., Astner, S.T., Vaupel, P., Nüsslin, F., Wilkens, J.J. and Ziegler, S.I. (2010) 'Quantitative Assessment of Hypoxia Kinetic Models by a Cross-Study of Dynamic 18F-FAZA and 15O-H2O in Patients with Head and Neck Tumors', Journal of Nuclear Medicine, 51(9), pp. 1386-1394.

Silver, M.S., Joseph, R.I. and Hoult, D.I. (1984) ‘Highly selective π/2 and π pulse generation’, Journal of Magnetic Resonance, 59(2), pp. 347-351.

Sims, J.L., Berger, S.J. and Berger, N.A. (1981) 'Effects of nicotinamide on NAD and poly (ADP-ribose) metabolism in DNA-damaged human lymphocytes', Journal of Supramolecular Structure and Cellular Biochemistry, 16(3), pp. 281-288.

Singer, R.M. (2010) A Review of gadolinium-based contrast agents in magnetic resonance imaging.

Solanky, B.S., Sanchez-Canon, G.J., Cobbold, J.F.L., Taylor-Robinson, S.D., Bell, J.D., Scudamore, C.L., Ross, E., Holder, J.C., So, P.-W. and Cox, I.J. (2012) 'Metabolic Profiling of the Rat Liver After Chronic Ingestion of Alpha-Naphthylisothiocyanate Using In Vivo and Ex Vivo Magnetic Resonance Spectroscopy', Toxicological Sciences, 126(2), pp. 306-316.

Spagnolo, L., Barbeau, J., Curtin, N.J., Morris, E.P. and Pearl, L.H. (2012) 'Visualization of a DNA-PK/PARP1 complex', Nucleic Acids Research 40(9), pp. 4168-4177.

Stefan, D., Di Cesare, F., Andrasescu, A., Popa, E., Lazariev, A., Vescovo, E., Strbak, O., Williams, S., Starcuk, Z., Cabanas, M., van Ormondt, D. and Graveron-Demilly, D. (2009) 'Quantitation of magnetic resonance spectroscopy signals: the jMRUI software package', Measurement Science and Technology, 20(10), pp. 1-9.

Talebpour, Z., Haghgoo, S. and Shamsipur, M. (2004) '1H nuclear magnetic resonance spectroscopy analysis for simultaneous determination of levodopa, carbidopa and methyldopa in human serum and pharmaceutical formulations', Analytica Chimica Acta, 506(1), pp. 97-104.

Tanaka, S., Louis, D.N., Curry, W.T., Batchelor, T.T. and Dietrich, J. (2012) 'Diagnostic and therapeutic avenues for glioblastoma: no longer a dead end?', Nature Reviews Clinical Oncology, advance online publication.

Thoeny, H.C., De Keyzer, F., Chen, F., Ni, Y., Landuyt, W., Verbeken, E.K., Bosmans, H., Marchal, G. and Hermans, R. (2005) 'Diffusion-weighted MR Imaging in Monitoring the Effect of a Vascular Targeting Agent on Rhabdomyosarcoma in Rats1', Radiology, 234(3), pp. 756-764.

Thomas, C.P., Dixon, R.M., Tian, M., Butler, S.A., Counsell, C.J.R., Bradley, J.K., Adams, G.E. and Radda, G.K. (1994) 'Phosphorus metabolism during growth of lymphoma in mouse liver: a comparison of 31P magnetic resonance spectroscopy in vivo and in vitro[ast]', British Journal of Cancer, 69(4), pp. 633-640.

Thomas, H.D., Calabrese, C.R., Batey, M.A., Canan, S., Hostomsky, Z., Kyle, S., Maegley, K.A., Newell, D.R., Skalitzky, D., Wang, L.-Z., Webber, S.E. and Curtin, N.J. (2007) 'Preclinical selection of a novel poly(ADP-ribose) polymerase inhibitor for clinical trial', Molecular Cancer Therapeutics, 6(3), pp. 945-956.

Tu, Z., Chu, W., Zhang, J., Dence, C.S., Welch, M.J. and Mach, R.H. (2005) 'Synthesis and in vivo evaluation of [11C]PJ34, a potential radiotracer for imaging the role of PARP-1 in necrosis', Nuclear Medicine and Biology, 32(5), pp. 437-443.

Ullrich, R., Backes, H., Li, H., Kracht, L., Miletic, H., Kesper, K., Neumaier, B., Heiss, W.-D., Wienhard, K. and Jacobs, A.H. (2008) 'Glioma Proliferation as Assessed by 3'-Fluoro-3'-Deoxy-l-Thymidine Positron Emission Tomography in Patients with Newly Diagnosed High-Grade Glioma', Clinical Cancer Research, 14(7), pp. 2049-2055.

Van Boogaart, A.D., Howe, F.A., Rodrigues, L.M., Stubbs, M. and Griffiths, J.R. (1995) 'In vivo31p mrs: absolute concentrations, signal-to-noise and prior knowledge', NMR in Biomedicine, 8(2), pp. 87-93.

van den Boogaart, A., Van Hecke, A., Van Huffel, P., Graveron-Demilly, S., van Ormondt, D., de Beer, R. (1996) 'MRUI: a graphical user interface for accurate routine MRS data analysis.' Proceedings of the ESMRMB 13th Annual Meeting, Prague, pp. 318.

van den Boogaart, A. (1997) 'MRUI MANUAL V. 96.3. A user's guide to the Magnetic Resonance User Interface Software Package', Delft Technical University Press, Delft.

Vanhamme, L., Boogaart, A.v.d. and Huffel, S.V. (1997) 'Improved Method for Accurate and Efficient Quantification of MRS Data with Use of Prior Knowledge', Journal of Magnetic Resonance, 129(1), pp. 35-43.

Virág, L. and Szabó, C. (2002) 'The Therapeutic Potential of Poly(ADP-Ribose) Polymerase Inhibitors', Pharmacological Reviews, 54(3), pp. 375-429.
Virchow, R.C. (1859) Cellular Pathology, Special edition.

Visvader, J.E. (2011) 'Cells of origin in cancer', Nature, 469(7330), pp. 314-322.

Wahlberg, E., Karlberg, T., Kouznetsova, E., Markova, N., Macchiarulo, A., Thorsell, A.-G., Pol, E., Frostell, Å., Ekblad, T., Öncü, D., Kull, B., Robertson, G.M., Pellicciari, R., Schüler, H. and Weigelt, J. (2012) 'Family-wide chemical profiling and structural analysis of PARP and tankyrase inhibitors', Nature Biotechnology, 30(3), pp. 283-288.

Walenta, S., Dellian, M., Goetz, A.E., Kuhnle, G.E. and Mueller-Klieser, W. (1992) 'Pixel-to-pixel correlation between images of absolute ATP concentrations and blood flow in tumours.', British Journal of Cancer, 66(6), pp. 1099-1102.

Walker-Samuel, S., Leach, M.O. and Collins, D.J. (2006) 'Evaluation of response to treatment using DCE-MRI: the relationship between initial area under the gadolinium curve (IAUGC) and quantitative pharmacokinetic analysis', Physics in Medicine and Biology, 51(14), pp. 3593-3602.

Walsh, P.S., Metzger, D.A. and Higuchi R. (1991), 'Chelex 100 as a medium for simple extraction of DNA for PCR-based typing from forensic material', Biotechniques, 10(4), pp. 506-513.

Wanek, T., Kuntner, C., Bankstahl, J., Bankstahl, M., Stanek, J., Sauberer, M., Mairinger, S., Strommer, S., Wacheck, V., Löscher, W., Erker, T., Müller, M. and Langer, O. (2012) 'A comparative small-animal PET evaluation of [11C]tariquidar, [11C]elacridar and (R)-[11C]verapamil for detection of P-glycoprotein-expressing murine breast cancer', European Journal of Nuclear Medicine and Molecular Imaging, 39(1), pp. 149-159.

Warburg, O., Wind, F. and Negelein, E. (1927) 'The Metabolism of Tumors in the body', The Journal of General Physiology, 8(6), pp. 519-530.

Weil, M.K. and Chen, A.P. (2011) 'PARP Inhibitor Treatment in Ovarian and Breast Cancer', Current Problems in Cancer, 35(1), pp. 7-50.

Wood, P.J., Stratford, I.J., Sansom, J.M., Cattanach, B.M., Quinney, R.M. and Adams, G.E. (1992) 'The response of spontaneous and transplantable murine tumors to vasoactive agents measured by 31p magnetic resonance spectroscopy', International Journal of Radiation Oncology*Biology*Physics, 22(3), pp. 473-476.

Workman, P., Aboagye, E.O., Chung, Y.-L., Griffiths, J.R., Hart, R., Leach, M.O., Maxwell, R.J., McSheely, P.M.J., Price, P.M. and Zweit, J. (2006) 'Minimally Invasive Pharmacokinetic and Pharmacodynamic Technologies in Hypothesis-Testing Clinical Trials of Innovative Therapies', Journal of the National Cancer Institute, 98(9), pp. 580-598.

Wright, N.A. and Poulsom, R. (2012) 'Omnis cellula e cellula revisited: cell biology as the foundation of pathology', Journal of Pathology, 226(2), pp. 145-147.

Yamada, K., Hara, N., Shibata, T., Osago, H. and Tsuchiya, M. (2006) 'The simultaneous measurement of nicotinamide adenine dinucleotide and related compounds by liquid chromatography/electrospray ionization tandem mass spectrometry', Analytical Biochemistry, 352(2), pp. 282-285.

Yamamoto, Y., Nishiyama, Y., Ishikawa, S., Nakano, J., Soo Chang, S., Bandoh, S., Nobuhiro Kanaji, Haba, R., Kushida, Y. and Ohkawa, M. (2007) 'Correlation of 18F-FLT and 18F-FDG uptake on PET with Ki-67 immunohistochemistry in non-small cell lung cancer ', European Journal of Nuclear Medicine and Molecular Imaging, 34(10), pp. 1610-1616.

Yang, D., Kuang, L.-R., Cherif, A., Tansey, W., Li, C., Lin, W.J., Liu, C.W., Kim, E.E. and Wallace, S. (1993) 'Synthesis of [18F]Fluoroalanine and [18F]Fluorotamoxigen for Imaging Breast Tumours', Journal of Drug Targetinnh, 1, pp. 259-267.

Yang, H., Yang, T., Baur, J.A., Perez, E., Matsui, T., Carmona, J.J., Lamming, Dudley W., Souza-Pinto, N.C., Bohr, V.A., Rosenzweig, A., de Cabo, R., Sauve, Anthony A. and Sinclair, D.A. (2007) 'Nutrient-Sensitive Mitochondrial NAD+ Levels Dictate Cell Survival', Cell, 130(6), pp. 1095-1107.

Yoon, H., Catalano, P., Murphy, K., Skaar, T., Philips, S., Powell, M., Montgomery, E., Hafez, M., Offer, S., Liu, G., Meltzer, S., Wu, X., Forastiere, A., Benson, A., Kleinberg, L. and Gibson, M. (2011) 'Genetic variation in DNA-repair pathways and response to radiochemotherapy in esophageal adenocarcinoma: a retrospective cohort study of the Eastern Cooperative Oncology Group', BMC Cancer, 11(1), pp. 176-183.

Yuan, Z., Ye, X.-D., Dong, S., Xu, L.-C. and Xiao, X.-S. (2011) 'Evaluation of Early Imaging Response After Chemoembolization of Hepatocellular Carcinoma by Phosphorus-31 Magnetic Resonance Spectroscopy—Initial Experience', Journal of vascular and interventional radiology : JVIR, 22(8), pp. 1166-1173.

Yun, M., Oh, S.J., Ha, H.-J., Ryu, J.S. and Moon, D.H. (2003) 'High radiochemical yield synthesis of 3′-deoxy-3′-[18F]fluorothymidine using (5′-O-dimethoxytrityl-2′-deoxy-3′-O-nosyl-β-D-threo pentofuranosyl)thymine and its 3-N-BOC-protected analogue as a labeling precursor', Nuclear Medicine and Biology, 30(2), pp. 151-157.

Zhang, M., Herion, T.W., Timke, C., Han, N., Hauser, K., Weber, K.J., Peschke, P., Wirkner, U., Lahn, M. and Huber, P.E. (2011) 'Trimodal Glioblastoma Treatment Consisting of Concurrent Radiotherapy, Temozolomide, and the Novel TGF-β Receptor I Kinase Inhibitor LY2109761', Neoplasia, 13(9), pp. 537-549.

Zissen, M.H., Kunz, P., Subbarayan, M., Chin, F.T., Conti, P.S., Fisher, G.A. and Quon, A. (2011) '18F-5-fluorouracil dynamic positron emission tomography/computed tomography shows decreased tracer activity after bevacizumab in colorectal metastases', Nuclear Medicine Communications, 32(5), pp. 343-347.